Development of Biocatalysts for Organic Synthesis by Protein Engineering based on Metal Replacement and Directed Evolution

Wissenschaftliche Arbeit
zur Erlangung des
Doktorgrades der Naturwissenschaften
(Dr. rer. nat.)

vorgelegt der
Fakultät für Chemie
der Universität Bielefeld

Ji Eun Choi

aus Seoul, Südkorea

Januar 2020

Development of Biocatalysts for Organic Synthesis by Protein Engineering based on Metal Replacement and Directed Evolution

Wissenschaftliche Arbeit
zur Erlangung des
Doktorgrades der Naturwissenschaften
(Dr. rer. nat.)

vorgelegt der
Fakultät für Chemie
der Universität Bielefeld

Ji Eun Choi

aus Seoul, Südkorea

Januar 2020

Erstgutachter: Prof. Dr. Harald Gröger

Zweitgutachter: Prof. Dr. Gabriele Fischer von Mollard

Ort: Bielefeld

Die vorliegende Arbeit wurde an der Fakultät für Chemie der Universität Bielefeld im Arbeitskreis Industrielle Organische Chemie und Biotechnologie unter Leitung von Prof. Dr. Harald Gröger im Zeitraum von Oktober 2015 bis November 2019 angefertigt.
Zudem wurde im Enzyme Laboratory des Biotechnology Research Center der Toyama Prefectural University, Toyama, Japan, im April 2018 daran gearbeitet. Darüber hinaus wurde die vorliegende Arbeit von dem Deutschen Akademischen Austauschdienst (DAAD) und der Japan Society for the Promotion of Science (JSPS) unter dem gemeinschaftlichen Programm für Bildungsförderung "PPP Japan 2017" gefördert (DAAD Bewilligungsnummer: 57345566). Zusätzlich wurde diese Arbeit von 2015 bis 2018 von der API Corporation unterstützt.

Diese Dissertation wurde selbstständig verfasst und hat weder in aktueller oder anderer Fassung einer anderen Fakultät oder Hochschule vorgelegen. Sie wurde bisher nicht als Prüfungsarbeit für eine staatliche oder andere wissenschaftliche Prüfung eingereicht. Dritte haben weder unmittelbar noch mittelbar geldwerte Leistungen für Vermittlungstätigkeiten oder für Arbeiten von der Verfasserin erhalten, die im Zusammnehang mit dem Inhalt dieser Dissertation stehen.

Es wurden keine anderen als die in der Arbeit angegebenen Hilfsmittel und Quellen verwendet. Textabschnitte von Dritten oder eigener Prüfungsarbeiten wurden nur mit Kennzeichung übernommen.

Der Verfasserin ist die geltende Promotionsordnung der Fakultät für Chemie bekannt.

Ji Eun Choi

Teile dieser Arbeit sind bereits veröffentlicht oder wurden im Rahmen von Konferenzen vorgestellt:

Publikationen

N. Adebar, J.E. Choi, L. Schober, R. Miyake, T. Iura, H. Kawabata, H. Gröger, Overcoming Work-Up Limitations of Biphasic Biocatalytic Reaction Mixtures Through Liquid-Liquid Segmented Flow Processes. *ChemCatChem*. **2019**, *11*, 5788-5793.

J. E. Choi, S. Shinoda, R. Inoue, D. Zheng, H. Gröger, Y. Asano, Cyanide-free synthesis of an aromatic nitrile from a biorenewable-based aldoxime: Development and application of a recombinant aldoxime dehydratase as a biocatalyst *Biocat. Biotransf.* **2019**, *37*, 414-420.

S. Wedde, M. Biermann, J.E. Choi, K. Oike, N. Zumbrägel, H. Gröger, The Recent Developments of Enzymatic Oxidation in: *Green Oxidation in Organic Synthesis* (Hrsg.: N. Jiao, S. S. Stahl), *John Wiley & Sons, Hoboken.* **2019**, chapter 16, p. 439-496.

Patent

T. Iura, Y. Dekishima, T. Sakamoto, M. Hara, H. Hiraoka, H Gröger, J.E. Choi, Carbonyl reductase, gene encoding it and process for producing optically active compounds using the same, API Corporation, JP 2019-211797, submitted at 22-11-2019.

Vortrag

Tailor-made artificial Metalloenzymes and applications in organic synthesis, Cebitec retreat symposium, August 2016, Loccum, Germany.

Posterpräsentation

Tailor-made artificial polyoxometalate-type proteins and applications as biocatalyst in organic synthesis, BIOTRANS, July 2017, Budapest, Hungary.

Acknowledgement

First, I would like to thank Prof. Gröger for the continuous support of my Ph.D. study, his patience, motivation, and immense knowledge. His guidance led me to Germany and help me in all the time of research.

Besides my supervisor, I would like to thank my second referee Dr. Prof. Gabriele Fischer von Mollard.

I am also grateful to fellow labmates for their great help, cooperation, friendship, all the fun we have had in the last four years. In addition, I would like to express my gratitude to Thomas, Angelika, Anika, and Anke. I am also grateful to the technical staff of NMR department.

I would like to thank Prof. Asano and Japanese colleagues in Toyama Prefecture University for showing me warm welcome and friendship.

Nevertheless, I would like to convey my gratitude to Kawabata-San, Royma-San, and Iura-San in API Corp. for your cooperation and kindness.

I would like to thank my friends for accepting me as I am. Last but not the least, I would like to thank my husband and my family. I could not have believed I can finish my Ph.D. study without Jiajun's great support and love.

서른이 훌쩍 넘어 독일로 박사학위 가는 철없는 딸을 지지해준 부모님, 사년동안 곁에서 큰 힘이 되어 준 열추 이십년지기 시애, 지연, 지원, 지윤, 그리고 독일 생활의 비타민 재진언니, 경원언니, 정임언니에게 큰 감사 드립니다.

사랑합니다.

Table of Contents

Abbreviation

ADH	Alcohol dehydrogenase
ADP	Adenosine diphosphate
ATP	Adenosine triphosphate
BSA	bovine serum albumin
DEAE-Sephacel	Diethylaminoethyl–Sephacel
DMSO	Dimethyl sulfoxide
DOLE	(3*R*,5*S*)-(*E*)-7-[2-cyclopropyl-4-(4-fluorophenyl]-quinolin-3-yl]-3,5-dihydroxyhept-6-enic acid ester
DOXE	(*E*)-7-2-cyclopropyl-4-(4-fluorophenyl)-quinolin-3-yl)-3,5-dioxohept-6-enic acid ethyl ester
FPLC	Fast protein liquid chromatography
GC	gas chromatography
GDH	glucose dehydrogenase
HPLC	High-performance liquid chromatography
IPTG	Isopropyl *β*-D-1-thiogalactopyranoside
Lactone	(4*R*,6*S*)-6-[(*E*)-2-[2-cyclopropyl-4-(4-fluorophenyl)quinolin-3-yl]ethenyl]-4-hydroxyoxan-2-one
Mo	Molybedate (Na_2MoO_4)
5S-MOLE	(*E*)-7-2-cyclopropyl-4-(4-fluorophenyl)-quinolin-3-yl)-5-hydroxy-3-oxohept-6-enic acid ethyl ester
3R-MOLE	(*E*)-7-2-cyclopropyl-4-(4-fluorophenyl)-quinolin-3-yl)-3-hydroxy-5-oxohept-6-enic acid ethyl ester
MosA	MoWSto subunit α
MosB	MoWSto subunit β
MOPS	3-morpholinopropanesulfonic acid
MTBE	methyl-tert-butylether
MoWSto	Molybdate/ tungstate storage protein
NADPH	The reduced form of nicotinamide adenine dinucleotide phosphate (NADPH)
$NADP^+$	Nicotinamide adenine dinucleotide phosphate
NMR	Nuclear Magnetic Resonance
OCR	carbonyl reductase from *Ogataea minuta*
Oxd	aldoxime dehydratase
OxdA	aldoxime dehydratase isolated from *P. chlororaphis* B23
OxB-1	aldoxime dehydratase isolated from *Bacillus* sp
OxdRG	aldoxime dehydratase isolated from *R. globerulus* A-4
OxdRE	aldoxime dehydratase isolated from *R. erythropolis* N-771
oxdFG	aldoxime dehydratase isolated from *F. graminearum* MAFF305135
OxdK	aldoxime dehydratase isolated from *Pseudomonas* sp. K-9
OxdYH3-3 WT	aldoxime dehydratase *isolated from Rhodococcus* sp. YH-3-3 wild-type
Rt	Residence time
PCR	Polymerase chain reaction
RT PCR	Real time PCR
PTC	phase transfer catalyst ($[CH_3(n\text{-}C_8H_{17})_3N]HSO_4$)
PTFE	Polytetrafluoroethylene
SDS-PAGE	sodium dodecyl sulfate–polyacrylamide gel electrophoresis
TB	Terrific Broth medium
TFAP	2,2,2-trofluoroacetophenone
TFMBA	α-(trifluoromethyl)benzyl alcohol
Tm	Melting temperature
Tris-HCl buffer	Tris(hydroxymethyl)aminomethane hydrogenchloride buffer
W	Tungstate (Na_2WO_4)

Abstract

Broadening the scope of biocatalysts could be achieved by giving new functionality to non-functional proteins or by improving enzymatic features such as stability and catalytic activity. To develop new biocatalysts for application in organic synthesis, three enzymes were introduced in this study.

The metalloprotein MoWSto from *Azotobacter. Vinelandii* was chosen for organic synthesis due to its large metal loading in the enzyme cavity. The tungstate amounts in MoWSto was measured as 20 ions per protein molecule after purifications. Chemical synthetic condition of acetophenone from (*R,S*)-1-phenylalcohol was modified for the biocatalytic oxidation. Subsequently, the Metalloprotein was used for the oxidation in combination with 3-5% hydrogen peroxide and phase transfer catalyst at 50 °C. The maximum conversion using cell crude extract was 12.4% in 13 days at 50 °C with 0.14 mM tungstate in MoWSto, indicating that oxidation proceeded slowly in the presence of metalloenzyme. However, the repeated experiments with tungstate salt and crude extracts showed lower conversion; furthermore, protein degradation was accelerated in the reaction solution. On the other hand, the moderative kinase activity was observed from MoWSto that suggests the possibility for utilization in the production of metabolic intermediates.

For organic synthesis using biocatalysts in the pharmaceutical industry, OCR was a perfect example of engineering of an enzyme to increase catalytic specificity. The substrate specificity of a new type of carbonyl reductase OCR toward pitavastatin intermediates was improved by error-prone PCR. After directed evolution of OCR, The productivity was dramatically enhanced up to 70% from 15% toward 10 $g \cdot L^{-1}$ DOXE and up to 95% from 60% toward 2.6 $g \cdot L^{-1}$ MOLE using OCR mutant D54V. To enhance the mixing condition, a segmented flow reactor was applied. OCR successfully converted 2,2,2-trifluoroacetophenone to the corresponding alcohol, showing approximately 70% conversion in 2 h in the presence of MTBE as an organic solvent. The segmented flow reactor improved phase separation to a great extent and showed the same conversion quality per each residence time.

Finally, aldoxime dehydratase isolated from *Rhodococcus* sp. YH3-3 was constructed to the recombinant enzyme in *E. coli*. The optimal condition for overexpression was observed using overexpression vector pET28b containing C-terminus histidine tag and BL21(DE3) as a host cell. Directed evolution of OxdYH3-3 was conducted to improve the substrate loading up to 100 mM. OxdYH3-3 mutant N266S showed four and three times higher activities toward 50 and 100 mM *E*-pyridine-3-aldoxime, respectively. Also, the mutant exhibited 4 and 5 times higher activities towards 2-furfuryl aldoxime compared to OxdYH3-3 WT. Since 2-furfuryl aldoxime has high potential as fine chemicals, the increment of substrate loading implies the utilization of OxdYH3-3 mutants in the food ingredient industry or pharmaceuticals.

1. Preface

There has been a long journey to search for an environmentally sustainable and economical method of organic synthesis for application in chemicals manufacturing. The terms “green chemistry” and “sustainable development” were introduced in 1990, at a time when an enormous amount of waste from the chemical industry raised growing concerns[1]. A major cause of waste is the use of stoichiometric, mainly inorganic, reagents, such as metals, metal hydride reagents, and products of oxidations with permanganate, in the manufacturing of fine chemicals and pharmaceuticals[1]. One of the alternative sustainable chemistry approaches is the use of biocatalysis in organic synthesis. The use of biocatalytic methods provides numerous economic and environmental benefits because biocatalysts are readily biodegradable and non-toxic. In addition, biocatalytic reactions can avoid the subsequent costs required for end-product purification and functional-group modification, and consequently, generate less waste than conventional organic synthesis. For example, the green oxidation without toxic organic solvents and halides were introduced by Noyori and his coworkers[2–5]. Alcohols, aldehydes, cyclohexene, and sulfides were oxidized by using oxidant hydrogen peroxide, phase transfer catalysts, and transition metals (**Figure 1**). Recently, metal catalyst have been replaced by non-native metalloenzymes. The metalloenzymes have drawn attention due to their high selectivities and specificities as well as their capability of performing challenging reactions, such as the reduction of dinitrogen or ammonium or the oxidation of water[6,7]. In particular, artificial metalloenzymes containing a transition metal have been abundantly studied through three different approaches; (1) covalent anchoring of a ligand/metal[8,9]; (2) supramolecular noncovalent anchoring[9,10]; and (3) the design of a protein scaffold, that binds transition metal salts directly[9,11]. A metalloprotein containing abundant molybdate ions was found from nitrogen-fixing bacteria, and its function was limited to supplying molybdenum ions to nitrogenase in a molybdenum-deficient environment[12]. An attempt to give the metal-containing protein a new function as a metalloenzyme to catalyze oxidation is introduced in this thesis. This metalloenzyme could be considered as a new type of metalloenzyme by omitting metal-anchoring steps. A state-of-the-art study will be described in Chapter 2.

Apart from the application of artificial metalloenzyme in organic synthesis, there has been impressive progresses in the development of biocatalysts, which work in an organic solvent. Since lipase was revealed to be tolerant of various organic solvents at high temperatures by Zaks and Klibanov[13], research on biocatalysis has grown impressively owing to the development of DNA-technology in the field of recombinant strain production. The market for biotechnology products was estimated to grow by 11.6% from 2012 to 2017 to reach 414.5 billion USD[14]. Pure amino acids, amino alcohols, amines, alcohols, and epoxides have been classified as essential compounds for the synthesis of abundant

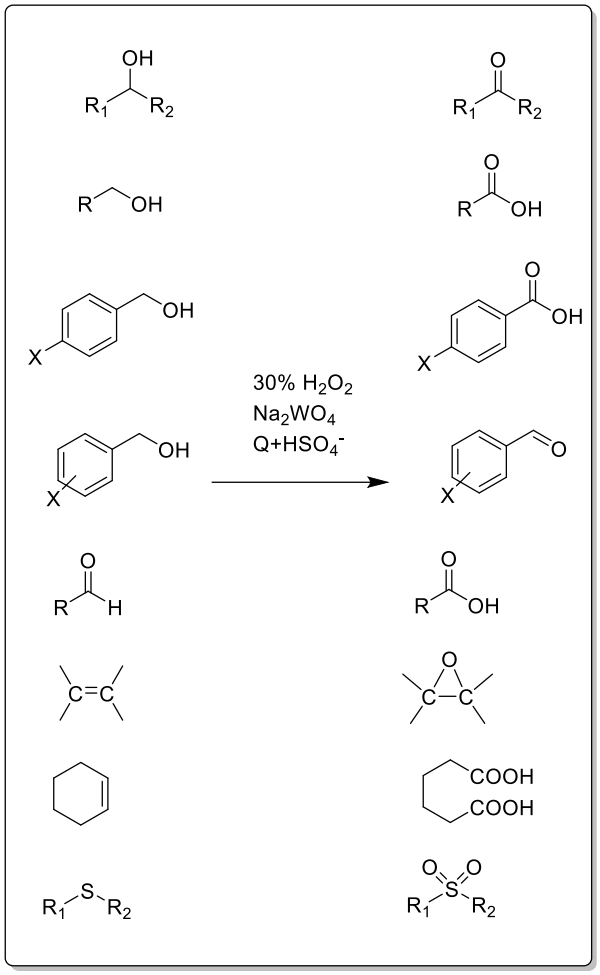

Figure 1. The solvent-free green reaction proposed by Noyori's group. Oxidation of primary alcohols, aldehyde, olefins, cyclohexene, and sulfide in an aqueous solution containing H_2O_2, PTC, and Na_2WO_4[58].

pharmaceutical and agrochemical products[14,15]. The most frequently used biocatalysts are hydrolases and alcohol dehydrogenases, while; Baeyer–Villiger monooxygenases have been used in the past for the oxidation of various linear and cyclic ketones to provide enantiomerically pure intermediates[16,17]. The novel C-C, C-N, and C-O bond-forming biocatalysts, including aldolases, hydroxynitrile lyases, and thiamine diphosphate dependent lyases, are also considered to be important in the production of sugars and carbocycles as well as in the synthesis of acyloins and cyanohydrins[16–18]. Some biocatalysts are able to convert non-natural substrates under harsh conditions in vitro, such as at high temperatures or in non-aqueous media. One representative example is a lipase isolated from *Thermomyces lanuginosus*, which was commercialized by DSM Andeno in 1980 to synthesize the key chiral intermediate of the anti-hypertensive drug, diltiazem (**Figure 2**)[19,20]. However, there is still a growing need for novel biocatalysts to replace inefficient and toxic conventional chemical synthesis. Therefore, biocatalysts need to be "engineered" to have high space-time yields and high selectivities at high

substrate concentrations and low enzyme loading by enzyme engineering techniques, such as error-prone PCR, DNA shuffling, and rational design with computational calculation. An example of rational design was presented by Codexis and Merck to convert a ketone precursor to sitagliptin using (*R*)-selective transaminase, which initially showed a poor activity of 0.7% conversion in 24 h towards prositagliptin[21]. Intensive work on the polypeptides resulted in 27 mutations; the transaminase could then convert 100 $g \cdot L^{-1}$ substrates with >99.95% ee at a 92% yield, which was a 53% increase in productivity ($kg \cdot L^{-1} \cdot day^{-1}$) (**Figure 3**).

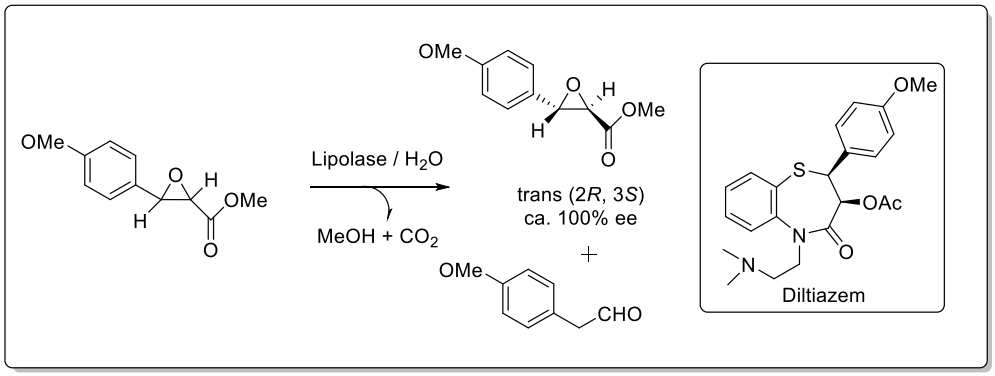

Figure 2. Synthesis of a chiral diltiazem intermediate using lipase[19].

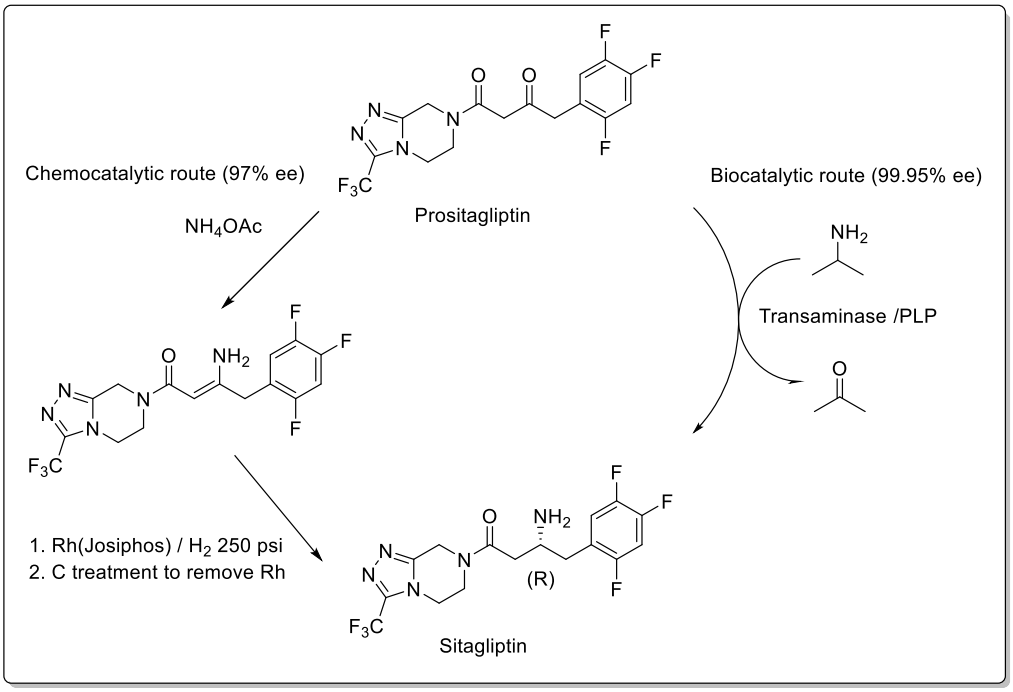

Figure 3. Synthesis of sitagliptin by biocatalytic transamination[21].

Another astonishing example of enzyme engineering is the use of ketoreductase for synthesizing a key intermediate of atorvastatin, which was evolved by DNA shuffling to improve the activity and stability of the biocatalysts[9]. Moreover, the key intermediate in the manufacture of montelukast (an anti-asthmatic agent) was synthesized by ketoreductase, resulting in a >95% yield and >99.9% ee with 100 $g \cdot L^{-1}$ substrate loading and 3 $g \cdot L^{-1}$ enzyme concentration over 24 h at 45 °C[22] (**Figure 4**). There are many ketoreductases utilized for the synthesis of active pharmaceutical ingredients, and these ketoreductases are isolated from various strains like *Candida, Hansenula, Pichia, Rhodotorula, Saccharomyces, and Sphingomonas* sp.[23]. The novel ketoreductase found from *Ogataea minuta* was also reported to be active towards pharmaceutical ingredients[24]. In this thesis, we demonstrate a novel ketoreductase for synthesizing an intermediate drug in cooperation with API Corporation (Mitsubishi Chemical Holdings, Japan) and its activity toward the intermediate compound by enzyme engineering in Chapter 3.

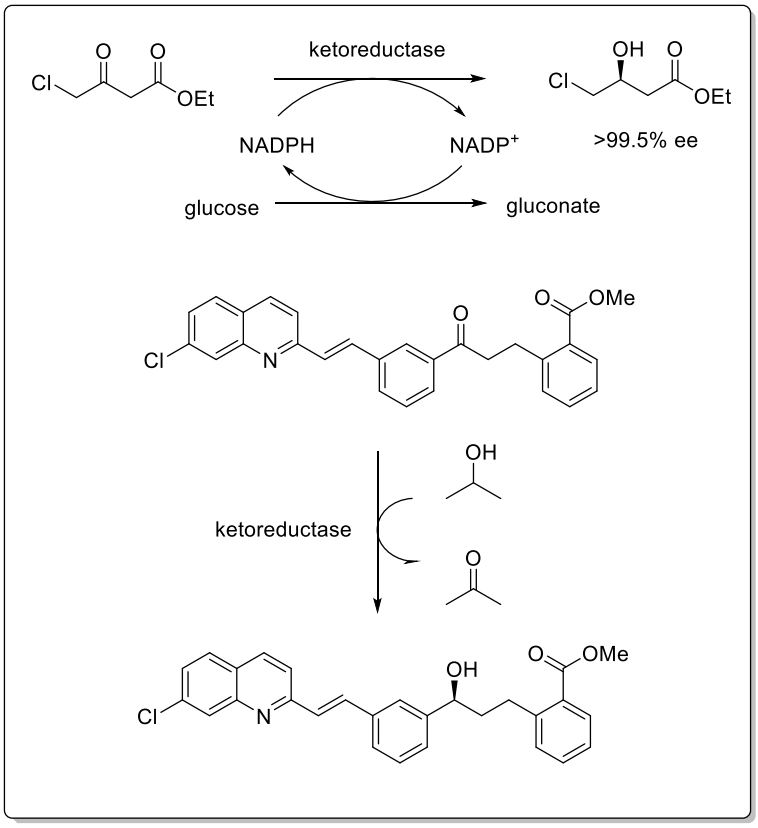

Figure 4. Process for atorvastatin production (above) and montelukast intermediate (below) by ketoreductase reduction[22].

Finally, the development of a new recombinant aldoxime dehydratase was investigated in this study, as shown in Chapter 4. In the environmental aspect, the introduction of aldoxime dehydrating enzymes for nitrile synthesis by the Asano group is an excellent alternative nitrile production method because toxic cyanide compounds are not required in the biosynthetic pathway. The nucleotide sequences of aldoxime

dehydratase YH3-3 were analyzed in 2016, and the recombinant enzyme was constructed in this study to show its feasibility in aromatic nitrile synthesis by enzyme engineering to increase substrate loading.

2. Application of a novel metalloenzyme containing an enormous transition metal in organic synthesis

2.1. History of artificial enzymes and its application in organic synthesis

2.1.1. The conventional approach to exploring new functional biocatalysts

Novel biocatalysts showing new catalytic activities are extensively researched to broaden the application of biocatalysis in organic synthesis. One well-known example of the exploration of unknown biocatalysts is the isolation of ideal microorganisms from nature. Current estimates indicate that only 1% of microorganisms are culturable, while the remaining 99% of the microorganisms in many natural environments grow poorly in an experimental environment and are, therefore, not accessible for biotechnology or basic research[25]. Consequently, obtaining DNA or protein from the environment followed by the construction of libraries with various kinds of vector and host organisms could provide opportunities to find novel biocatalysts. A broad range of biocatalysts for the development of novel biotechnological and pharmaceutical products, including polysaccharide-modifying enzymes[26,27], vitamin synthesizing enzyme[28], and nitrilase[29] has been found using metagenome libraries. However, functional searches for novel genes in metagenomic libraries has been challenging due to the low transcription level of metagenome-derived genes in host strains[25].

Enzyme engineering has been intensively studied to give unnatural properties to conventional enzymes, and the great potential for novel organic syntheses based on engineered enzymes has been summarized in various reviews[30,31]. Engineered enzymes are evolved from wild-type natural enzymes to have desired activities for non-natural reactions with artificial substrates based on similar reaction mechanisms. Some strategies have been developed in the field of enzyme engineering[20], such as random mutagenesis by error-prone PCR and directed evolution through DNA shuffling to give enhanced enantioselectivity to existing catalytic activity[32,33] or novel catalytic activity[31]. For example, oxynitrilases catalyzing the addition of HCN to aldehydes have been successfully utilized for the nitroaldol reaction (Henry reaction) of aldehydes with nitromethane, which also represents a nucleophilic C1-building block[31]. Another example is the utilization of tailor-made P450-monooxygenase mutants for C-H amination instead of C-H hydroxylation, when using azo compounds instead of molecular oxygen[34]. The rational design of enzymes based on a calculated transition state of the mechanism of the desired reaction is a further approach and has been successfully demonstrated by the Baker group, e.g., for Kemp elimination[35].

2.1.2. The development of artificial metalloenzymes

Artificial metalloenzymes refer to the hybrid catalysts in which biomolecules, such as DNA or polypeptides, are combined with a catalytically-active transition metal complex[36]. Artificial metalloenzymes have great advantages in terms of broad catalytic scope and high selectivity under mild conditions[36]. Enzymatic catalysts provide biomolecular scaffolds, such as proteins and nucleotides, which provide excellent catalytic activity and selectivity by hydrogen bonding and hydrophobic interaction. The metal-containing moiety is connected to the host biomolecule via noncovalent or covalent anchoring[36,37] (**Figure 5**). Supramolecular anchoring uses strong and highly specific covalent interactions between biopolymers and small molecules (**Figure 5**a). This approach is based on the biotin/(strept)avidin interaction and DNA-based asymmetric catalysis involving supramolecular anchoring. Dative interaction is a closely related anchoring approach which consists of coordinative bonds between the catalytic metal ion and functionalities presented by the biomolecular scaffold (**Figure 5**b)[36]. The initial studies from Wilson and Whitesides presented an asymmetric hydrogenation catalyst based on embedding an achiral biotinylated rhodium-diphosphine moiety in avidin[38] (**Scheme 1**a). A later study by Chan indicated that an enantiopure biotinylated pyrphos-Rh(I) complex in conjunction with avidin could catalyze the enantioselective reduction of itaconic acid with enhanced enantioselectivity[39] (**Scheme 1**b). A diverse range of noncovalent anchoring examples have also been reported, including sulfoxidation of thioanisole by $\{(Salophen)Cr(III)\}^+$ complex and ruthenium (II) porphyrin cofactor and hydrogenation catalyzed by a Pd cluster[37,40–42].

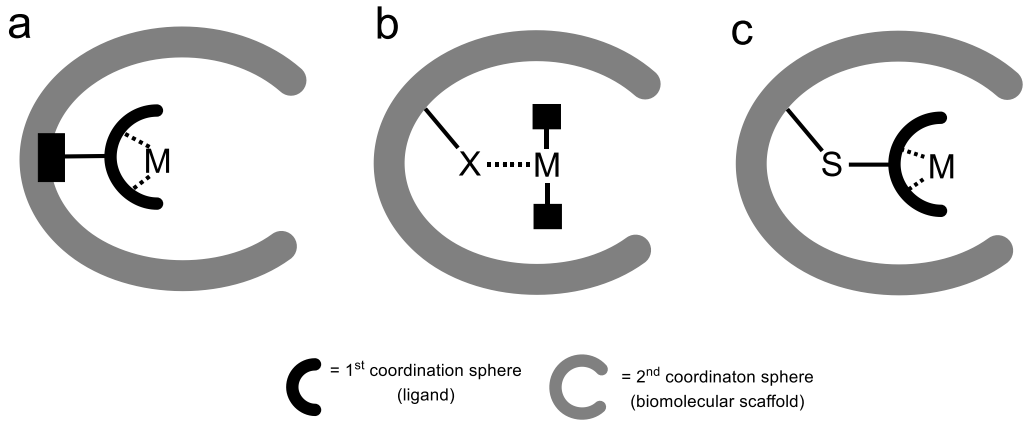

Figure 5. Representation of the concept of artificial metalloenzymes and the various anchoring strategies: (a) supramolecular, (b) dative, and (c) covalent. M denotes the catalytically active transition metal[43]; S denotes the thiol group of cysteine[44].

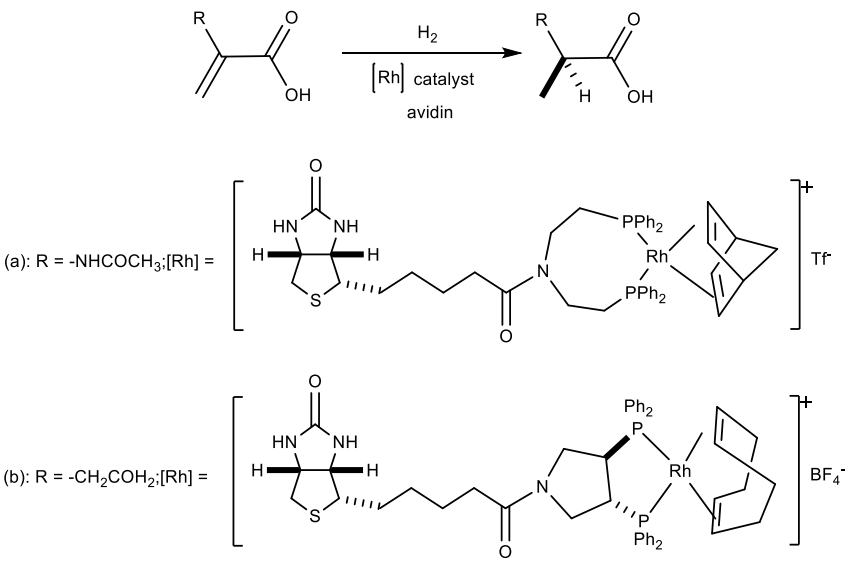

Scheme 1. (a) Enantioselective hydrogenation of acetamidoacrylic acid catalyzed by Whitesides' system[38]. (b) Enantioselective hydrogenation of itaconic acid catalyzed by Chan's system[39].

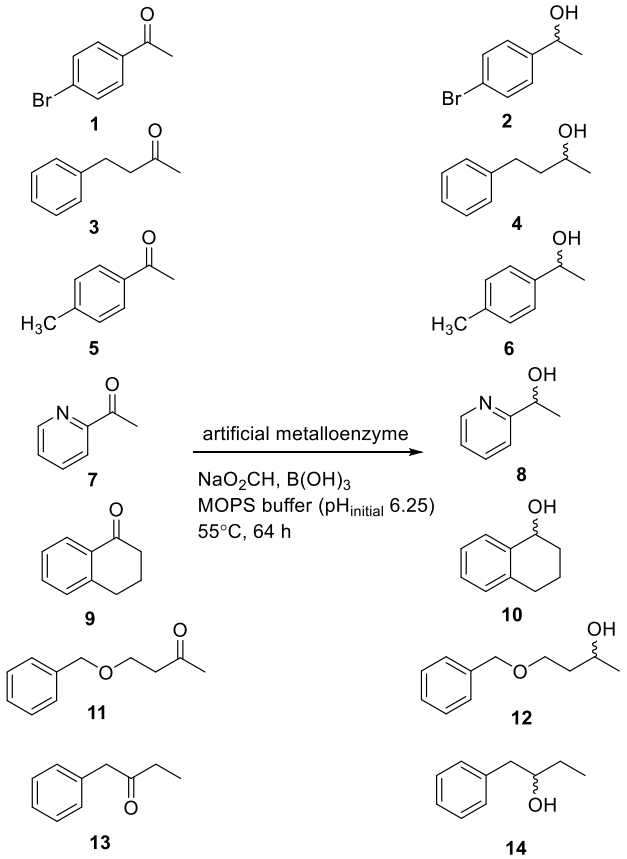

Scheme 2. Substrates, reduction products, and operating conditions used for the designed evolution of artificial transfer hydrogenases[45].

As a biomolecular scaffold, the biotin-avidin system was considered the most promising system since the biotin-avidin complex can be readily prepared with further genetic and chemical modification. Streptavidin is a biotin-binding protein that has a deeper binding pocket compared to avidin. The Ward group[45] reported the advanced utilization of metalloenzymes in a combination of enzyme engineering approaches. In their work, they optimized enantioselectivity by saturation mutagenesis of streptavidin, resulting in good levels of conversion and selectivity for methyl alkyl and methyl aryl ketones (**Scheme 2; Table 1**).

Table 1. Summary of selected results from the catalytic experiments with either biotin–sepharose immobilized or purified homogeneous artificial metalloenzymes [h6 -(arene)RuH(Biot-p-L)]CSav.

Entry	Arene	Sav isoform	Ketone	ee (conv [%])	
				extract[a, b]	pure[a, c]
1	p-cymene	WT Sav	**1**	65 (81)	87 (93)
2	benzene	WT Sav	**1**	-39 (31)	-57 (43)
3	p-cymene	L124V	**1**	83 (90)	91 (96)
4	benzene	S112A K121N	**1**	-55 (99)	-75 (98)
5	p-cymene	S112A K121N	**1**	50 (63)	70 (89)
6	benzene	S112A K121N	**3**	-62 (95)	-72 (quant.)
7	p-cymene	S112A K121N	**3**	58 (81)	70 (78)
8	benzene	S112K L124H	**1**	-59 (64)	-65 (94)
9	p-cymene	S112A K121T	**3**	82 (84)	88 (99)
10	benzene	K121R	**1**	-64 (96)	-68 (95)
11	p-cymene	S112A K121S	**3**	59 (80)	77 (98)
12	benzene	S112A K121W	**3**	80 (86)	84 (99)
13	p-cymene	L124V	**5**	—	96 (97)
14	benzene	S112A K121N	**7**	—	-92 (quant.)
15	p-cymene	S112A K121T	**11**	—	90 (quant.)
16	p-cymene	L124V	**9**	—	87 (20)
17	benzene	S112A K121N	**9**	—	-92 (54)
18	p-cymene	S112A K121T	**13**	—	46 (50)

[a] Positive and negative ee values correspond to the *R* and *S* enantiomers, respectively. [b] Immobilized protein from the crude cellular extract. [c] Purified non-immobilized protein. –=not performed.

Covalent anchoring is an approach using the covalent incorporation of a transition metal complex through the ligand into a specific position in the biomolecular scaffold (**Figure 5**c). Kaiser first showed that new activities were introduced to enzymes by changing specific amino acid residues along with designed coenzyme analogs[8]. His group explained that papain could be converted to oxidoreductase by the covalent modification of the sulfhydryl group of the active site cysteine residue at 25 with flavins such as 8-bromoacetyl-10-methylisoalloxazine (**Figure 6**).

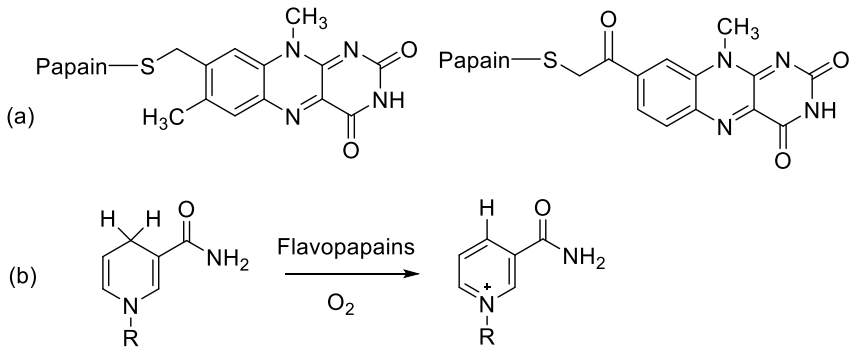

Figure 6. (a) Examples of flavopapain derivatives synthesized by Kaiser. (b) The reaction catalyzed by flavopapains[8].

A later study by Rana Meares proposed that using ferrous-EDTA as a metal chelate for the incorporation of transition metals into proteins resulted in protein cleavage with a high regiospecificity, yielding three- and two protein fragments respectively[45]. Distefano and his coworkers showed that the enantioselectivity of an artificial metalloenzyme could be improved by application of a lipid-binding protein. Adipocyte lipid-binding protein (ALBP-Phen) was conjugated with 1,10-phenanthroline, resulting in ALBP-Phen-Cu(II), to catalyze the enantioselective hydrolysis of several inactivated amino acid ester substrates[46] (**Scheme 3**).

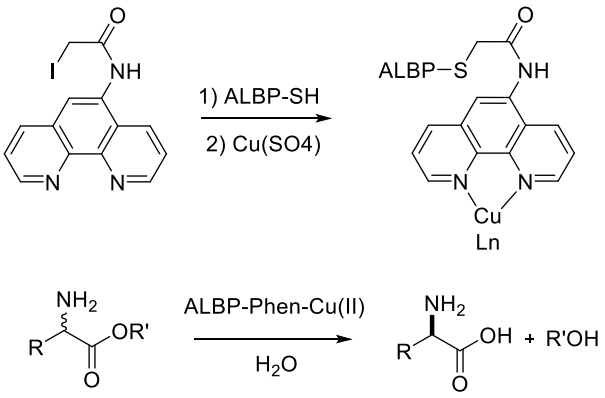

Scheme 3. Preparation of adipocyte lipid-binding protein-Cu(II) (ALBP-Phen–Cu(II)) conjugates. (b) Enantioselective hydrolysis of amino acid ester derivatives catalyzed by ALBP–Phen–Cu(II)[46].

2.2. Motivation to search for a new approach to producing an artificial enzyme

A further conceivable approach towards novel catalytically-active metalloproteins, that to the best of our knowledge has been unexplored so far, is the use of metal storage proteins as catalysts in organic

synthesis. The molybdate (Mo) storage protein was known as a Mo-release protein to nitrogenase in several N_2 fixing organisms; however, its function as an enzyme was not clear. The distinctive characteristic of molybdate/tungstate storage protein (MoWSto) from *Azotobacter vinelandii* is that it can contain up to approximately 100 Mo ions per mol of protein[47,48] (**Figure 7**). This unique property has raised questions regarding its metal storage mechanism. Recently, the Elmeler group intensively studied MoWSto and revealed that various combination of metal compositions in protein cavities are available using wild-type and recombinant MoWSto[49]. Furthermore, the Mo release mechanism in association with ATP was explained by Schemberg and Brünle[50,51]. The mechanism for the formation of polyoxometalate clusters was very recently explained by the following two processes: (1) spontaneous stabilization of transient species by protein binding/protection; and (2) protein-driven by exploiting the nucleation, catalytic binding and shielding capabilities of the polyoxometalate binding pocket[49]. Consequently, various states of polyoxometalates are produced in the cage-like structure, including one Mo_3 (trimolybdate), three $Mo_{5\text{-}7}$ (penta-/hexa-/hepta-molybdate), and six Mo_8 (octamolybdate) clusters[47]. These polyoxometalate clusters bind to the residues His156, Glu129, and His140 which play an essential role in stabilization.

The motivation for the use of such type of non-catalytic proteins as artificial enzymes is that one protein contains not only one but numerous metal ions. This characteristic would be highly advantageous when considering that catalyst loading is often relatively high for metal-catalyzed transformations compared to enzymes as catalysts, resulting in lower turnover numbers. In catalytically-active metalloproteins, the protein amount must be adjusted to the required metal amount. Accordingly, a high molar ratio of metal to protein would be required. In an attempt to overcome this limitation, we were interested in exploring the use of metal storage proteins, specifically MoWSto. Furthermore, previous studies of a metal storage protein from *A. vinelandii* proved that molybdate could be replaced by tungstate[48,52]. Vanadium (V) and iron-containing nitrogenase were also found from *A. vinelandii* grown in a Mo-depleted medium, which supports the idea that the molybdate ion can be replaced by another transition metal[53]. Therefore, in the following section, we report our results on the characterization of storage proteins containing polyoxomolybdate and polyoxotungstate clusters in terms of stability under typical organic synthesis conditions, as well as their evaluation as potential catalysts for organic-synthetic transformations.

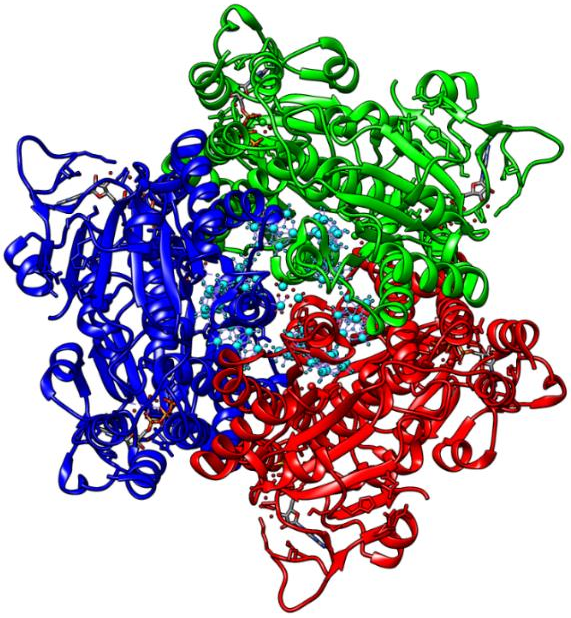

Figure 7. Crystal structure of molybdate storage protein with a fully Mo-loaded cavity (PDB number: 4NDO). Skyblue balls are the molybdenum ions, red dots are water, sticks are ATP, and blue, green and red ribbon are subunits of the protein[49].

2.3. Preparation of MoWSto containing tungstate clusters

2.3.1. Comparison of cell growth depending on metal contents and metal concentrations in cell crude extracts

MoWSto was cultivated at 30 ºC in modified Burk's medium optimized in a previous study by Schemberg[12]. In the first culture, *A. vinelandii* was inoculated in non-metal containing medium to completely remove trace metal from MoWSto for accurate measurement of the incorporated metal amount. The cell culture was inocubated again in modified Burk's medium containing 1 mM Na_2MoO_4 and 100 µM $Na_2WO_4{\cdot}2H_2O$ and respectively showed the same growth tendency as the bacterial cells grown in the non-metal containing medium (**Figure 8**). The optical densities at 436 nm of the cultures from non-, molybdate (Mo) and tungstate (W)-containing media showed a similar range of growth, with an optical density of 7 after 20 h, indicating that a Mo concentration up to 1 mM does not inhibit the growth of *A. vinelandii*.

A colorimetric assay using a microplate reader was performed to measure the incorporated metal concentrations in MoWSto using cell crude extract after 7 h of cultivation. The ratio of Mo to protein concentrations (16.64 µmol·g^{-1}) was similar to that found in Fenske's study (16.8 µmol·g^{-1}), which

reported expression and structure of MoWSto for the first time[12] (**Table 2**). The ratio of W to protein was 20.52 μmol·g^{-1}, which was slightly higher than the Mo loading.

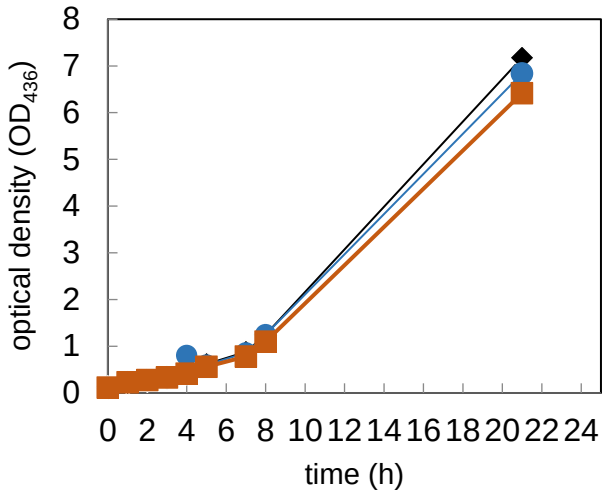

Figure 8. Growth curve of *A. vinelandii* in non-metal, Mo-, and W- containing medium. Black close diamond; optical density of culture in non-metal containing medium, blue close circle; optical density of culture in 1 mM Mo containing medium, brown close square; optical density of culture in 100 μM W containing medium.

Table 2. The concentration of metals and protein determined by colorimetric assay.

	Volume [mL]	Total Mo [μmol]	Total W [μmol]	Total Protein [mg]	Metal/protein [μmol/g]
Mo	100	0.4	-	21.7	16.1
W	100	-	0.2	11.2	20.5

2.3.2. Purification of wild-type MoWSto from *A. vinelandii*.

MoWSto was cultured in modified Burk's medium containing 1 mM W to purify MoWSto using an ÄKTA FPLC (fast protein liquid chromatography) system[12]. Nonspecific and smeared protein bands were observed in crude extracts of *A. vinelandii* after lysis with ultrasonication (**Figure 9**). After the first purification with a DEAE (diethylaminoethyl)-Sephacel anion exchange column, clear bands were observed at protein sizes of 25 and 50 kDa. The target-bands were shown at approximately 28 and 29 kDa for the alpha subunit and the beta subunit of MoWSto, respectively (**Figure 9**, lane 2). Most nonspecific proteins were excluded after ammonium sulfate fractionation and following size exclusion chromatography (**Figure 9**, lane 4). The concentration of protein and the tungstate amount for each

purification steps were measured to calculate the purification yield (**Table 3**). The W concentration was dramatically decreased after anion exchange and ammonium sulfate fractionation from 252 µmol to 4.25 µmol. It was supposed that free unbound W was washed out during purification. The remaining W contents after all purification procedures was 21.7 W ions per protein molecule, which was 5 times lower than the previous result[52]. MoWSto can contain up to 110 W ions per protein molecule, which is 5.5 times higher than the number of Mo ions in MoWSto in the presence of ATP[52]. The reason for the severe loss of W ions during purification was suspected to be due to an insufficient purification environment and culture condition. ATP and $MgCl_2$ play an important role in metal transportation into the metal-binding site, and their concentrations, temperature, and pH are significant for the uptake and release of Mo/W[52]. It was supposed that the purification environment at room temperature could influence on the cluster formation of W in the MoWSto cavity, even in the presence of a high enough concentration of ATP and $MgCl_2$. This is supported by a previous study[52], which shows that incubation at 30 °C for 1 h had already released over 50% of Mo from MoWSto at the optimal pH for Mo binding (pH 6.5). Interestingly, once the W ions were released from MoWSto, the re-incorporation of W ions into MoWSto was less favorable after release from MoWSto, showing fewer W ions in MoWSto (60 ions per protein molecules)[52]. This was attributed to the difference of cluster formation between the first W assembly and the second assembly after W release. This result could explain the difference in W concentrations depending on the condition for W cluster formation.

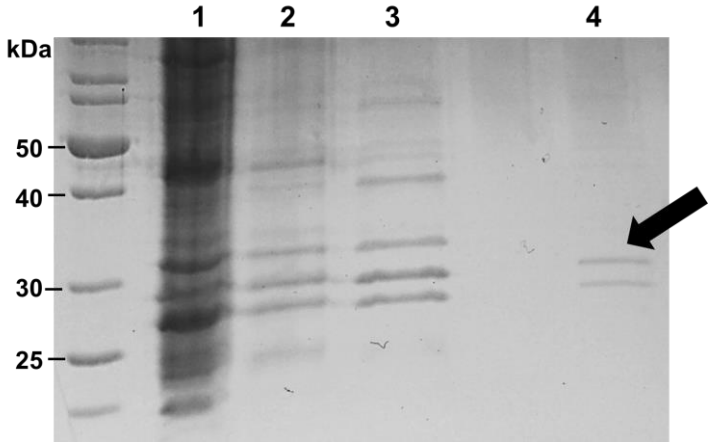

Figure 9. Polyacrylamide gel electrophoresis (PAGE) analysis of MoWSto purification (lane 1, cell crude extract; lane 2, DEAE anion exchange; Lane 3, sodium sulfate fractionation; Lane 4, gel filtration. The arrow indicates MoWSto subunits, MosA (28 kDa) and MosB (29 kDa).

Table 3. Protein concentration and metal concentration at each purification step.

Purification procedure	Volume [mL]	Total W [µmol]	Total protein [mg]	W/protein [µmol/g]	Ions/ MoWSto molecule
Crude extract	10	252.1	46.2	5455.8	**349.2**
Ammonium phosphate precipitation	2	4.3	8.4	508.1	**32.4**
Size exclusion	4	1.6	4.7	339.3	**21.7**

2.3.3. Overexpression of MoWSto subunits "MosA" and "MosB"

The MoWSto protein is organized as an $(\alpha\beta)_3$ heterohexamer consisting of a trimer of αβ dimers, and its subunits have molecular weights at 28 and 29 kDa for MoWSto subunit α (MosA) and MoWSto subunit β (MosB), respectively[48]. Due to difficulties in several purification steps using the wild-type microorganism, the overexpression using *E. coli* as a host organism was attempted. A recombinant MoWSto has been prepared in *E. coli* by co-expression with molecular chaperones in the previous studies[50,51]. In this study, *mosa* and *mosb* genes were cloned to the overexpression vector pET28a and transformed to *E. coli* BL21(DE3). *E. coli* containing MosA and MosB were cultured at 18 °C and 37 °C with various concentrations of isopropyl β-d-1-thiogalactopyranoside (IPTG) induction, simultaneously. After cultivation, the culture solution was disrupted by an ultrasonicator, and the supernatant was separated by a centrifuge. The supernatant and pellet were analyzed by sodium dodecyl sulfate polyacrylamide gel electrophoresis (SDS-PAGE) (**Figure 10**). MosA was highly overexpressed at 18 and 37 °C. The protein expression of MosA in the total fraction was quantified with the image analysis program ImageJ, and the band intensity in this picture was approximately 48%. However, most of the overexpressed protein was detected in the insoluble fraction rather than in the soluble fraction. Nevertheless, the overexpression of MosA in soluble protein at 18 °C was more prevalent than the overexpression at 37 °C. On the other hand, the overexpression of MosB was not observed at 18 and 37 ºC in the same expression conditions as MosA. The results were attributed to the different influences of the histidine tag on the MosA and MosB, which was added to the C-terminus. Poly-His tags may negatively affect the expression or activity of certain proteins and may sometimes be ineffective in native conditions due to their small size and variable accessibility at protein termini[54]. Therefore, we continued to use MoWSto from wild-type *A. vinelandii* in further study.

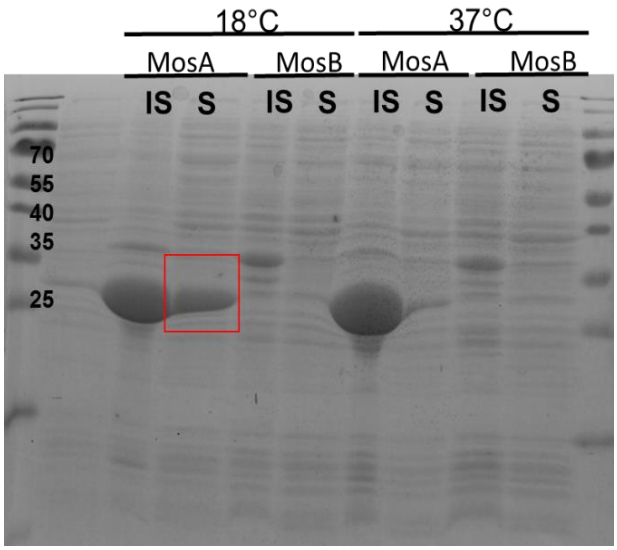

Figure 10. PAGE analysis of overexpression of MosA and MosB. The *mosa* and *mosb* genes were synthesized and cloned to pET21a overexpression vector. The transformant BL21a(DE3) containing mosa and mosb, seperatively, was overexpressed under different temperatures at 18 and 37 °C. The cell was disrupted, following separation of soluble and insoluble fraction by centrifugation. IS in the picture means insoluble protein, while S means soluble protein.

2.3.4. Characterization of wild-type protein

As a part of the effort to understand the mechanism of formation of the metal clusters in MoWSto, structural studies of MoWSto combined with and without polyoxometalate were conducted by X-ray crystallography[47,49,52]. Furthermore, the roles of ATP, pH, and temperature in the metal uptake and release process were intensively investigated[49,50,52]. However, apart from structural research, there are no known studies about the characterization of MoWSto as a biocatalyst. In this study, we focused on understanding the stability of MoWSto as a metalloprotein for the application of the enzyme in green chemistry, which will be discussed in section 2.4.

2.3.4.1. Determination of the melting temperature of MoWSto

Enzymatic stability was tested for the application of MoWSto in organic synthetic reactions. The melting temperature was estimated using thermofluor screening[55], which is a fluorescence-based thermal stability assay using a fluorescent dye. The fluorescent dye interacts with exposed hydrophobic regions generated by the partial or full unfolding of proteins; thus, the thermostability of a protein can be measured by observing fluorescence intensity as a consequence of the increment of temperature[55]. The results showed that the optimal condition for stability of MoWSto was pH 6.0 of 100 mM PIPES

buffer, where the melting temperature was approximately 81.6 °C (**Figure 11**). MoWSto showed relatively lower thermostability in acidic buffers below pH 5 and in basic buffers above pH 8.5 (**Figure 11**). MoWSto exhibited thermostability in a narrow range of pH values from 5 to 8.5 however, the melting temperature at optimum pH was surprisingly high. Due to the aggregation, the lipophilic residues could not be properly exposed to the solvent and remained buried, as reflected by the unchanged fluorescence emission maximum[56]. The impressively high melting temperature (Tm) of MoWSto in this experiment could be because of the existence of unexposed lipophilic residues; thus, the actual Tm value was supposed to be lower than 81.6 °C. Thermostability regarding intact protein concentrations after incubation at 50 °C will be discussed in the following section.

2.3.4.2. MoWSto stability at various H_2O_2 concentrations and temperatures

The Noyori group has shown that the green oxidation of aldehydes and benzylic alcohols in an organic solvent-free solution can be achieved using 30% hydrogen peroxide, tungstate salt, and a phase transfer catalyst, as will be further explained in the following section[3–5,57]. Since the transition metal salt can be replaced with MoWSto, the stability of MoWSto in an aqueous H_2O_2 solution was tested. The protein

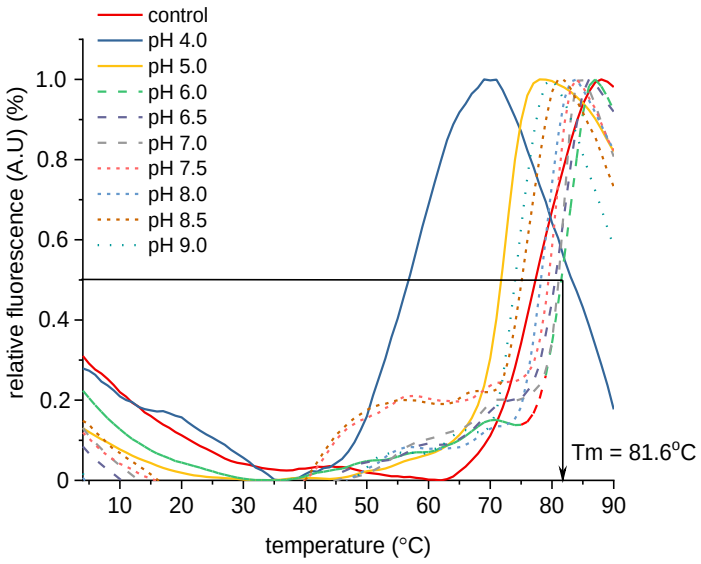

Figure 11. Melting temperature measurement of MoWSto. (A) Melt curve of MoWSto in various pH conditions. The relative fluorescence was measured by real time PCR and various pH buffer solutions were used for determination of optimal pH condition: pH 4.0, citric acid; pH 5.0, citric acid; pH 6.0, PIPES; pH 6.5, Bis-Tris; pH 7.0, PIPES; pH 7.5, TEA; pH 8.0, Tris-HCl; pH 8.5, Tris-HCl; and pH 9.0, Tris-HCl.

and metal concentrations of MoWSto were measured after incubation of the protein with an H_2O_2 solution at 4 °C. MoWSto was incubated in the H_2O_2-containing buffer solution for 20 h, and the degraded protein was then removed using a centrifuge tube with a cutoff of 10 kDa. The results indicated that protein concentrations were slightly decreased after incubation in various concentrations of H_2O_2 at 0 ºC; however, the decrease was not significant (**Figure 12**). It is assumed that the protein concentration was reduced because a minor amount of protein was lost in the centrifugation procedure by being adsorbed onto the membranes of the centrifuge tube (**Figure 12**A). The metal concentrations in the solution were unaffected by the hydrogen peroxide concentrations (**Figure 12**B), which shows that hydrogen peroxide up to 20% did not inhibit the protein stability or influence its integrity after 20 h at 4 °C. Combining the above results with respect to protein stability for application in organic synthesis, the optimal conditions for the reaction without losing enzyme integrity are at pH 6-8, over a broad range of temperatures from 50 to 70 °C, with a hydrogen peroxide concentration of up to 20%.

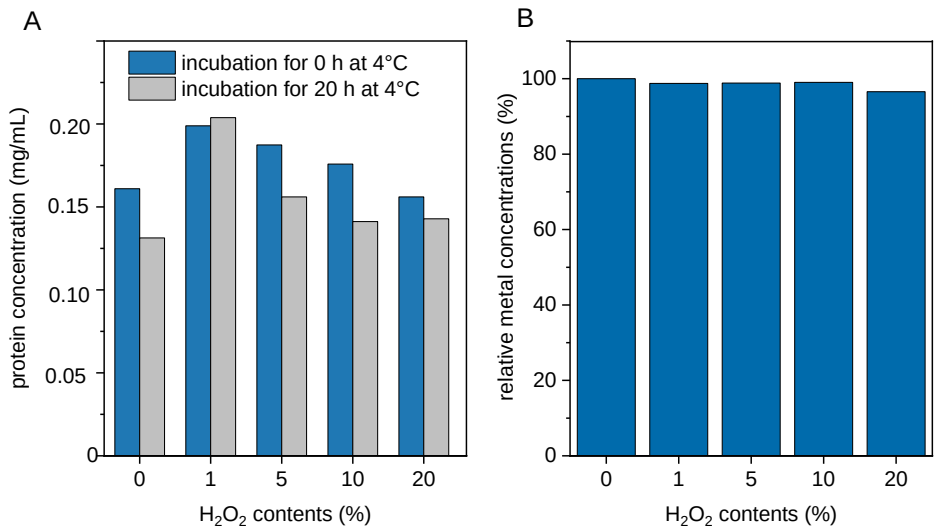

Figure 12. The protein concentration of MoWSto at 4°C for 0 and 20 h incubations in MOPS buffer (pH 6.5, 50 mM) (A). The relative W concentrations after a 20 h incubation at 4°C (B). The W concentration at 0 h was 100% and the relative ratios compared to the W concentrations at 0 h were calculated.

2.4. The exploration of green oxidation for further application of biocatalysts in organic synthesis

Oxidation is a significant technology needed to convert petroleum-based materials into useful chemicals. Noyori and his coworkers have shared brilliant results for the green oxidation of alcohols, aldehydes, cyclohexene, and sulfides using phase transfer catalysts (PTCs), sodium tungstate, and the oxidant

H_2O_2[2–5] (**Figure 13**). Sodium tungstate and PTC could affect the organic-aqueous biphasic oxidation using H_2O_2 without any harmful organic solvents and halides. Studies of green oxidation in the presence of sodium tungstate gave us the idea of exchanging sodium tungstate with MoWSto, which has huge amounts of W in the enzyme cavity. However, the green oxidation required extreme conditions that are not suitable for most biocatalysts, such as a high temperature of 90 °C. Therefore, the optimal condition of oxidation using biocatalysts was explored.

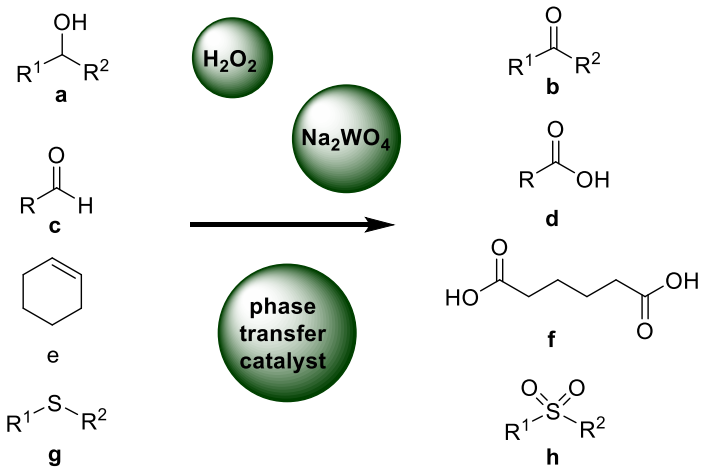

Figure 13. Green reaction proposed by Noyori's group without organic solvents. Oxidation of secondary alcohols (a), aldehyde (c), cyclohexene(e), and sulfide (g) to ketones (b), carboxylic acids (d), adipic acid (d), and sulfone (h) in an aqueous solution containing H_2O_2, PTC, and Na_2WO_4[58].

2.4.1. An example of a benchmark reaction: Oxidation of cyclohexene to adipic acid

For the first benchmark reaction, the oxidation of cyclohexene to adipic acid was chosen. Five grams of cyclohexene was oxidized to adipic acid in an aqueous solution containing Na_2WO_4, PTC ($[CH_3(n\text{-}C_8H_{17})_3N]HSO_4$), and 30% H_2O_2. Adipic acid was produced as a white precipitate after prolonged incubation at 4 °C and was dissolved in DMSO to analyze the conversion by ^{1}H-NMR. Most of the cyclohexene was oxidized into adipic acid (**Figure 14**). Since only a limited amount of MoWSto is available in the benchmark reaction, an accordingly small amount of substrate was required in further experiments; therefore, we gradually reduced the cyclohexene amounts down to 0.5 g, and no adipic acid was extracted to organic phase due to its extremely high water solubility, even though the conversion was fully undergone. Consequently, the oxidation of cyclohexene was excluded from the model reaction.

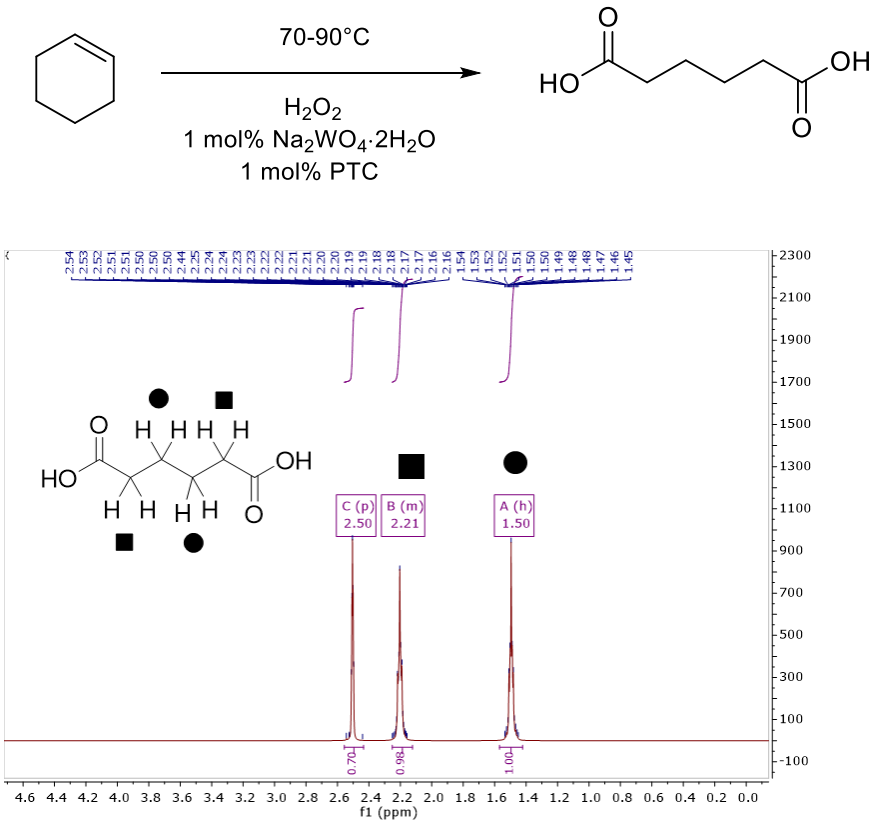

Figure 14. ^{1}H-NMR peaks of adipic acid.

2.4.2. Another example of a benchmark reaction: Oxidation of (*R,S*)-1-phenylethanol to acetophenone

The green oxidation of a secondary alcohol was attempted by adding 4 M (*R,S*)-1-phenylethanol to a reaction solution containing 15% H_2O_2, 15.4 mM $Na_2WO_4 \cdot 2H_2O$, and 15.4 mM PTC ($[CH_3(n\text{-}C_8H_{17})_3N]HSO_4$). After a 1 h reaction at 90 °C, (*R,S*)-1-phenylethanol was completely converted to acetophenone in the presence of water, and was analyzed by ^{1}H-NMR (**Figure 15**). At the same time, the conversion from alcohol to acetophenone was measured by gas chromatography (GC), which showed the clean separation of substrate and product with retention times of 15.9 and 16.2 min for (*R,S*)-1-phenylethanol, and 11.5 min for acetophenone (**Figure 16**).

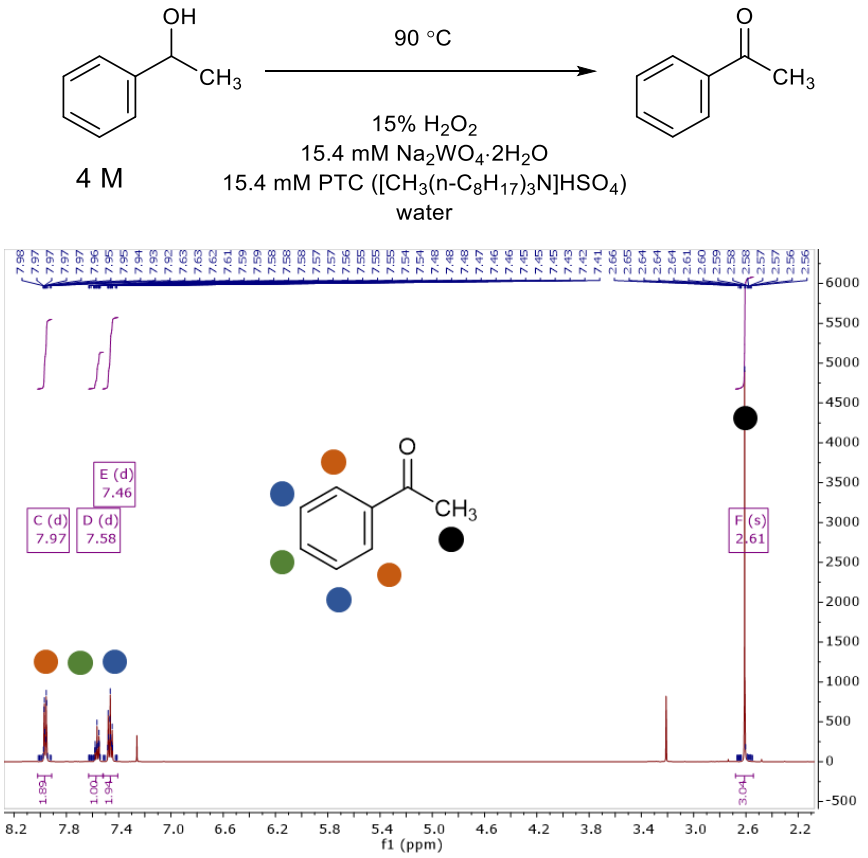

Figure 15. ^{1}H-NMR peaks of acetophenone.

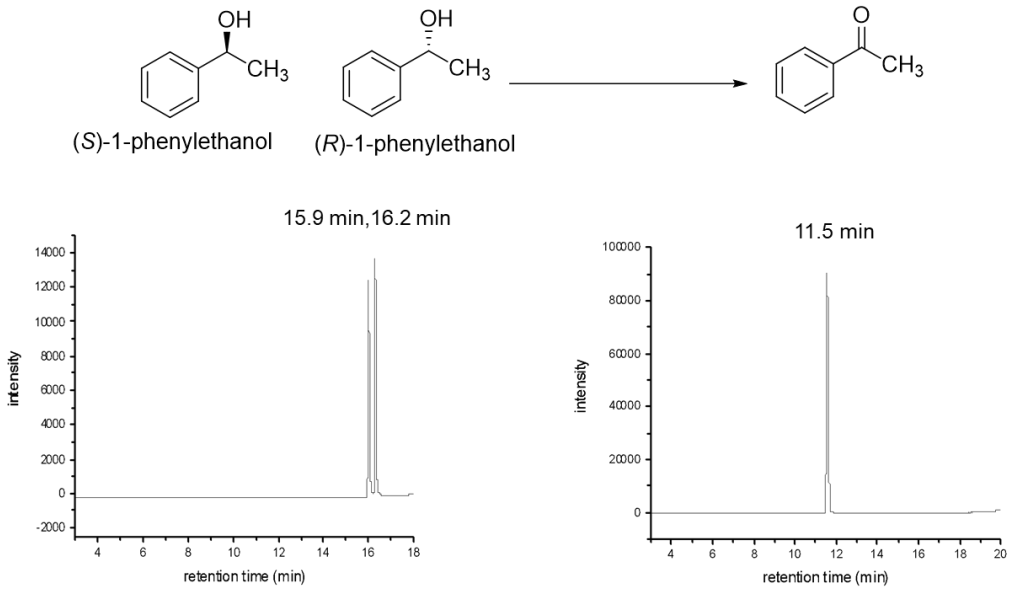

Figure 16. The GC analysis of (*R*,*S*)-1-phenylethanol (left) and acetophenone (right).

In the next step, amounts of (*R*,*S*)-1-phenylethanol that were 5 to 500 times lower than the initial concentration was applied for the reaction. Other conditions, including the amounts of H_2O_2, W, and PTC, were proportionally lower, with the exception of H_2O_2 which was held fixed at 3% (v/v). An extended reaction time up to 5 h was required for 100% conversion yield using 82 mM of (*R*,*S*)-1-phenylethanol (**Table 4**: entries 2 and 3). The concentration of (*R*,*S*)-1-phenylethanol was decreased even lower to10 times lower than entry 3, and subsequently showed complete conversion in 5 h. Step by step, the reaction temperature was also decreased from 90 °C to 50 °C for the enzymatic reaction. Prolonged reaction times were required at 50 °C to obtain almost the same yield as in the previous study. Therefore (*R*,*S*)-1-phenylethanol (8.2 mM) was incubated for 65 h with stirring at 1,000 rpm (**Table 4**: entry 5).

Table 4. Oxidation of (*R*,*S*)-1-phenylethanol at 90 and 50 °C with various concentrations of alcohol.

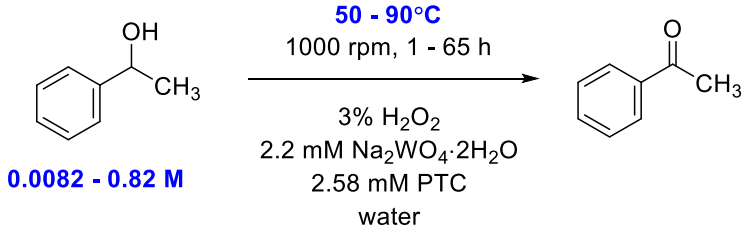

entry	reaction time [h]	temperature [ºC]	(*R*,*S*)-1-phenylethanol concentration [M]	conversion [%]
1	1	90	0.82	100
2	1	90	0.082	58.9
3	5	90	0.082	99.7
4	5	90	0.0082	100
5	65	50	0.0082	97.6

Oxidation reactions without W, PTC, and H_2O_2 were tested at 50 °C for 26 h to understand how each element in the oxidation of (*R*,*S*)-1-phenylethanol contributes to oxidation. In previous studies[58], the oxidation of alcohol revealed that the mechanism for the dehydrogenation of alcohol required both PTC and H_2O_2. First, H_2O_2 is necessary to oxidize the catalytic precursor Na_2WO_4 to $Na_2[WO(O_2)_2(OH)_2]$ + H_2O, which is a form that is active toward alcohol[58]. Afterward, PTC is required to transfer W from the aqueous phase to the organic phase in order for the dehydrogenation of alcohol to occur[58]. In this study, the oxidation of (*R*,*S*)-1-phenylethanol to acetophenone was barely observed (3%) without a metal catalyst. Furthermore, no conversion was shown without H_2O_2 (**Table 5**). Interestingly, the conversion without PTC was approximately 27%, indicating that oxidation of alcohol takes place without the PTC carrier.

Table 5. Oxidation of (*R*,*S*)-1-phenylethanol without tungstate, phase transfer catalyst, and hydrogen peroxide, respectively.

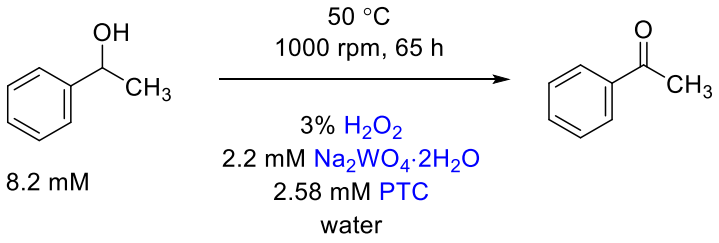

entry	Reaction condition	reaction temperature [°C]	reaction time [h]	(*R*,*S*)-1-phenylethanol concentration [mM]	conversion [%]
1	**Without WO_4^{2-}**	50	65	8.2	3.1
2	**Without PTC**	50	65	8.2	26.6
3	**Without H_2O_2**	50	65	8.2	0

The activity of enzymes strongly relies on the pH in the reaction mixture[59]. In this study, the catalytic activity of MoWSto depends on the acidity of the reaction medium. This is because $Na_2[WO(O_2)_2(OH)_2] + H_2O$, which is readily transferable to the organic phase by PTC, is predominantly formed in acidic conditions with a pH range of 0.4-3. An acidic condition below pH 6 influenced the structural integrity of MoWSto (**Figure 11**); therefore, the pH in the reaction solution needed to be adjusted to a more basic condition. Correspondingly, 20 mM of potassium phosphate and Tris-HCl buffer solution (pH 6.0) were added into the reaction mixture containing (*R*,*S*)-1-phenylethanol to see whether the buffers affected the conversion, and distilled deionized water without buffer was used as a negative control. The reaction solution without buffer had pH 5 due to the high acidity of PTC, and it showed a relatively high conversion of 76%. Conversion in the 20 mM Tris-HCl buffer at pH 6.0 after 26 h was 73.3%, respectively, indicating that there was no difference between the water and buffer solutions (**Table 6**). However, the conversion dropped to 29% in 20 mM potassium phosphate buffer at the same pH (**Table 6**). It is supposed that conversion is not affected by a buffer solution composed primarily of amine salts; however, the potassium phosphate buffer showed a seriously adverse effect on conversion. Therefore, Tris-HCl buffer or non-potassium phosphate buffer were selected for further reactions.

Table 6. Oxidation of (*R,S*)-1-phenylethanol in various buffer solutions.

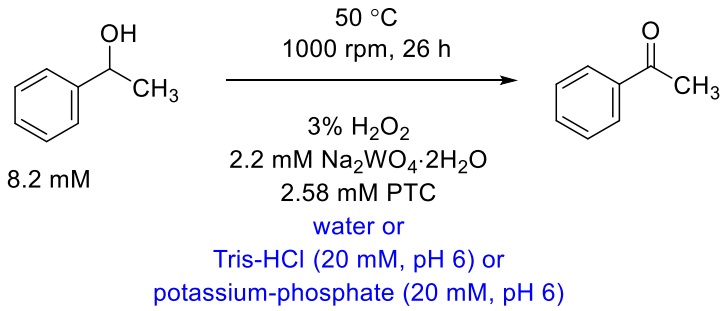

entry	reaction temperature [°C]	reaction time [h]	(*R,S*)-1-phenylethanol concentration [mM]	buffer condition	conversion [%]
1	50	26	8.2	Water	75.9
2	50	26	8.2	Tris-HCl, pH 6.0, 20 mM	73.3
3	50	26	8.2	Potassium-phosphate, pH 6.0, 20 mM	29

2.4.3. Oxidation of (*R,S*)-1-phenylethanol to acetophenone using cell crude extract of wild-type *A. vinelandii* containing MoWSto

In the previous section 2.4.2, we explored the possibility of catalytic oxidation in mild conditions with W salts. In this section, the artificial metalloenzyme, MoWSto was applied to the catalysis of oxidation by substituting the W salt with W-containing MoWSto (**Figure 17**). In order to save time and prevent the loss of W during purification, a cell crude extract of *A. vinelandii* was prepared for biocatalytic oxidation. The conversions from (*R,S*)-1-phenylethanol to acetophenone using tungstate salt in water were already 95% in 2 days and increased up to 99% in 13 days in Tris-HCl buffer solution when 1.9 mM W salt was used as a catalyst (**Table 7**: entries 1-3). The metal concentration in the cell crude extract added into the reaction solution was up to 0.14 mM, which was 15 times lower than the concentration of tungstate salt in the reaction solution. The conversion using cell crude extract reached 4.8% and 5.4% after 2 and 6 days, respectively, showing no major difference between 2 and 6 days of continuous reaction (**Table 7**: entries 5-6). Furthermore, the conversion was slower and less complete compared to that with tungstate salt due to its insufficient metal amount. Hence, the conversion between oxidation with metal salt and metalloenzyme under the same metal concentration was measured. Surprisingly, only a 7.7% conversion was observed at up to 5 days with W salt and 2.9% with purified MoWSto (**Table 7**: entries 4 and 8). The purified MoWSto showed much less conversion while the W salt and MoWSto crude extract showed a similar yield with the same metal concentration, which was suggested that the lysate could stabilize the MoWSto. The reaction with performed non-W-containing

MoWSto to check the background reaction showed no oxidation. Nevertheless, the prolonged incubation of the reaction solution up to 13 days increased the conversion up to 12% in the presence of cell crude extract (**Table 7**: entry 7).

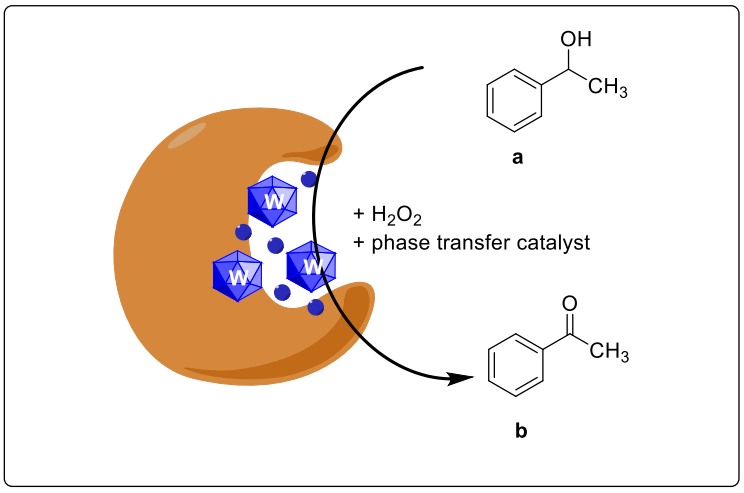

Figure 17. Green reaction proposed in this study using MoWSto as a metalloenzyme. The tungstate salt is replaced to tungstate containing MoWSto. The figure demonstrates the conversions from (*R*,*S*)-1-phenylethanol (a) to acetophenone (b) by W-containing MoWSto.

It was supposed that the polyoxometalate in the cage-like enzymatic structure gives the oxidation reaction an advantage because a high number of tungstate ions are packed into a small cavity of the enzyme. However, the results showed that the oxidation yield was similar regardless of the type of metal catalyst, and the oxidation yield was even lower in the case of the application of purified MoWSto. For these reasons, the question was raised whether W stably remains in MoWSto or is released to the reaction solution. We showed previously that MoWSto has a relatively high Tm value at 80 ºC, and that the protein was not degradable under hydrogen peroxide up to 20% at 4 ºC. We measured the protein stability again in the actual reaction conditions by determining the protein and metal concentrations after the reaction. The reaction solution containing purified MoWSto after several times or days was filtered through the centrifuge filter with a cutoff 10 kDa to remove decomposed proteins and to isolate intact proteins. The reaction solutions were washed with 3 mL of MOPS buffer containing 1 mM ATP and $MgCl_2$ and were then concentrated again until approximately 200 µL remained. The protein concentration before the reaction was 1.4 $mg \cdot mL^{-1}$; however, the protein concentration after 5 days of the reaction was only 0.04-0.08 $mg \cdot mL^{-1}$ (data not shown). In the case of the metal concentration, W was not detectable in the concentrated solution; in contrast, approximately 208 µM W was measured in

the first wash-out solution. The decrease in the protein and metal concentrations means that the protein was degraded and that most of the W contained in MoWSto had leaked out from the protein.

Table 7. Oxidation of (*R*,*S*)-1-phenylethanol using W salt and MoWSto cell extracts.

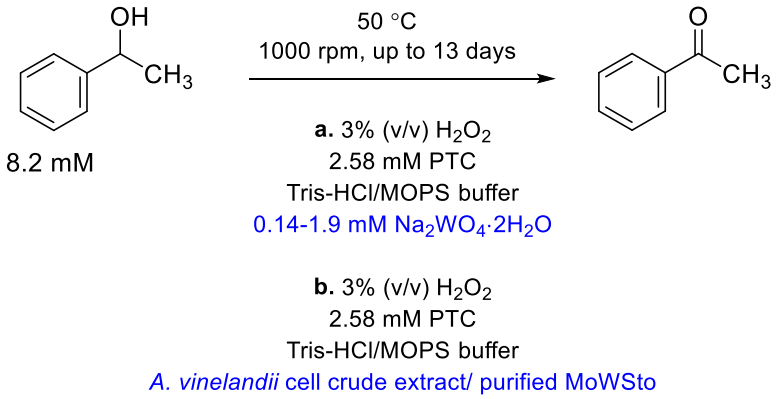

entry	reaction time [d]	Buffer	Types of metal catalyst	conversion [%]
1	2	20 mM Tris-HCl, pH 6		94.5
2	6	20 mM Tris-HCl, pH 6	WO_4^{2-} salt ,1.9 mM	98.8
3	13	20 mM Tris-HCl, pH 6		96.6
4	5	50 mM MOPS, pH 6.5	WO_4^{2-} salt, 0.14 mM	7.7
5	2	20 mM Tris-HCl, pH 6	Crude extract of MoWSto containing W, 0.14 mM	4.8
6	6	20 mM Tris-HCl, pH 6		5.4
7	13	20 mM Tris-HCl, pH 6		12.4
8	5	50 mM MOPS, pH 6.5	Purified MoWSto, 0.14 mM	2.9
9	6	50 mM MOPS, pH 6.5	Crude extract without W	n.d.

In order to identify the mechanisms affecting the protein stability, we incubated MoWSto in various concentrations of H_2O_2 in MOPS buffer for 20 h at 50 °C and measured the protein concentrations again. We observed protein precipitation after a 20 h incubation at 50 °C and additionally found that the metal concentration was severely reduced with and without H_2O_2. In contrast, the metal concentrations were relatively stable with various concentrations of H_2O_2 at 4 ºC (**Figure 18**). The significant W loss at 50 °C implied two possibilities: MoWSto may be unstable at 50 °C and, consequently releases W from the degraded protein; or W leaking happened due to temperature-induced metal-releasing even without thermal denaturation of MoWSto. This results suggested that the reaction conditions were not favorable for enzyme stability, even though the MoWSto is highly stable at a high temperature and high amount of H_2O_2. Previously, in section 2.3.4, we suggested that the buried lipophilic residues in aggregated proteins could be the reason why the Tm measured higher than actual Tm.

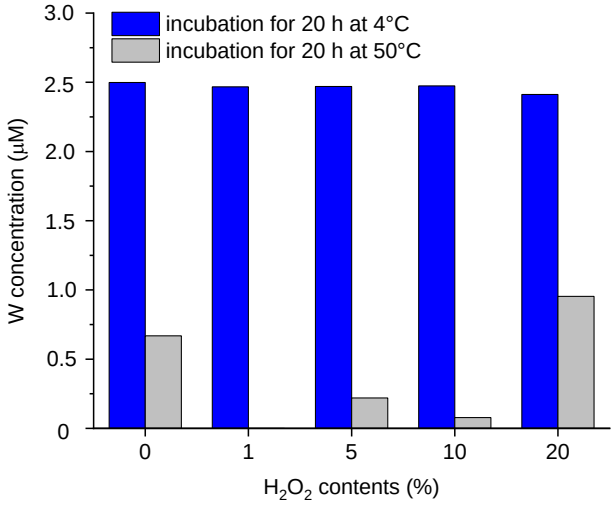

Figure 18. The metal concentration of MoWSto at 4 °C and 50 °C for 20 h incubation in MOPS buffer (pH 6.5, 50 mM)

2.5. Exploring a new function of MoWSto based on homology study

In a biological system, aspartate is converted to aspartate-β-phosphate by aspartate kinase, which is subsequently converted to aspartate semialdehyde by aspartate-semialdehyde dehydrogenase[60]. Aspartate semialdehyde is a vital element for the synthesis of essential amino acids such as lysine, threonine, and methionine[60] (**Scheme 4**). In addition, aspartate-β-phosphate participates in two-component signaling system in bacteria and plants, which is related to regulation processes, such as ripening and circadian rhythms, and is initiated by the sensor histidine kinase via a response regulator of DNA transcription factors[60].

MoWSto has shown high similarities with uridine kinase based on comparisons of its peptide sequences with existing protein sequences by BLAST analysis (**Table 8**). So far, the function of MoWSto as a biocatalyst has not been spotlighted. Therefore, we explored the kinase activity of MoWSto. Furthermore, the regioselectivity of MoWSto was studied for the application of MoWSto to phosphorylated metabolic intermediate production (**Scheme 5**).

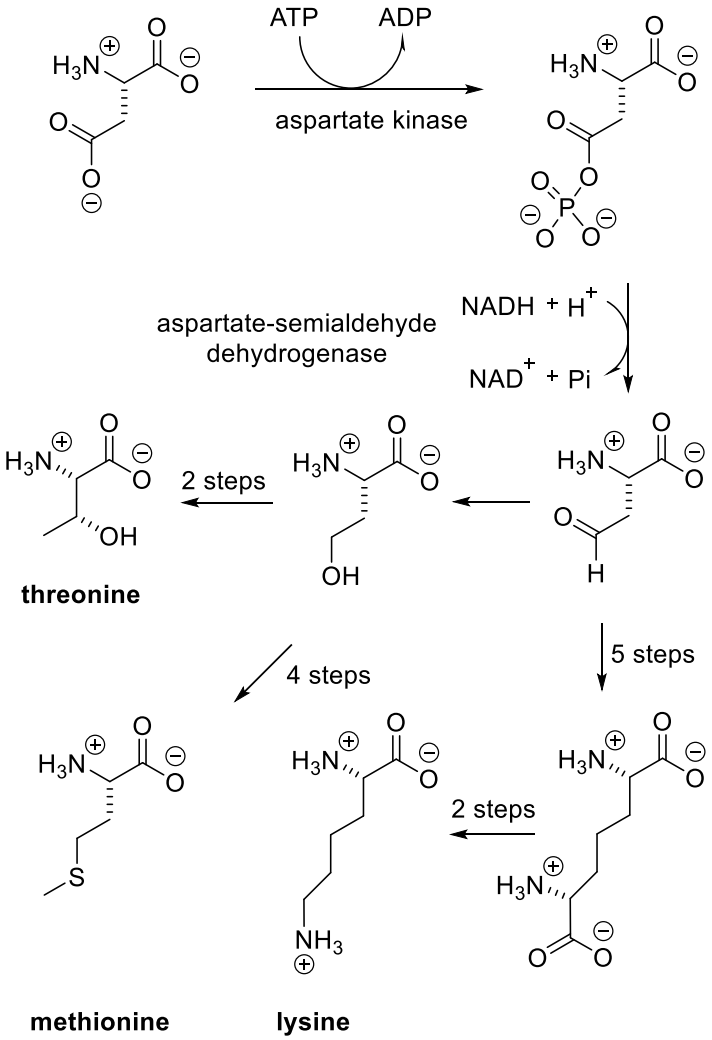

Scheme 4. Participation of phosphoaspartate as an intermediate in the pathways of lysine, threonine and methionine biosynthesis[60].

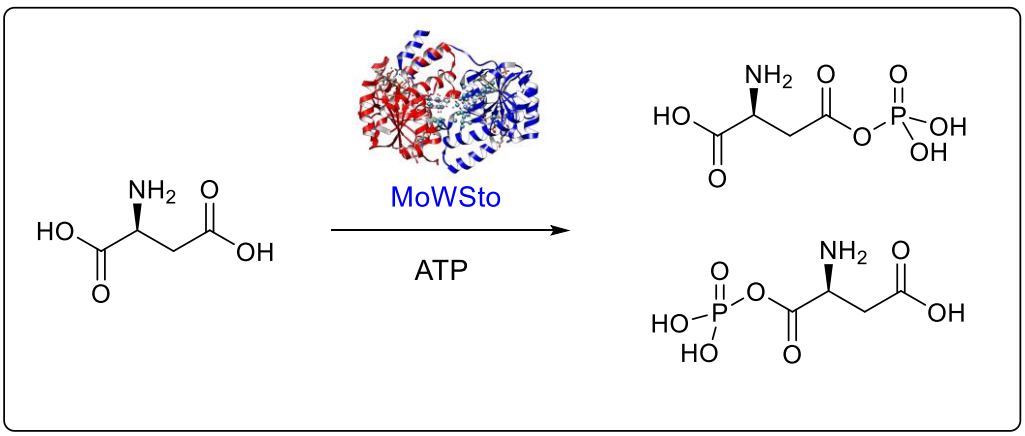

Scheme 5. The biocatalytic phosphorylation of aspartate by MoWSto: β-carbon phosphorylated aspartate (above) and α-carbon phosphorylated aspartate (below).

Table 8. Homology of the amino acid sequence between MoWSto and reported proteins: A, Molybdate storage protein subunit A [*A. vinelandii* DJ]; B, Molybdate storage protein beta subunit, MosB [*A. vinelandii* DJ].

A.

entry	Description	Identity	GenBank accession number
1	aspartate/glutamate/uridylate kinase [*Phaeospirillum fulvum*]	84%	WP_021133240.1
2	aspartate/glutamate/uridylate kinase [*Terriglobus saanensis SP1PR4*]	41%	ADV83113.1
3	uridylate kinase [*Bradyrhizobium* sp. BR 10245]	44%	WP_063704114.1

B.

entry	Description	Identity	GenBank accession number
1	uridine kinase [*Azotobacter chroococcum*]	94%	WP_039801168.1
2	uridine kinase [*Methylocystis parvus*]	91%	WP_026016403.1
3	uridine kinase [*Methylomonas* sp. LWB]	90%	WP_071156806.1
4	uridine kinase [*Methylomonas koyamae*]	89%	WP_064027539.1
5	uridine kinase [*Bradyrhizobium neotropicale*]	88%	WP_063676351.1
6	uridine monophosphate kinase [*Azospirillum lipoferum*]	89%	WP_012978510.1

2.5.1. Homology analysis and kinase activity

In general, MoWSto shares a conserved region that is related to uridine monophosphate kinase (UMPK) enzymes. UMPK catalyzes the phosphorylation of uridine monophosphate (UMP) with ATP and yields UDP. UMPK plays a key role in pyrimidine nucleotide biosynthesis[12,61]. In the BLAST results, MosA showed homology with aspartate/glutamate/uridylate-kinase derived from *Phaeospirillum fulvum* (84%; GenBank accession No. WP_021133240.1), *Terriglobus saanensis* SP1PR4 (41%; ADV83113.1), and uridylate kinase from *Bradyrhizobium* sp. BR 10245 (41%; WP_063704114.1) (**Table 8**A). These kinases catalyze the formation of phosphoric anhydrides, generally with a carboxylate, and use ATP as the source of the phosphoryl group and are involved in amino acid biosynthesis[61]. MosB showed even higher similarities with uridine kinase from *Azotobacter chroococcum* (94%; WP_039801168.1), *Methylocystis parvus* (91%; WP_026016403.1), *Methylomonas* sp. LWB (90%; WP_071156806.1), and *Bradyrhizobium neotropicale* (88%; WP_063676351.1) (**Table 8**B). Amino acid residues in MosA and MosB share the similarity with the P-loop motif of the ATP binding site of the kinase family[12]. Apart from the ATP binding site, the putative nucleotide-binding site was observed at residues at 45, 47-49,

211-212, and 215-216 of the MosA and 42, 44-46, 210-211, and 214-215 of MosB based on their similarity to carbamate kinase and N-acetyl-L-glutamate kinase (NAGK) which are structural and functional prototypes for the amino acid kinase family[62,63].

2.5.2. Application of Mo/W-storage protein as an enzyme with kinase activity

Based on homology analysis with published amino acid kinases, aspartate kinase activity was measured. Kinase activity was measured by quantification of aspartate hydroxamate formed in the presence of hydroxylamine at 540 nm[64]. MoWSto showed approximately 0.027 μmol·min^{-1}·mg^{-1}. In previous studies, kinase in wild-type microorganisms showed 0.00036 μmol·min^{-1}·mg^{-1} in *Lactobacillus plantarum*[65], 0.034-0.28 μmol·min^{-1}·mg^{-1} in *Corynebacterium glutamicum*[64,66], and 0.055 μmol·min^{-1}·mg^{-1} in *Brevibacterium flavum*[67], which suggested that the activity of MoWSto is in the middle range among bacterial aspartate kinases. MoWSto without tungstate showed a similar activity (0.021 μmol·min^{-1}·mg^{-1}) to MoWSto containing 258 μM W. This result showed that MoWSto could act as aspartate kinase using aspartate as a substrate, and that tungstate is not necessary for kinase activity. Most kinases need a divalent metal cation such as Mg^{2+}, Mn^{2+}, or Fe^{2+} [68–70] to activate ATP and orient the γ-phosphate group for phosphotransfer[71]. Therefore, the presence of 1 mM ATP and $MgCl_2$ was highly demanded for the formation of Mo- and W- clusters in MoWSto[48] as well as for catalyzing phosphorylation. A recent study explained that ATP plays an important role in polymolybdate storage in MoWSto[50] by pumping molybdate into the protein cage with ATP hydrolysis. However, the absence of tungstate clusters did not significantly affect the nucleotide content in the study. Furthermore, ATP hydrolysis presumably proceeds at subunit α, inferred from a highly occupied α-ATP/Mg^{2+} and a weaker occupied β-ATP/Mg^{2+}-binding site[50]. Interestingly, MosA expressed in *E. coli* as a host cell showed activity of 0.184 μmol·min^{-1}·mg^{-1}, which is approximately 9 times higher than the activity of MoWSto. Therefore, this result suggested that the whole MoWSto enzyme is not necessary for kinase activity.

2.5.3. Determination of regioselectivity of aspartic acid

The regioselectivity of phosphorylated aspartate was determined by NMR analysis. MoWSto act as an amino acid kinase (EC 2.7.2.4) based on putative conserved domain analysis and kinase classification[61,71] and, is known for converting L-aspartate to 4-phospho-L-aspartate[72]. Therefore, the phosphorylated carbon in L-aspartic acid was expected to be β-carbon instead of α-carbon. Due to analytical convenience, the phosphoryl group of phosphorylated L-aspartate was replaced with hydroxylamine so that ^{1}H-NMR could indirectly detect the position of the phosphorylated carbon. The ^{1}H-NMR spectrum of the end-product of a reaction containing 10% D_2O showed doublet of doublet

signals from the methylene hydrogens coupling with the carboxyl group and the adjacent CH at δ 2.56 and δ 2.69 (**Figure 19**D). In addition, it showed a doublet of doublets at δ 3.78 from the coupling of the single H of the $CHNH_2$ with the CH_2 group between the COOH and $CHNH_2$ groups. However, adding L-β-hydroxamate aspartate to reaction mixture produced a new peak at δ 3.89 (**Figure 19**E), which corresponds to a single H at H-$CHNH_2$ group of L-β-hydroxamate aspartate in D_2O and reaction solution without hydroxylamine (**Figure 19**B and C). The ^{1}H-NMR of aspartate was measured, showing singlet shifts at δ 3.66 from the coupling of the single H of the $CHNH_2$ and at multiplet δ 2.57 for the methylene hydrogens coupling with a carboxyl group (**Figure 19**A). This result suggests that aspartate was completely converted to an L-hydroxamate aspartate isomer, L-α-hydroxamate aspartate, which has a different structure from L-β-hydroxamate aspartate. In the literature, N-methyl-DL asparagine and N-methyl-DL-isoasparagine are isomers with an amide group at the α (N-methyl-DL-isoasparagine) and β carbon (N-methyl-DL asparagine)[73]. Isoasparagine showed a signal shift of the peak belonging to a single H at H-CNH (3.43 ppm) compared to the same H of asparagine (3.39 ppm). The coupling constant between H-$CNHCH_3$ and C-H were differentiated as well in two isomers (4.0 Hz; asparagine, 4.77 Hz; isoasparagine).

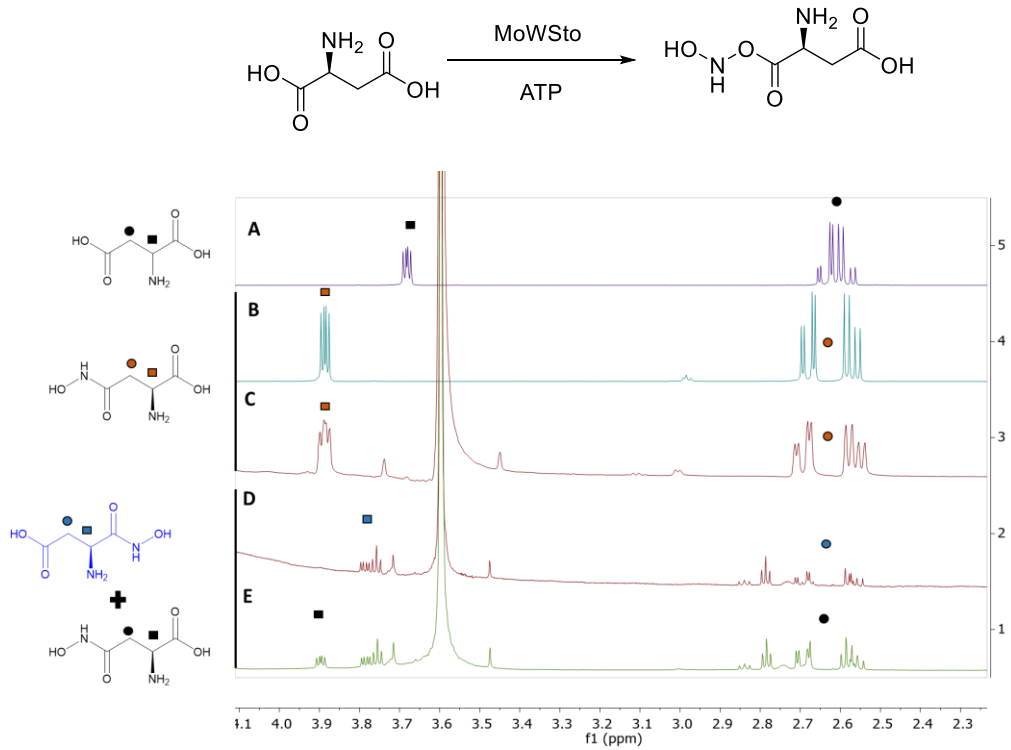

Figure 19. 1H-NMR spectra of aspartate in D_2O (A), L-aspartate-β-hydroxamate in D_2O (B), L-aspartate-β-hydroxamate in 10% D_2O-reaction solution without hydroxylamine and MoWSto (C), the reaction mixture containing 10% D_2O after biocatalytic phosphorylation (D), and the reaction mixture prepared in (C) containing L-aspartate-β-hydroxamate (E).

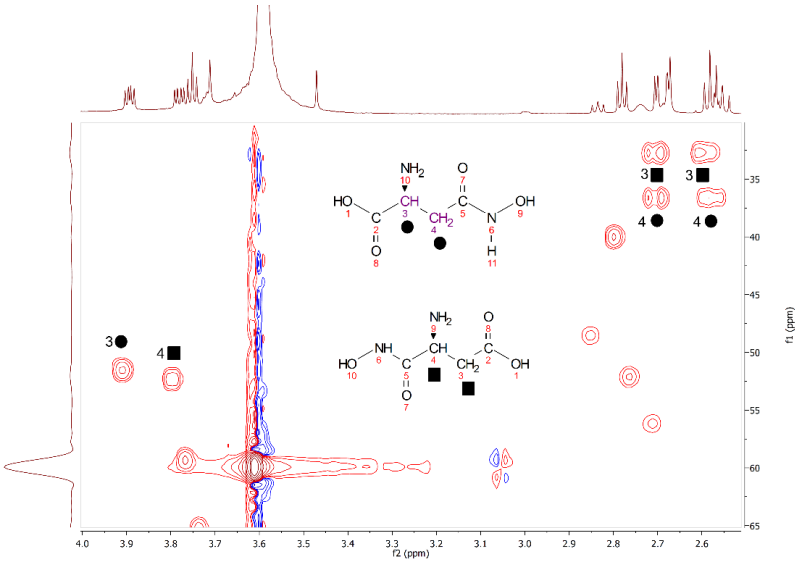

Figure 20. 2D ^{13}C–^{1}H correlation spectra of the reaction mixture after phosphorylation by MoWSto kinase. β-hydroxamate aspartate added in the reaction mixture for the comparison of 2D-NMR of each isomer. A; L-aspartate-β-hydroxamate (■), B; L-aspartate-α-hydroxamate(●).

Two-dimensional ^{1}H-^{13}C coupled NMR supported the idea that the product from our kinase reaction the isomer of β-hydroxamate aspartate (**Figure 20**). The β-carbon (-NH-CH_2-CO-) of L-aspartate-β-hydroxamate bound to two hydrogens was observed at ^{13}C 36.6 ppm (indicated by 3■ in **Figure 20**). However, its isomer α-hydroxamate aspartate showed shifted β-carbon above 35 ppm (indicated by 4● in **Figure 20**). The signal assigned for γ-carbon and coupled single hydrogen from α and β-hydroxamate isomer showed different peaks.

2.6. Summary and outlook

Biocatalysts have several advantages in organic synthesis, such as an excellent enantiomeric selectivity and an economical production method for their preparation[74]. Metalloenzymes have distinct characteristics compared to conventional biocatalysts, such as having a wide range of substrates because the substrate-binding site of metalloenzymes is not specified for a particular type of substrate. MoWSto is unique among metalloenzymes due to its ability to store over 100 Mo or W ions in the form of polyoxometalate, which is a tremendous amount relative to other known metalloenzymes. Published research has focused on Mo-storage and release mechanisms related to the structure of MoWSto. The introduction of MoWSto in organic synthesis attempted for the first time in this study.

Wild-type MoWSto from *A. vinelandii* was prepared in modified Burk's medium by inoculating several times, first in a metal-depleted medium and later in a Mo- and W-containing medium. *A. vinelandii*

showed no difference in growth in the metal and non-metal-containing media. The fully-grown cells were subjected to measurements of their metal concentrations and to the purification of their enzymes. The concentrations of Mo and W in cell crude extract were 16.6 and 20.5 μmol·g^{-1}, respectively. MoWSto was purified through several steps including size exclusion, ammonium sulfate precipitation, and anion exchange purification. The numbers of tungstate ions per mole of protein, was found to be 21.7, which was 5 times lower than the previously known amount[12,47,48]. The low metal contents in MoWSto were attributed to insufficient purification and cultural conditions. Nonetheless, 20 W ions per protein molecules was a much higher metal per enzyme ratio compared to conventional metalloenzymes, which typically have only one or two metal ions. Purified MoWSto showed clear bands on SDS-PAGE at 28 kDa for MosA and 29 kDa for MosB. The construction of recombinant cells using *E. coli* as the host cell was conducted to overexpress subunits of MoWSto. The results showed that MosA was overexpressed well at 18 °C with 0.5 mM IPTG through in the soluble fraction; however, MosB was not overexpressed in the same condition (**Figure 9**).

The melting temperature of MoWSto was determined by thermofluor screening. Good thermostability was observed in pH range from 6 to 8, and the optimal condition showing the highest melting temperature of 81.6 ºC was at pH 6.0 with PIPES buffer. MoWSto was stable in the H_2O_2 solution at an H_2O_2 concentration up to 20% at 4 °C. These results support that MoWSto would tolerate reaction condition in a broad range of temperatures within a weak acidic to neutral pH range containing H_2O_2 up to 20%.

Oxidation with H_2O_2 and tungstate in aqueous solutions was first reported in 1997[75] and has gradually been applied in the oxidation of a broad range of organic compounds[58]. Solvent-free green oxidation with secondary alcohol was selected as a benchmark reaction for the later substitution of tungstate salt with polyoxotungstate caged in MoWSto. (*R,S*)-1-phenylethanol was completely converted to acetophenone in a reaction solution containing tungstate salt, hydrogen peroxide, and PTC at 90 °C over 1 h. Consequently, the experimental conditions of the green oxidation were adjusted for a biocatalytic reaction. The concentration of (*R,S*)-1-phenylethanol was subsequently decreased from 820 mM to 8.2 mM and, furthermore, the oxidation reaction was performed at a lower temperature of 50 °C instead of 90 °C (**Table 4**). The oxidation of (*R,S*)-1-phenylethanol by the tungstate salt catalyst was prolonged at 50 °C in Tris-HCl buffer at pH 6.0 up to 26 h to achieve a 73% conversion. For the next step, (*R,S*)-1-phenylethanol was oxidized with cell crude extract containing MoWSto (**Table 6**).

The conversions using W salt, cell crude extract, and purified enzyme containing the same concentration of W (0.14 mM) showed that W salt and cell crude extract exhibited similar conversion rates of 6-7% while the purified MoWSto exhibited 3% conversion (**Table 7**). Extended reaction to 13 days increased the conversion to 12% with MoWSto cell crude extract. Furthermore, the background reaction due to the harboring of non-specific proteins by the cell lysate was not observed. Protein and tungstate concentrations were measured before and after the reaction to confirm whether the oxidation was catalyzed by polyoxotungstate located in the MoWSto cavity or by tungstate ions leaked from

MoWSto resulting in a loss of its oxidative power. After 5 days of reaction at 50 ºC, both the metal concentration and protein concentration in purified MoWSto were dramatically decreased. The incubation of MoWSto in MOPS buffer at 50 °C showed that the W concentration was diminished, in contrast to the metal amount when incubated at 4 °C. This result suggested either the instability of MoWSto at 50 °C or the spontaneous leakage of W from intact proteins.

To study an aspect of the application of MoWSto as a biocatalyst involved in metabolism, the amino acid sequences of MoWSto were analyzed by BLAST. Both MosA and MosB showed homology with plant and bacterial kinases. The kinase activity of MoWSto was measured by spectrophotometer, which yielded a specific activity in the middle range of bacterial kinases, 0.027 $\mu mol \cdot min^{-1} \cdot mg^{-1}$. MoWSto with and without W showed similar specific kinase activities. This result showed that metal clusters located in the middle of enzyme pockets do not have an important role in enzyme catalysis. The regioselectivity of aspartate was measured by ^{13}C- and ^{1}H-NMR. The phosphorylated aspartate was substituted by hydroxylamine, and hydrogen coupling at the position of substituted hydroxylamine was measured by NMR. ^{1}H-NMR showed different spectra from commercially available aspartate-β-hydroxamate, which suggested that the α carbon at aspartic acid was phosphorylated (**Figure 19**). Even though further proof with the reference compound is necessary, this result can be understood as indicating that MoWSto participates in the signaling pathway in a biosystem by phosphorylating small molecules. MoWSto has kinase activity, which is first reported here, and expected to be a possible biocatalytic candidate for organic synthesis.

3. Process development of a biocatalytic reduction of a pitavastatin key intermediate

* The finding of this section has been published in Journal ChemCatChem[76].
* The result was obtained by the cooperative work with AIP Corporation in Japan, and the patent was submittedc.

3.1. The synthesis of pitavastatin (HMG-CoA reductase inhibitors)

3.1.1. Conventional pitavastatin synthesis

A high cholesterol level in blood increases the risk of heart disease and stroke by clogging arteries. The synthesis of sterols, including cholesterol, begins with acetyl CoA, and the rate-limiting enzymatic reaction is two steps farther down the chain with the conversion of HMG-CoA (3-hydroxy-3-methylglutaryl-coenzyme A) to mevalonate by HMG-CoA reductase[78] (**Figure 21**). Statins-HMG-CoA reductase inhibitors inhibit this reaction and the production of mevalonate, thereby reducing total cholesterol (TC) and significantly lowering harmful low-density lipoprotein cholesterol (LDL-C). Most importantly, statins cause major reductions in almost all clinical manifestations of atherosclerotic disease, including coronary events, stroke, and the incidence of revascularization. On the other hand, many types of statins were isolated from fungi and synthesized in laboratories[78].

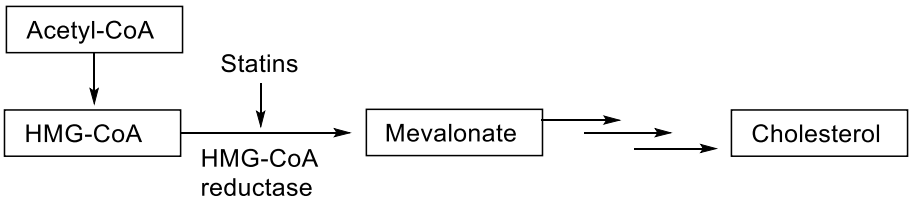

Figure 21. The rate-limiting step in the conversion of Acetyl CoA to cholesterol is 3-hydroxy-3-methylglutaryl-CoA to mevalonate. This reaction is mediated by the enzyme HMG-CoA reductase and HMG-CoA reductase inhibitors, or statins, competitively inhibit this activity[78].

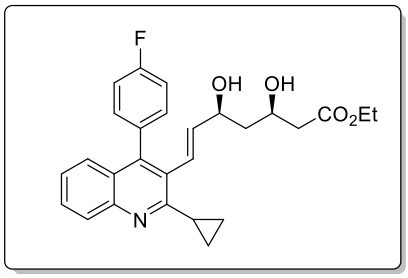

Figure 22. The structure of pitavastatin.

Pitavastatin, ((+)-monocalcium bis (3*R*,5*S*,6*E*)-7-[2-cyclopropyl-4-(4-fluorophenyl)-3-quinolyl]3,5-dihydroxy-6-heptanoate ($C_{50}H_{46}CaF_2N_2O_8$)), is a potent HMG-CoA reductase inhibitor which induces a substantial increase in LDL receptor activity and lowers LDL-C[79,80]. Pitavastatin is a statin, which was chemically synthesized by Nissan Chemical Industries, Ltd., Tokyo, Japan, and developed by Kowa Company, Ltd., Tokyo, Japan[81]. Pitavastatin has a characteristic structure (**Figure 22**) with a quinoline ring at the core, a cyclopropyl moiety, and a fluorophenyl group. This structure improves pharmacokinetics with better absorption and activity. The synthesis of a pair of anti-diol isomers (3-epimer and 5-epimer) was accomplished effectively by the asymmetric aldol reaction followed by anti-stereoselective reduction as key steps[80] (**Scheme 6**).

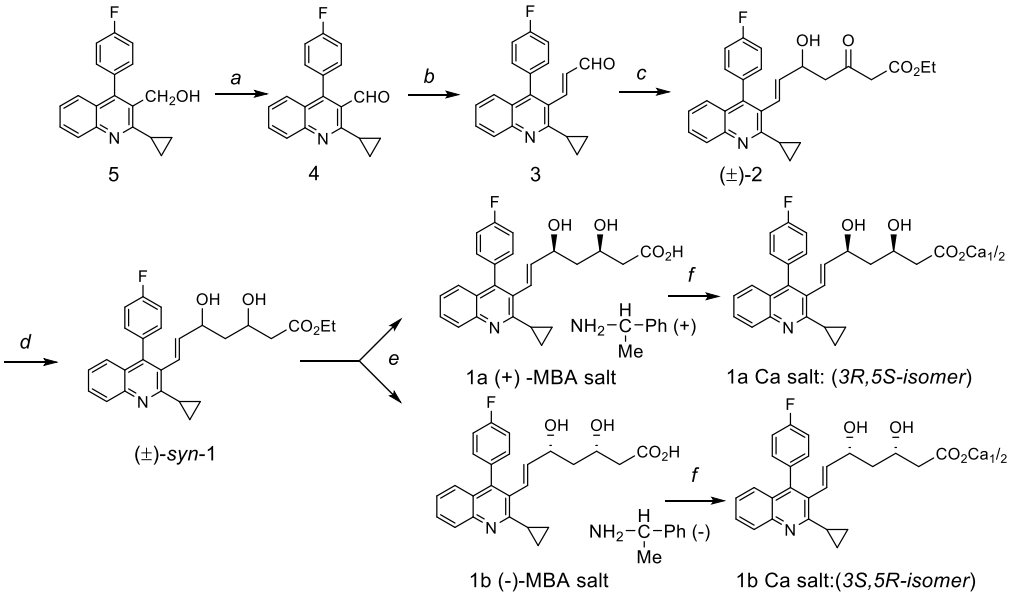

Reagents: (*a*) DMSO, P_2O_5, Et_3N; (b) i: $(EtO)_2POCH_2CN$, NaOH, (*n*-octyl)$_3$MeNCl, toluene and H_2O; ii: DIBAH; (*c*) $CH_3COCH_2CO_2Et$, NaH, *n*-BuLi; (*d*) $NaBH_4$, Et_2BOMe; (*e*) i: NaOHaq; ii: HClaq; iii: (+) -MBA or (-) -MBA; iv: recrystallized from MIBK and DMF; (*f*) i: HClaq; ii: NaOHaq; iii: $CaCl_2$.

Scheme 6. Synthesis of NK-104 (pitavastatin, 1a) and its enantiomer (1b) by diastereomeric resolution[80].

On the other hand, the chemical synthesis of pitavastatin started from 3-(bromomethyl)-2-cyclopropyl-4-(4'-fluorophenyl)quinoline with a Wittig reagent such as triphenylphosphine in suitable nonpolar solvents to obtain phosphonium bromide compound of formula **6**[79] (**Scheme 7**). In the presence of alkaline metal bases, an olefin compound of formula **8** was prepared following hydrolyzing the olefinic compound and forming a diol compound **9**. Pitavastatin synthesis was suggested in several ways with different approaches[79,82,83].

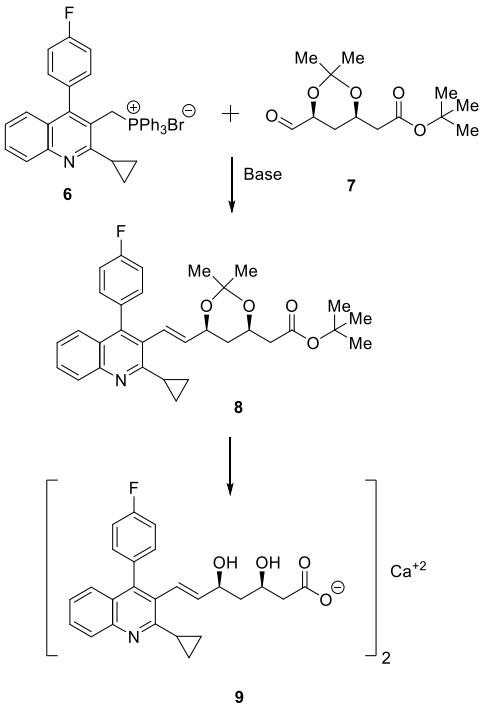

Scheme 7. A process for the preparation of storage-stable pitavastatin calcium in the crystalline form[79].

3.1.2. Application of biocatalysts in drug synthesis

The synthetic method of (±)-*syn*-**1** starting from compound **3** (**Scheme 6**) has been known in previous studies[80,82]; however, separation and purification of the desired stereoisomer in the downstream process required further steps such as flash chromatography, which is expensive and inefficient on an industrial scale. Using microbial cells to produce optically active alcohol is recommended as a cost-effective method for manufacturing enantiomerically active drug intermediates. The process is known for producing an optically active alcohol product by biocatalytic stereoselective reduction of a keto group in a compound **10** (**Scheme 8**). A key intermediate of the antiasthma drug, montelukast **12**, in this synthesis was prepared with the biotransforming organism, *Microbacterium campoquemadoensis* (MB5614)[84]. The enzyme isolated from MB5614 could reduce the corresponding keto to the desired (*S*)-hydroxyester with an enantiomeric excess greater than 95% at the optimum temperature 30 ºC. The

other case of using biocatalysts in optically active alcohol synthesis was done by baker's yeast, in which mappicine ketone **13** was converted to (*S*)-mappicine **14** with a 74% yield and 86% ee (**Scheme 9**)[85].

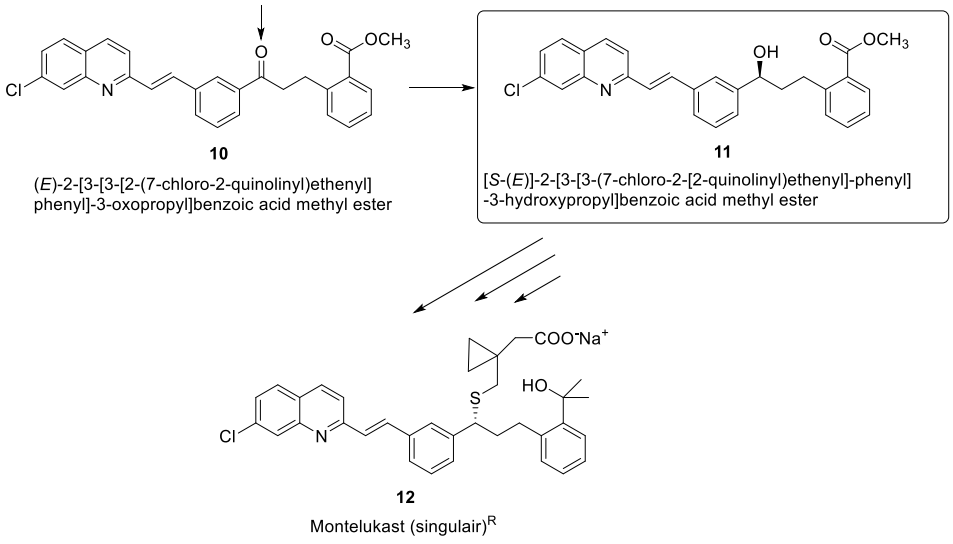

Scheme 8. The synthesis of montelukast. the stereospecific reduction of a keto ester intermediate, [(*E*)-2-[3-[3-[2-(7-chloro-2-quinolinyl)ethenyl]phenyl]-3-oxopropyl]benzoic acid methyl ester using MB5614 was involved[84].

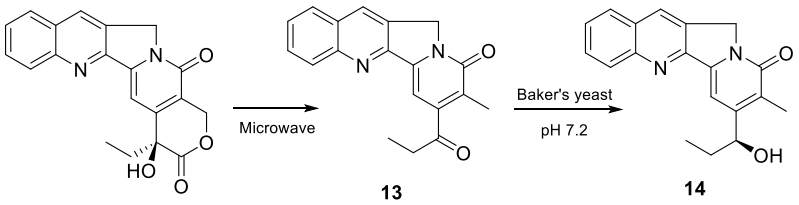

Scheme 9. Chemoenzymatic process for the conversion of camptothecin to (*S*)-mappicine[85].

Apart from the above examples, a well-presented example of an active alcohol drug is the β3-receptor agonist intermediate for the treatment of gastrointestinal disorders, diabetes, and obesity. The β3-receptor agonist intermediate was synthesized from ketone to (*R*)-alcohol using *Sphingomonas paucimobilis* (SC16113) (**Scheme 10**)[86,87]. Finally, the synthesis of another type of anti-HMG CoA reductase inhibitor was proposed using *Acinetobacter calcoaceticus* SC13876, giving a yield of 85% (ee 97%) (**Scheme 11**)[87,88].

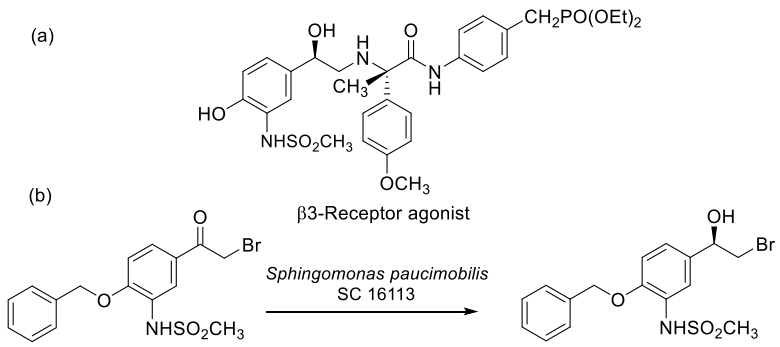

Scheme 10. Enzymatic synthesis of chiral intermediates to produce β3-receptor agonist (a)**.** Enantioselective reduction of 4-benzyloxy-3-methanesulfonylamino-2′-bromoacetophenone to (*R*)-alcohol[86] (b).

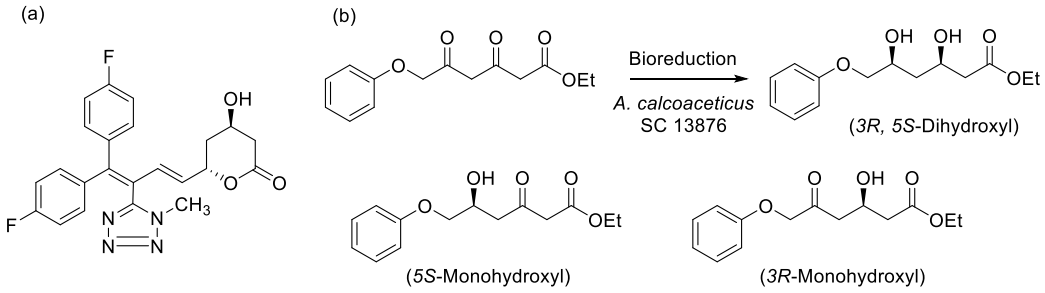

Scheme 11. Preparation of chiral synthons to anticholesterol drugs: (a) HMG CoA reductase inhibitor; (b) enantioselective microbial reduction of 3,5-dioxo-6-(benzyloxy) hexanoic acid ethyl ester to the corresponding diol ethyl (3*R*,5*S*)-dihydroxy-6-(benzyloxy) hexanoate[88].

3.1.3. Application of biocatalyst from *Ogataea minuta* to pitavastatin synthesis

Extensive studies were conducted to search for the desired biocatalysts to synthesize pitavastatin intermediate **18** from the chemically synthesized compound **15** (**Scheme 12**)[24]. The first application of microorganisms for pitavastatin production was done by screening microorganisms including genera *Metschnikowia, Cryptococcus, Candida, Filobasidium, Ogataea, Citeromyces, Rhodotorula, Exophiala, Schizosaccharomyces, Wickerhamiella, Pichia, Saccharomycopsis, Saitoella, Saccharomyces, Rhodosporidium, Brevibacterium,* and *Corynebacterium*. Many organisms showed catalyzing reduction of DOXE **15** ((*E*)-7-2-cyclopropyl-4-(4-fluorophenyl)-quinolin-3-yl)-3,5-dioxohept-6-enic acid ethyl ester) to DOLE **18** ((3*R*,5*S*)-(*E*)-7-[2-cyclopropyl-4-(4-fluorophenyl]-quinolin-3-yl]-3,5-dihydroxyhept-6-enic acid ester). Among them, *Candida* sp. and *Ogataea* sp. showed relatively good yield and enantioselectivity toward DOXE **15** and 5S-MOLE **16** ((*E*)-7-2-cyclopropyl-4-(4-

fluorophenyl)-quinolin-3-yl)-5-hydroxy-3-oxohept-6-enic acid ethyl ester) (**Table 9** and **Table 10**)[24]. Also, *Rhodotorula* sp. showed good activity toward 3R-MOLE **17** ((*E*)-7-2-cyclopropyl-4-(4-fluorophenyl)-quinolin-3-yl)-3-hydroxy-5-oxohept-6-enic acid ethyl ester) (**Table 11**).

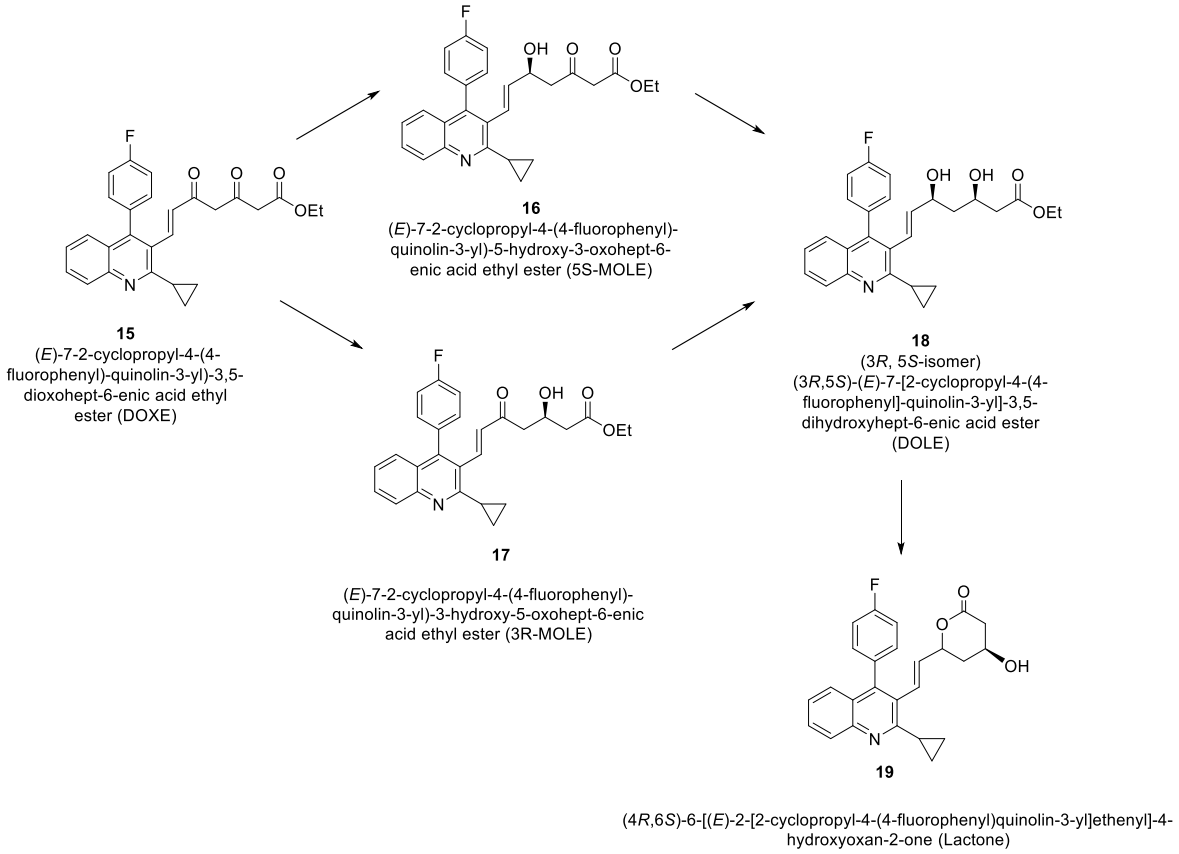

Scheme 12. The biocatalytic reduction process based on recombinant whole-cells[24].

3.2. Motivation of the study

The following study by the Mitsubishi Chemical Corporation showed that a carbonyl reductase from *Ogataea minuta var. nonfermentans* IFO 1473 (*O. minuta*) has an activity to reduce DOXE **15** and 5S-MOLE **16** to convert them to optically active alcohols, DOLE **18**[89–91]. The corresponding enzyme carbonyl reductase was later isolated from *O. minuta*, and the recombinant enzyme was constructed by Mitsubishi Chemical Corp.[90] The study showed that 319 µg yield of DOLE from 1mg DOXE **15** to give a 31.9% yield with 100% ee. and 0.6% anti-isomer, and a 80.7% yield and 15.3% anti-isomer toward 5S-MOLE **16**. However, the yield of wild-type enzyme has been still far from an industrial application. Development of a cost-effective and environmentally friendly method is required to synthesize enantiomerically pure pitavastatin intermediate on an industrial scale. Therefore, based on

the continuous interest in mass production of the pitavastatin intermediate, DOLE **18**, we developed an improved biocatalyst using *O. minuta* by directed evolution. We conducted directed evolution to improve conversion and enantioselectivity of the corresponding enzyme, a carbonyl reductase from *O. minuta* for an enantiomerically pure statin derivative. We reconstructed the OCR recombinant provided by API Corp. (separated from Mitsubishi Chemical Corp.), which will be explained in the next section.

Table 9. Production of DOLE **18** form DOXE **15**. Each kind of strain was cultured in 2.5 mL liquid medium and collected after 21 h. The cells were incubated in a reaction solution containing 0.3 $g \cdot L^{-1}$ DOXE **15** following extraction with an organic solvent. The extracted compounds were loaded on TLC plate for separation, and the concentration of each compound was measured after extraction of separated compounds from TLC plate[24].

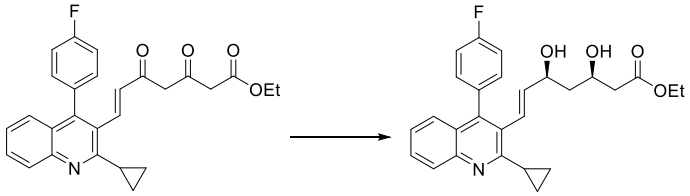

15 18

Microorganism used	The concentration of TLC-scraped-off sample (Excess diastereomer ratio, excess enantiomer ratio)
***Candida famata* var. *fmnata* RIFY7455**[24]	7.1 $mg \cdot L^{-1}$ (97.1% de, 100.0% ee)
Cryptococcus laurentii IFOO609[24]	0.4 $mg \cdot L^{-1}$ (100.0% de,100.0% ee)
Filobasidium capsuligenum IFO1185[24]	2.7 $mg \cdot L^{-1}$ (100.0% de,100.0% ee)
***Ogataea minuta var nonfermentans* IFO1473**[24]	7.4 $mg \cdot L^{-1}$ (92.0% de,100.0% ee)

Table 10. Production of DOLE **18** from 5S-MOLE **16.** Each kind of strain was cultured in 2.5 mL liquid medium and collected after 21 h. The cells were incubated in a reaction solution containing 0.38 g·L^{-1} 5S-MOLE **16** following extraction with an organic solvent. The extracted compounds were loaded on TLC plate for separation, and the concentration of each compound were measured after extraction of separated compounds from TLC plate[24].

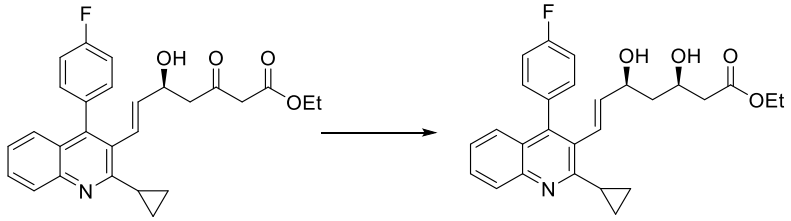

16 **18**

Microorganism used	Concentration of TLC-scraped-off sample (Excess diastereomer ratio, excess enantiomer ratio)	3-position asymmetric reduction selectivity from 5S-MOLE **16**
Saitoella complicate IAM12963[24]	13.28 mg·L^{-1} (96.1 % de, 96.6% ee)	100.0%
Candida solani IFO0762[24]	18.00 mg·L^{-1} (94.7% de, 93.3% ee)	100.0%
Metschnikowia pulcherrima IAM12197[24]	38.53 mg·L^{-1} (90.5% de, 97.8% ee)	100.0%
Shizosaccharomyces pombe IFO0344[24]	26.93 mg·L^{-1} (88.3% de, 93.3% ee)	96.6%
Metschnikowia pulcherrima IFO10796[24]	12.62 mg·L^{-1} (87.6% de, 97.2% ee)	100.0%
***Ogataea glucozyma* IFO1472**[24]	87.69 mg·L^{-1} (84.7% de, 98.4% ee)	100.0%
***Ogataea minuta var nonfermentans* IFOl473**[24]	77.02 mg·L^{-1} (79.4% de, 98.2% ee)	100.0%
Saccharomyces cerevisiae IFO0565[24]	1.67 mg·L^{-1} (81.8% de, 78.4% ee)	100.0%
Saccharomyces cerevisiae JCM1818[24]	1.87 mg·L^{-1} (77.0% de, 70.4% ee)	100.0%
Metschnikowia bicuspidate IFO1408[24]	11.76 mg·L^{-1} (74.5% de, 94.3% ee)	100.0%
Shizosaccharomyces pombe IFO1628[24]	12.32 mg·L^{-1} (74.1 % de, 96.4% ee)	96.4%
Candida molischiana IFO10296[24]	36.72 mg·L^{-1} (73.3% de, 94.7% ee)	93.4%
Rhodosporidium toruloides IFO0559[24]	20.27 mg·L^{-1} (67.7% de, 95.7% ee)	100.0%
***Candida famata* var. *famata* IFO0856**[24]	114.54 mg·L^{-1} (64.0% de, 98.2% ee)	93.0%
Filobasidium capsuligenum IFO1185[24]	116.20 mg·L^{-1} (61.2% de, 98.6% ee)	94.4%
Citeromyces matritensis IFO0954[24]	6.02 mg·L^{-1} (59.0% de, 82.0% ee)	82.6%
Cryptococcus humicolus IFO10250[24]	5.02 mg·L^{-1} (58.9% de, 97.8% ee)	100.0%
Yarrowia lipolytica IF01209[24]	0.90 mg·L^{-1} (50.9% de, 56.6% ee)	100.0%
***Candida intermedia* IFO0761**[24]	84.19 mg·L^{-1} (49.4% de, 98.4% ee)	89.7%
Trigonopsis variabilis CBS1040[24]	7.89 mg·L^{-1} (23.9% de, 91.9% ee)	84.6%

Table 11. Production of DOLE **18** from 3R-MOLE **17**. Production of DOLE from 3R-MOLE **17**. Each kind of strain was cultured in 2.5 mL liquid medium and collected after 48 h. The cells were incubated in a reaction solution containing 0.4 g·L^{-1} 3R-MOLE **17** following extraction with an organic solvent. The extracted compounds were loaded on TLC plate for separation, and the concentration of each compound was measured after extraction of separated compounds from TLC plate[24].

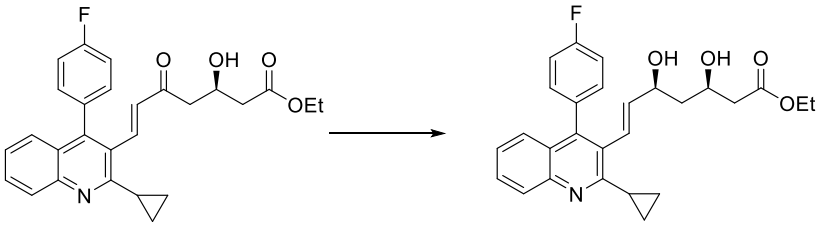

17 **18**

Microorganism used	Concentration of TLC-scraped-off sample (mg·L^{-1}) (Excess diastereomer ratio, excess enantiomer ratio)
Candida famata var. *famata* IFO0856[24]	59.9 (100% de, 100% ee)
Filobasidiun capsuligenum IFO1185[24]	24.0 (100% de, 100% ee)
Pichia anomala IFO0118[24]	1.0 (100% de, 100% ee)
Pichia petersonii IFO1372[24]	2.8 (78.6% de, 100% ee)
Cryptococcus laurentii var. *laurentii* CBS2174[24]	23.8 (75.6% de, 100% ee)
Cryptococcus laurentii var. *laurentii* CBS5746[24]	40.4 (73.3% de, 100% ee)
Cryptococcus laurentii var. *laurentii* CBS7140[24]	32.4 (75.3% de, 100% ee)
Cryptococcus laurentii var. *laurentii* CBS7235[24]	18.9 (75.7% de, 100% ee)
Cryptococcus fiavus IFO0407[24]	36.7 (81.5% de, 100% ee)
***Rhodotornla mucilaginosa* IFO0003**[24]	81.5 (100% de, 100% ee)
Rhodotorula glutinis var. ***dairenensis* IFO0415**[24]	53.3 (83.9% de, 100% ee)
***Rhodotorula aurantiaca* IFO0754**[24]	108.6 (100% de, 100% ee)
Cryptococcus laurentii var. *laurentii* CBS2174[24]	51.3 (75.8% de, 100% ee)
Cryptococcus laurentii var. *laurentii* CBS57 46[24]	29.3 (74.7% de, 98.4% ee)
Cryptococcus laurentii var. *laurentii* CBS7140[24]	79.8 (74.4% de, 100% ee)
Cryptococcus laurentii var. *laurentii* CBS7235[24]	88.4 (73.5% de, 99.2% ee)
***Rhodotorula mucilaginosa* IFO0003**[24]	97.3 (100% de, 100% ee)
***Rhodotorula glutinis* var. *dairenensis* IFO0415**[24]	101.6 (83.9% de, 100% ee)
***Rhodotorula aurantiaca* IFO0754**[24]	91.6 (100% de, 100% ee)

3.3. Process development of pitavastatin synthesis and directed evolution of OCR

3.3.1. Importance of cofactor stability in biocatalytic reaction

Nicotinamide cofactors transfer electrons to an intermediate of biosynthesis, which can be applied in various reactions for catalyzing selective redox reactions along with dehydrogenases[92]. Although many of these reactions have great value in synthesis, the cofactors required are expensive and significantly unstable in solutions[93]. Stability of nicotinamide cofactor under extreme acidic and basic conditions was studied in the early stage of cofactor stability to show that acids and bases could catalyze hydration and hydrolysis of the cofactor, respectively[92]. Recently, there were studies about irreversible nicotinamide cofactor degradation to nicotinamide and ADP-ribose by heat, and consequently, metabolic engineering to reuse such a decomposed cofactor unit in vivo was tried[94–96]. OCR from *O. minuta* needs nicotinamide cofactors for catalytic reduction like other alcohol dehydrogenases. In section 3.3.3, the reaction temperature was kept at 50 ºC to enhance substrate solubility in a two-phase reaction mixture. Consequently, the behaviour of NADPH at high temperature in organic solvents was considered to be investigated first.

3.3.1.1. Factors decreasing NADPH stability

The decomposition rate of NADPH was measured by monitoring the absorbance at 340 nm after incubation of NADPH mixture at 25-50 °C, and the relative amount of NADPH in a time course was drawn (**Figure 23**). NADPH decomposed very slowly at room temperature up to 6 h to show less than a 20% decrease in initial absorbance in phosphate buffer at pH 7.0, which was the favorable condition for NADPH stability (**Figure 23**A). However, dramatic losses of absorbance of NADPH in a phosphate buffer were observed at higher temperatures of 40 and 50 ºC. Only 34% and 13% of initial absorbance were found in 5 h of incubation at temperature increments of 40 and 50 ºC, respectively (**Figure 23**B and D). It is known that decomposition of NADPH is highly dependent on temperature and pH, especially, the presence of phosphate salt[92,93]. Also, acids having pKa values up to 7 exhibit the same ability to provide rapid catalysis of decomposition of NAD(P)H[93]. In this study, the tendency of absorbance decrease of NADPH in phosphate buffer corresponded to previous research, which showed a higher decomposition than that in other conditions.

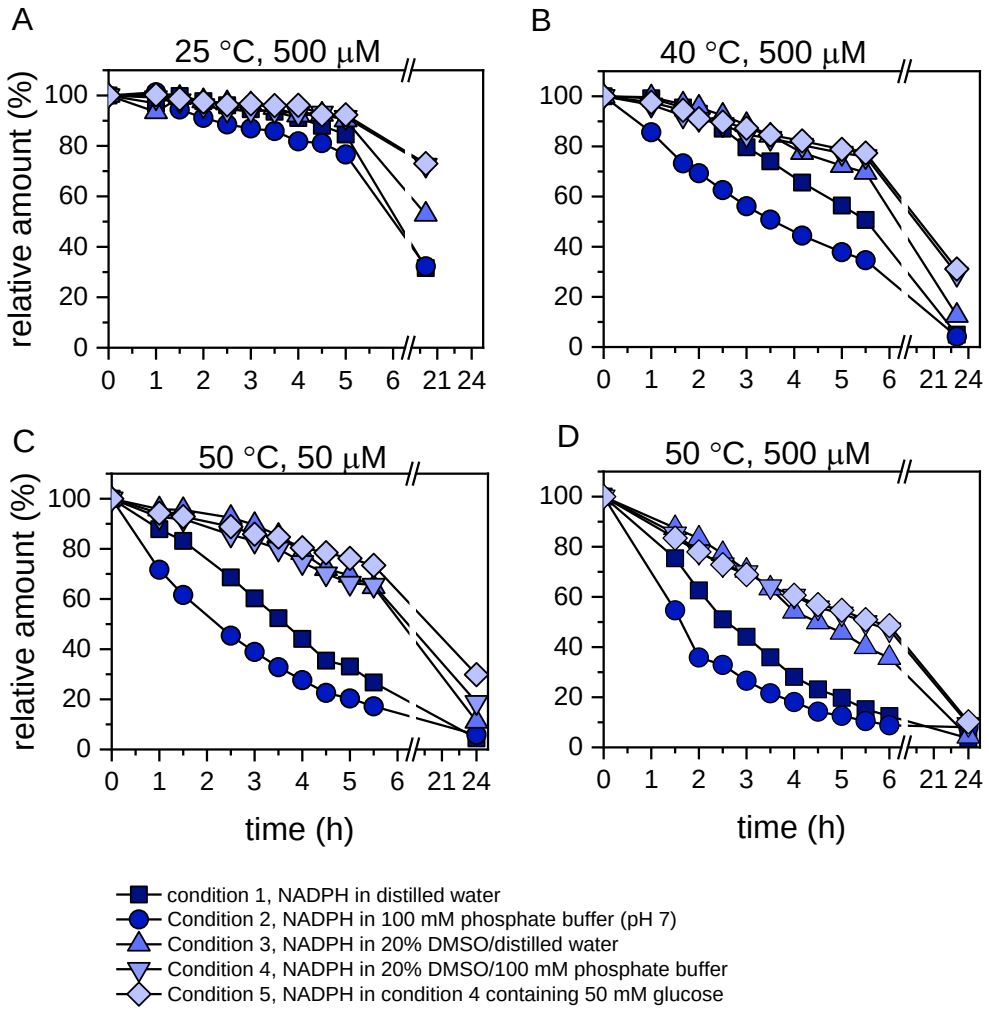

Figure 23. The relative amount of NADPH based on absorbance loss in a time course up to 24 h. Relative amount means the ratio of the percentage of A_t at a specific time compared to A_0 at 0 h. The solution containing NADPH was incubated at 25 ºC (A), 40 ºC (B), 50 ºC (C and D). In general, 500 µM NADPH was used for the experiment; furthermore, the difference of degradation between difference NADPH concentration was tested at 50 ºC with 50 and 500 µM NADPH (C and D, respectively). Condition1 (closed square), NADPH in distilled water; Condition2 (closed circled), NADPH in 100 mM phosphate buffer (pH 7.0); Condition3 (blue triangle), NADPH in 20% DMSO-distilled solution; Condition4 (gray inverted triangle), NADPH in 20%DMSO-100 mM phosphate buffer (pH 7.0); Condition5 (paled blue diamond), NADPH in 20%DMSO-100 mM phosphate buffer (pH 7.0) containing 50 mM glucose.

Interestingly, the loss of absorbance was less severe in a 20% DMSO solution. Approximately 20% higher residual amount of NADPH was observed in 20% DMSO-water mixture compared to that in distilled water at 40 and 50 ºC after 5.5 h (**Figure 23**B and D). The results showed that adding DMSO lowers the rate of NADPH decomposition up to 6 h at 40-50 °C. This observation corresponds to the calculation of a first-order rate constant (**Figure 24**). The loss of absorbance at 340 nm followed first-

order kinetics[97]. As the temperature was increased, the degradation rate of NADPH in water and phosphate buffer was dramatically elevated (**Figure 24**). On the contrary, the degradation of NADPH was diminished with DMSO addition. Interestingly, a 20% DMSO and phosphate mixture seems more stable compared to a 20% DMSO-water solution, which shows a slightly lower-rate constant (**Figure 24**). This suggests that DMSO can stabilize the initial conformation of NAD^+[98].

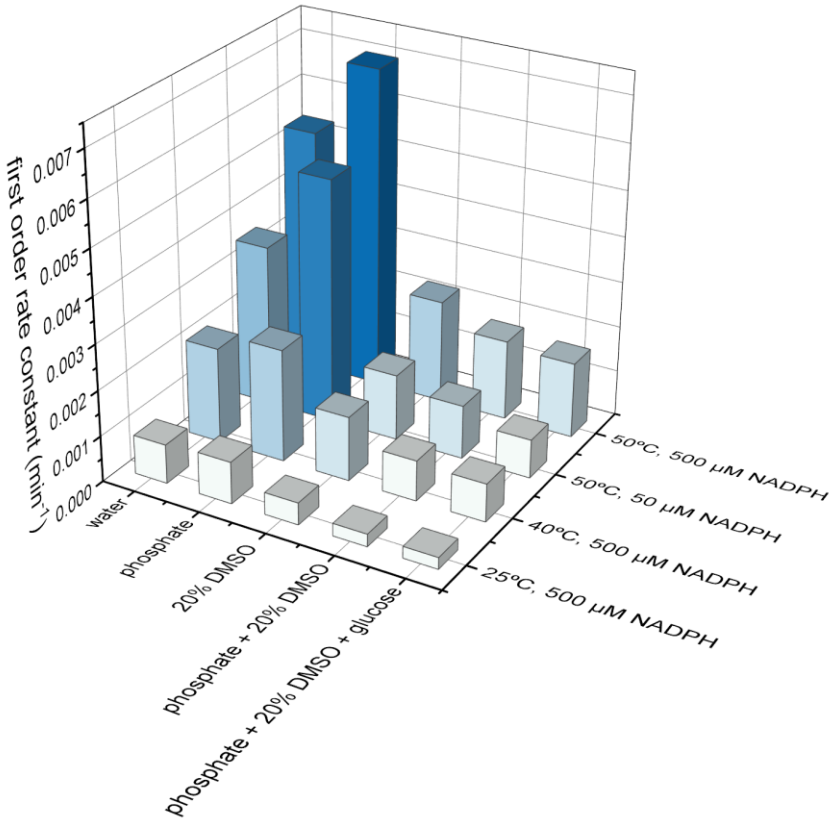

Figure 24. Effect of temperature and additives on the stability of NADPH.

The half-life of NADPH in various condition (**Table 12**) showed the half-life at 50 ºC in a 20% DMSO-water solution was approximately 4 times longer (7 h) compared to it in phosphate buffer without DMSO at the same temperature (2 h). The half-life was increased at the same temperature by adding additives such as phosphate salt and glucose in a 20% DMSO solution (**Table 12**). Phosphate in the water had a negative effect on NADPH stability. However, the existence of phosphate in a 20% DMSO aqueous solution showed it contributes to enhancing the stability of NADPH. In the previous study, organic cosolvents such as glycerol, poly(ethylene glycol), and 1-propanol showed stabilization of NADPH against phosphate-catalyzed decomposition[93].

Table 12. The half-life of NADPH in various buffer solutions and temperatures. NADPH was dissolved in various aqueous solution to make 500 µM following incubation at 25-50 °C.

Half-life (h)				
Buffers	temperature (ºC)			
	25	40	50*	50
water	14	6	3	2
100 mM phosphate buffer (pH 7.0)	13	5	2	2
20% DMSO in water	24	8	8	5
20% DMSO in 100 mM phosphate buffer (pH 7.0)	42	13	10	7
20% DMSO in 100 mM phosphate buffer (pH 7.0) containing 50 mM glucose	45	14	14	7

*concentration of NADPH was 50 µM.

3.3.1.2. Effect of NADPH stability on the conversion

3.3.1.2.1. Thermostability of OCR

OCR wild-type (OCR-WT) can catalyze the reduction of ketones such as 2,2,2-trifluoroacetophenone (TFAP) **20** to a corresponding chiral alcohol[99,100]. OCR-WT uses NADPH as a cofactor, and glucose dehydrogenase (GDH) was used for the cofactor regeneration[99]. In this study, GDH2 (glucose dehydrogenase 2), which has been engineered by Bommarius group to have stability at high temperature, was used[101] to regenerate the cofactor at 50 °C. Therefore, the cofactor stability, as well as OCR-WT stability at high temperature, was measured. The residual activity was measured after incubation of the OCR-WT at various temperatures for 1 h (**Figure 25**). In this experiment, OCR-WT showed approximately 85% of remaining activities at 20, 30, and 40 °C, which means OCR-WT would not lose its activity in 1 h up to 40 °C. However, residual activity was severely decreased at 50 °C down to 45%; furthermore, OCR-WT completely lost its activity at 60 °C. Compared to the previous study done by Honda[99], OCR-WT in this study showed approximately 60% residual activity at 30 and 40 °C. Because OCR-WT with a 6xhistidine tag was used in Honda's study, it is possible that the presence of a histidine-tag has effects on thermostability. On the contrast, OCR-WT does not contain any tagging polypeptides in our study (section 6.2.5.1. see the vector map). However, both results from this study and Honda agree that OCR-WT loses over 50% of its activity at 50 °C in 1 h. Therefore, 50 °C is the optimal temperature for excellent catalytic activity but not for stability. Thus, bioconversion of TFAP **20** to determine effective cofactor addition was performed at 40 °C.

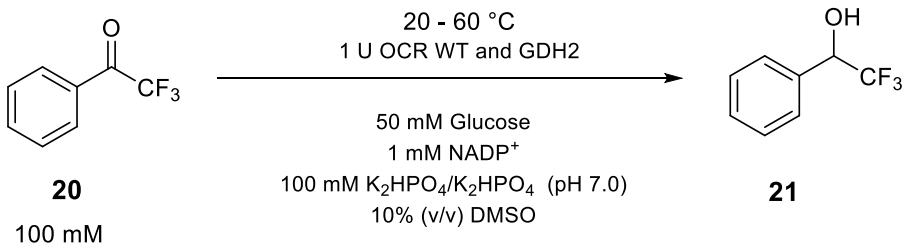

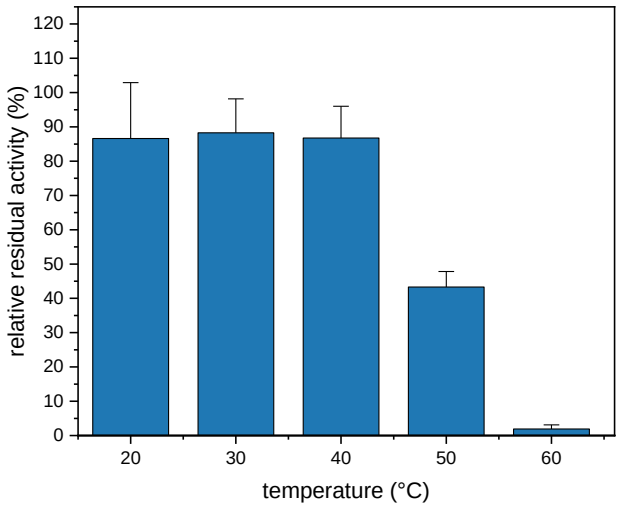

Figure 25. Residual activity of OCR at different temperatures.

3.3.1.2.2. The optimal condition for bioconversion with nicotinamide cofactor.

Bioconversion using 100 mM TFAP **20** and 1 U of OCR-WT and GDH2 at 40 ºC was measured after 1 and 4 h of reaction. We determined the K_m value of NADPH following the Michaelis-Menten equation to conduct the experiment under an NADPH-saturated condition. Enzyme kinetics for NADPH was measured using 10 mM TFAP as a substrate, resulting in K_m values of 0.19 mM. Approximately 0.4 mM $NADP^+$ (double concentration of K_m) was added at 0 h to the reaction mixture, and the same concentration of the cofactor was added at 0 and 2 h in the other reaction mixture. On the contrary, 0.8 mM $NADP^+$ was added at 0 h to the reaction mixture to see whether the stepwise addition of $NADP^+$ is beneficial in terms of preventing cofactor degradation. The conversion was similar between each experiment at 1 h (38-45%). It was expected that the degradation of NADPH was not severe in 1 h (**Figure 26**). However, the conversion was gradually differentiated in between each experimental condition at 4 h. The conversion with the addition of 0.4 mM NADPH at 0 and 2 h was 20% higher than the conversion with the addition of 0.4 mM NADPH at 0 h. The conversion with the addition of 0.8 mM NADPH at 0 h was 56%, which is still 10% lower than the cofactor addition. Even though the stepwise addition of cofactor showed approximately 10% increased conversion, the result suggested

that it is worth adding a lower concentration of cofactor several times instead of adding a high concentrated cofactor at the beginning of the reaction. The previous study showed that adding a ten times higher concentration of cofactor increased conversion up to two times higher; however, 100 times greater cofactor addition did not show any further increment of conversion[102]. Besides, some ADHs such as *Thermoanaerobacter brockii* ADH showed very low cofactor saturation with 5 µM NADPH[103]. Therefore, the increment of the initial concentration of NADPH is not beneficial for improvement in alcohol production due to cofactor saturation.

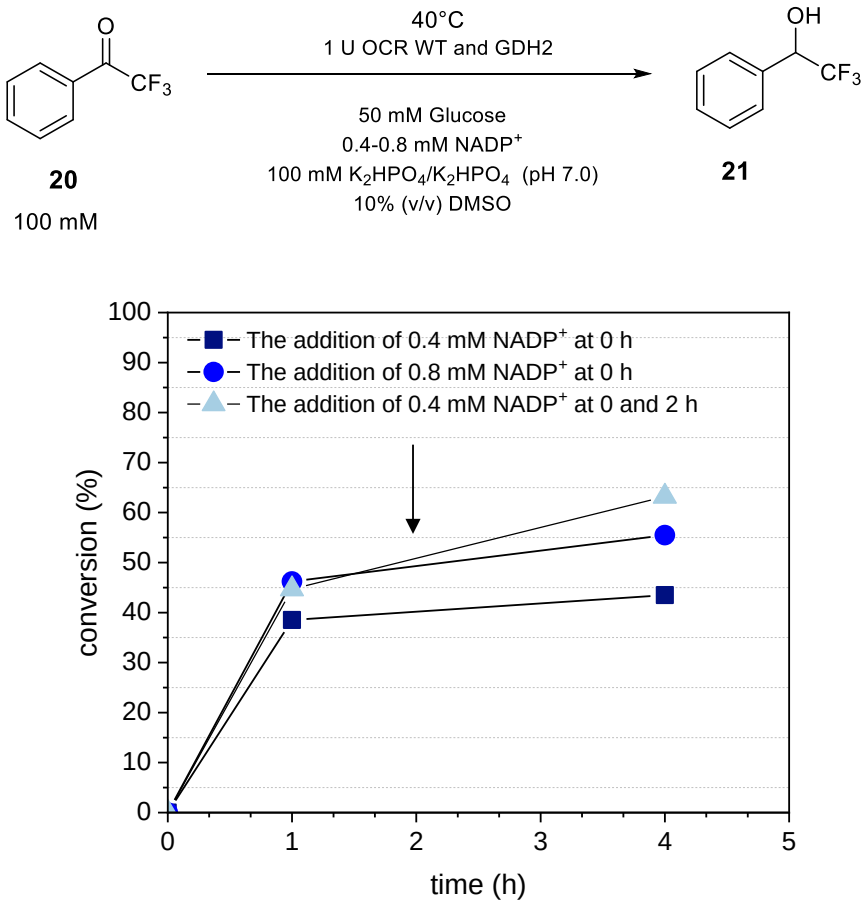

Figure 26. Effect of NADPH addition as time course on the conversion of TFAP **20**. The concentration of $NADP^+$ corresponding to twice K_m, 0.4 mM, was added at 0 h (squire), and the same concentration of $NADP^+$ was added at 0 and 2 h (triangle). Four times higher K_m concentration, 0.8 mM, was added at 0 h (circle). The arrow means the addition of $NADP^+$ at 2 h.

3.3.2. Stability of OCR for organic solvents

Most of the biocatalysts can catalyze chemical transformation with high enantioselectivity in the aqueous solution under predominantly ambient conditions. However, the advantage of using biocatalysts is incompatible with a water-free environment, which is required for the vast majority of organic synthesis[104]. A few biocatalysts such as lipase from *Brevibacillus agri* 52, *Pseudomonas* sp., *Burkholderia cepacia* strains, *Bacillus* sp., thermophilic archaea, fungi and yeast showed tolerance for organic solvents[105]. The behavior of OCR-WT in various conditions needs to be determined to understand the stability of the enzyme in the reaction solution. Enzyme stability in various organic solvents was measured by spectrophotometry using OCR-WT. Briefly, 500 µL cell crude extract

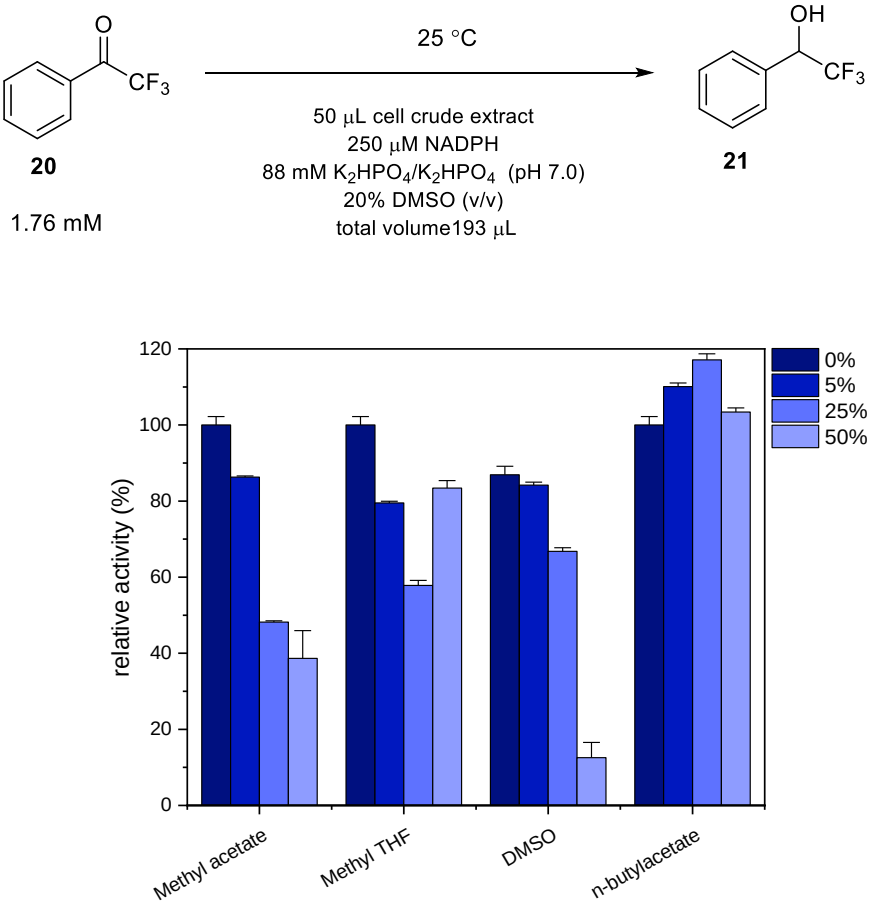

Figure 27. Enzyme stability of OCR WT; enzyme stability after 4 h incubation in 0-50% organic solvents.

containing OCR-WT was incubated for 4 and 16 h in 5, 25, and 50% organic solvent solutions including methyl acetate, and methyl tetrahydrofuran (THF), DMSO, and *n*-butyl acetate at 25 °C shaking incubator. The catalytic activities were measured with a microplate reader using TFAP **20** as a substrate.

Most of the organic solvents showed minor effects on OCR-WT enzyme stability with 5% organic solvents (**Figure 27**). Relative activities of OCR-WT were 86% in methyl acetate 80% in methyl THF, 84% in DMSO and 110% in *n*-butyl acetate. However, the residual activities in 25-50% of methyl acetate were severely decreased to 48% and 36%, which suggested that highly concentrated methyl acetate causes harmful effects on enzyme stability. Also, 50% DMSO dramatically reduced relative activity. Nevertheless, the relative activity in 25% DMSO was kept to 67%, not being strictly reduced the catalytic activity of OCR-WT. Interestingly, *n*-butyl acetate was the only organic solvent with enhanced the relative activities regardless of its concentrations. However, *n*-butyl acetate has relatively high hydrophobicity (logP 1.82), which could prevent the dissolution of the DOXE **15** and 5S- and 3R-MOLE **16** and **17** (MOLEs) in the buffer and limit the accessibility of biocatalysts to substrates. Therefore, DMSO was chosen for an organic solvent for further study.

3.3.3. Improvement of enzyme specificity toward pitavastatin intermediate

3.3.3.1. Construction of mutagenesis library by error-prone PCR and colorimetric screening of enhanced activity.

DNA encoding OCR-WT was amplified by error-prone PCR to produce mutated DNA having random mutated residues. The mutant library was constructed by using pKV32_OCR as a template, 0.5 μM primers of FP-BamH1-OCR and RP-BmgBI-OCR (see the experimental section 6.2.5.3), 0.4 mM of dNTPs, 0.25 mM $MnCl_2$ and 4.5 mM $MgCl_2$. Taq polymerase (0.025 $U \cdot \mu L^{-1}$) was used for the DNA amplification. The mutation rates were calculated to be from 2 to 3 mutations per 1,000 bp based in this study. The mutated DNA was restricted by BamHI and BmgBI restriction enzymes, cloned to customized vector pKV32 plasmid, and transformed to JM109(DE3) *E. coli*. Every single mutant clone on agar plates was inoculated and cultured in 96 well plates containing TB medium and cultured overnight, and the fully grown cells were re-inoculated in fresh autoinduction medium again. The cell was harvested, and the crude extract was prepared by Bugbuster protein lysis reagent. The cell crude extracts of OCR mutants were screened using 5S-MOLE **16** as a substrate. Bromothymol blue is blue at neutral pH, and it turns to green and yellow as mutants catalyze reduction of 5S-MOLE **16** to DOLE **18** and produce acid (**Scheme 13**). After 16 h incubation of OCR-WT in a phosphate buffer at pH 8 containing 5S-MOLE **16**, GDH2, glucose and bromothymol blue, the reaction mixture turned into yellow-green from cobalt blue. Afterward, we screened approximately 450 mutant clones and collected mutants, which showed relatively greener or yellower color than OCRI-WT (**Figure 28**). The background without cell crude extracts changed to dark green (see the white box in **Figure 28**); however,

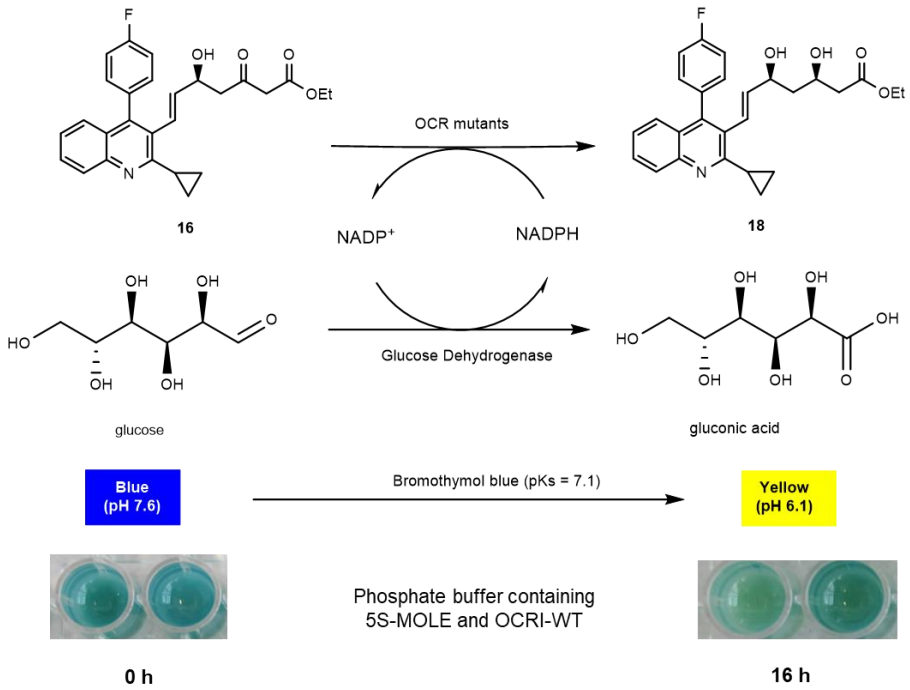

Scheme 13. A screening method using bromothymol blue for isolating clones, having enhanced activity for 5S-MOLE **16**.

further color change to green was not observed. The color change was monitored at 0, 4, and 16 h, and 6 clones (P2G6, P2F12, P2G11, P3F4, P4D2, P5B4) showing relatively greener or yellower color than OCRI-WT were isolated (**Figure 28**). Also, we collected 2 clones (P2F11 and P3A5) which showed a relatively blue color compared to OCR-WT. The overexpression was analyzed with SDS-PAGE to confirm that OCR-WT and mutant proteins in the autoinduction medium is well overexpressed (**Figure 29**). The result explained that OCR-WT was overexpressed well in the autoinduction medium as a soluble protein. The expression of selected mutants was analyzed, which showed a similar expression with OCR-WT (data not shown). Therefore, we can put aside the possibility of false-negative and positive because of the difference in overexpression.

The second screening was conducted using selected 6 clones apart from P4D2 and P5B2, which did not show the same color change through colorimetric assay, by measuring activity toward $1 g \cdot L^{-1}$ 5S-MOLE **16**. Before the biocatalytic reduction of 5S-MOLE **16**, the specific activity was measured using TFAP **20** following the addition of the same unit of OCR-WT and mutants for the reduction of MOLEs. Afterward, the reaction mixture was prepared in a 100 mM phosphate buffer (pH 6.0) containing GDH2, glucose, and OCR-WT and mutants. The reaction was started by adding $NADP^+$ cofactor and 5S-MOLE **16**. DOXE **15**, 5S-, 3R-MOLE **16** and **17**, and DOLE **18** are highly insoluble in an aqueous mixture; therefore, those compounds were prepared in DMSO stock solutions and resuspended in the aqueous mixture (20%, v/v). Surprisingly, mutant clones, including P2F12, P2G6, P2G11, and P3F4 showed above a 95% conversion. OCR-WT also showed about a 96% conversion and only 0.3% 5S-MOLE **16**

remained (**Table 13**). Both OCR-WT and mutants showed a good conversion toward 5S-MOLE **16** at the second screening, while mutant P2F11 and P3A5 showed no conversion to DOLE **18**.

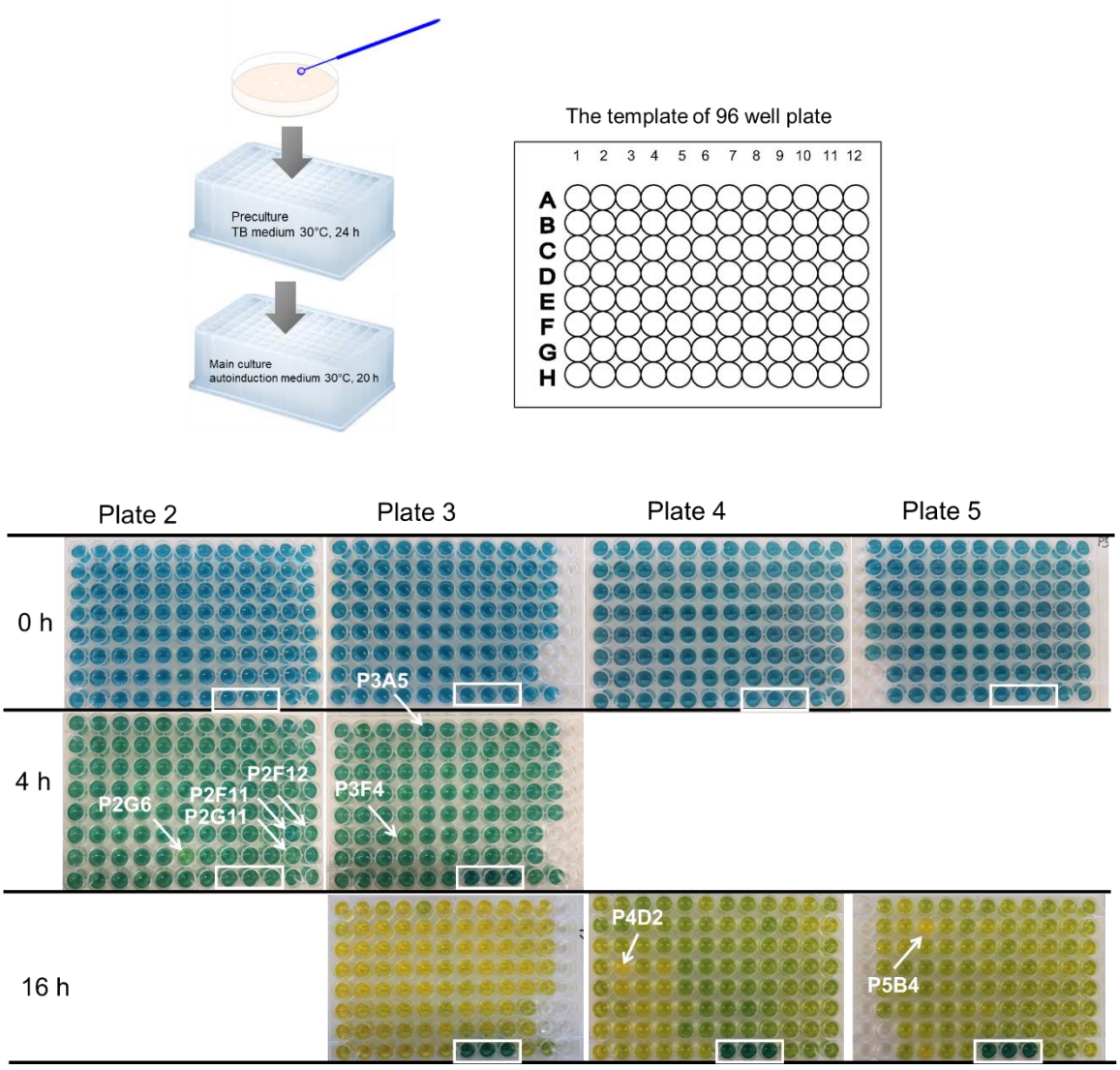

Figure 28. Observation of color change of OCR mutant screening plates by time course. Each mutant's clone was named based on vertical number and horizontal alphabet of the 96 well plate. The arrows indicate each mutant clone, and the white box showed background which does not contain the cell crude extract.

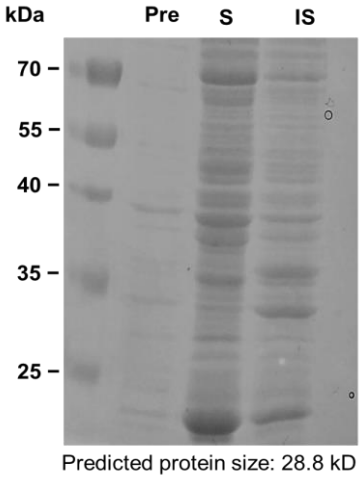

Figure 29. SDS-PAGE analysis of OCR-WT after induction with an autoinduction solution. Pre means total protein before induction, and S and IS mean that soluble and insoluble protein after induction following cell disruption with ultrasonication.

Table 13. HPLC analysis of biocatalytic reduction of 5S-MOLE **16** by OCR-WT and mutants[77].

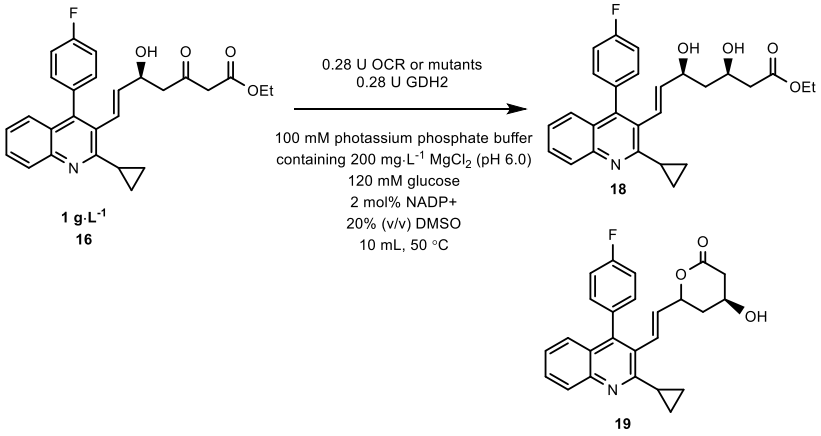

Conversion measured by HPLC (%)			
OCR	Lactone **19**	DOLE **18**	5S-MOLE **16**
WT	3.4	96.2	0.3
P2F11	0	1	99
P2F12	4.5	92.8	2.7
P2G6	4.2	95.8	0
P2G11	2.3	97.1	0
P3A5	0	0.7	99.3
P3F4	2.3	97.4	0.3
negative control (NC)	0	0.8	99.2

Deduced amino acid sequences of the above mutant clones were analyzed for the next screening procedure. The deduced peptide sequences of mutants were aligned with OCR-WT (**Figure 30**). The clones showing higher or similar conversion with OCR-WT exhibited single mutation at Asp54Val, Asp193Gly, and Glu43Lys in P2G6, P2F12, and P3F4, respectively (conversion: 96, 93, and 97%, respectively). P2G11 showed no mutation in amino acid sequences. Among the above mutants, P2G6 was chosen for further study. Additionally, mutants having no activity contained multiple mutated residues. P2F11 had four mutations at amino acid Tyr6, Ser62, Asn91, Lys124, and Ile144Thr, and P3A5 had mutations at amino acid Tyr6, Met93, Lys124, Thr138. and Lys161Stop codon (see the table in **Figure 30**). The length of polypeptides of P3A5 was shortened. The results implied that the changed four residues in P2F11 are essential for the catalytic reaction.

Mutants	Changed amino acid sequences
P2G6	Asp54Val
P2G11	Same as wild-type
P2F12	Asp193Gly
P3F4	Glu47Lys
P2F11	Tyr6Cys, Ser62Gly, Asn91Asp, Lys124Met, Ile144Thr
P3A5	Tyr6His, Met93Val, Lys124Arg, Thr138Arg

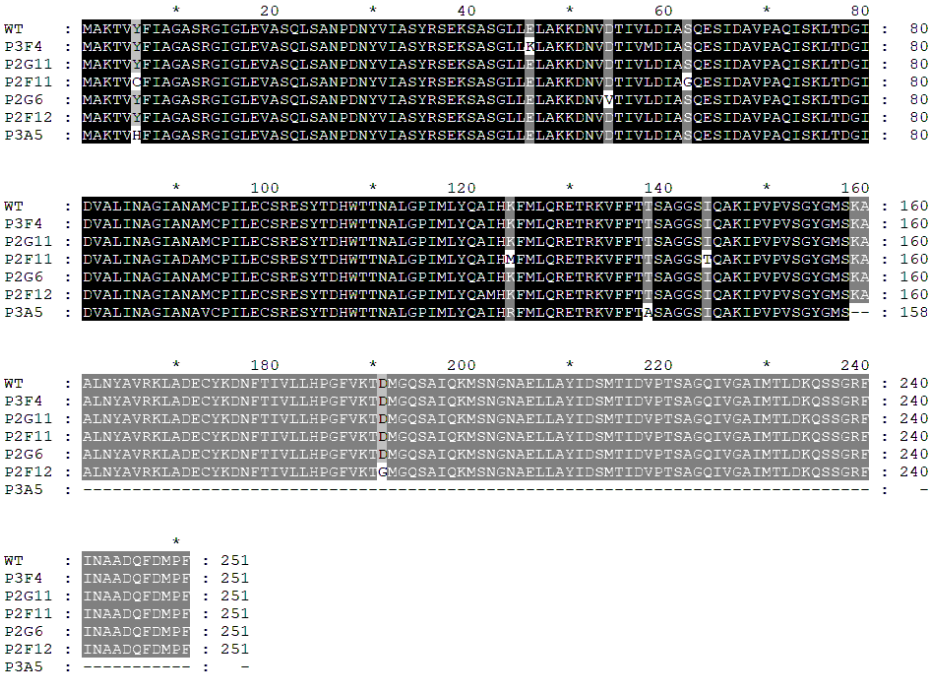

Figure 30. Alignment of deduced amino acid sequences of OCR-WT and mutants[77].

OCR is one of the NADPH-dependent carbonyl reductases, and it belongs to the carbonyl reductase sniffer-like (SDRs) family, which has structurally conserved active sites and NADPH-binding region (Rossmann fold) based on the conserved domain analysis[61]. Classical SDRs have TGxxx[AG]xG cofactor binding motif and a YxxxK active site motif (**Figure 31**: the blue background, the conservative region of cofactor binding sites; The yellow background and red characters, the conservative regions of active sites). However, the mutated residue in P2G6 is located at 54 residue which is far from the conserved active site and cofactor binding site (see the red dot on the sequences in **Figure 31**). In previous studies, eukaryotic ADH showed that amino acid substitution at the non-catalytic site caused enhanced cofactor binding due to structural rearrangements[106]. Also, a recent study using alcohol dehydrogenase from *Chryseobacterium* sp. CA49 showed that distant mutations enhanced activity toward (1*S*)-2-chloro-1-(3,4-difluorophenyl) ethanol due to its mode of reduced side-chain mutations, which reduces steric hindrance of bulk substrates[105]. It is presumed that the rearrangement of related residues could affect the activity.

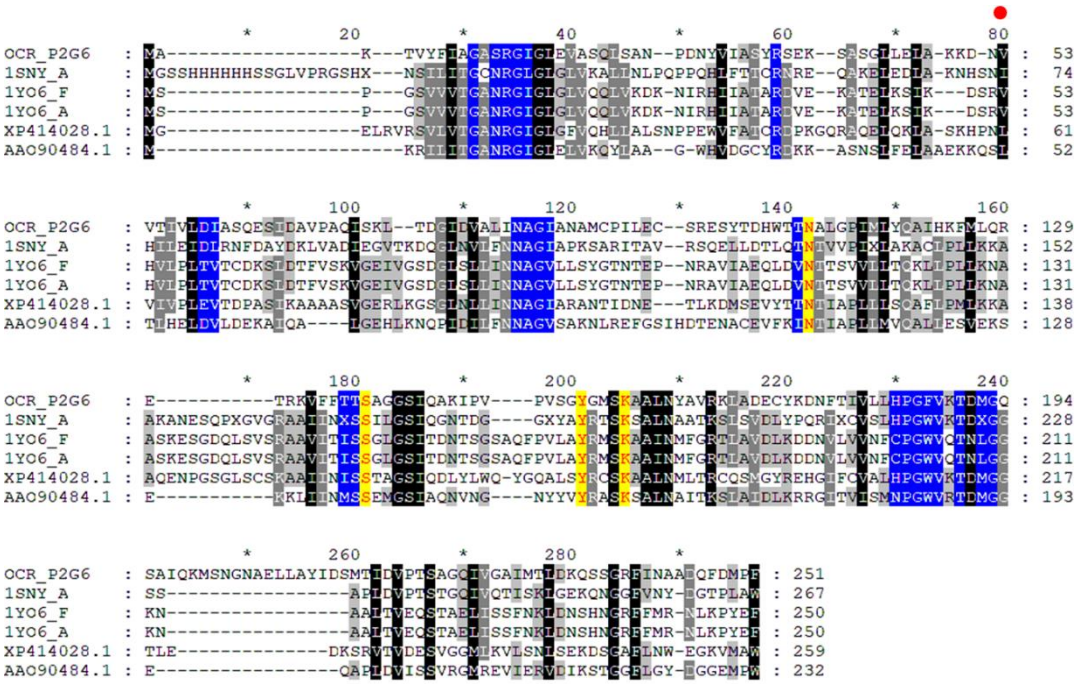

Figure 31. Alignment of OCR-P2G6 with representative SDRs proteins[61]. The residues with the blue background are the conservative region of cofactor binding sites. The residues with a yellow background and red characters are the conservative regions of active sites. The red dot on the sequences showed a mutated residue on OCR-P2G6.

3.3.3.2. Improved activity of OCR-D54V toward DOXE and MOLEs

Due to the difficulty of chemical synthesis and purification of MOLE isomers, MOLE was prepared by biocatalysts performing the reaction under unfavorable condition (a high loading of a substrate and high concentration of an organic solvent) for the biocatalyst to slow down the reaction and produce intermediate MOLEs. The bioconversion was done with 40 $g \cdot L^{-1}$ DOXE **15** to synthesize 3R-, 5S-MOLE **16**, **17** using a biocatalyst. The reaction solution contained 100 mM potassium buffer (pH 6.0), glucose, 2 mol% $NADP^+$, 40% DMSO, and 10 U of OCR-WT. The reaction was stopped after 24 h by extracting with the same volume of ethyl acetate twice, followed by evaporating the solvent with a rotary evaporator. The reaction mixture containing pitavastatin intermediates (67.3% DOLE **18**, 21.5% MOLEs, and 10.1% DOXE **15**) was purified by flash chromatography to prepare a 3R-, 5S-MOLE mixture **16**, **17** (**Figure 32**).

The selected mutant OCR-P2G6 was renamed as OCR-D54V according to its mutated residue. The reaction was performed with 2.6 $g \cdot L^{-1}$ MOLEs, 0.6 U OCR-WT, and D54V (**Figure 34**). OCR-WT and D54V showed the specific activity of 2.33 $U \cdot mL^{-1}$ and 0.55 $U \cdot mL^{-1}$, respectively. Therefore, we added a four times higher amount of OCR D54V-cell crude extract to the reaction mixture. The reaction with a low volume of less than 10 mL was done using a magnetic stirrer equipped with a metal glass-vial holder, which can hold 10 mL vials safely and transfer heat efficiently (**Figure 33**). The reaction was started by adding MOLEs to the 50 °C pre-heated solution containing phosphate buffer, GDH2, glucose, and a cofactor following the condition in **Figure 34**. The cofactor was added stepwise at 0, 2, 3, and 4 h to prevent the cofactor degradation by heat. MOLEs contained approximately 90% of 3S-MOLE **17** and less than 10% 5S-MOLE **16**. The initial conversion rate of OCR-D54V from MOLEs to DOLE **18** was incredibly fast compared to OCR-WT, showing an approximately 90% decrease in MOLEs in 30 min while OCR-WT only showed a 30% decrease in MOLE at the same time. OCR-D54V exhibited a 5% increase in conversion from 0.5 to 20 h, in contrast, OCR-WT slowly converted MOLEs up to 3 h to show an increase in yield from 30 to 60%. (**Figure 34**). However, the significant reduction of MOLEs was not observed after 3 h in both OCR-WT and D54V, which indicates that OCR was deactivated or the access of the biocatalyst to the substrate was physically restricted due to a formation of MOLEs aggregates. After the reaction, the aggregates consisting of MOLEs and degraded proteins were observed on the wall of the reactor and magnetic bar (**Figure 33**). At 20 h of reaction, the difference in residual MOLEs between OCR-WT and D54V was approximately 40%. OCR-D54V showed dramatically fast initial activity compared to WT, suggesting that OCR mutant D54V could have better specificity toward MOLEs. Spontaneous conversion from DOXE **15** to lactone **19** in the presence of OCR-D54V was observed since DOLE **18** was only 95% even though MOLEs was almost completely consumed. The yield of lactone **19** was presumed to be 5-10% after 20 h (data not shown).

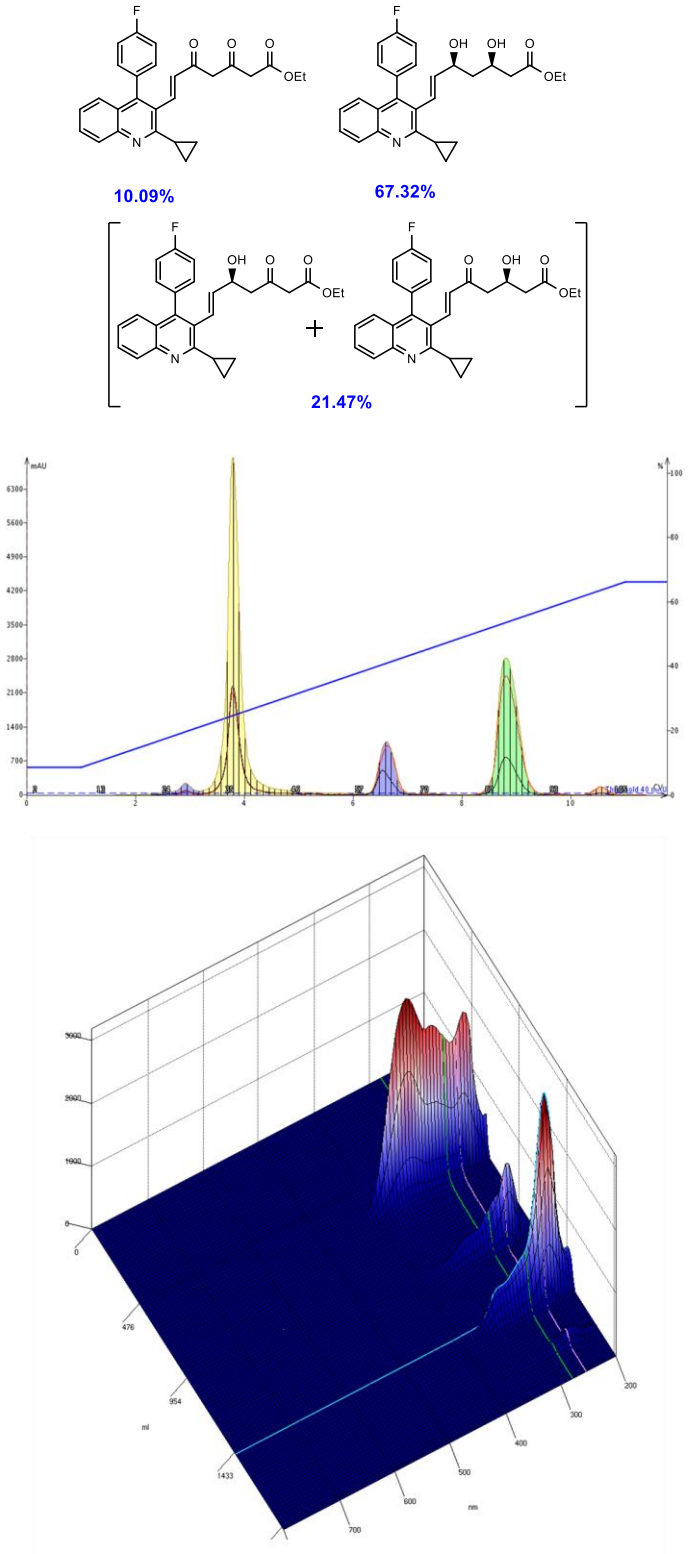

Figure 32. Separation of DOXE **15**, MOLEs, and DOLE **18** from the reaction mixture by automated flash chromatography (top). 2D (middle) and 3D (bottom) chromatogram, recoreded by Biotage Isolera One equipped with an UV detector.

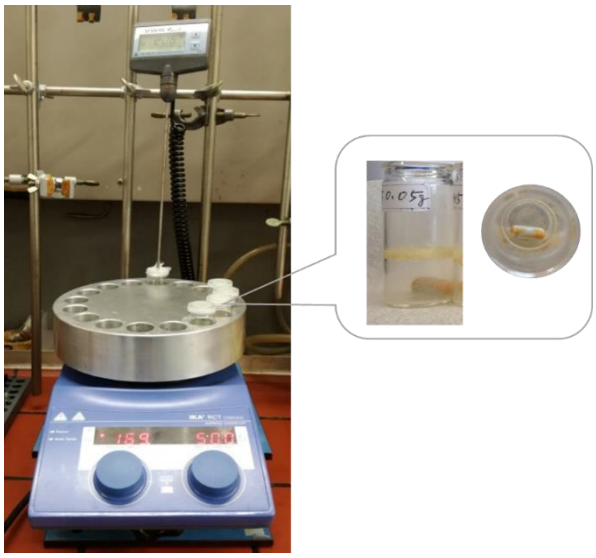

Figure 33. The small-scale reactor consisting of a magnetic stirrer, a glass vial holder, and a thermometer (left). The empty vial after reaction contained aggregated DOXE **15** and MOLE mixtures **16** and **17** on the wall and a magnetic bar (right).

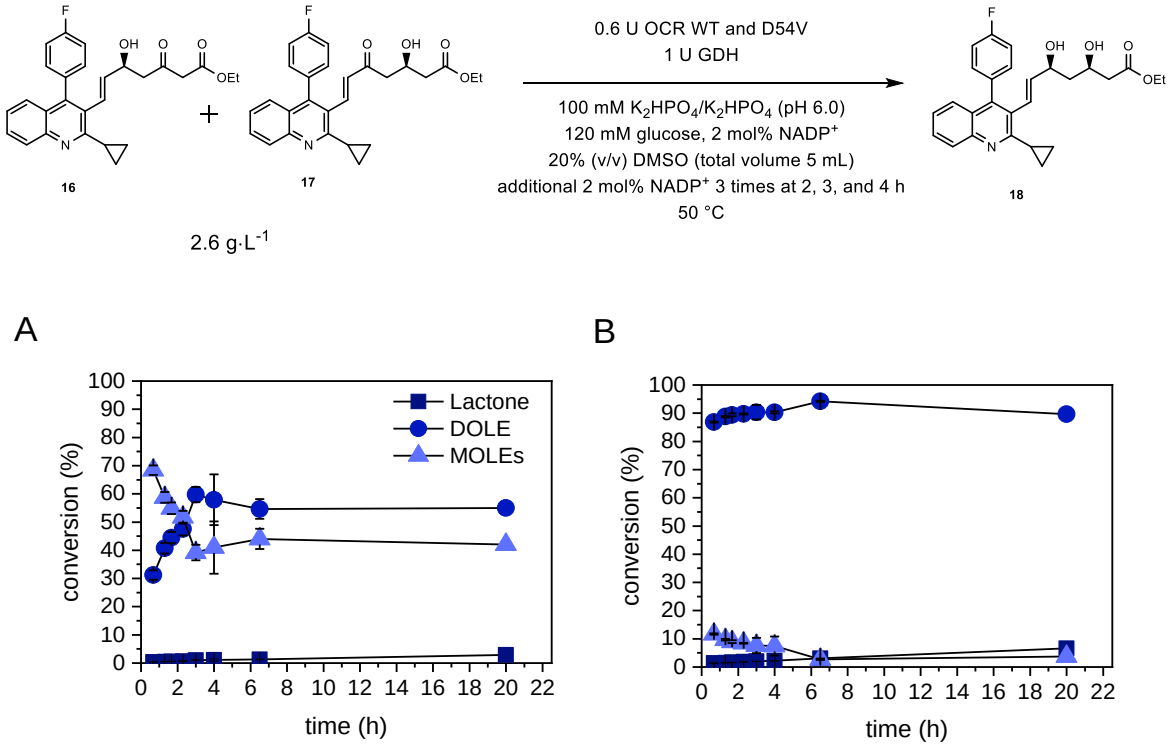

Figure 34. Reduction of MOLEs to synthesize DOLE **18** by OCR-WT (A) and D54V (B)[77].

Table 14. The conversion of 10g·L^{-1} DOXE **15** to DOLE **18** using OCR-WT and D54V[77]

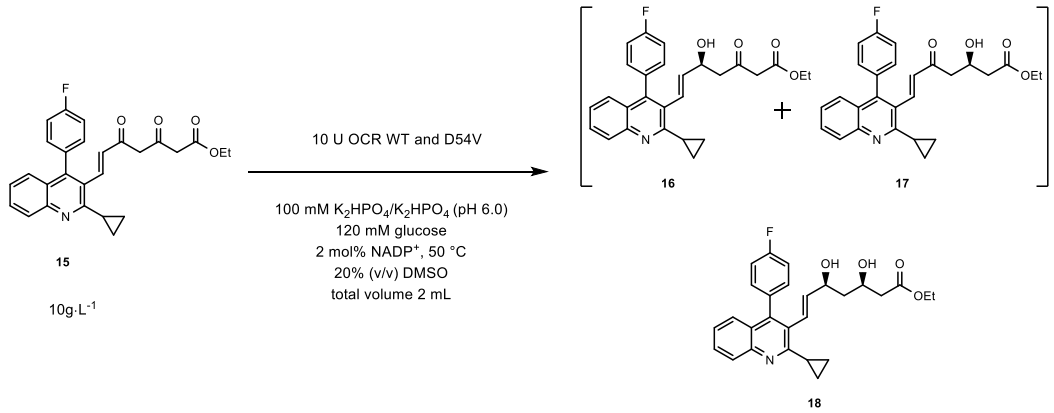

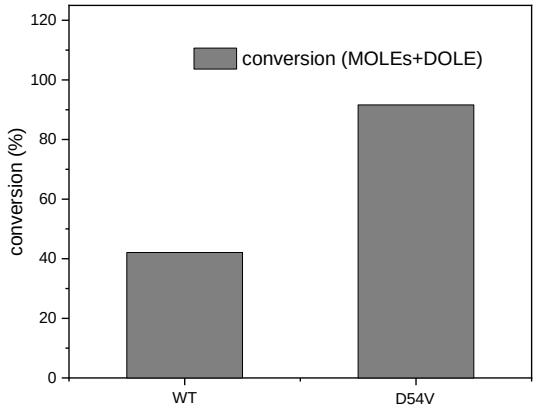

Conversion measured by HPLC (%)								
	1 h		2 h		3 h		4 h	
	MOLEs (**16+17**)	DOLE **18**	MOLEs (**16+17**)	DOLE **18**	MOLEs (**16+17**)	DOLE **18**	MOLEs (**16+17**)	DOLE **18**
WT	-	-	27.6	**14.5**	27.4	14.8	26.8	14.6
D54V	23.7	67.2	23.3	**68.3**	23	68.3	22.8	70.1

The preference of OCR for 5S-MOLE **16** was proved previously (**Table 13** and **Figure 34**); therefore, The activity of OCR-WT and D54V toward DOXE **15** was determined. Ten times higher concentration (10 g·L^{-1}) of DOXE **15** was used in this experiment to discern the increased activity of the OCR mutant. The reaction was started by adding DOXE **15** to an aqueous reaction solution containing GDH2, glucose, cofactor, and 10 U OCR-WT or D54V at 50 °C. OCR-WT showed 14.5% of conversion to DOLE **18** up to 2 h, and 27% of residual MOLEs was observed (**Table 14**). On the other hand, OCR-D54V showed approximately 4.5 times higher conversion (68.3%) to DOLE **18** compared to OCR-WT, which

suggested that D54V has a greater specificity toward DOXE **15.** However, the yields were not significantly improved after 2 h (**Table 14**).

We observed the conversion of DOXE **15** and MOLEs to DOLE **18**, and OCR-D54V showed a significantly fast initial conversion rate; however, the remaining 1-5% of MOLEs were not fully converted to DOLE **18**. Therefore, the conversion under the experimental condition in the presence of a high concentration of DOLE **18** and low concentration of DOXE **15** and MOLEs was studied. The reaction mixture of DOXE **15**, MOLEs and DOLE **18** (67% DOLE **18**, 22% MOLEs, and 10% DOXE **15**) was obtained by biocatalytic reduction with 40 $g \cdot L^{-1}$ DOXE **15** in the above study (**Figure 32**). Two grams of the reaction mixture were used for the reaction with OCR-WT and D54V following the condition in **Table 15** and analyzed by HPLC. Conversions to DOLE **18** were 92% and 94% using OCR-WT and D54V, respectively, wherein OCR WT showed high conversion as well as D54V, and DOXE **15** was completely consumed in one hour (**Table 15**).

Table 15. Biotransformation of 2 gL^{-1} reaction mixture containing DOLE **18**, MOLEs, and DOXE **15**[77].

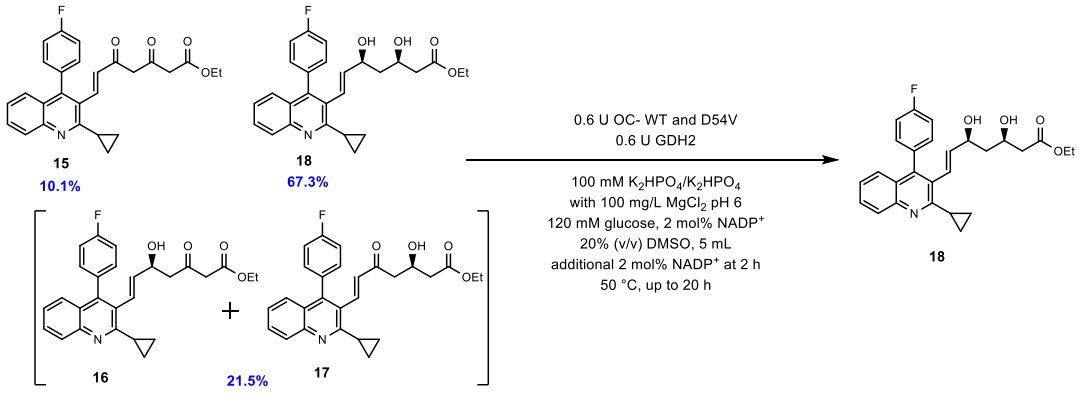

Conversion measured by HPLC (%)			
	The contents of reaction mixture	OCR-WT	OCR-D54V
lactone **19**	1.1	5.1	5.1
DOLE **18**	67.3	**92.3**	**93.9**
MOLEs	21.5	2.7	1.0
DOXE **15**	10.1	0	0

The result suggested that rapid biocatalytic reduction of DOXE **15** occurred first; consequently, bioconversion of MOLEs slowly occurred. Furthermore, it indicated that DOXE **15** and MOLEs could easily be converted by OCR-WT and D54V when its concentration is low (0.2 g·L^{-1} DOXE **15** and 0.4 g·L^{-1} MOLEs). However, as the concentrations of the substrate were increased, the slow conversion rate was observed in the experiments using 2.6 g·L^{-1} of MOLE mixture **16** and **17** (**Figure 34**) and 10 g·L^{-1} of DOXE **16** (**Table 14**), which suggests that substrate inhibition by DOXE **16** and MOLEs has happened. Moreover, bioconversion with D54V could reduce the residual MOLEs amount to 1%, which is approximately 2% lower compared to residual MOLEs using OCR-WT. It is presumed that DOXE **15** having two ketone groups has a higher specificity for OCR than MOLEs, which have one ketone and one alcohol moiety. Therefore, lowering the MOLEs less than 1% in conversion is meaningful in this experiment.

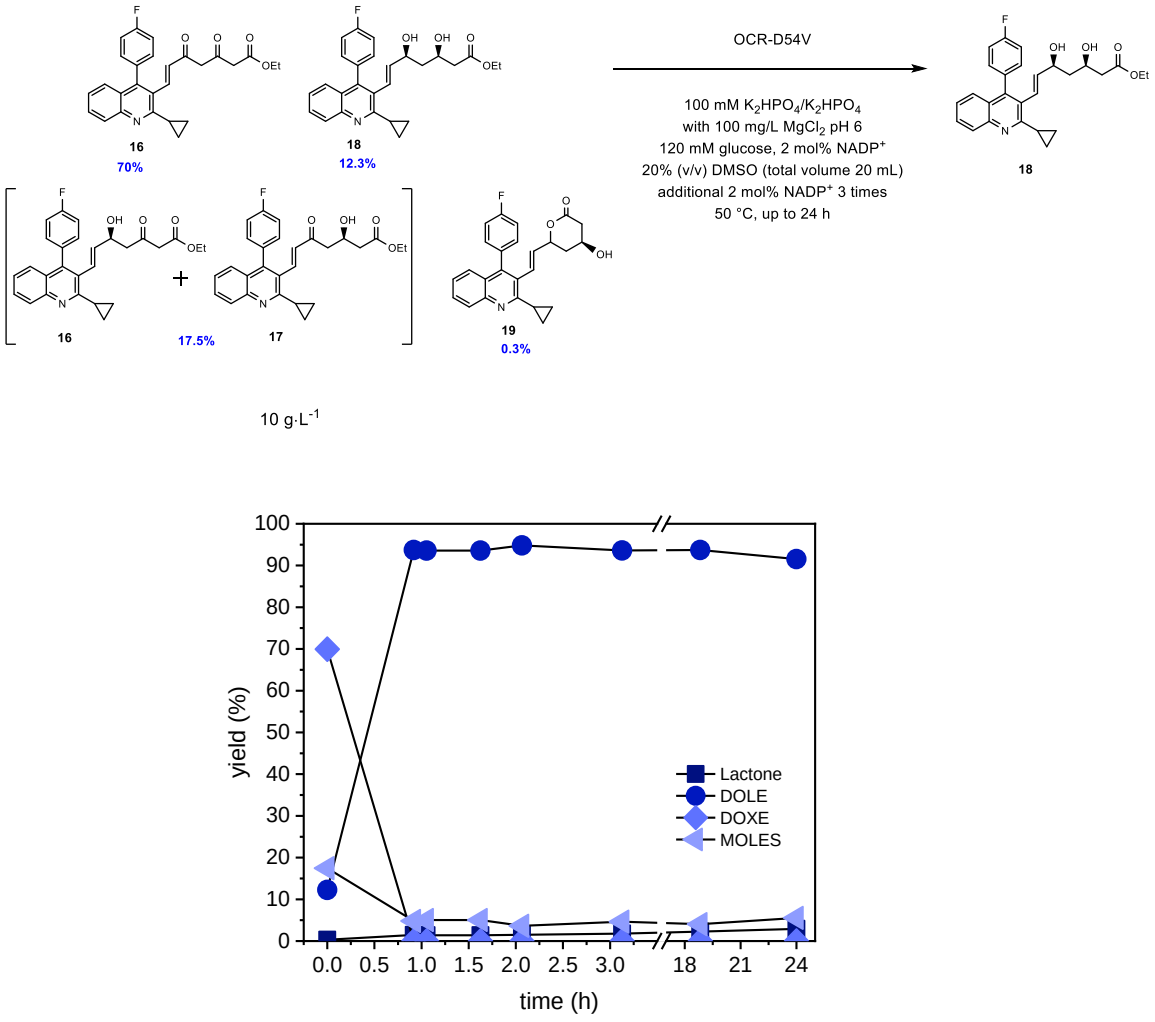

Figure 35. Scaling up of biotransformation using D54V cell crude extract containing 10 g·L^{-1} reaction mixture[77].

The biocatalytic reduction with OCR D54V in ten times increased volume up to 20 mL was observed using an automatic pH titrator (**Figure 35**). pH value was adjusted to pH 6 by the addition of a 0.5 M NaOH solution. The reaction mixture was prepared by the biocatalytic reduction using 40 $g \cdot L^{-1}$ DOXE **15** previously described, but the reaction was stopped in 2 h to obtain higher DOXE **15** ratio versus MOLEs and DOLE **18** in the mixture. The obtained crude reaction mixture contained 70% DOXE **16**, 18% MOLEs, and 12% DOLE **18** (**Figure 35**). Afterward, the biocatalytic reduction was prepared in a solution containing cofactor, glucose, GDH2, and OCR-D54V without the reaction mixture, and titration started simultaneously by adding the reaction mixture. DOXE **15** was completely consumed in one hour, showing a 81% increment of DOLE **18** and decrease in 13% of MOLEs. Approximately 5% of residual MOLEs remained for 20 h after the considerable reduction of DOXE **15** and MOLEs in 1 h. Also, Lactone **19** concentrations were gradually increased up to 3%. Even though D54V showed a good conversion toward DOXE **15** and MOLEs in a large-scale reaction, full conversion to DOLE **18** was hard to achieve. The aggregation of compounds including MOLEs and DOLE **18** was observed in this experiment using a 40 mL glass vessel,which was the same as the small scale experiment with 10 mL glass vial (**Figure 33**). It was assumed that DOXE **15** was consumed quickly, therefore DOXE **15** would not be found in aggregate. Once the aggregates formed, the biocatalyst could not access MOLEs. A better mixing system or cosolvent is necessary to achieve full conversion.

3.3.4. The comparison of thermostability of OCR-WT and D54V

The relative activity of OCR-WT and D54V was studied to compare thermostability in the organic solvent (**Figure 36**). The activities using OCR-WT and D54V at 4 °C were measured and set up as a control for comparing the relative activities at different temperatures. The cell crude extracts containing OCR-WT and D54V were incubated for 4 h at 4-60 °C and 10 µL of supernatants were taken for measurements of residual activities using TFAP **20**. In addition, OCR was incubated in 20% DMSO-phosphate buffer solution at 4-60 °C to evaluate the effect of 20% DMSO on catalytic stability depending on temperatures. OCR-WT and D54V showed relatively good activity in a range of 70-120% up to 40 ºC without severe decrement in phosphate buffer at pH 6 (**Figure 36**A). OCR-WT and D54V exhibited a substantial decrease in activities at 50 ºC in a phosphate buffer; nevertheless, D54V showed 20% higher activity (30%) compared to WT (10%) (**Figure 36**A). OCR-WT and D54V completely lost its activity at 60 °C. In a 20% DMSO-phosphate buffer solution, OCR-D54V showed 20% higher activities at 30 and 40 ºC compared to OCR-WT having 70-80% at the same temperature (**Figure 36**B). At higher temperatures above 50 ºC, OCR-WT and D54V started losing their activities severely (35-40%), and at 60 °C, no residual activity was observed. This result could explain the observation of the total loss of its activity at 6 h in the benchmark reaction using OCR-WT and D54V. Furthermore, it was expected that the mutation at aspartic acid 54 in OCR-D54V does not contribute to improving

thermostability because OCR-WT and D54V appeared having similar residual activities at 50 °C in 20% DMSO solution. OCR-D54V is suggested to have enhanced specificity rather than thermostability.

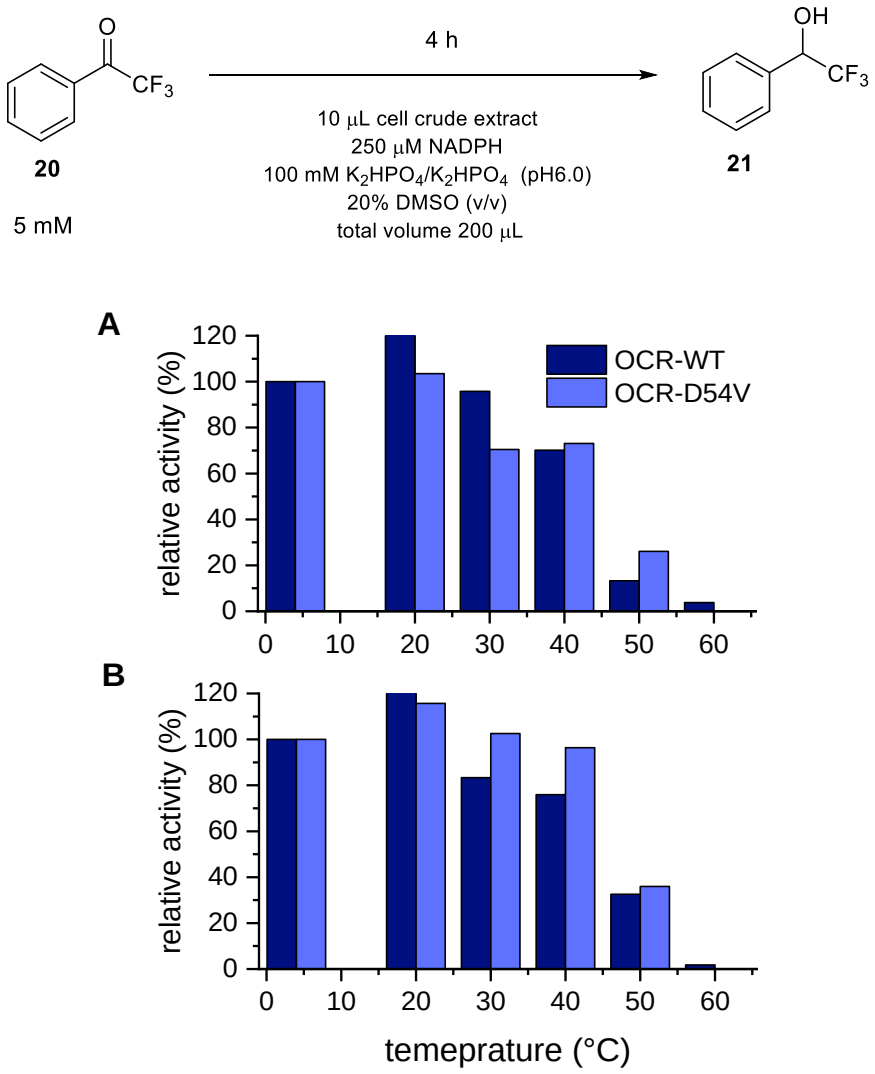

Figure 36. Relative activity of OCR-WT and D54V at various temperatures for 4 h without (A) and with 20% DMSO (B) in potassium phosphate buffer.

3.4. Introduction of flow chemistry to biocatalytic reduction using OCR-WT

The solubility of DOXE **15** in DMSO was 54.05 $g \cdot L^{-1}$ DOXE **15** in this study, which implies high potential increments of substrate loading. However, a biocatalyst's activities, apart from some exceptions such as lipase CalB, is dramatically diminished in a biphasic system containing aqueous and organic phases due to its diffusional limitations, structural changes of biocatalysts, active center

blockage, transition state destabilization, and suboptimal pH situation[107]. Therefore, the increment of substrate loading in a batch reactor is not ideal because the yield will not be proportionally increased along with the increase of the substrate concentration. Some strategies include demonstrating that immobilization, propanol-rinsed enzyme preparation, ionic liquid coating, and protein evolution could enhance enzymatic stability in the presence of organic solvents[108]. However, those strategies have been applied for different biocatalysts which cannot guarantee they will work for the specific type of ADH such as OCR.

The flow reactor equipped with immobilized urease was first introduced in 1964 to remove urea from an aqueous solution[109]. Subsequently, the application of the immobilized flow reactor has been widely used[110]. Research on microreactors with biocatalysts has shown that they can be used to obtain detailed information regarding reaction kinetics, substrate specificity, and operational stability. This facilitates a facile translation of synthetic methodology from bench-scale to production-scale[111–114]. A good example of the synthesis of enantiomerically pure compounds using a flow reactor was presented by Rutjes, who synthesized a series of (*S*)-cyanohydrins in a glass microstructured reactor under a biphasic laminar flow with an aldehyde in the organic phase and potassium cyanide and enzyme lysate in the aqueous phase[115]. Therefore, we suggested that a flow reaction with a continuous flow could be an alternative way to synthesize the enantiomerically pure compound without the severe loss of enzymatic activity and solubility of substrates by applying a two-phase segment-flow reactor[76]. In this study, OCR-WT was introduced to flow chemistry, and furthermore, TFAP **20** was used as the model substrate. The results in this section were published in ChemCatChem[76].

3.4.1. Utilization of segmented flow reaction in the synthesis of a chiral alcohol using OCR-WT

The illustration in **Figure 37** demonstrates how the segmented flow reactor was configured. The flow reactor was equipped with an automatic syringe pump that can pump aqueous and organic phases at the same speed to a tube reactor. The mixer in the middle of the syringe pump and tube reactor forms segments of organic and aqueous phases by turns; consequently, the tube reactor contains the same volume of an organic and aqueous solution. Reduction of TFAP **20** to α-(trifluoromethyl)benzyl alcohol **21** occured in the tube reactor at 30 °C. The reaction solution was collected at the end of the reactor, which is connected to glass vial harboring HCl to quench the reaction after a specific reaction time. In this study, methyl-tert-butylether (MTBE) was used as an organic solvent because MTBE has lower logP value (0.94-1.06), which is slightly mixable with water so that TFAP **20** could be transferred from the organic to the aqueous phase. Furthermore, DMSO is highly mixable in water; therefore, DMSO did not form an organic segment in the tube reactor. To increase the enzyme loading in the segmented flow reaction, OCR-WT was prepared as a lyophilized powder.

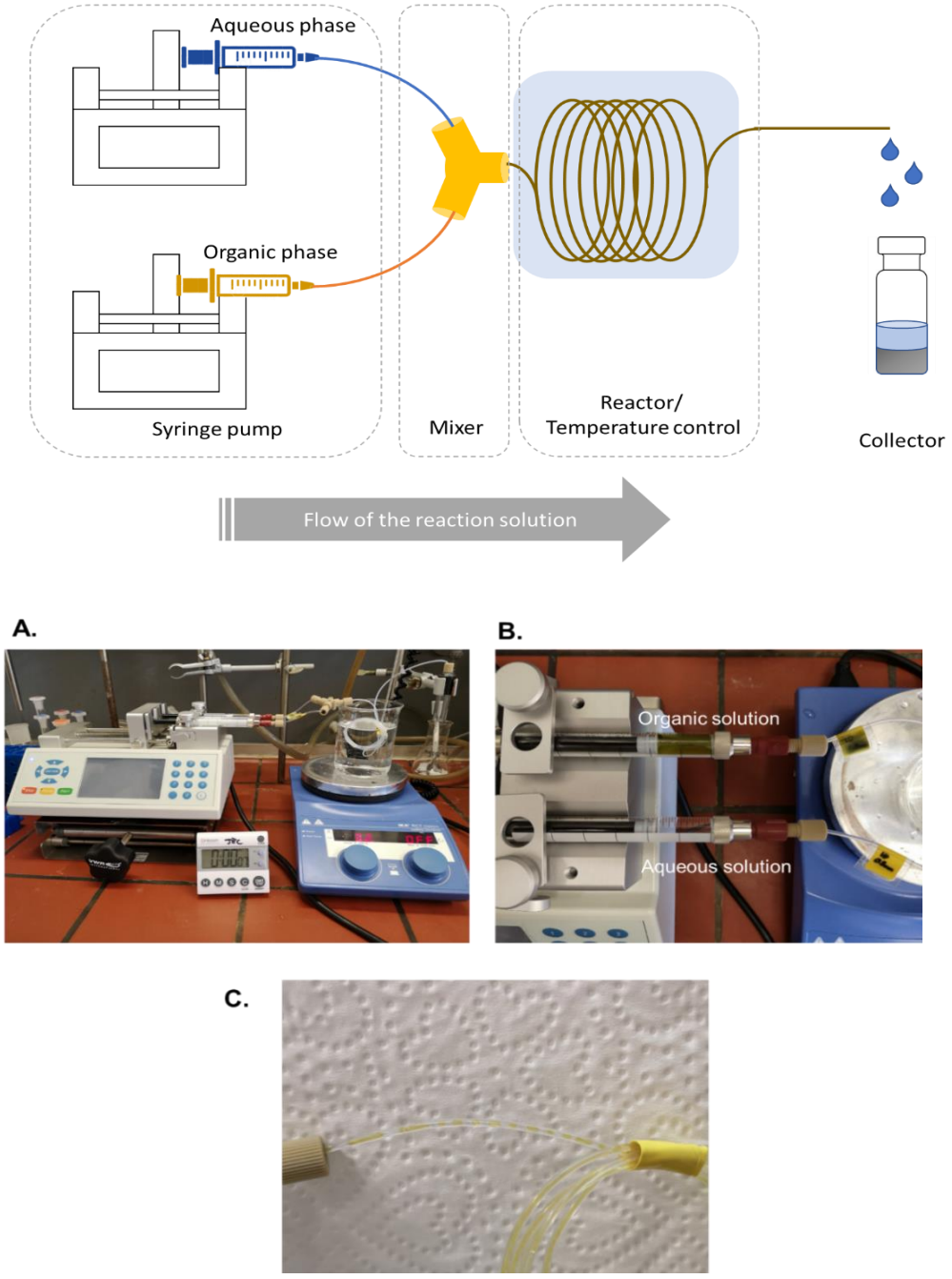

Figure 37. The overview of the segment flow reactor (above). Segmented flow reactor equipped with a syringe pump, a stirrer, and a tube reactor connected to the collector (A). The syringe pump containing organic and aqueous solution were connected to separated tube reactor (B). The segmented flow in the reaction tube was observed in the tube reactor (C).

To begin, the syringe pump was equipped with glass syringes containing biocatalysts and cofactors in an aqueous solution and 200 mM TFAP in the organic solvent (overall concentration of TFAP: 100 mM). The reaction was started by injecting an aqueous and organic solution at 0.5 mL·h^{-1} to the tube reactor having 0.8 mm ID (inner diameter) and 0.5 mL volume[76]. The two-phase solution was collected

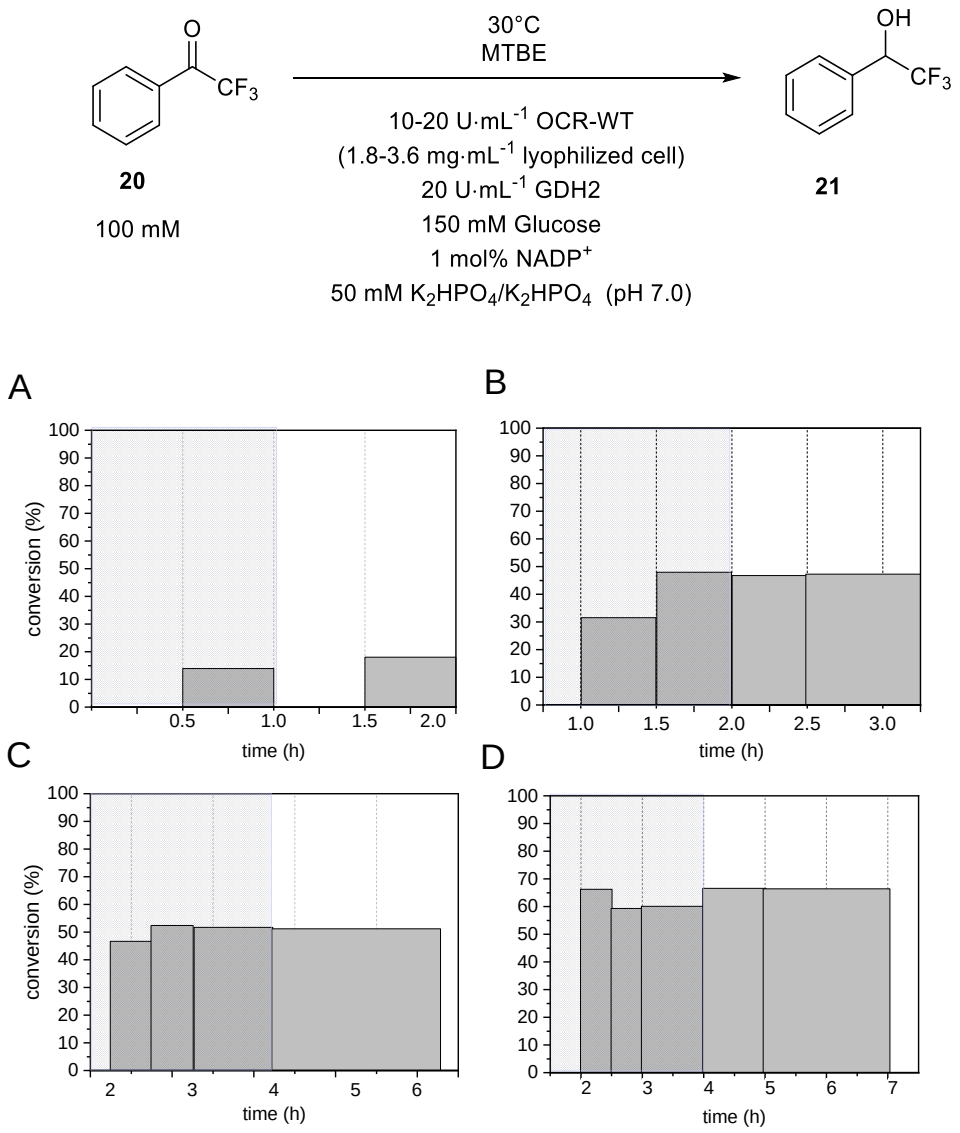

Figure 38. Conversion (%) from TFAP **20** to α-(trifluoromethyl)benzyl alcohol **21** by flow reaction using OCR-WT. The flow reactor consisted of a Y-shape mixer and a tube reactor (0.8 mm ID) having 0.5 (A) and 1 mL (B, C and D) of reaction volume. The residence time was gradually increased to 0.5 (A), 1 (B), and 2 (C and D) h, respectively. Ten units of biocatalyst were prepared in aqueous solution at 30 ºC, and organic solvent was prepared by adding 200 mM TFAP to MTBE. The conversion was determined by collecting reaction mixture at a specific time. Increased amount of OCR-WT up to 20 U·mL^{-1} was used (D). The blue box refers to equilibrium[76].

in a glass vial for a residence time (0.5 h) after the first drop was observed. The residence time means the reaction time in, which the two-phase solutions stay in the tube reactor. The maximum conversion was 15% after four residence times (2 h; **Figure 38**A)[76]. Also , time in a horizontal axis of **Figure 38** means the time at the reaction was started. The increment of residence time from 0.5 h to 1h increased the conversion to 51% in three residence times (3 h; **Figure 38**B)[76]. Extension of residence time from 1 to 2 h without a proportional increase in biocatalysts loading showed no increment of conversion (**Figure 38**C). When the biocatalyst loading was increased from 10 $U \cdot mL^{-1}$ to 20 $U \cdot mL^{-1}$ along with the extension of residence time, the conversion was also enhanced to 67% (**Figure 38**D)[76]. This result shows that the biocatalyst amount needs to be raised corresponding with an increment of retention time. In addition, the difference in the conversions was observed up to two residence times, which refers stagnation time until the flow reactor is stabilized; consequently, conversions were the same at any time

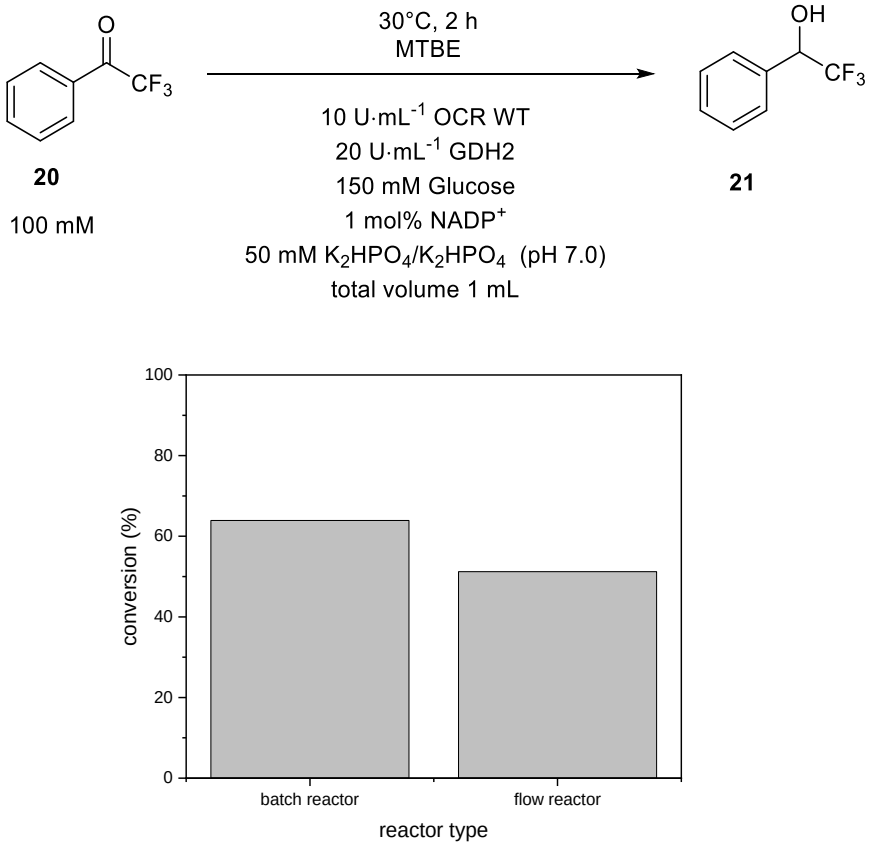

Figure 39. Comparison of a conversion using a conventional batch reactor equipped with a magnetic stirrer with a flow reactor. The flow reactor consisted of a Y-shape mixer, 0.8 mm ID reaction tube with 1 mL volume. The residence time was 2 h. Ten units of biocatalyst was prepared in aqueous solution at 30 ºC, and organic solvent was prepared by adding 200 mM TFAP to MTBE. The conversion was determined by collecting reaction mixture at a specific time. The reaction was done at 30 ºC for 2 h following quenching and extraction with ethyl acetate.

after equilibration (blue box in **Figure 38**). A study by Adebar showed that the equilibration time takes twice of residence time[76]. The great advantage of a segmented flow reactor is constant yield over the time after equilibration, giving the reliability of quality control in drug intermediate production.

In terms of improved yield using the segmented flow reactor, the conversion in 1 h with 10 $U \cdot mL^{-1}$ OCR WT in a batch reactor equipped with a stirrer and magnetic bar showed a 12% higher conversion (63%) compared to the segmented flow reactor (**Figure 39**). Even though the conversion from the batch reactor was higher than that of the flow reactor, the phase separation between the aqueous and organic phase was much clear in the segmented flow reaction. The collected reaction mixture in the segmented flow reaction was readily separated to the aqueous and organic phases without further purification steps (**Figure 40**A), which is beneficial for isolation of the final product from the two-phase solution. In the case of a batch reactor, the reaction mixture became cloudy as the reaction was started and was mixed

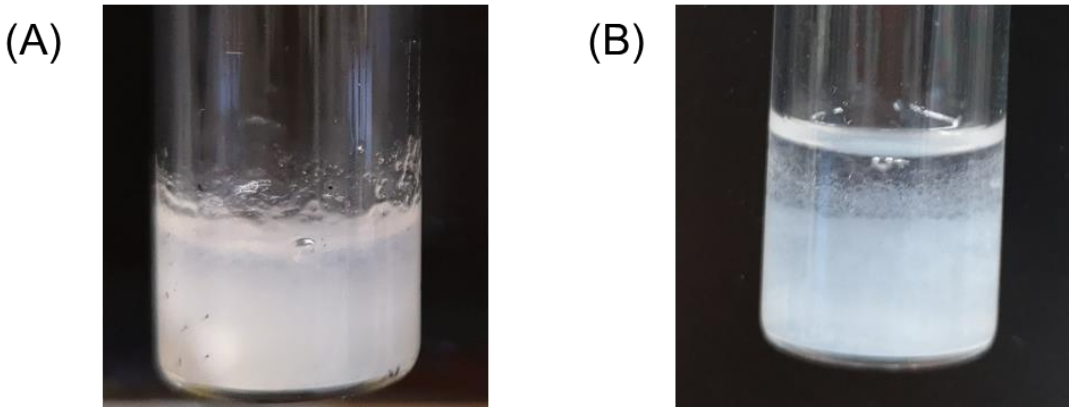

Figure 40. Reaction mixtures after reaction using a conventional magnetic bar with a stirrer (A) and the segmented flow reactor (B).

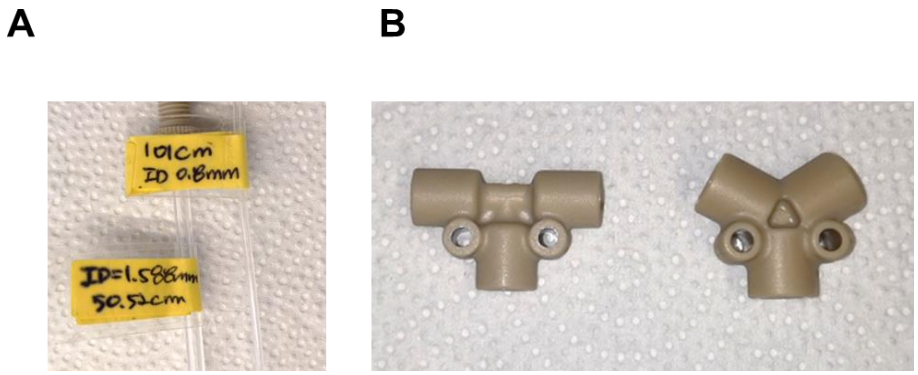

Figure 41. The tube reactors containing ID 0.8 mm and 1.588 mm (A). The T-shape mixer (left) and Y-shape mixer (B)

by a magnetic bar and stirrer (**Figure 40**B). The two phases were not clearly divided after reaction even if the reaction mixture was left without stirring for a while.

The influence of the size of the tube reactor and type of mixer on conversion was examined. The reaction condition was the same as in the above experiment. The reaction time was fixed at 1 h, the concentration

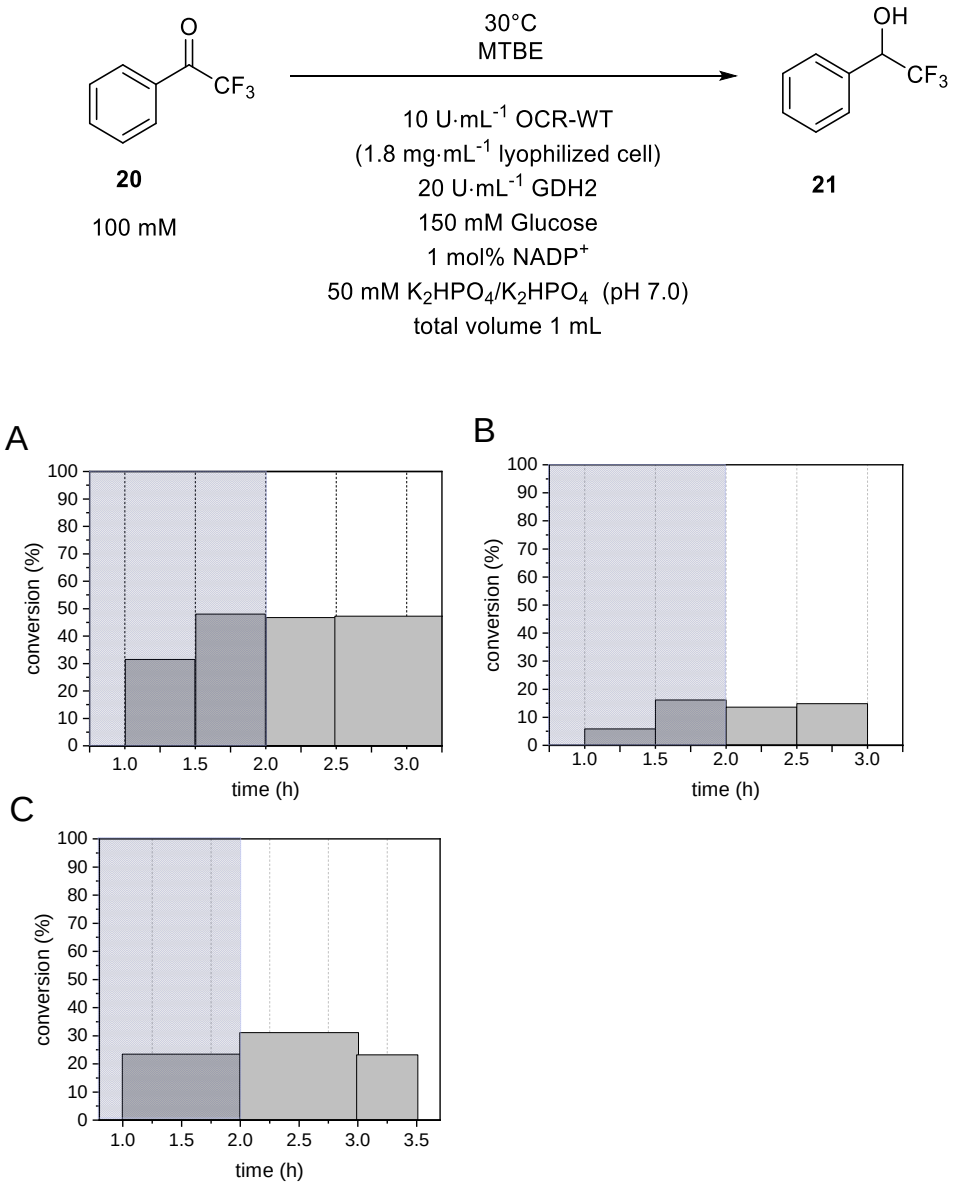

Figure 42. Conversion (%) from TFAP to α-(trifluoromethyl)benzyl alcohol by flow reaction using OCR-WT. The flow reactor consisted of a Y-shape mixer, 0.8 mm ID reaction tube with 1 mL volume (A). The residence time was 1 h. Ten units of biocatalyst was used at 30 °C, and 200 mM TFAP was dissolved in MTBE. The conversion was determined by collecting reaction mixture at a specific time. The same experiment was performed but the ID of tube reactor was changed to 1.588 mm (B). Finally, the same reaction condition as (A) but T-shape mixer was used for mixing (C).

of biocatalyst was set at 10 U·mL^{-1} OCR-WT (20 U·mL^{-1} GDH2, 150 mM glucose, 1 mol% NADP^{+}, and 50 mM phosphate buffer (pH 7.0)). When the inner diameter of the reaction tube was increased from 0.88 to 1.588 mm (**Figure 41**), the conversion was decreased approximately three times compared to the conversion with the same condition but a smaller diameter (**Figure 42**A and B). The previous study using a segmented flow capillary microreactor also showed that increment in diameter of the capillary lower conversion of 100 mM 1-heptaldehyde by ADH[116]. The result suggests that a smaller diameter of the reactor is beneficial for the mass transfer rate. In addition, a different mixer having a T-shape was used in the reaction (ID 0.88 mm, 10 U·mL^{-1} OCR-WT, 20 U·mL^{-1} GDH2, 150 mM glucose, 1mol% NADP^{+}, and 50 mM phosphate buffer (pH 7.0); **Figure 41**B). Interestingly, the conversion showed 1.5 times lower than the result with the same condition with Y-shape mixer, which suggests that T shape mixer provides less efficient mixing (**Figure 42**C). The experiment using water stained with bromothymol blue and *n*-butyl acetate, which has much lower solubility in water (6.8 g·L^{-1} for *n*-butyl acetate and 42 g·L^{-1} for MTBE), showed that the segments sized with the T- and Y-shape mixers had a difference in segment size of the organic and aqueous phase at the same flow rate and volume (**Figure 43**). The T-shape mixer showed irregular segment size, indicating bad mass transfer through the phases.

We searched for the possibility of an application for a segmented flow reactor in alcohol reduction. For pharmaceutical compounds synthesis, a segmented flow reactor has significant advantages since the yield is constant per residence time, guaranteeing a good quality control in production. Particularly, pitavastatin synthesis using a segmented flow reactor could give a hint on how to avoid the aggregation on the surface of the surface.

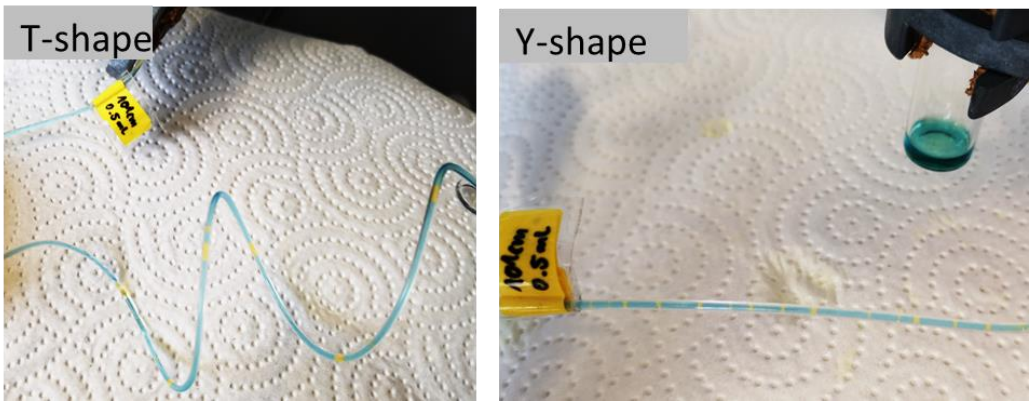

Figure 43. The segments differentiation depending on type of mixer. The blue solution was water contained bromothymol blue, and the yellow solution was *n*-butyl acetate containing TFAP **2**0. The left picture showed the two-phase segmented by T-shape mixer (left) and Y-shape mixer (right).

3.5. Summary and outlook

Pitavastatin was developed to decrease the risk of heart disease and help prevent strokes and heart attacks by controlling the cholesterol level in the blood. A method for synthesis using a biocatalyst was proposed by API Corporation[24,90] using a newly isolated carbonyl reductase from *Ogataea minuta*. We focused on the enhancement of conventional OCR biocatalysts to increase pitavastatin production and lower byproducts.

Cofactor stability was first examined to understand the behavior of cofactors in the reaction solution. In this study, we demonstrated that the cofactor, especially NADPH, was very unstable in a phosphate buffer condition even at pH 7. The cofactor was stable at room temperature up to 6 h; however, it showed severe degradation in distilled water and phosphate buffer at room temperature after 21 h. The degradation was accelerated by an increment of temperature following a first-order elimination rate, even though the addition of cosolvent DMSO offsets acidic catalysis of NADPH degradation. Therefore, we generated the idea that stepwise addition of NADPH through the reaction time. The bioconversion of TFAP **20** at 40 ºC showed that the concentration of the cofactor did not affect conversion in1 h which is the initial phase of the reaction. However, the stepwise addition of cofactor at 0 and 2 h increased the conversion 10-20% higher at 4 h compared to the conversion when the same concentration of cofactor was at 0 h. This result suggests that NADPH addition in a time course could be helpful to compensate for the decomposition of NADPH. Consequently, NADPH in the redox reaction using biocatalysts was added stepwise several times to compensate for the decrease in available NADPH concentration.

Following by the cofactor study, a directed evolution using error-prone PCR was done using OCR-WT, and the mutant clones were screened by colorimetric assay. The color change of bromothymol blue from blue (pH 7.0) to greenish-yellow (pH 5-6) indicated that 5S-MOLE **16** was reduced to DOLE **18**. Eight OCR mutants showed intense yellowish color change compared to OCR-WT or no color change at all; therefore, those mutants were subjected to the next screening. The second screening with an increased amount of 5S-MOLE **16** resulted in the isolation of one mutant OCR-D54V which has a single mutation residue at D54 to valine. This mutation site was not exactly on the predicted catalytic triads or cofactor binding sites; nevertheless, it contributes to enhancing catalytic activity. Increased activity was presumed because of the rearrangement of the amino acid residues network which could reduce steric hindrance of the bulk substrate. OCR-D54V displayed a much higher conversion when 90% 3R-MOLE **17** and 10% 5S-MOLE **16** were used as a substrate, which suggests that the specific activity of OCR-D54V toward not only 5S-MOLE **16** but also 3R-MOLE **17** is higher compared with WT (**Figure 33**). In this result, the conversion to DOLE **18** already was 90% in 2 h with OCR-D54V, In comparison, it was approximately 60% at 4 h using OCR-WT. The conversion using 10 $g \cdot L^{-1}$ DOXE **15** also showed that total conversion to MOLEs and DOLE **18** was 2.5 times higher with OCR mutant D54V compared to the conversion using OCR-WT (**Table 14**). One of the difficulties of proceeding with the bioconversion was that the complete conversion is hard to achieve due to the irreversible formation of

aggregation that contains non-reduced DOXE **15** and MOLEs. The small scale of bioconversion using a reaction mixture having DOXE **15**, as well as MOLEs, showed that OCR-D54V could lower the residual amount of MOLE to 1% which was not achieved by OCR-WT. However, the reaction with an increased amount of reaction mixture up to 10 $g \cdot L^{-1}$ showed approximately 5% of residual MOLEs. The reason was supposed due to the high hydrophobicity of MOLEs, causing sticky aggregation on the surface of the reactor. Therefore, the better mixing system or cosolvent is required for further study.

Flow chemistry has some advantages compared to conventional batch reaction such as rapid reaction optimization, easy scale-up, and production of cleaner products. For the sake of better mixing, flow chemistry was introduced in the biocatalytic reduction of an organic compound. As a model substrate, TFAP **20** was used in this experiment. 10-20 $U \cdot mL^{-1}$ of lyophilized OCR-WT and GDH2 were used for biocatalysts. A biphasic reaction condition was achieved by simultaneous pumping aqueous solution and organic solution from separate glass syringes. The conversion at 0.5, 1, 2 h increased up to approximately 20, 50, 70% after equilibrium, respectively, using overall 100 mM TFAP in MTBE as the increment of reaction time as well as biocatalysts loading (**Figure 39**). On the contrary, the experiments with the T-shape mixer and reactor having a bigger diameter decreased conversion, indicating that the Y-shape mixer and a larger diameter of the tube were not beneficial for mass transfer. The result demonstrates that the biocatalytic reduction could easily be improved by changing residence time and biocatalyst loading. In addition, the quality of the product was the same in each batch. Quality control in a pharmaceutical company is the key requirement for drug synthesis. The biocatalytic reduction of a drug intermediate in the flow reactor is strongly recommended for the pharmaceutical industry. Furthermore, the result shows that cleaner products can be obtained after flow reaction due to its good phase separation, which can simplify the purification step in drug synthesis and reduce production costs.

4. Application of new type of aldoxime dehydratase isolated from *Rhodococcus* sp. YH3-3 for aldoxime synthesis and its directed evolution

*The findings of this section have been published in the journal Biocatalysis and Biotransformation[117].

4.1. Introduction

4.1.1. The broad application of nitrile compounds in industry and pharmaceuticals

The integration of biorenewables into the industrial product tree has gradually highlighted due to the increasing importance and abundant availability of such feedstocks[117]. A particular challenge represents aromatic compounds as they are important for today's industrial chemicals, but at the same time more difficult to access from biorenewable feedstocks. Another focus in this area of the future product tree is on functional groups being less common in nature but widely applied in the industry such as, for example, nitriles[118]. Nitrile compounds have a broad range of applications in the chemical industry, which encompasses from low price-bulk chemicals to expensive small-scale drugs[119]. One of the most common usages of nitrile is nitrile rubber which is a synthetic copolymer of acrylonitrile and butadiene. This form of rubber is used to make protective gloves, hoses, and seals (**Figure 44**).

The number of nitrile-containing compounds in pharmaceuticals has increased to over 30 due to its benefits in pharmaceuticals production[120,121]; (1) the nitrile group has moderate reactivity toward free nucleophiles without activation by adjacent electron-withdrawing groups[120,122]. (2) it is nonmetabolized, which means that the nitrile compounds can penetrate our body to reach the right place to function[123–125]. Most nitrile-containing pharmaceutical compounds are aromatics with aliphatic-, alkene-, and nitrogen-bearing nitriles being progressively less frequent[120]. Nitrile compounds in pharmaceuticals play a role as aromatase and aldolase inhibitors, non-steroidal receptor antagonists, anti-HIV agents and so on. Anastrozole, verapamil, and gallopamil are widely prescribed and the best-studied nitrile-containing pharmaceuticals[120] (**Figure 45**). Notably, the blockbuster drug anastrozole for the treatment of breast cancer after surgery marketed by Astra Zeneca under the trade name Arimidex and entered the WHO list of most essential drugs. Besides, recently released aminonitrile-containing antidiabetic drug, vildagliptin and saxagliptin are examples of widely used nitrile-containing drug[120] (**Figure 46**).

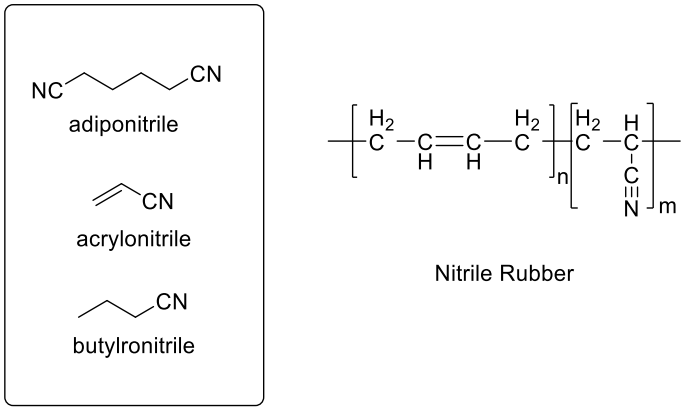

Figure 44. The examples of bulk chemicals (left) and structure of nitrile rubber as an representative example in the industrial application of nitrile compounds[119].

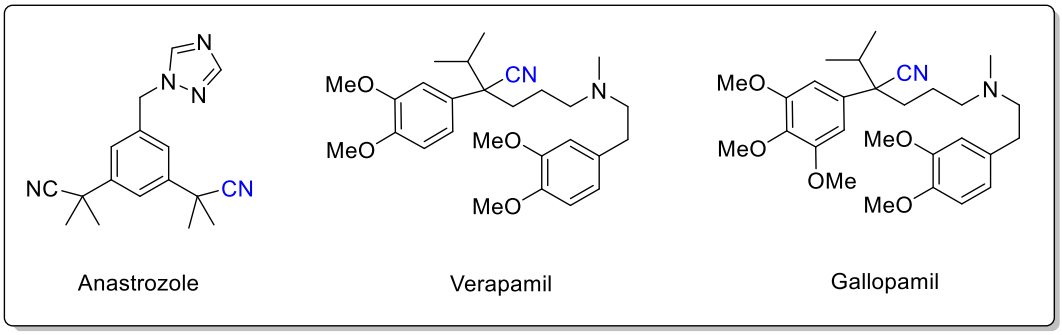

Figure 45. Most widely prescribed nitrile-containing pharmaceuticals[120].

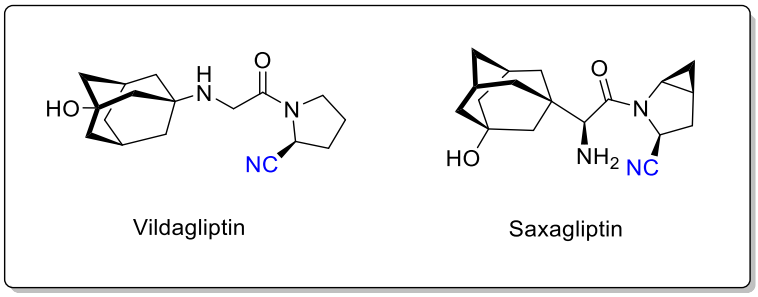

Figure 46. Antidiabetic drugs containing a nitrile functional group[120].

Nitrile can be prepared from aldehyde or ketone, halogenoalkanes, and amide (**Figure 47**). General industrial technology is based on ammoxidation under high-temperature transformation in the gas phase (**Figure 48**)[119,126]. The most popular approach for nitrile synthesis is a substitution or addition reaction with hydrogen cyanide or other derivatives as a source of the cyano functionality (**Figure 48**)[119]. However, those synthetic procedures are not environmentally friendly due to the high toxicity of cyanide.

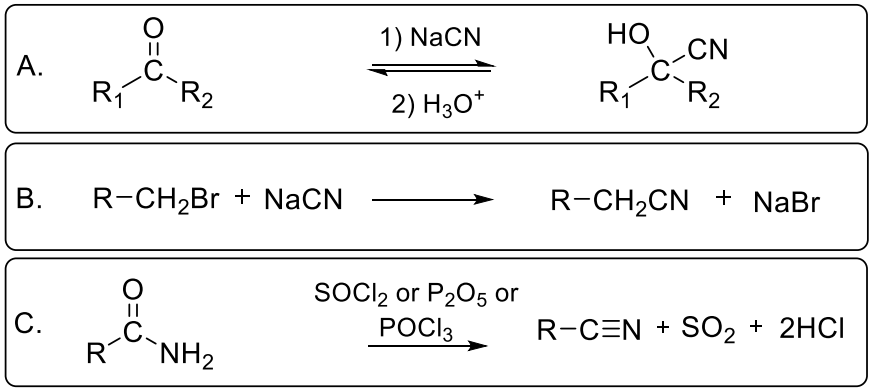

Figure 47. Synthesis of nitrile from aldehyde or ketone (A), halogenalkane (B), and amide (C).

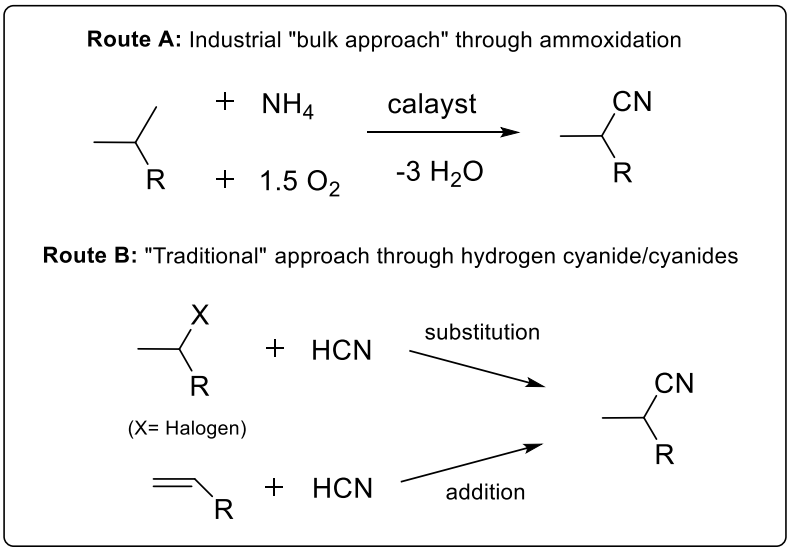

Figure 48. Synthetic approaches toward nitriles based on the classic chemical way in industry.

2-Furonitrile serves as an intermediate in the field of fine chemicals, and pharmaceuticals. This compound also was reported as a potential sweetener due to an approximately 30-fold higher sweetening power compared to sucrose[118]. Recently, 2-furonitrile was successfully applied as a catalyst with CeO_2 for utilization of CO_2 to polycarbonates, which is a promising way to alleviate global warming caused by the increase of atmospheric CO_2 concentrations[118]. Furthermore, 2- furonitrile is a building block of the pharmaceutical compound S1P1 receptor modulator, which has applications for pain relief, cancer, treatments, rubber composition, and treatments for Alzheimer disease[127–129] (**Figure 49**).

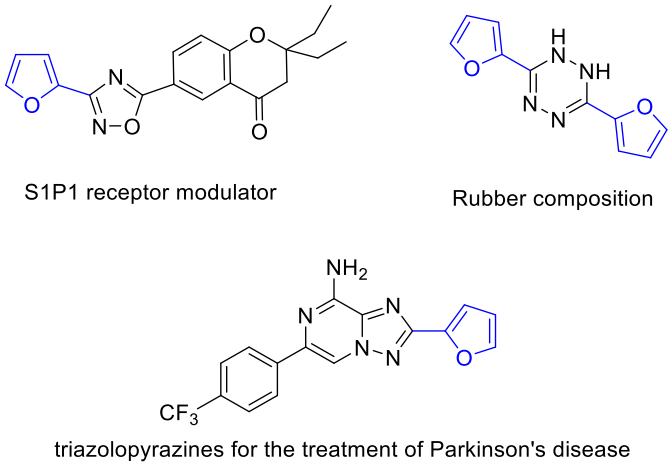

Figure 49. Application of 2-furonitrile into pharmaceutical building blocks[127–129].

Up to now, 2-furonitrile was produced either by ammoxidation of furfural with ammonia or as a gas phase process running at >400 °C[118] (**Figure 50**). On a lab scale, broad ranges of synthetic methods were proposed starting from 2-furfural, 2-furfuryl alcohol, furfuryl amine, and 2-furfuryl aldoxime in the presence of metal catalysts, organic solvents, and at too high or low temperature (**Figure 51**)[130–137]. Nevertheless, compounds containing furan moiety commonly used for the nitrile synthesis, which can be prepared from natural waste sources or readily constructed in substituted form. For example, Furfural is obtained by acid-catalyzed dehydration of cellulose biomass, thereby large production of furfural from biomass is not economically competitive[138]. More importantly, the nitrile synthesis using such an environmentally sustainable compound as a starting material provides value on its process development.

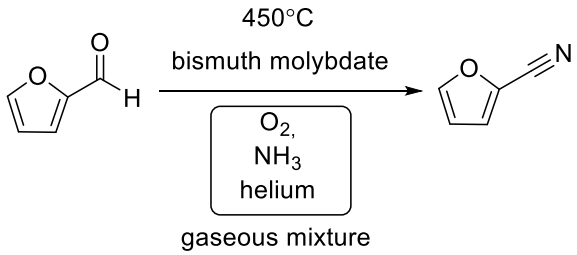

Figure 50. Process for preparing 2-furonitrile under vapor phase at high temperature[118].

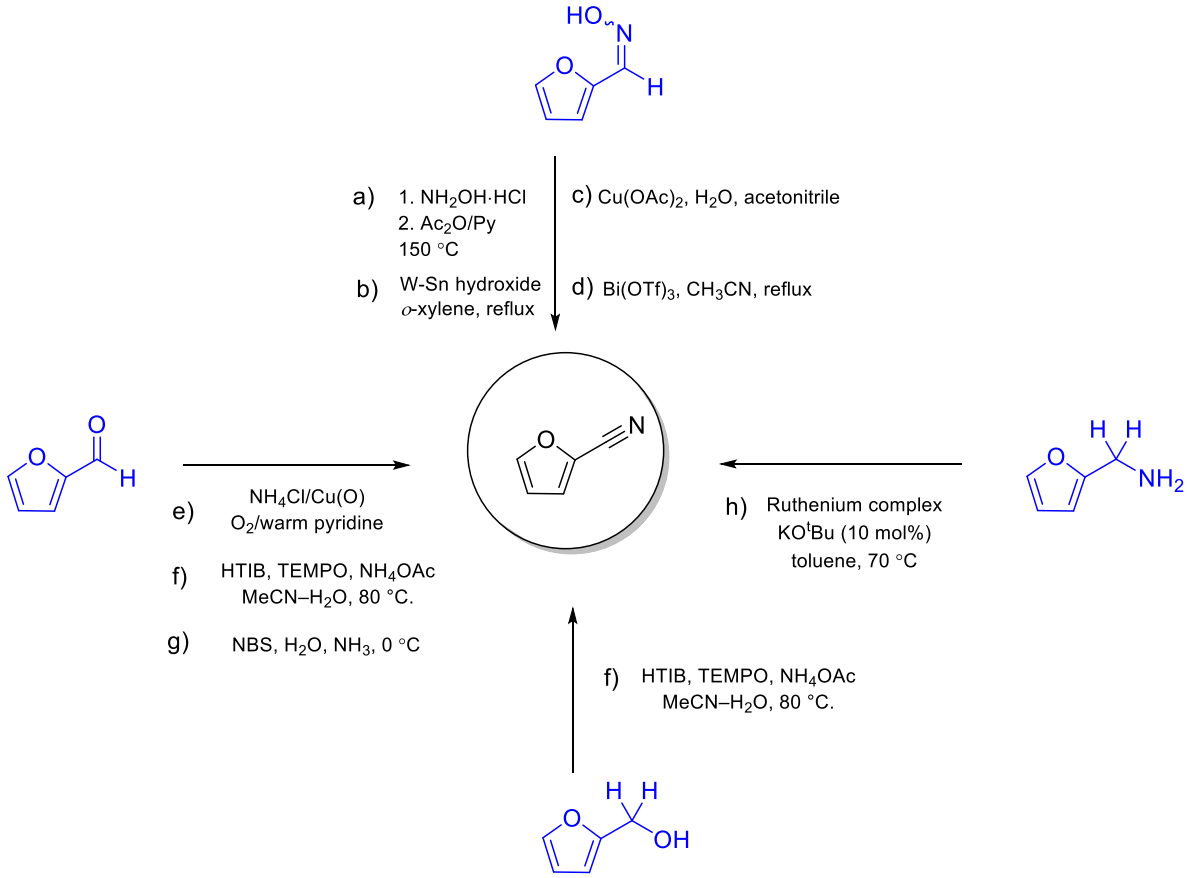

Figure 51. Process for preparing 2-furonitrile from 2-furfural, 2-furfuryl alcohol, furfuryl amine, and 2-furfuryl aldoxime[130–137].

4.1.2. Application of biocatalyst usage in nitrile synthesis and its mechanisms

Biocatalysts are essential for producing valuable compounds with efficient and environment-friendly ways. Change has enabled a range of promising building blocks as alternatives to current bulk chemicals derived from fossil sources. Aldoxime dehydratase is one of the biocatalysts which has value in

synthesis of the raw material. As a green alternative towards furonitrile, aldoxime dehydratases are capable of dehydrating an aldoxime under formation of a nitrile in water (**Scheme 14**).

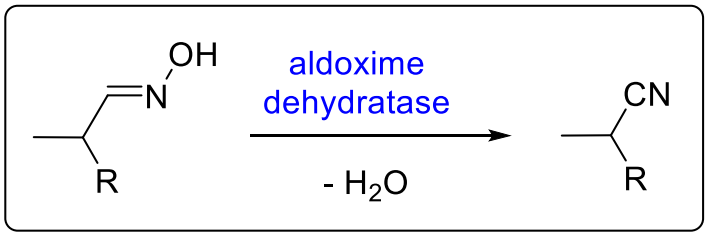

Scheme 14. Enzymatic dehydration of aldoxime using aldoxime dehydratase.

Aldoxime dehydratase was firstly found from Asano's group which has isolated various aldoxime degrading microorganisms such as actinomyces, fungi, and yeast come from soil including *Bacillus* sp. strain OxB-1 and *Rhodococcus* sp. strain YH3-3[139–141]. Asano group has screened approximately 975 microorganisms and found that 31 bacterial and 9 fungal aldoxime dehydratase mainly from *Arthrobacter*, *Bacillus*, *Rhodococcus*, and *Fusarium* sp. showing both the *Z*-phenylacetaldoxime and pyridine-3-aldoxime dehydration activities. The aldoxime dehydratase (Oxd) from *Bacillus* sp. OxB-1 was firstly isolated, and consequently, OxdYH3-3, OxdA, OxdRG, OxdRE, OxdFG, and OxdK were found from *Rhodococcus* sp. YH3-3, *P. chlororaphis* B23, *R. globerulus* A-4, *R. erythropolis* N-771, *F. graminearum* MAFF305135, and *Pseudomonas* sp. K-9, respectively[140,142,143]. Oxds have a molecular weight of in the range of 40-45 kDa which containing heme b as a prosthetic group[119,144]. Apart from OxdA and FG, Oxds showed optimal activity and stability at neutral pH. OxdB, RE, and RG have relatively higher specific activity toward *Z*-phenylacetaldoxime (562-851 $U \cdot mg^{-1}$) compared to OxdK, exhibiting approximately 400 times lower specific activity[119,144].

Oxds contain heme b group, and its iron ion should be existed as ferrous (FeII) state rather than ferric state (FeIII) to proceed the dehydration of oximes to nitrile, which are observed by wavelength change in UV/Vis and EPR spectra measurement[119,145,146]. These studies revealed that the aldoxime substrates bound to ferrous heme via N-coordination to proceed dehydration[145,147]. Along with state of iron, the histidine residue in active site played an important role in catalysis as proximal ligands of the heme group and other histidine residues, which acted as distal ligands[145,147,148]. All together with UV/Vis, EPR, FTIR[149], Raman spectroscopy[149], and quantum mechanics/molecular mechanics (QM/MM) calculations[150,151], a structural study using crystal structure finally explained the detailed mechanism of catalysis[152,153](**Figure 52**).

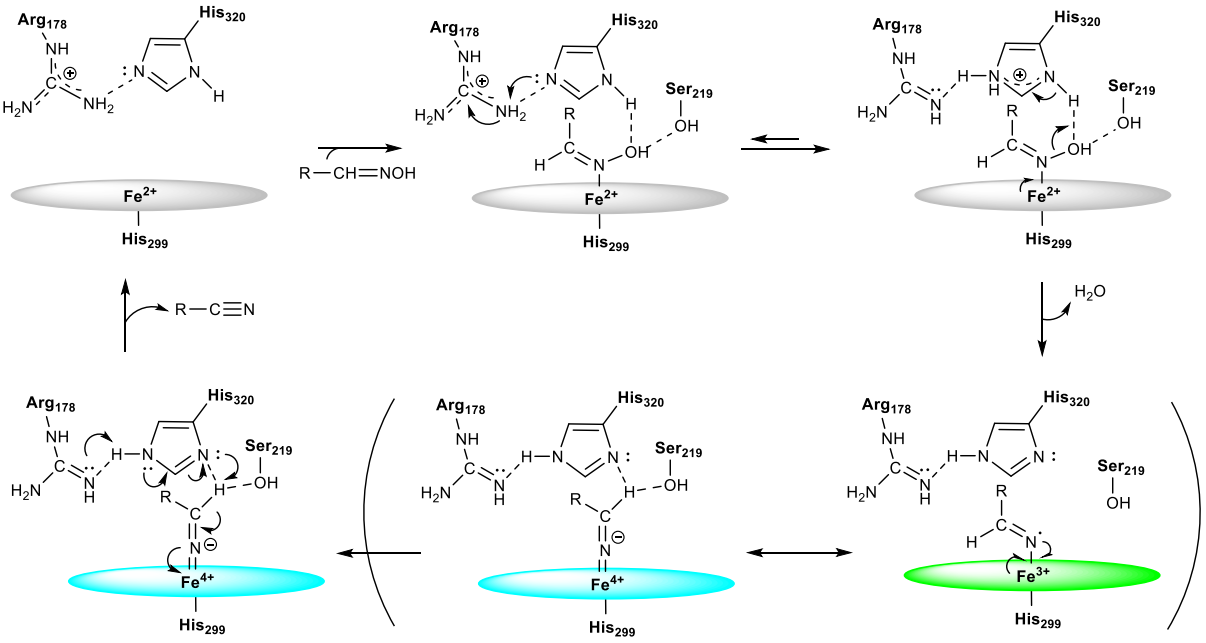

Figure 52. A possible reaction mechanism for the synthesis of a nitrile by aldoxime dehydratase[119,152].

At the first step, the substrate enters to heme pocket following binding N atom of the substrate to ferrous heme, and proximal serine and histidine residues fix the hydroxy group of the substrate. In addition, the hydrogen-bond network in the distal heme pocket fixes the proper orientation of distal histidine toward the heme-bound substrate. The proton transfers from the protonated arginine to histidine enhancing electrophilicity of the histidine imidazole. Subsequently, protonated histidine donates a proton to the hydroxyl group of the substrate to eliminate it as a water. The ferrous center donates an electron to substrate hydroxy group, and α-carbon of the dehydrated substrate is oriented to histidine. The hydrogen bond between a hydrogen atom of α-carbon and hydroxy group of serine is formed following dissociation of the protein from acidic C-H bond of the dehydrated substrate to yield nitrile product. After nitrile leaving, protonated histidine imidazole would protonate arginine back to the original state. The catalytic triad arginine, histidine, and serine in adjacent heme b are crucial for catalytic activity.

4.2. The motivation of the study

The substrate scope of Oxd enzymes has been studied, including aliphatic and aromatic aldoximes, as well as arylaliphatic aldoximes[119]. So far, most of the aldoxime dehydratases turned out to be suitable for aliphatic aldoximes, whereas, aldoxime dehydratases for aromatic nitrile synthesis are rare. An exception is the aldoxime dehydratase from *Rhodococcus* sp. YH-3-3[141,154,155], which has known for its activity toward aromatic aldoximes such as *E*-2-furfuryl aldoxime and *E*-pyridine-3-aldoxime[154]. Concerning 2-furonitrile, the corresponding aldoxime can be easily prepared from furfural, which itself can be easily synthesized from pentoses as a biorenewable feedstock[156,157]. In 1999, the whole cell

containing OxdYH3-3 was used for the conversion of various aldoximes to nitrile by Kato et al. [154] (**Table 16**).

Table 16. Substrate specificity of *Rhodococcus* sp. YH3-3[154].

Substrate	Relative activity (%)
E-Pyridine-3-aldoxime	100
Z-Pyridine-3-aldoxime	18
E-Pyridine-2-aldoxime	2.4
E-Pyrazinealdoxime	5.5
E-*p*-Tolualdoxime	1.1
E-*p*-Chlorobenzaldoxime	1.0
E-*p*-Methoxybenzaldoxime	0.22
E-*p*-Nitrobenzaldoxime	0.08
E-2-Furfurylaldoxime	1.8
E-Indole-3-aldoxime	0.27
E/Z-Pyridine-3-aldehyde hydrazone	0.35
O-Acetyl-*E*-pyridine-3-aldoxime	5.5
E-Pyridine-3-aldoxime-N-oxide	5.1
E/Z-Acetaldoxime	5.7
E/Z-*n*-Butyraldoxime	33

The drawbacks using a whole-cell catalyst is that nitrile is converted to amide and carboxylic acid by nitrile hydratase and amidase successively[139,140]. To inhibit the nitrile degrading enzymes, heat treatment or cell drying with acetone were required. Although an aldoxime dehydratase from *Rhodococcus* sp. YH-3-3 could be identified as a suitable biocatalyst for aromatic nitrile synthesis, the limited enzyme activity, as well as substrate concentration, raises demand for highly active biocatalysts and a process running at elevated substrate loading.

The recombinant Oxd from *Rhodococcus* sp. YH-3-3 (OxdYH3-3) has not been available up to now, even though OxdYH3-3 was found relatively earlier than other Oxd enzymes. Later in 2016, the whole genome sequences of *Rhodococcus* sp. YH3-3 has been revealed by Asano group[158], which gives a possibility to construct recombinant OxdYH3-3 with bacterial hosts for overexpression. Therefore, the continuous work was done by collaborative work with Gröger and Asano group in this study to produce recombinant OxdYH3-3 WT for the biosynthesis of the nitrile compound, mainly focusing on 2-furonitrile (**Scheme 15**). Furthermore, an increment of substrate loading was shown by applying engineered OxdYH3-3 to 2-furonitrile synthesis.

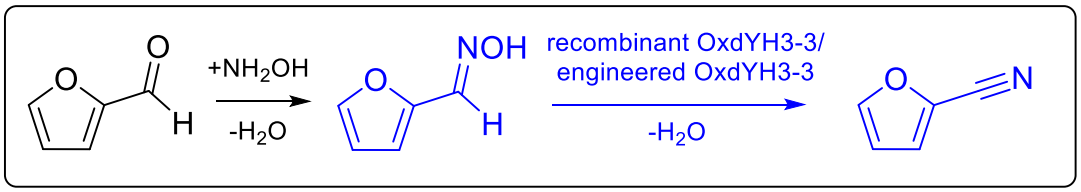

Scheme 15. Two-step synthesis of 2-furonitrile from furfural. 2-furonitrile was converted through spontaneous condensation of furfural with hydroxylamine followed by dehydration via aldoxime dehydrate OxdYH3-3.

4.3. Preparation of 2-furfuryl aldoxime and 2-furonitrile

The 2-furfuryl aldoxime was synthesized from furfural and separated by flash chromatography using a silica column. Freshly synthesized 2-furfuryl aldoxime showed one type of ^{1}H-NMR peaks; ^{1}H-NMR of 2-furfuryl aldoxime was determined (δ2.05 (brs, 1H), 5.8-7.2 (m, 3H), 7. 3 (s, 1H))[159] (**Figure 53**).

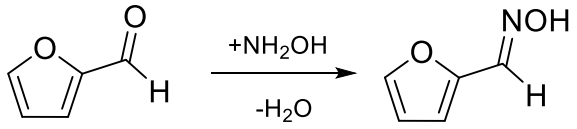

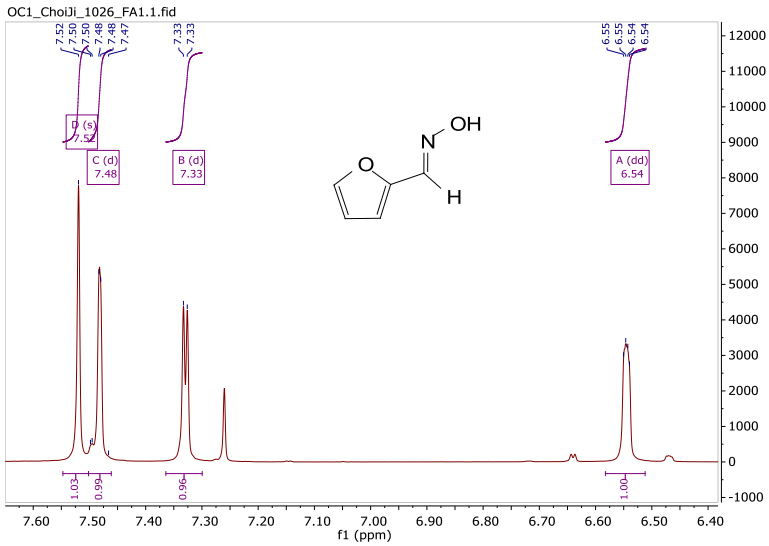

Figure 53. ^{1}H-NMR of 2-furfuryl aldoxime.

2-Furfuryl aldoxime and 2-furonitrile were analyzed by normal phase HPLC, and the signals related to 2-furfuryl aldoxime and 2-furonitrile showed an excellent separation at 4.08 and 3.16 min, respectively (**Figure 54**). *E*-Pyridine-3-aldoxime and 3-cyanopyridine showed retention times at 8.15 min and 5.80 min, respectively (data not shown).

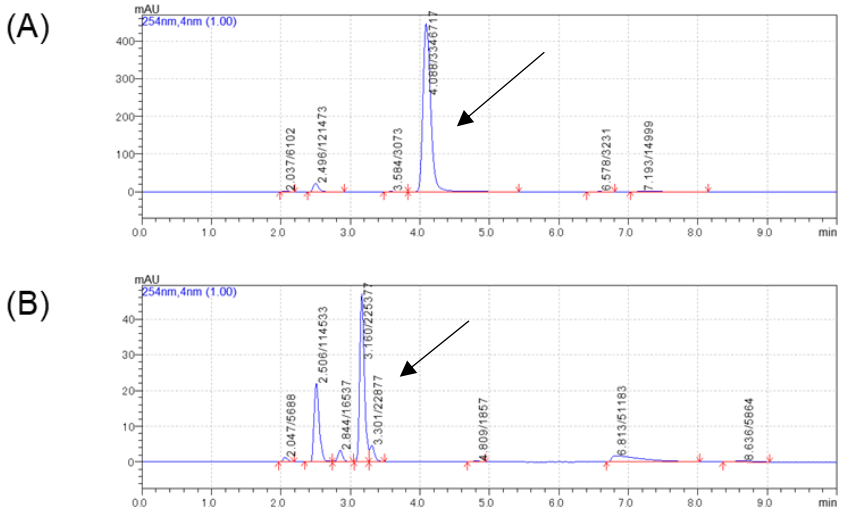

Figure 54. HPLC analysis of 2-furfuryl aldoxime (A) and 2-furonitrile (B). The arrows indicate peaks of 2-furfuryl aldoxime and 2-furonitrile, respectively.

4.4. Preparation of nitriles through bioconversion of aldoximes using wild-type OxdYH3-3

4.4.1. Construction of transformant strains for overexpression of OxdYH3-3 and optimization of its overexpression

Since an aldoxime dehydratase was found from *Rhodococcus* sp. YH3-3, substrate screening study was done using this wild-type OxdYH3-3[139,155]. The recombinant enzyme using *E. coli* as the host had not been attempted before nucleotide sequences of OxdYH3-3 were thoroughly analyzed by the genome sequencing of *Rhodococcus* sp. YH3-3[158]. However, apart from OxdYH3-3, various Oxds recombinant enzymes were successfully expressed in *E. coli*[119]. For examples, OxB-1 from *Bacillus* sp. was cloned into pUC18 and pOxd-90F vectors and overexpressed in *E. coli* JM109 at 30 °C with one mM IPTG[160], and OxdRG from *Rhodococcus* sp. A-4 was also overexpressed in *E. coli*[155]. OxdA from *Pseudomonas chlororaphis* B23 was cloned to pET24a(+) and transformed into *E. coli* BL21CodonPlus(DE3)-RIL to show 10% of the total amount of soluble protein[143]. OxdRE found in *Rhodococcus* sp. N-771 showed the highest activity toward phenylacetaldoxime when it was cloned into pOxS19 and overexpressed in *E. coli* BL21(DE3)[142]. OxdK and OxdFG were isolated from *Pseudomonas* sp. K-9 and *Fusarium graminearum* MAFF305135, and recombinant enzymes of above Oxds were constructed using *E. coli* as a host cell[144,146]. Recently, newly isolated aldoxime dehydratase (OxdBr1) from *Bradyrhizobium* sp. was inserted into pET28b and transformed into *E. coli* BL21(DE3)[161]. Comparison of OxdYH3-3 with conventional Oxds showed that OxdYH3-3 has the highest identity with OxdRG (GenBank accession

number BAE48794.1; 99%) and OxdRE (GenBank accession number BAD17969.1; 96%). Apart from those enzymes, OxdYH3-3 showed 77, 75, 46, 18, and 9% identities with OxdA (GenBank accession number BAC81537.1), OxdK (GenBank accession number BAD98528.1), OxdBr1 (GenBank accession number WP_044589203.1), OxdFG (GenBank accession number BAE48794.1), and OxB-1 (GenBank accession number BAA90459.1), respectively. OxdYH3-3 showed intermediate and high sequential identities (46-99%) with Oxd enzymes apart from OxdF and OxdB-1 which are very different from other Oxd enzymes. Since wild-type *Rhodococcus* sp. YH3-3 contains nitrile degrading enzymes, including nitrile hydratase and amidase, it is necessary to use non-nitrile degrading bacteria for high production of OxdYH3-3. Successively the various types of recombinant OxdYH3-3 were constructed[162].

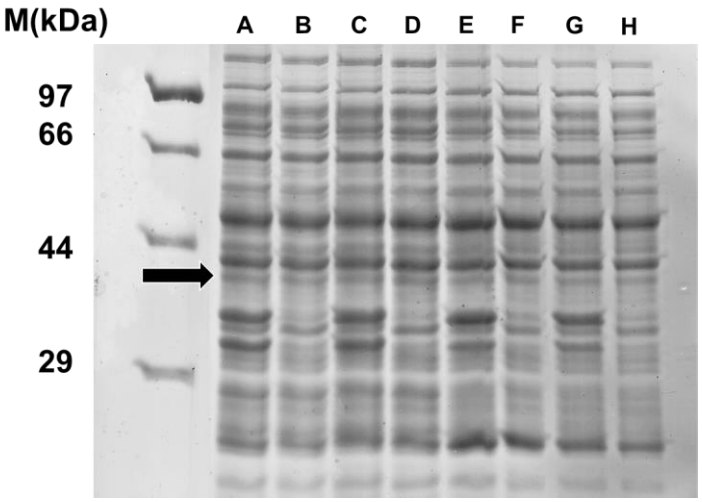

Figure 55. PAGE analysis of overexpression of OxdYH3-3. *OxdYH3-3* was cloned to pET22b vector and overexpressed in BL21Codonplus(DE3) *E. coli* cell: A and B, total protein and soluble protein of BL21Codonpuls(DE3)/pET22b induced by 0.2 mM IPTG at 18 °C for 48 h; C and D, total protein and soluble protein of BL21Codonpuls(DE3)/pET22b induced by 0.8 mM IPTG at 18 °C for 48 h; E and F, total protein and soluble protein of BL21Codonpuls(DE3)/pET22b induced by 0.2 mM IPTG at 30 °C for 20 h, G and H; total protein and soluble protein of BL21Codonpuls(DE3)/pET22b induced by 0.8 mM IPTG at 30 °C for 20 h. The arrow indicates the size of OxdYH3-3 in SDS-PAGE gel[162].

For the first attempt, OxdYH3-3 was cloned to pET22b vector and overexpressed in *E. coli* BL21CodonPlus(DE3). The overexpression was done in low temperature at 18 °C for 48 h and intermediate temperature at 30 °C for 20 h with 0.2 and 0.8 mM IPTG, respectively, to find the optimal expression condition. The overexpression level was analyzed by SDS-PAGE (**Figure 55**). The OxdYH3-3 with 6xhistidine at N-terminus has approximately size of 42 kDa including 6xhistidine tags and thrombin cleavage site. In the above condition, the overexpression level of OxdYH3-3 was very

low in SDS-PAGE, and there were no differences in overexpression level regardless of temperatures, IPTG concentrations, and incubation times (**Figure 55**).

In a previous study, OxdRE showed 33% of conversion toward aryl aliphatic aldoxime even though the expression level of OxdRE was relatively low, showing 10% of total soluble protein[163]. This study suggested that Oxds could show a reasonable activity even without high overexpression. Therefore, the activity of OxdYH3-3 toward *E*-pyridine-3-aldoxime was measured to see whether it has a catalytic activity or not. Unfortunately, the desired activity was not observed from any overexpressed enzymes in various overexpression conditions (data not shown). Consequently, the expression vector and *E. coli* host cell were changed to improve the expression condition. Toward this end, plasmid pET15b, pET22b, and pET28b harboring *OxdYH3-3* were transformed to *E. coli* BL21Codonplus(DE3)[162]. The overexpression of the protein was analyzed by SDS-PAGE (**Figure 56**, lane E-J). However, any type

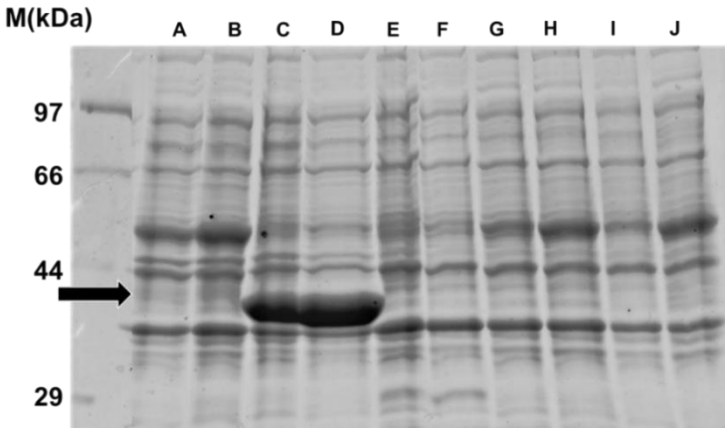

Figure 56. The SDS-PAGE analysis of OxdYH3-3 in difference overexpression system using autoinduction medium. The size of OxdYH3-3 was approximately 41 kDa. A and B; BL21(DE3)/pET22b-*OxdYH3-3* after 14 and 20 h incubation at 30 °C, C and D; BL21(DE3)/pET28b-*OxdYH3-3* after 14 and 20 h incubation at 30 °C, E and F; BL21Codonplus(DE3)/pET15b-*OxdYH3-3* after 14 and 20 h incubation at 30 °C, G and H; BL21Codonplus(DE3)/pET22b-*OxdYH3-3* after 14 and 20 h incubation at 30 °C, I and J; BL21Codonplus(DE3)/pET28b-*OxdYH3-3* after 14 and 20 h incubation at 30 °C, respectively. The arrow points the band of OxdYH3-3 on SDS-PAGE gel[162].

of overexpression plasmids did not contribute to the enhancement of overexpression. Therefore, the *E. coli* host cell was changed to BL21(DE3), which shows a higher growth rate than BL21codonPlus(DE3)[162]. The optimal vector for overexpression was pET28b, which contains 6-histidine residues at C-terminus. The total protein size containing 6-histidine tag is 41.4 kDa. In the previous attempt for overexpression, OxdYH3-3 was cloned into pET22b, and the histidine residues and thrombin cleavage site were located at N-terminus of the protein. So far, in this study, pET28b is

the only vector which has 6-histidine residues at C-terminus (**Figure 56**, lane C-D), in contrast, other plasmids such as pET15b and pET22b have 6-histidine residues at N-terminus. The result suggested that OxdYH3-3 with histidine at N-terminus could lower protein overexpression. The previous study with OxdK showed that 6-histidine tag at its C-terminus decreased the production of the enzyme[146], which was opposed to this study. OxdYH3-3 showed 75% of similarity with OxdK. We supposed that sequence difference between OxdYH3-3 and OxdK is related to enzyme folding so that the histidine residues at N or C terminal of proteins could affect enzyme folding differently.

4.4.2. Measurement of catalytic activity of various types of recombinant OxdYH3-3

The activity toward *E*-pyridine-3-aldoxime was measured to see the correlation between overexpression and activity. *E*-pyridine-3-aldoxime was used as a standard substrate to isolate aldoxime-degrading bacteria from soil[139] and was highly active for OxdYH3-3. Therefore, *E*-pyridine-3-aldoxime was used for the standard substrate. In this study, a fully grown cell culture was incubated with *E*-pyridine-3-aldoxime for 20 h at 30 °C. The aldoxime degrading activities were corresponding with OxdYH3-3 overexpression (**Figure 57**). The OxdYH3-3 in BL21(DE3)/pET28b showed the full conversion of *E*-pyridine-3-aldoxime to 3-cyanopyridine in 20 h (**Figure 57**). However, OxdYH3-3 in pET15b and pET22b transformed into BL21(DE3) and BL21Codonplus(DE3) showed low conversion, approximately 5%, which was assumed due to weak overexpression using recombinant cells containing pET22b-*OxdYH3-3* and pET15b-*OxdYH3-3*. Among the un-optimized recombinant cells, Only OxdYH3-3 in BL21Codonplus(DE3)/pET28b showed 15% conversion.

4.4.3. Bioconversion of aldoximes to nitriles using a whole-cell by time course

The activity toward *E*-pyridine-3-aldoxime was measured by time course[162]. 10 mM *E*-pyridine-3-aldoxime was added to 500 µL reaction solution containing a whole-cell OxdYH3-3 biocatalyst, then the conversion at 30 ºC from aldoxime to nitrile was measured at 3, 4, 5, and 9 h by HPLC (**Figure 58**). A previous study by Kato et al. showed that the relative activity of *E*-2-furfuryl aldoxime was 1.8% compared to *E*-pyridine-3-aldoxime using *Rhodococcus* sp. YH3-3 whole-cell cultivated in 25 mL culture[154]. After heat inhibition of nitrile degrading enzymes, the yield was increased to 62% to 2-furonitrile when the conversion to 3-cyanonitrile was 98% at the same time[154]. In this study, the conversion of *E*-pyridine-3-aldoxime to the corresponding nitrile was approximately 88% after 3 h, 93% after 5 h and >99% after 9 h reaction time (**Figure 58**). In the case of the synthesis of 2-furonitrile, the achieved conversion with the recombinant strain was 75% after 3 h when starting from *E*-2-furfuryl aldoxime (**Figure 58**). The conversion increased to 85% after 5 h reaction time, and after 9 h the conversion of this aldoxime reached >99%. Although the results showed that *E*-pyridine-3-aldoxime is

a more favorable substrate in terms of a faster reaction rate, *E*-2-furfuryl aldoxime also led to a high reaction rate as well as excellent conversion. It is noteworthy that this is the first case of showing the activity toward aromatic aldoxime with recombinant OxdYH3-3, and we could prove the whole cell biocatalyst reach full conversion up to 9 h without losing its activity. This result supports the study of Kato et al., which maintained the same tendency as in the current study with the recombinant enzyme[154].

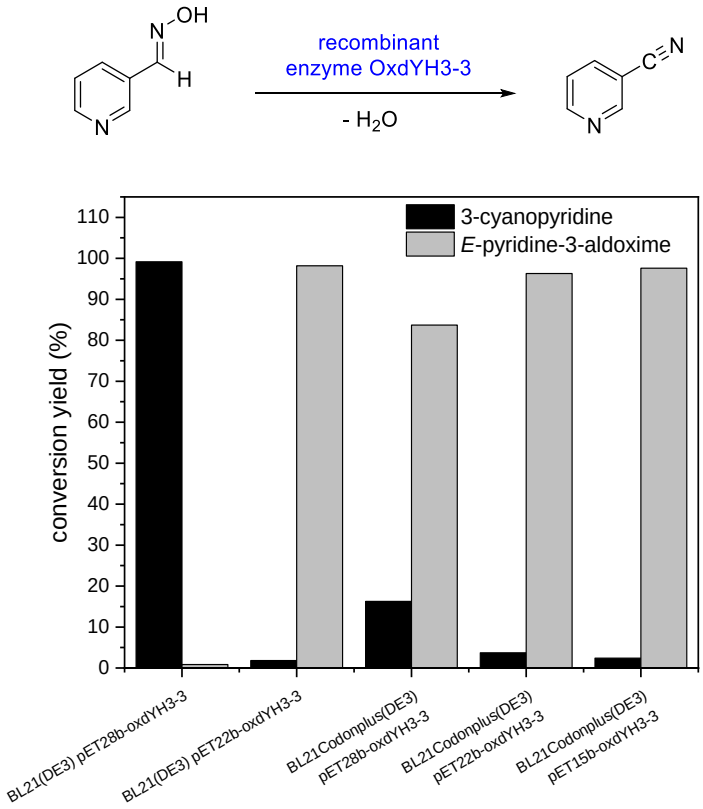

Figure 57. Conversion measured by HPLC. OxdYH3-3 was cloned to various pET plasmids and transformed to different hosts. The activity for 10 mM *E*-pyridine-3-aldoxime was measured after 20 h of reaction[162].

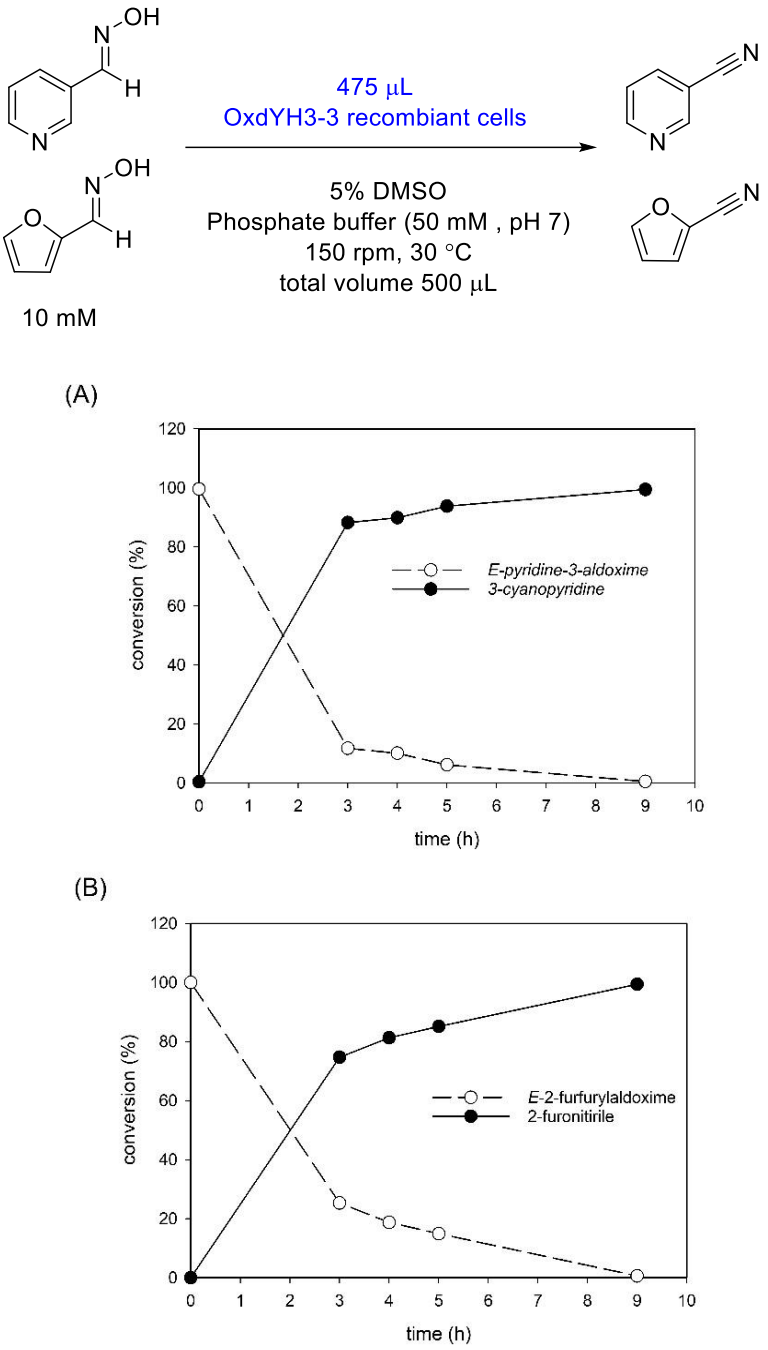

Figure 58. The conversion of *E*-pyridine-3-aldoxime and 2-furfuryl aldoxime using BL21(DE3)/pET28b-OxdYH3-3. The biocatalytic conversion was done with 10 mM *E*-pyridine-3-aldoxime in a potassium phosphate buffer up to 9 h: (A) Conversion of *E*-pyridine-3-aldoxime to 3-cyanopyridine; (B) Conversion of *E*-2-furfuryl aldoxime to 2-furonitrile.

4.5. Directed evolution of OxdYH3-3

4.5.1. Construction of a mutant library and screening of the activities of mutants

The mutant library of OxdYH3-3 was produced by error-prone PCR and cloned to pET28b vector following transformation into BL21(DE3). The mutant library was constructed following the procedures of PCR random mutagenesis kit (Agilent). T7-promoter/terminator primers and pET28b-OxdYH3-3 plasmid as a template were used. The random mutagenesis was started by adding Taq polymerase and increased $MgSO_4$ (640 µM) to have up to 5 mutations per 1,000 nucleotides. The amplified DNA was cloned into NcoI and HindIII digested pET28b vector. Approximately 1,000 clones were obtained. Every single colony on agar plates was inoculated to 96 deep well plate and cultured for 18 h to complete the full growth in autoinduction medium. The mutant screening was simplified by measuring the UV absorbance of the reaction mixture at the distinct wavelength which aldoximes and nitriles showed its maximum absorbance. *E*-pyridine-3-aldoxime and 2-furfuryl aldoxime, 3-cyanopyridine and 2-furonitrile have shown the maximum absorbance at 245 and 267 nm, 265 and 230 nm, respectively (**Figure 59**). Among aldoximes, 2-furfuryl aldoxime was chosen for the OCR mutant screening. Therefore, the absorbance at 270 nm was measured for mutant screening because the mutants which consumed 2-furfuryl aldoxime would show a decrease in absorbance at 270 nm.

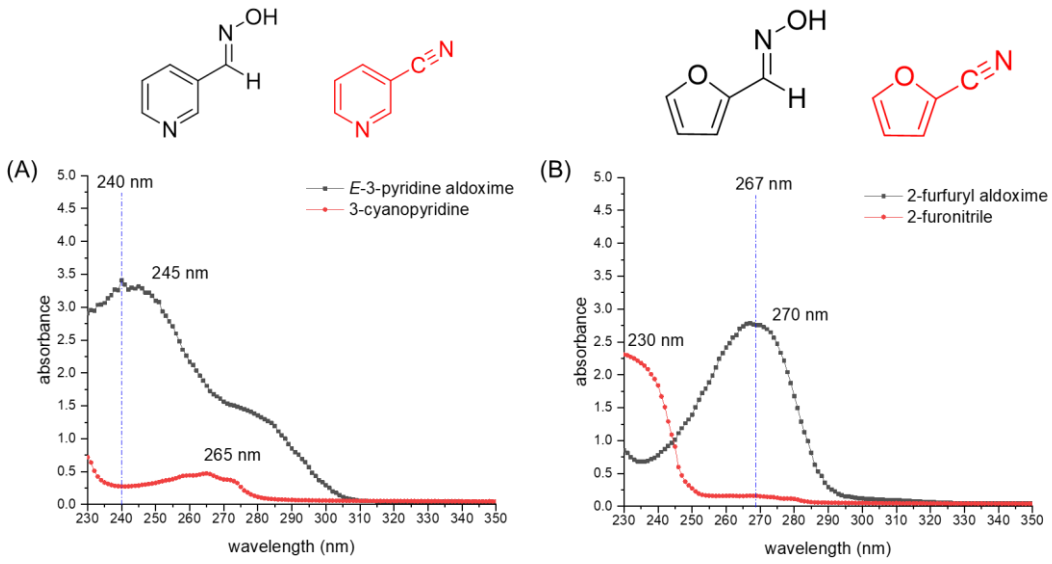

Figure 59. Absorbance scan of *E*-pyridine-3-aldoxime and 3-cyanopyridine (A), 2-furfuryl aldoxime and 2-furonitrile (B).

The high throughput screening was performed using a colony picker and a liquid handler, which was equipped in Toyama Prefecture University. It made the cultivation and sampling-handling time decrease, resulting in complete the screening process within 4 days for 1,000 clones (**Figure 60**).

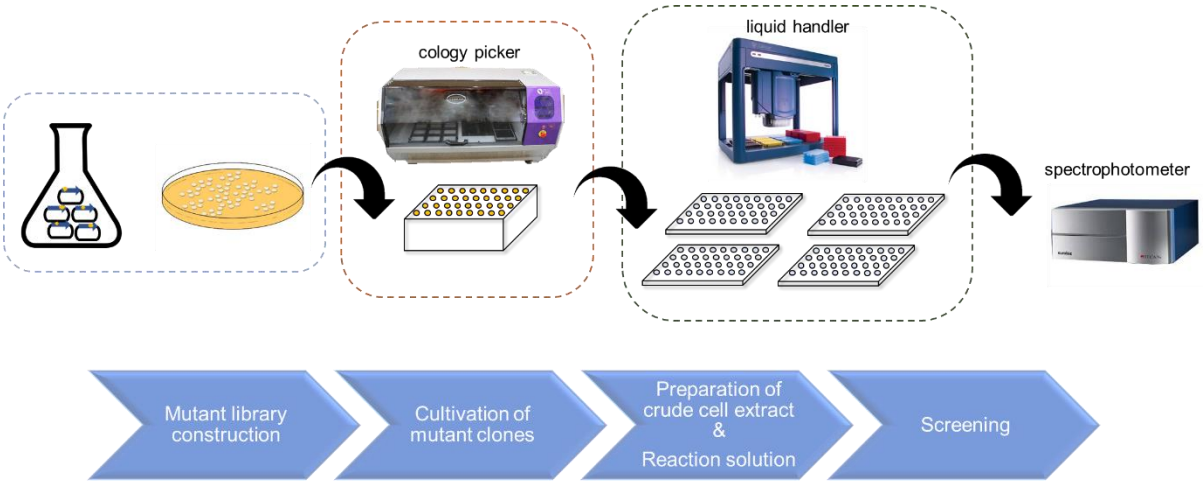

Figure 60. High throughput screening system.

We observed a slighter decrease in absorbance at 270 nm in the range of 2-2.5 by using cell crude extract after the first incubation. Therefore, the inoculated cell was fully cultured, and the first culture was inoculated again in fresh medium (the second culture) to optimize the cell growth. Consequently, the aldoxime consumption by using cell crude extracts from the second culture was increased, showing the absorbance change in the range of 0.5-2 at 270 nm. It implies that multiple inoculations are necessary due to the inappropriate cultural environment of 96 deep well plate, such as limited mixing and oxygen penetration into the medium. The clones which showed absorbance between 0-1 (lower 10%) at 270 nm were chosen for further screening. Three clones (N266S, A224T, P7H4) were finally selected after the repeated experiment (**Figure 61**). The three clones showed diminished absorbance in the repeated absorbance measurement. DNA sequences of the three mutants were analysed. N266S and A224T showed a single mutation at residue Ans266 and Ala224, which were changed to serine and threonine, respectively. On the other hand, P7H4 contained 3 mutated residues of Val264Ala, Ile302Ser, Gln330Leu (**Figure 62**).

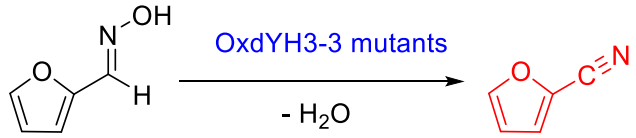

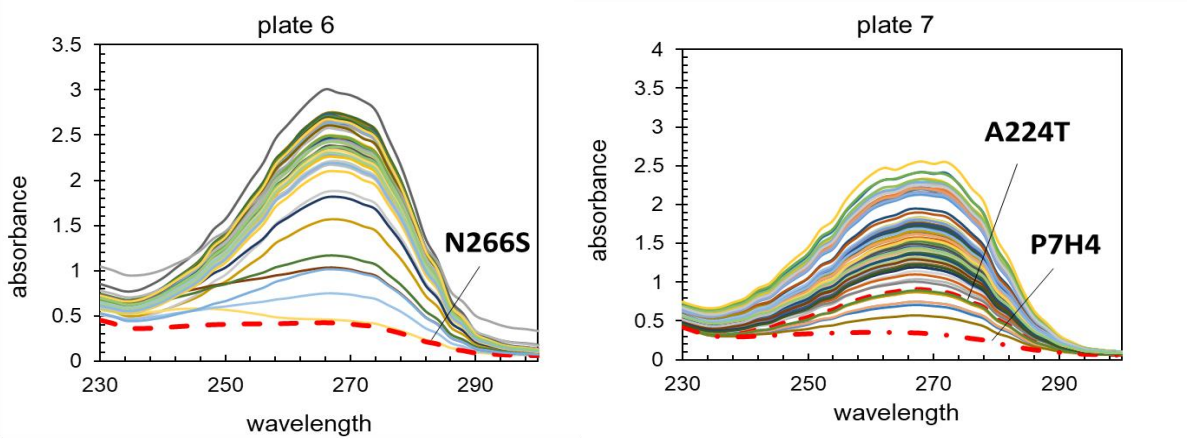

Figure 61. The UV spectrum scan of OxdYH3-3 mutants. 10 mM 2-furfuryl aldoxime was added in the plate, and after overnight, the reaction mixture was isolated and diluted. The UV absorbance between 230 and 300 nm was measured. The red dash line means the UV absorbance of selected mutants directed by arrows.

Figure 62. Alignment of protein sequences of OxdYH3-3 WT and Mutants: WT, OxdYH3-3 wild-type; N266S, OxdYH3-3 N266S; A224T, OxdYH3-3 A224T; P7-H4, OxdYH3-3 P7H4.

4.5.2. Overexpression of OxdYH3-3 mutant

The overexpression level of OxdYH3-3 wild-type (WT) and mutant proteins were analyzed on SDS-PAGE. Thick bands at 41.3 kDa were observed on an SDS-PAGE, showing approximately the same overexpression level with OxdYH3-3 WT and mutants (**Figure 63**). However, most of the proteins were overexpressed as an insoluble fraction.

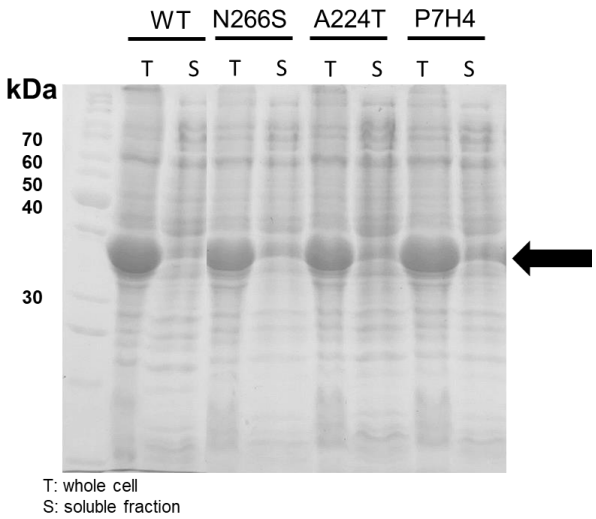

Figure 63. Expression of OxdYH3-3 WT and its mutants. Overexpressed proteins under cultivation in autoinduction medium was disrupted and separated to soluble and insoluble protein following analysis by electrophoresis. The first lane was protein size marker corresponding the number on left side. The size of OxdYH3-3 WT and mutants were approximately 41.3 kDa (arrow): T, total protein; S, soluble protein.

4.5.3. The improved catalytic activity of OxdYH3-3 mutants

OxdYH3-3 WT displayed 75% and 88% conversions from 10 mM 2-furfuryl aldoxime and *E*-pyridine -3-aldoxime to 2-furonitrile and 3-cyanopyridine in 3 h in the previous section (section 4.4.3). The concentrations of 2-furfuryl aldoxime and *E*-pyridine-3-aldoxime were increased up to 100 mM which is 10 times higher concentrations compared to the previous experiment, and the conversion was measured again with OxdYH3-3 WT and mutants. The OxdYH3-3 cells were prepared by the cultivation of the OxdYH3-3 WT and mutant transformants in TB medium at 37 °C overnight, following re-cultivation in the modified autoinduction medium at 30 °C for 18 h with shaking. The collected cell pellet was resuspended in 5 mL phosphate buffer (pH 7.0, 50 mM) and kept at 4 °C.

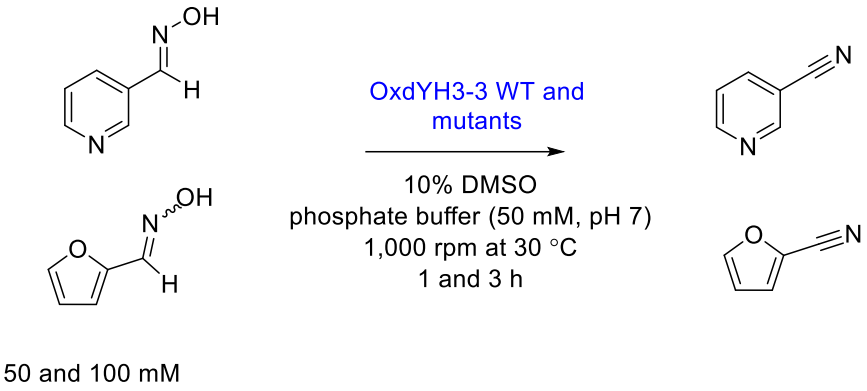

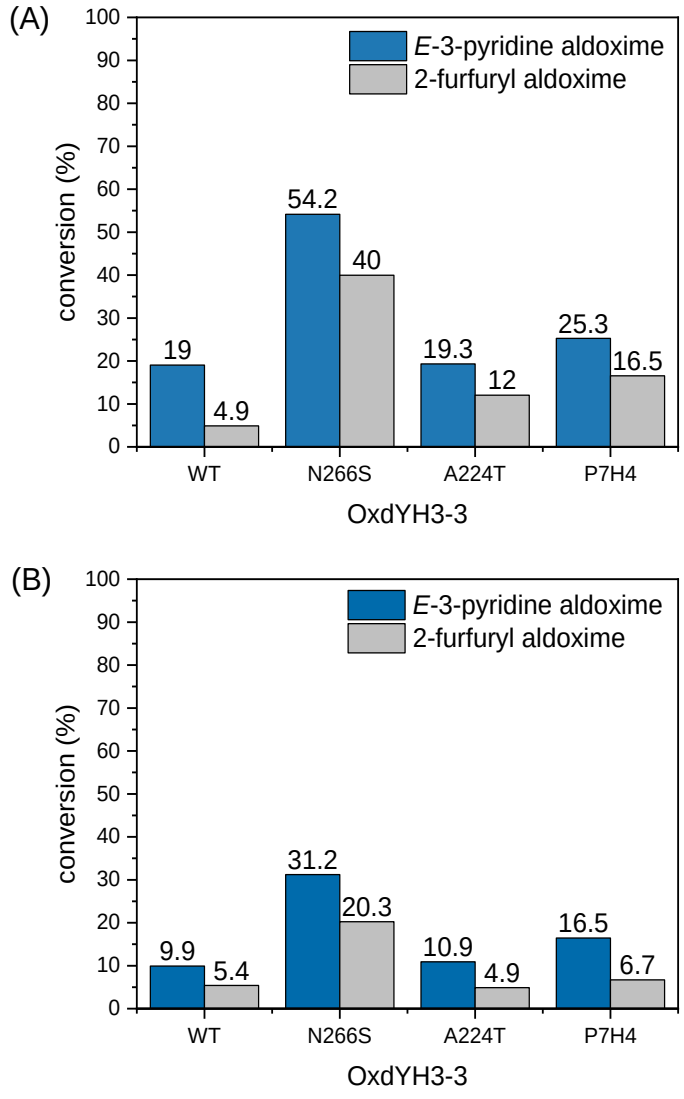

Figure 64. The conversion of OxdYH3-3 WT and mutants. The conversion in 1 h toward *E*-pyridine-3-aldoxime and 2-furfuryl aldoxime were compared. The conversion was measured for 50 mM aldoximes (A) and 100 mM aldoximes (B).

Among the resuspension, 900 µL of the solution was taken and mixed with 100 µL *E*-pyridine-3-aldoxime and 2-furfuryl aldoxime stock solution (0.5 and 1 M in DMSO). The mixtures were incubated in a shaker at 30 °C with 1,000 rpm for 1 h, and the 100 µL reaction mixture was taken to measure GC. The substrate preference of OxdYH3-3 toward *E*-pyridine-3-aldoxime was evident when the conversions using OxdYH3-3 WT and mutants were compared. The activities toward 50 mM *E*-pyridine-3-aldoxime at 1 h were relatively higher than that toward 2-furfuryl aldoxime in OxdYH3-3 WT and mutants (**Figure 64**). Also, OxdYH3-3 WT and mutants showed approximately 1.5 times higher activity ($U \cdot g^{-1}$) toward 100 mM *E*-pyridine-3- aldoxime compared to 2-furfuryl aldoxime (**Table 17**).

The conversions using 50 mM aldoximes were relatively lower compared to the conversions using 10 mM substrates by OxdYH3-3 WT which was almost 80% of conversion in 3 h. The conversions of 50 mM aldoximes by OxdYH3-3 WT exhibited a dramatic decrease, showing 19% of conversion for *E*-pyridine-3-aldoxime and 5% of conversion for 2-furfuryl aldoxime (**Figure 64**A). In contrast to OxdYH3-3 WT, OxdYH3-3 N266S presented maximum 3 times (54.2%) and 9 times (40%) higher conversion for 50 mM *E*-3-pyridine and 2-furfuryl aldoxime in 1 h, respectively (**Figure 64**A). OxdYH3-3 A224T and P7H4 exhibited 3 (12%) and 4 (16.5%) times improved conversion toward 2-

Table 17. The activity of OxdYH3-3 WT and mutants. The activities in 1 h toward 50 mM and 100 mM *E*-pyridine aldoxime and 2-furfuryl aldoxime were compared.

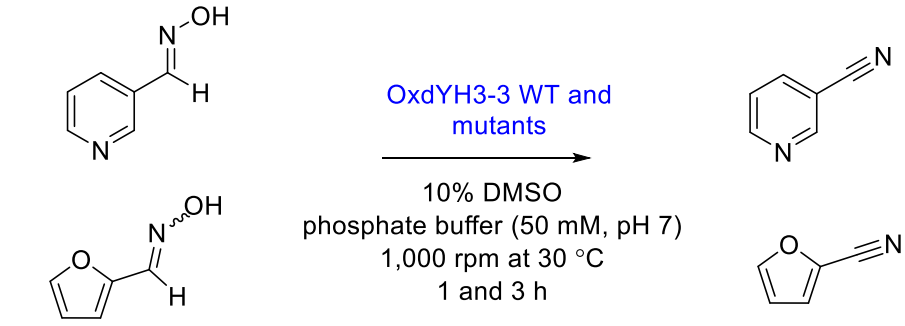

OxdYH3-3	$U \cdot g^{-1}$ (µmol·min^{-1}·g^{-1})			
	E-pyridine-3-aldoxime		2-furfuryl aldoxime	
	50 mM	100 mM	50 mM	100 mM
WT	0.6	0.5	0.2	0.3
N266S	**1.9**	**1.7**	**1.2**	**1.2**
A224T	0.7	0.5	0.4	0.3
P7H4	0.8	0.8	0.5	0.4

furfuryl aldoxime than that of WT; however, those mutants displayed almost the same range of yields (19.3 and 25.3% for A224T and P7H4, respectively) toward *E*-pyridine-3-aldoxime compared with WT. In terms of activity, OxdYH3-3 N266S had 3 times higher activity (1.73 $U \cdot g^{-1}$) toward 100 mM *E*-pyridine-3-aldoxime than that of OxdYH3-3 WT in 1 h (**Table 17**). In addition, OxdYH3-3 N266S showed an excellent activity and conversion for 100 mM 2-furfuryl aldoxime, which was 4 times (1.16 $U \cdot g^{-1}$) higher than OxdYH3-3 WT. On the other hand, OxdYH3-3 A224T and P7H4 displayed a slightly

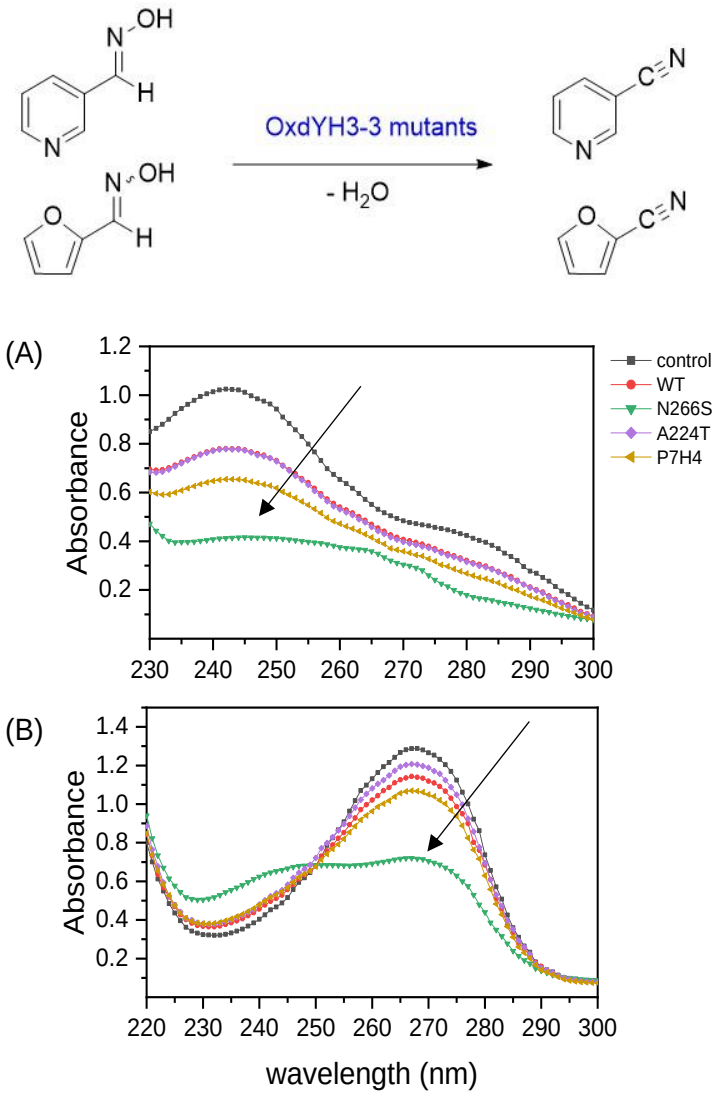

Figure 65. Absorbance scans of the reaction solution at 1 h. The reaction was done with 50 mM *E*-3-pyridine aldoxime (A) and 2-furfruyl aldoxime (B). The reaction solution was diluted with phosphate buffer up to 100 times to measure UV-scan. The arrows indicate a decrease in absorbance at 245 and 270 by OxdYH3-3 N266S, which are corresponding to decrease in *E*-pyridine-3-aldoxime and 2-furfuryl aldoxime, respectively.

higher activity or similar activity toward 100 mM 2-furfuryl aldoxime compared to WT towards 100 mM aldoximes (**Table 17**).

E-Pyridine-3-aldoxime and 2-furfuryl aldoxime were incubated with OxdYH3-3 to verify that the decrease in UV is corresponding to a decrease in aldoxime concentration measured by GC. In an earlier study (section 4.5.1), the decrease in UV at 245 and 270 nm corresponded to a decrease in *E*-3-pyridine aldoxime and 2-furfuryl aldoxime, respectively. OxdYH3-3 N266S showed a significant decrease in absorbance at 245 (**Figure 65**A) and 270 nm (**Figure 65**B) compared to OxdYH3-3 WT and other mutants, indicating higher catalytic abilities for nitrile synthesis and reflecting improved conversion (%) measured by GC. So far, the isolation of aldoxime-utilizing bacterial strains or biocatalysts has relied on medium enrichment[139–141,164,165] following measurement of activities by HPLC or TLC. Therefore, UV spectra scan is suggested as a simple alternative way to screen new biocatalysts and mutants toward various aldoximes.

4.5.4. Homology modelling of OxdYH3-3 WT and N266S

The improved catalytic activity of OxdYH3-3 N266S as a representative mutant model, which has the most enhanced activity, was explained along with analysis of homology modelling. The homology structures of OxdYH3-3 WT and N266S were constructed based on OxdRE crystal structure (PDB No. 3A17_A), co-crystallized with heme and butyl aldoxime[153], and the constructed homology structure was incorporated with *E*-2-furfuryl aldoxime (**Figure 66**). The docking result was reasonable, showing nitrogen of N-OH in 2-*E*-furfuryl aldoxime was facing to Fe in the heme group (2.7 Å; **Figure 66**), which corresponded to previous mechanism studies explained in section 4.1.2. Histidine at 320 (His320) and Serine at 219 (Ser219) in OxdYH3-3 WT and N266S formed hydrogen bonds with N-OH of *E*-2-furfuryl aldoxime (**Figure 66** and **Figure 67**). However, the distance of the hydrogen bonds of *E*-2-furfuryl aldoxime with His320 and Ser219 did not show a significant difference between OCR-WT and N266S. Nonetheless, network analysis between residues using Ring2 and Cytoscape [166,167] suggested that the mutation at asparagine 266 (Asn266) changed the interaction of residues at the distal and proximal binding pocket (**Figure 68**). The residue-network analysis suggested that the long-range interaction of residues could change structure flexibility and subsequently substrate specificity. The previous study with P450, which is one of the heme-containing enzymes, supported this result by showing the mutated sites far from active pocket could improve the metabolism of the biocatalyst due to the long-range interaction through interaction between residues[168,169]. Further study regarding molecular dynamics will be considered in future.

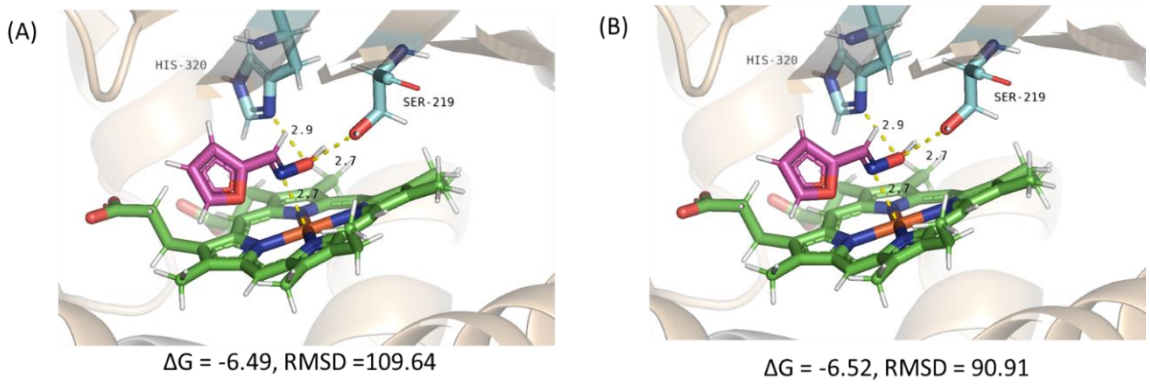

Figure 66. Homology modelling of OxdYH3-3 WT (A) and N266S (B). The model structured was combined with *E*-2-furfruyl aldoxime by docking. His320 and Ser219 form hydrogen bonds with ligand in the pictures. Heme, *E*-2-furfruyl aldoxime, and residues are shown as sticks colored green, purple, and sky blue, respectively. The dashed lines showed distance between the atoms in a range of 2-3 Å. O atom of hydroxylamine in ligand is forming possible hydrogen bond with Ser219 and His320 residues, and it is shown as dashed line between atoms. The free binding energy (ΔG) and RMSD value of each model models were calculated by autodock4.

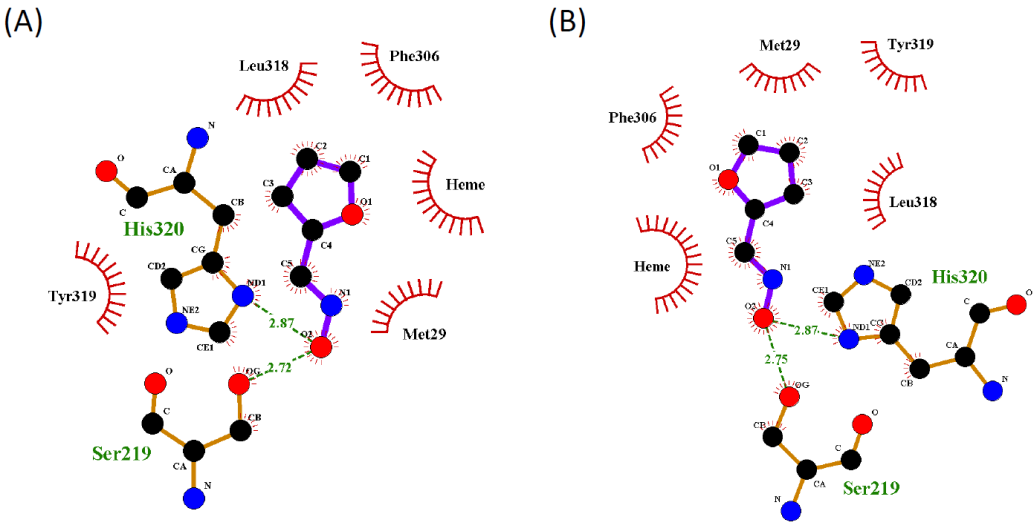

Figure 67. Diagram of interactions between OxdYH3-3 WT (A) and N266S (B) to *E*-2-furfuryl aldoxime. The purple and yellow lines showed ligand and non-ligand bond, respectively. The green dashed line indicates hydrogen bonds and their length. Protein residues involving hydrophobic contacts were shown as red half circle with spikes.

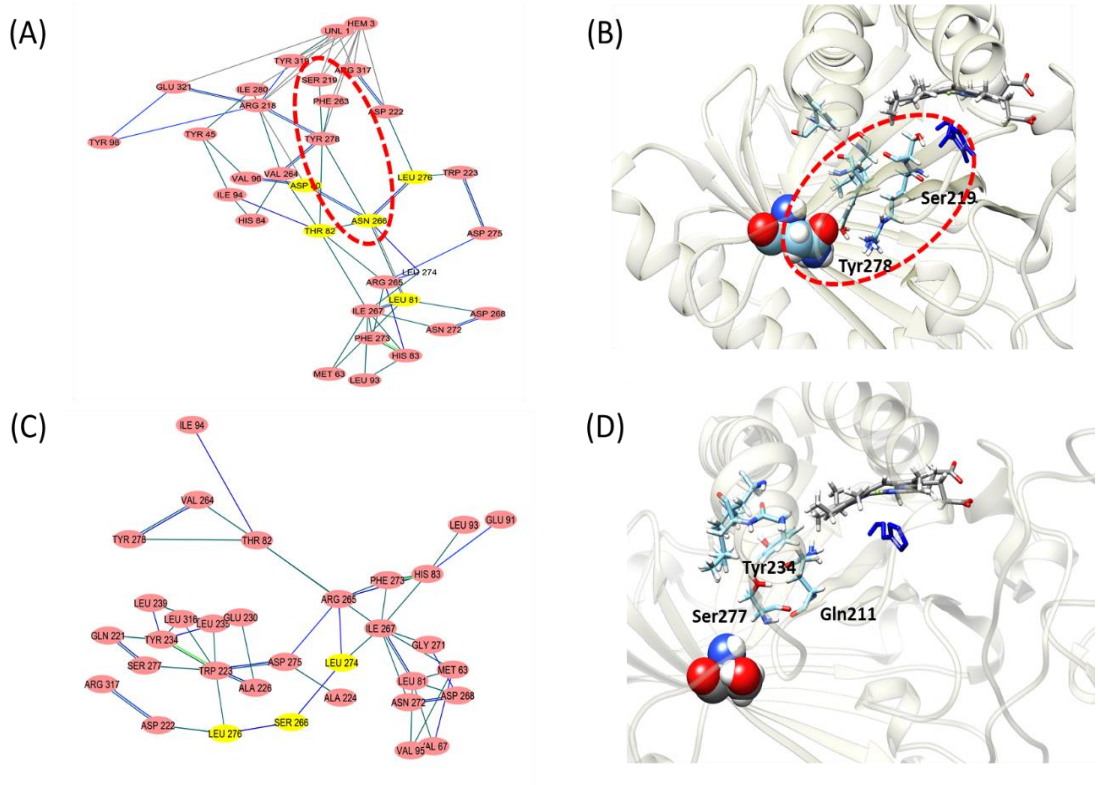

Figure 68. Residue interaction networks (RINs) of OxdYH3-3 WT ((A) and (B)) and mutated residue Asn266Ser of N266S ((C) and (D)). Pink nobs are interacted residues with Asn266 and Asn266Ser, and yellow nobs are the residues directed interacted to them. Asn266 in OxdYH3-3 WT interacts with Asp60, Thr82, Leu276, and Leu81 through hydrogen bond, and Tyr278 through Van der Waals interaction which forming interaction with Ser219 (A), and it was visualized as 3D structure (B). ball structure shows Ans266, and sticks are networking residues with Asn266 within 5 Å of ligand. The blue stick is *E*-2-furfruyl aldoxime. On the other hands, Ans266Ser in OxdYH3-3 N266S shows only two hydrogen bond interactions with Leu276 and Leu 274 (C), suggesting interaction with residues in binding pocket was changed (D).

4.6. Summary and outlook

Seven aldoxime dehydratases have been found by Asano group[139,140,143,148,155], and recently new aldoxime dehydratase has been reported by Rädisch in 2018[161]. In 2016, the genome sequences of aldoxime dehydratase OxdYH3-3, reported to convert aromatic aldoximes to corresponding nitriles, was finally entirely known. These Oxd enzymes have a great advantage in synthesis of nitrile from aldoxime compounds in mild condition without using highly toxic cyanide derivatives[119]. Nitrile compounds have a wide range of application in the chemical and pharmaceutical industry which is

represented by nitrile rubber and antidiabetic drugs[120,163]. Especially, 2-furonitrile, which can be derived from cellulose biomass, is utilized for fine chemicals, pharmaceuticals, and as a potential sweetener[118,127–129]. The purpose of this study was the construction of recombinant OxdYH3-3 to synthesize 2-furfuryl nitrile and provide it improved activity.

We studied the feasibility of over-production of recombinant OxdYH3-3 in *E. coli*. In this study, we showed that the best condition for the overexpression was BL21(DE3)/pET28b-*OxdYH3-3*, which has a C-terminus 6xhistidine tag. On the contrary, BL21(DE3)/pET22b-*OxdYH3-3* which has N-terminus 6xhistidine tag did not show activity under the same expression and reaction condition. Furthermore, the SDS-PAGE results showed that BL21Codonplus(DE3) was not a good host strain for overexpression (**Figure 55** and **Figure 56**). The activity toward *E*-pyridine-3-aldoxime using the whole cell in various expression conditions demonstrated that only well-overexpressed Oxd under an optimal overexpression condition could show reasonable catalytic activity. BL21(DE3)/pET28b-*OxdYH3-3* showed an excellent activity toward 10 mM *E*-2-furfuryl aldoxime, showing full conversion in 9 h (**Figure 58**). In this study, we only used 10 mM 2-furfuryl aldoxime for biotransformation, which gives a possibility to increase the substrate loading for further experiments. In this aspect, OxdYH3-3 mutant library was constructed by random mutagenesis to improve catalytic activity. The screening method was simplified by observing a decrease in UV absorbance at 270 nm, which is the maximum wavelength of 2-furfuryl aldoxime. Approximately 1,000 mutant clones were screened; consequently, three different clones showing significantly lower absorbance at 270 nm were chosen. Among the three mutants, OxdYH3-3 N266S showed remarkable activity compared to OxdYH3-3 WT. The OxdYH3-3 N266S showed up to 55% conversion in 1 h with 50 mM 2-furfuryl aldoxime, while the OxdYH3-3 WT only showed 15% conversion (**Figure 64**). Moreover, toward 100 mM aldoximes, OxdYH3-3 N266S showed up to 3 and 4 times higher conversion for *E*-3-pyridine and 2-furfuryl aldoxime in 1 h, respectively, compared to OxdYH3-3 WT (**Figure 64** and **Table 17**). The above results show that the OxdYH3-3 biocatalyst may have favorable applications for the production of nitrile ingredients in pharmaceutical and food industries. Furthermore, the engineered biocatalyst OxdYH3-3 could be utilized for the bioconversion of aromatic aldoximes, which is known to be non-reactive for other types of Oxd.

The observation of absorbance change at 245 and 270 nm for *E*-pyridine-3-aldoxime and 2-furfuryl aldoxime showed that the highly active OxdYH3-3 N266S severely lowered the absorbance, and OxdYH3-3 WT did not influence on the absorbance change (**Figure 65**). The observation strongly reveals that OxdYH3-3 N266S has enhanced catalytic ability to convert aldoximes to nitriles together with the GC results. We could suggest a more convenient way to screen aldoxime-catalyzing biocatalysts by UV-absorbance measurement. To understand how the mutated residue increases activity, homology modeling was conducted. The analysis of the interaction of amino acid residues suggested that Asn266Ser might change the interaction of adjacent and distal residues of an active pocket and consequently affect catalytic specificity (**Figure 68**).

5. Summary

Growing demand for developing novel enzymes and improving the catalytic ability of conventional enzymes in organic synthesis prompted examination of three different biocatalysts using different approaches: (1) introducing a new function to a non-functional metalloprotein, (2) enzyme engineering, and (3) combination of overexpression optimization and enzyme engineering (**Scheme S1).**

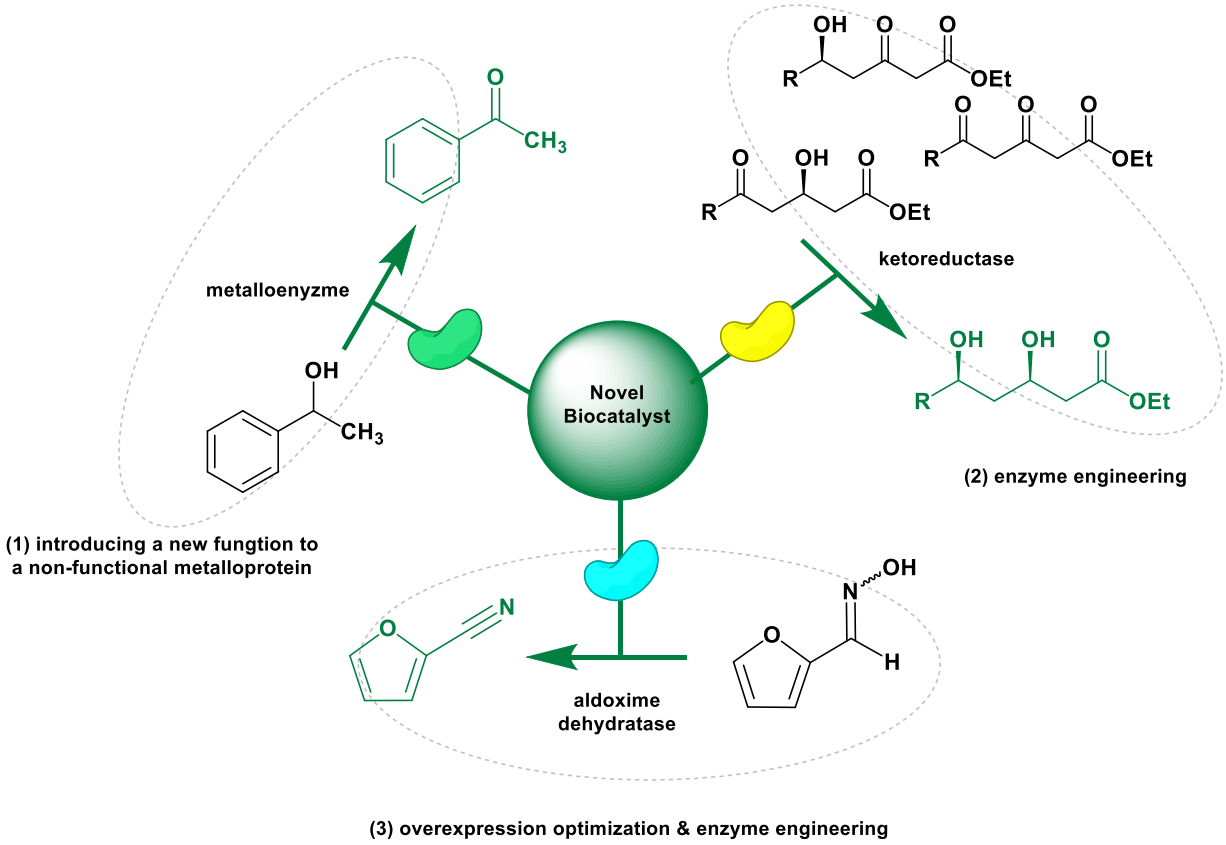

Scheme. S1. The overview of organic synthesis using the novel enzymes in this thesis.

The utilization of artificial metalloenzyme in organic synthesis have been studied for many years. Nevertheless, this study is the first approach to use non-functional metalloprotein without a metal-anchoring process. The molybdate/tungstate containing protein, MoWSto, isolated from *A. vinelandii* was subjected to building a new type of metalloenzyme. The purified MoWSto through three purification steps contained 22 ions of tungstate per protein molecule. The oxidation from 1-(*R*,*S*)-phenylethanol to acetophenone was conducted using the cell crude extract of *A. vinelandii* to prevent loss of tungstate in MoWSto during the purification. The conversion using the cell crude extract, having 0.14 mM tungstate, was 12% after 13 days continuous reaction (**Scheme** S2).

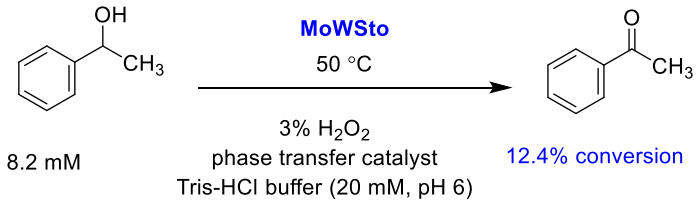

Scheme S2. MoWSto-catalyzing oxidation of 1-(*R*,*S*)-phenylethanol.

The conversion by purified MoWSto showed 3-5% in 5-6 day at 50 °C, which was lower than the conversion using tungstate salt (8%) in the presence of the same concentration of tungstate. The higher conversion (12%) by cell crude extracts implied that the cell crude extracts could compensate for the deleterious effects of harsh reaction conditions. It was presumed that the reaction condition, such as low pH due to phase transfer catalyst and the combination of high temperature with a high concentration of hydrogen peroxide, caused the destabilization of MoWSto. Besides, The catalytic activity of MoWSto was explored by comparing conserved domains with the known enzymes. MoWSto has a similarity with the reported kinase, and the kinase activity toward L-aspartic acid was observed by colorimetric assay (0.027 μmol·min^{-1}·mg^{-1}). The structural analysis using NMR suggested that phosphorylation was occurred at α-carbon of the amino acid.

Pitavastatin can significantly lower harmful low-density lipoprotein cholesterol in the body. Thereby, it can subsequently prevent atherosclerotic disease, including coronary events, stroke, and incidence of revascularization. Biocatalytic enantioselective synthesis of pitavastatin has a great advantage in terms of improving enantioselectivity and approaching the green process with fewer byproducts. A new type of carbonyl reductase originated from *Ogataea minuta* was intensively studied to improve the productivity of the pitavastatin intermediate.

Because cofactor regeneration by glucose dehydrogenase is necessary for the reaction system, the half-life of cofactor NADPH was determined as important to understanding the efficient way of using the cofactor. NADPH was quite unstable in the phosphate buffer at pH 7, showing 2 h of half-life at 50 °C. Nonetheless, 20% DMSO offset the degradation of the cofactor in phosphate buffer, extending the half-lives to 10 h at 50 °C. Based on this result, the cofactor was added in a stepwise manner in the biocatalytic synthesis of pitavastatin intermediate.

The following study aimed to improve the productivity of pitavastatin intermediate using a carbonyl reductase , OCR. The mutant library was constructed by error-prone PCR, following a screening of around 600 mutant clones. The first activity screening was done by pH-dependent colorimetric assay from blue to yellow, which narrowed the number of candidates to six. One clone named OCR-D54V, having a single mutation at Asp54 residue, was finally isolated through the second screening by activity measurement toward 5S-MOLE **16**. OCR-D54V exhibited an excellent conversion (93%) (23% MOLEs

and 70% DOLE **18**) toward 10g·L^{-1} DOXE **15,** while OCR-WT only showed a 42% conversion (27% MOLEs and 15% DOLE **18**) in the same condition (**Scheme** S3).

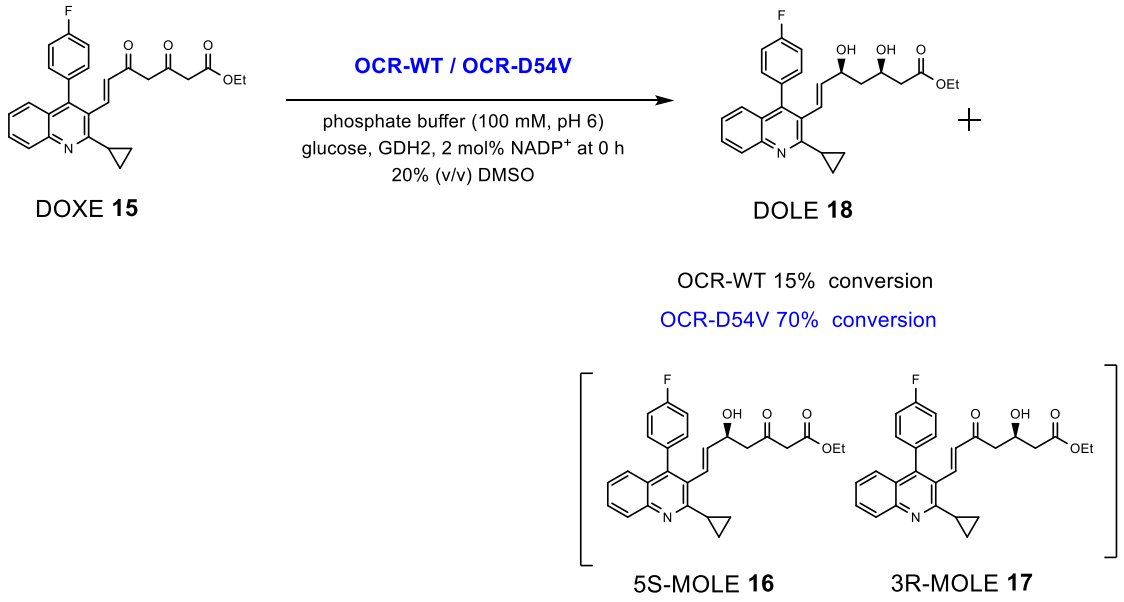

Scheme S3. The reduction of DOXE **15** to MOLEs and DOLE **18** by OCR-WT and D54V.

Moreover, OCR D54V showed an enhanced activity toward 2.6 g·L^{-1} MOLEs (90% 3R-MOLE **17),** which is a 35% higher conversion compared to OCR-WT and approximately 95% conversion to DOLE **18** (**Scheme** S4).

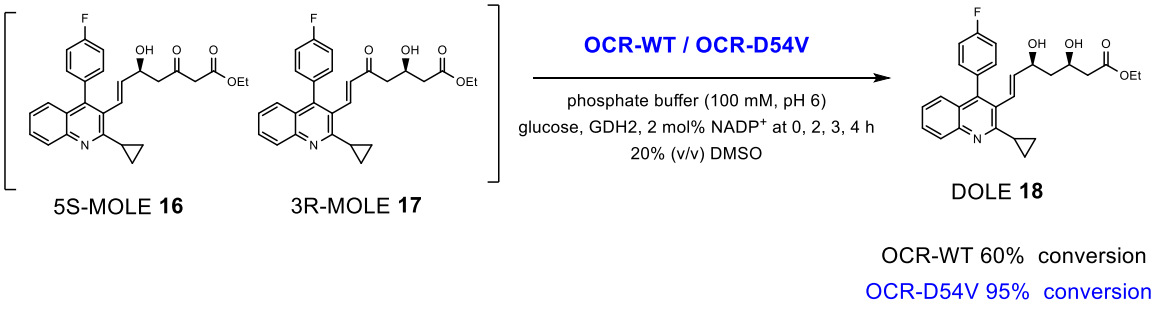

Scheme S4. The reduction of 3R-, 5S-MOLE **17** and **16** to DOLE **18** by OCR-WT and D54V.

The experiments with 10 $g \cdot L^{-1}$ of the reaction mixture containing DOXE **15**, MOLE, and DOLE **18** in the same reaction solution supported the finding that OCR-D54V could have a better specificity to MOLEs by showing a 93% conversion and 5% of residual MOLEs. Even though the conversion using OCR-D54V was over 90%, approximately 1-5% of trace compounds remained in the reaction solution. Nevertheless, the engineered enzyme showed excellent enhancement compared to OCR-WT, demonstrating OCR-D54V could be used for increased substrate concentration over 10 $g \cdot L^{-1}$. Moreover, it was shown that the reaction mixture that contains unreduced or partially reduced substances could be re-used again to save costs for pitavastatin production and reduce waste.

Since the batch reactor showed its limitation of homogeneous mixing, the segmented flow reaction was considered as an alternative way to synthesize an organic compound using OCR-WT. The conversion of 100 mM TFAP was improved from 20 to 70% according to an increase in residence time from 0.5 to 2 h as well as biocatalysts loading. Furthermore, the result showed that a cleaner product could be obtained after the segmented flow reaction due to its good phase separation, which can simplify the downstream process of drug synthesis resulting in saving production cost.

Finally, the aldoxime-utilizing enzyme was produced as a recombinant enzyme following enzyme engineering to obtain pure nitrile. There have been continuous studies to isolate novel aldoxime dehydratases from wild-type microorganisms and some yeasts since the Asano group first reported and classified aldoxime dehydratase. Since the nucleotide sequences of aldoxime dehydratase OxdYH3-3 from *Rhodococcus* sp. OxdYH3-3 were recently analyzed, OxdYH3-3 recombinant enzyme was constructed in this study for the first time. 2-Furfuryl aldoxime was chosen for further experiments because 2-furonitrile serves as an intermediate in the field of fine chemicals and pharmaceuticals. Also, 2-furonitrile is a potential sweetener due to a thirty-fold higher sweetening power compared to sucrose. OxdYH3-3 in the *E. coli* was highly overexpressed under the combination of pET28b as a vector and BL21(DE3) *E. coli* cell as a host cell. The overexpression of the protein was tightly controlled depending on types of vector and host cells. The conversion of 10 mM *E*-pyridine-3-aldoxime to the corresponding nitrile was 88% in 3 h, and the conversion of 10 mM *E*-2-furfuryl aldoxime to 2-furonitrile was 75% at the same time (**Scheme S5**). Both aldoximes were fully converted to nitriles in 9 h.

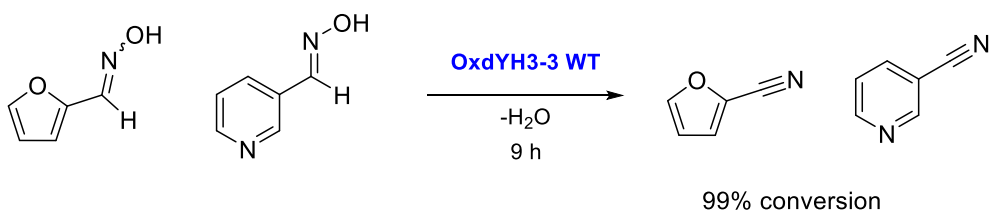

Scheme S5. The activity towards *E*-pyridine-3-aldoxime and 2-furfuryl aldoxime of OxdYH3-3.

In terms of increasing substrate loading, it is necessary to improve the enzyme's catalytic activity. The directed evolution through error-prone PCR was performed using the high throughput screening with an automatic inoculating and suspending system. Approximately 1,000 clones were screened through measurement of UV at 270 nm, which is the maximum wavelength of 2-furfuryl aldoxime; consequently, 3 clones were selected. The decrement of a UV absorbance at 270 nm corresponded to the concentration of aldoxime measured by GC, suggesting a convenient way to screen biocatalysts using aldoxime as substrate by UV-absorbance measurement. OxdYH3-3 N266S showed a remarkable activity compared to WT, displaying a maximum of six and four times higher activity toward 50 mM 2-furfuryl aldoxime and *E*-pyridine-3-aldoxime, respectively (**Scheme S6**). The residue-interaction analysis indicated that interaction change of residues within the distal active pocket could enhance the specific activity. Since aromatic aldoxime was used for only a few aldoxime dehydratases such as OxdRE, these results suggest the possibility of using various types of aromatic aldoximes as substrates in future.

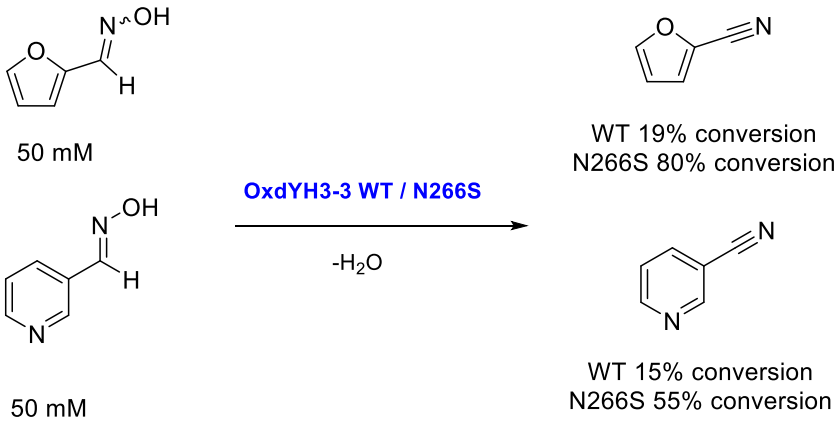

Scheme S6. The conversion (%) of *E*-pyridine-3-aldoxime and 2-furfuryl aldoxime to corresponding nitriles in 3 h by OxdYH3-3 WT and N266S.

6. Experimental section

6.1. Application of a novel metalloenzyme containing an enormous transition metal in organic synthesis

6.1.1. Preparation of wild-type metalloenzyme from *A. vinelandii*

6.1.1.1. Bacterial strain and general condition for microbial cultivation

The gram-negative bacterial strain *A. vinelandii* (DSMZ 366, ATCC 13705) was purchased from DSMZ (Deutsche Sammlung von Mikroorganismen und Zellkulturen GmbH, Braunschweig). *A. vinelandii* was firstly inoculated on 1.5% agar plate containing modified Burk's medium (**Table 18**) for 48 h at 30 °C. A single clone was inoculated into 5 mL of modified Burk's medium without metal for 5 h at 30 °C shaking incubator (150 rpm), and then the cultural solution transferred into 95 mL of fresh medium for further incubation for 13 h. The primary culture was inoculated into new 100 mL of Mo-depleted medium supplied with a mineral solution and a phosphate buffer and cultured for 22 h under general condition (30 °C in 150 rpm shaking incubator). The secondary culture with completely Mo-starved cells was inoculated into 100 mL of modified Burk's medium containing 1 mM Na_2MoO_4 or 100 µM $Na_2WO_4 \cdot 2H_2O$. The optical densities of growing cells were measured at OD_{436} with 1 mL of culture solutions by spectrophotometry at every 1-2 h. After 24 h, cell pellets were harvested and stored at -20 °C for further purification and analysis steps.

6.1.1.2. Cleaning of glassware and purification of the cultivation medium from trace Mo

Glassware such as glass flasks and bottles used for cultivation were soaked into 0.1 M nitric acid solution for 24 h and washed with distilled water for several times. The glasswares were rinsed again with 1 mM EDTA solution for 24 h and washed extensively with distilled water. In order to remove trace Mo from iron (III) citrate solution, the solution was treated with activated carbon suspension. The suspension (50 $g \cdot L^{-1}$ distilled water) was stirred for 48 h at room temperature and further stirred for 10 min at 100 °C. The suspension (200 mL) was cooled with 400 mL of Iron (III) citrate solution (38 mM, pH 2.3) and stirred again at room temperature for 16 h. The carbon-treated Iron (III) citrate solution was filtered with filter paper and syringe filter (d; 0.22 µm).

Table 18. Composition of modified Burk's medium.

Modified Burk's medium		
NL - components	Concentrations	
	g/L	mmol/L
Sucrose	20	58.4
Components of the mineral solution (added as 10-fold concentrated solution)		
$MgSO_4 \cdot 7H_2O$	0.2	0.811
$CaCl_2 \cdot 2H_2O$	0.09	0.612
NaCl	0.2	3.42
Iron (III) citrate $\cdot H_2O$	0.025	0.095
Components of the phosphate buffer (100 - fold concentrated solution)		
$KH_2PO_4 \cdot 2H_2O$	0.026	0.105
$K_2HPO_4 \cdot 3H_2O$	2.812	16.1
Other ingredients		
10 mM Na_2MoO_4	0.1 mL/L	0.01
100 mM Na_2WO_4	1 mL/L	0.1
NH_4Ac	10 mL/L	20

Mo and W-depleted medium were prepared using *A. vinelandii* to consume Mo or W in modified Burk's medium entirely. *A. vinelandii* was cultured for 20-24 h under the general condition in modified Burk medium without Mo until the optical density at 436 nm reached to 8. The culture was centrifuged at 130,000 rpm for 30 min at 4 °C. The cell pellet was resuspended in 2 mL of 50 mM 3-morpholinopropanesulfonic acid buffer (MOPS; pH 6.5). The suspension was transferred to Erlenmeyer flask containing 300 mL mixture of sucrose, iron (III) citrate and ammonia acetate, which is 1.5 times more concentrated than the concentration in **Table 18**, and cultured under general condition. After 2 h, the metal depleted medium was collected by centrifugation at 130,000 rpm and 4 °C for 30 min.

6.1.2. Preparation of recombinant MosA and MosB

6.1.2.1. Transformation of *E. coli* with MoWSto subunit MosA and MosB

The nucleotides encoding MoWSto protein subunits, MosA (GeneBank: CP001157.1; Appendix 6.4.1.) and MosB (GeneBank: CP001157.1; Appendix 6.4.2) were synthesized (Eurofins, Germany) and cloned to pET28a (**Figure 69**). The nucleotide sequences of both subunits were optimized for *E. coli*

codon usage and added restriction sequences of NcoI and XhoI to 5 and 3 ends of sequences. Also, a 6xhistidine tag was added to C- terminus. Synthesized genes in the pET28a vector were transformed into *E. coli* BL21(DE3) by heat shock at 42 °C for 45 s following spreading on Luria Bertani (LB)-agar containing 50 $\mu g \cdot L^{-1}$ ampicillin plate at 37 °C overnight. A single clone was inoculated in 200 mL of LB medium with antibiotics and cultured for 5-6 h at 37 °C in a shaking incubator until the OD_{600} was reached to 0.6. MosA and MosB were overexpressed at 18 and 30 °C, separately, for 20 h with 0.5 mM IPTG in 150 rpm shaking incubator. Cells were harvested by centrifugation at 4,000 rpm and 4 °C for 30 min and disrupted by ultrasonication. The supernatant was isolated to visualize protein expression levels of MosA and MosB. The lysate was resolved by SDS-PAGE (sodium dodecyl sulfate–polyacrylamide gel electrophoresis) and stained with Coomassie blue solution.

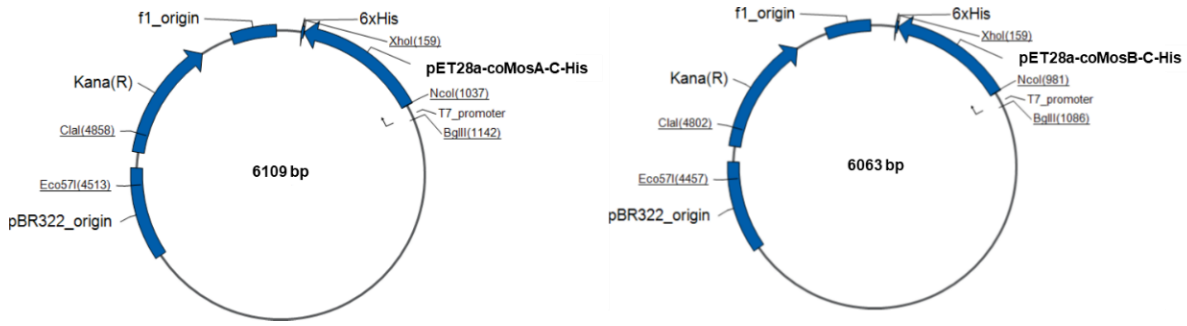

Figure 69. The plasmid map of MosA (left) and MosB (right).

6.1.2.2. Purification of wild-type MoWSto using Fast Protein Liquid Chromatography (FPLC)

A. vinelandii was grown in the modified Bulk medium for 2 days at 30 ºC and 150 rpm. Cells were isolated by centrifugation at 4,000 rpm and 4 ºC for 30 min. The harvested *A. vinelandii* cells were suspended in a MOPS buffer (pH 6.5, 50 mM) containing 1 mM adenosine triphosphate (ATP) and $MgCl_2$ and disrupted with ultrasonication. The supernatant was isolated by centrifugation at 10,000 rpm and 4 ºC for 30 min. Purification was done following a previously published method[12]. Briefly, the supernatant was filtrated using 0.25 µm syringe filter and loaded on a DEAE (diethylaminoethyl)-Sephacel anion exchange column (GE Healthcare, one column volume: 5 mL, flow rate: 0.5 $mL \cdot min^{-1}$, fraction size: 2 mL, Length of the gradient: 10 CV). The column was washed with 50 mM NaCl in a MOPS buffer (5 CV, approximately 25 mL) then was eluted with a linear NaCl gradient (50-250 mM). MoWSto was eluted at approximately 210 mM Cl. The combined MoWSto peak fractions were subjected to a 40–50% ammonium sulphate fractionation. The precipitated MoWSto was redissolved in a MOPS buffer, loaded on a Superdex 200 gel filtration column (2.5 x 60 cm, GE Healthcare,

Germany) and eluted with the same buffer (one column volume: 25 mL, flow rate: 0.5 mL·min^{-1}, fraction size: 2 mL, length of elution: 1.5 CV). The purification yield was determined by measuring protein concentration and metal concentration after each purification step (**Table 19**).

Table 19. Protein concentration and metal concentration at each purifications step.

Purification procedure	Volume [mL]	Total W [µmol]	Total protein [mg]	W/protein [µmol/g]	Ions/ MoWSto molecule
Crude extract	10	252.1	46.2	5455.8	349.2
Ammonium phosphate precipitation	2	4.3	8.4	508.1	32.4
Size exclusion	4	1.6	4.7	339.3	21.7

6.1.3. Catalytic molybdate and tungstate determination

The Mo- and W- concentrations were determined by a colorimetric method using dithiooxamide as a reagent, forming an intensive yellow oxidation product in an acidic solution in the presence of hydrogen peroxide[12]. Briefly, *A. vinelandii* crude cell extract and purified protein were harvested at 10,000 rpm and 4 °C for 15 min, and then washed with a MOPS buffer (pH 6.5, 50 mM). The cell pellet was resuspended in 1 mL of a MOPS buffer and diluted with deionized distilled water. The diluted solutions were denatured by heating at 99 °C for 15 min and were cooled to room temperature. The denatured samples were then centrifuged with a benchtop centrifuge (Eppendorf) at 13,000 rpm for 15 min and transferred to a clean microcentrifuge tube. The supernatants (130 µL) were placed in a 96-well microplate. Subsequently, 100 µL of 250 mM HCl and 10 µL of 100 mM dithiooxamide dissolved in ethanol were further added. The reaction was started by adding 10 µL of 50 mM H_2O_2 solution. The mixture was placed in a pre-heated 25 °C holder in the microphotometer, and the absorbance at 400 nm was measured after 10-20 min. To determine the Mo and W quantities, we created a calibration line of a series of 7 measurements in the molar range of 10-520 nmol MoO_4^{2-} or WO_4^{2-}. For calculation of the ratio of metal to protein concentration, the protein amounts were measured by Bradford assay.

6.1.4. Determination of melting temperature of MoWSto

The measurement of the melting temperature (Tm) was done following a previous publication[55]. All stock solutions were prepared and stored in a 96 well microplate. The buffer composition and preparation in a 96 well microplate are described in **Table 20**. The buffer solutions and salts were prepared as 5 times concentrated solution (100 mM). Afterward, 5 µL of each stock component was

added to the 96 well microplates, and then the volume was adjusted to 20 µL with distilled water. SYPRO Orange stock solution purchased from Invitrogen was diluted with water to make 62 times lower concentrated solution. Three microliters of freshly diluted SYPRO Orange solution was added to each well of the microplate. The protein concentration was approximately 1 $mg \cdot mL^{-1}$, and 2 µL of purified MoWSto was used for thermostability measurement. The final volume per well is 25 µL. A PCR plate is sealed with an optical clear lid, centrifuged (4 °C, 30 s, 2,500g) and is being analyzed on a real-time PCR machine using a temperature gradient of 1 $°C \cdot min^{-1}$ from 4 to 90 °C. The whole assay lasted approximately 2 h. The melting curves from each well have to be processed with CFX manager software (Biorad). The result is shown in **Figure 70**.

Table 20. Buffer composition and concentration for measuring the melting temperature

96-plate for Thermoflour-assay

	1	2	3	4	5	6	7	8	9	10	11	12
A	water	Citric acid pH 4.0	Citric acid pH 5.0	MES pH 5.5	Citric acid pH 6.0	KPi pH 6.0	PIPES pH 6.0	MES pH 6.5	Bis-Tris pH 6.5	MOPS pH 7.0	$NaPO_4$ pH7.0	KPi pH 7.0
B	HEPES pH 7.0	TEA pH 7.0	PIPES pH 7.0	$NaPO_4$ pH7.5	KPi pH 7.5	Tris-HCl pH 7.5	TEA pH 7.5	MOPS pH 7.9	TEA pH 8.0	Bicine pH 8.0	HEPES pH 8.0	Tris-HCl pH 8.0
C	KPi pH 8.0	Tris-HCl pH 8.5	Bicine pH 8.5	Tris-HCl pH 9.0	Bicine pH 9.0	water NaCl	Citric acid pH 4.0 NaCl	Citric acid pH 5.0 NaCl	MES pH 5.5 NaCl	Citric acid pH 6.0 NaCl	KPi pH 6.0 NaCl	PIPES pH 6.0 NaCl
D	MES pH 6.5 NaCl	Bis-Tris pH 6.5 NaCl	MOPS pH 7.0 NaCl	$NaPO_4$ pH7.0 NaCl	KPi pH 7.0 NaCl	HEPES pH 7.0 NaCl	TEA pH 7.0 NaCl	PIPES pH 7.0 NaCl	NaH_2PO_4 pH7.5 NaCl	KPi pH 7.5 NaCl	Tris-HCl pH 7.5 NaCl	TEA pH 7.5 NaCl
E	MOPS pH 7.9 NaCl	TEA pH 8.0 NaCl	Bicine pH 8.0 NaCl	HEPES pH 8.0 NaCl	Tris-HCl pH 8.0 NaCl	KPi pH 8.0 NaCl	Tris-HCl pH 8.5 NaCl	Bicine pH 8.5 NaCl	Tris-HCl pH 9.0 NaCl	Bicine pH 9.0 NaCl	custom	custom
F	50 mM Citric acid pH 6.0	100 mM Citric acid pH 6.0	200 mM Citric acid pH 6.0	300 mM Citric acid pH 6.0	10 mM KPi pH 7,0	50 mM KPi pH 7,0	100 mM KPi pH 7,0	250 mM KPi pH 7,0	500 mM KPi pH 7,0	10 mM HEPES pH 7.5	50 mM HEPES pH 7.5	100 mM HEPES pH 7.5
G	250 mM HEPES pH 7.5	10 mM $NaPO_4$ pH 7.5	50 mM $NaPO_4$ pH 7.5	100 mM $NaPO_4$ pH 7.5	200 mM $NaPO_4$ pH 7.5	10 mM Tris-HCl pH 8.0	50 mM Tris-HCl pH 8.0	100 mM Tris-HCl pH 8.0	250 mM Tris-HCl pH 8.0	50 mM Bicine pH 9.0	100 mM Bicine pH 9.0	250 mM Bicine pH 9.0
H	50 mM HEPES 50 mM NaCl pH 7.5	50 mM HEPES 125 mM NaCl pH 7.5	50 mM HEPES 250 mM NaCl pH 7.5	50 mM HEPES 500 mM NaCl pH 7.5	50 mM HEPES 750 mM NaCl pH 7.5	50 mM HEPES 1 M NaCl pH 7.5	50 mM Tris-Hcl 50 mM NaCl pH 8.0	50 mM Tris-Hcl 125 mM NaCl pH 8.0	50 mM Tris-Hcl 250 mM NaCl pH 8.0	50 mM Tris-Hcl 500 mM NaCl pH 8.0	50 mM Tris-Hcl 750 mM NaCl pH 8.0	50 mM Tris-Hcl 1 M NaCl pH 8.0

buffers were used at a concentration of 100 mM unless otherwise indicated. Sodium chloride was used at a concentration of 250 mM, unless otherwise indicated.

6.1.5. Stability of MoWSto in various concentration of H_2O_2

Thirty microliters of purified MoWSto were prepared (WO_4^{2-} 0.051 µmol, 0.6 mg) and added to 1.5 mL Effendorf microtube. The tube was filled with a 50 mM (pH 6.5) MOPS buffer up to 1 mL and incubated at 4 ºC in a thermoshaker at 500 rpm for 20 h. On the other hand, 0, 33, 166, 333, and 667 µL of 30% H_2O_2 were added to make 0, 1, 5, 10, and 20% H_2O_2 solution in Effendorf microtubes, and the buffer was added up to 1mL. After incubation, 200 µL solution was taken and added to micro-centrifuge filter (VWR international, Germany) following washing with 2 mL of a MOPS buffer. The protein solution was concentrated to 200 µL by centrifugation at 4,000-6,000 rpm, and protein and metal concentrations in the concentrated solution were measured. The result is shown in **Figure 71**. The same experiment was repeated at 4 and 50 °C. In this time, MoWSto was incubated for 20 h in the presence of 0, 1, 5, 10, and 20% H_2O_2 at the thermoshaker without mixing. The incubated solution was concentrated with a micro-centrifuge filter, and the concentrated protein was washed by 1mL of MOPS buffer once. The

metal concentrations of the wash-out solution and concentrated solution were measured. The result is shown in **Figure 72**.

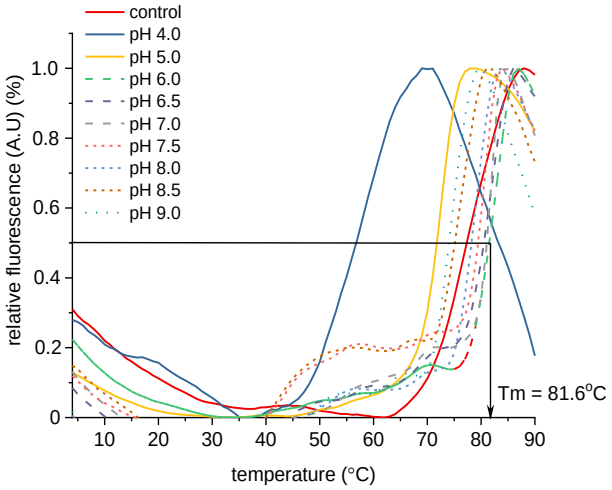

Figure 70. Melting temperature measurement of MoWSto. (A) Melt curve of MoWSto in various pH conditions. The relative fluorescence was measured by real time PCR and various pH buffer solutions were used for determination of optimal pH condition: pH 4.0, citric acid; pH 5.0, citric acid; pH 6.0, PIPES; pH 6.5, Bis-Tris; pH 7.0, PIPES; pH 7.5, TEA; pH 8.0, Tris-HCl; pH 8.5, Tris-HCl; and pH 9.0, Tris-HCl.

6.1.6. Stability of MoWSto in a reaction solution

The reaction solution after 5 h was subjected to measurement of protein concentration and W in MoWSto (the reaction condition is explained in section 6.1.8). (*R*,*S*)-1-Phenylethanol (8.2 mM) was added to MOPS buffer containing 3% H_2O_2, 0.26 mM PTC, and tungstate salt or purified MoWSto (approximately 1.43 mg·mL^{-1}) following incubation at 50 °C up to 5 days (total volume 2 mL). The 1 mM ATP and $MgCl_2$ were additionally introduced to enhance the incorporation of W to MoWSto.The reaction solution was concentrated by centrifugation at 4,000-6,000 rpm in a micro-centrifuge filter (VWR international) and washed with 3 mL of MOPS buffer containing 1 mM ATP and $MgCl_2$. The reaction solution was concentrated again until approximately 200 µL remained. The first flowthrough was collected and subjected to measurement of protein and metal concentration. The result showed the protein concentration before the reaction was 1.43 mg·mL^{-1}; however, the protein concentration after 5 days of reaction was 0.04-0.08 mg·mL^{-1} (data not shown). In the case of metal concentration, tungstate was not detectable in the concentrated solution; in contrast, approximately 208 µM W was measured in the first wash-out solution.

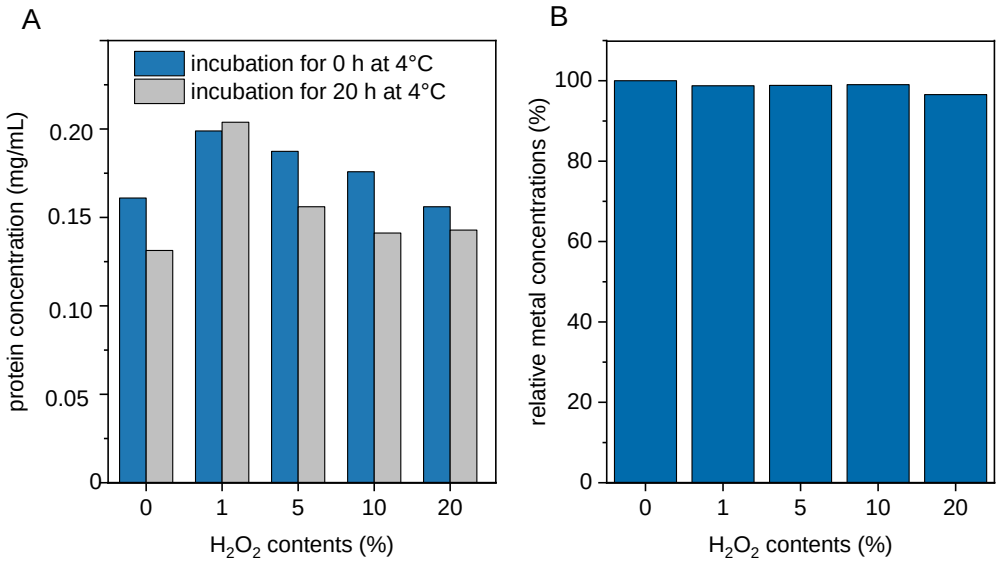

Figure 71. The protein concentration of MoWSto at 4°C for 0 and 20 h incubation in a MOPS buffer (pH 6.5, 50 mM) (A). Relative W concentrations after 20 h incubation at 4°C (B). The W concentration at 0 h was 100% and the relative ratio compared to W concentrations at 0 h was calculated.

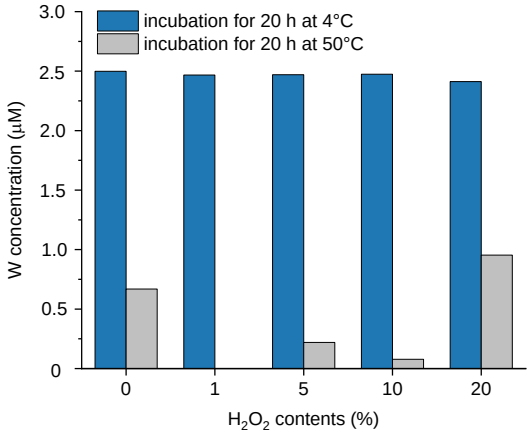

Figure 72. The metal concentration of MoWSto at 4 °C and 50 °C for 20 h incubation in a MOPS buffer (pH 6.5, 50 mM).

6.1.7. Benchmark reaction

6.1.7.1. Oxidation of cyclohexene using a W salt catalyst

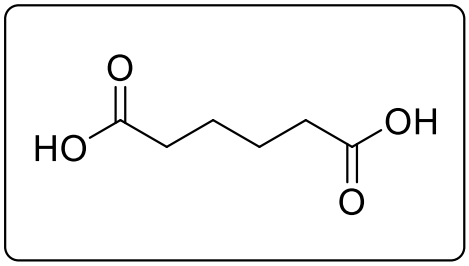

For oxidation of cyclohexene to adipic acid, a mixture of cyclohexene (5 g), 30% H_2O_2 (30.35 g), Na_2WO_4,$2H_2O$ (0.2 g), and $[CH_3(n\text{-}C_8H_{17})_3N]HSO_4$ (0.28 g; phase transfer catalyst, PTC) (cyclohexene:W:PTC molar ratio is 100:1:1) placed in a 50 mL round-bottomed flask equipped with a reflux condenser and was stirred at 1,000 rpm with a magnetic stirrer at 90 ºC for 8 h. The homogeneous solution was allowed to stand at 0 °C for 12 hours, and the resulting white precipitate was separated by filtration and washed with 20 mL of cold water. The product was dried in a vacuum as a white solid. Approximately 10 mg of adipic acid was dissolved in DMSO for ^{1}H-NMR analysis.

^{1}H NMR (500 MHz, DMSO-d_6) δ [ppm]= 2.20 (ddt, J = 7.3, 5.6, 2.0 Hz, 4H), 1.50 (h, J = 3.3 Hz, 4H).

6.1.7.2. Oxidation of (*R*,*S*)-1-phenylethanol using a W salt catalyst

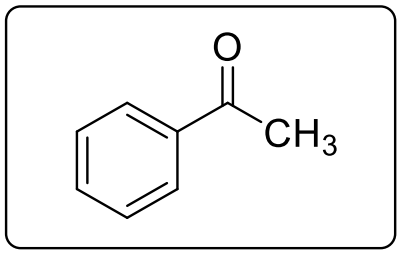

For oxidation of secondary alcohol, 8.3 g of (*R*,*S*)-1-phenylethanol (4 M) was added to a 17 mL reaction solution containing 8.7 mL of 30% H_2O_2 (84.4 mmol) , $Na_2WO_4{\cdot}2H_2O$ (0.15 mmol, 0.0507 g), and PTC (0.15 mmol, 0.0717 g) and incubated at 90 °C for 1 h. The reaction solution was cooled to room temperature, and then the organic phase was extracted by adding 30 mL of MTBE. For NMR analysis, 10 mL of solution was distilled for 2 h at 40 °C and 200-500 mbar vacuum followed by dissolving approximately 10 mg of acetophenone in chloroform for ^{1}H-NMR analysis.

^{1}H NMR (500 MHz, Chloroform-*d*) δ [ppm]= 7.97 (d, J = 202.2 Hz, 2H), 7.58 (d, J = 54.7 Hz, 1H), 7.46 (d, J = 2423.4 Hz, 2H), 2.61 (s, 3H), 1.26 – 1.13 (m, 1H).

For further analysis, the substrate amount was gradually reduced by 5 to 500 times (**Scheme 16**). The concentration of metal catalysts and PTC were decreased at the same time; thus 2.2 mM $Na_2WO_4{\cdot}2H_2O$ and 2.58 mM PTC were added to a 10 mL of reaction solution containing 3% H_2O_2(v/v) and water, and the reaction was kept up to 65 h at 90 and 50 °C. The reaction mixture was extracted by adding 10 mL of MTBE twice. The result is shown in **Table 21**. The oxidation of alcohol was measured for 65 h using 8.2 mM alcohol under the same above-mentioned condition at 50 °C. However, H_2O_2, $Na_2WO_4{\cdot}2H_2O$, and PTC were excluded, respectively, from the reaction mixture to observe the difference in the conversion. The result is shown in **Table 22**.

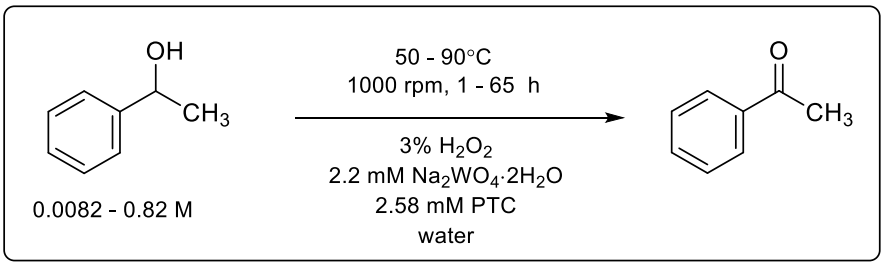

Scheme 16. Oxidation of (*R,S*)-1-phenylethanol to acetophenone with lower alcohol concentration.

Table 21. Oxidation of (*R,S*)-1-phenylethanol at 50 and 90 °C.

entry	reaction time [h]	temperature [ºC]	(*R,S*)-1-phenylethanol concentration [M]	conversion [%]
1	1	90	0.82	100
2	1	90	0.082	58.9
3	5	90	0.082	99.7
4	5	90	0.0082	100
5	65	50	0.0082	97.6

Table 22. Oxidation of (*R,S*)-1-phenyl ethanol without tungstate, phase transfer catalyst, and hydrogen peroxide.

entry	reaction condition	temperature [°C]	reaction time [h]	(*R,S*)-1-phenylethanol concentration [mM]	conversion [%]
1	Without WO_4^{2-}	50	65	8.2	3.1
2	Without PTC	50	65	8.2	26.6
3	Without H_2O_2	50	65	8.2	0

Furthermore, oxidation of alcohol was conducted in various buffer solutions at 50 °C. The reaction solution contained 2.58 mM PTC, 2.2 mM $Na_2WO_4 \cdot 2H_2O$, and 8.2 mM alcohol. In addition, water, 20 mM potassium phosphate (pH 6.0), and a 20 mM Tris-HCl buffer (pH 6.0) were added to reaction solution, respectively (**Scheme 17;** total volume 20 mL). The reaction was done at 50 °C for 26 h with stirring at 1,000 rpm. The result is shown in **Table 23**.

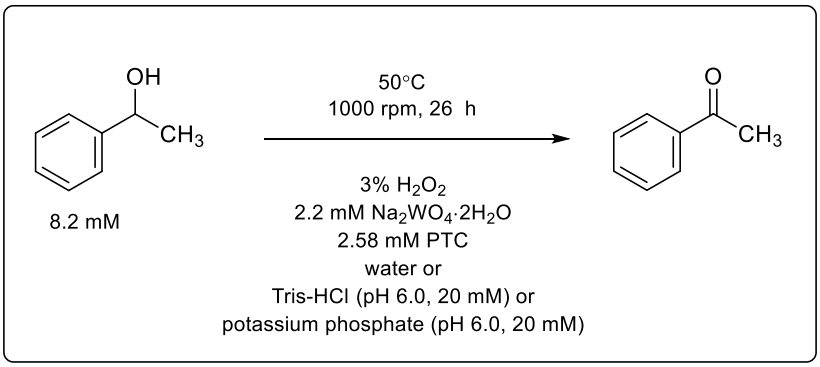

Scheme 17. Oxidation of (*R,S*)-1-phenylethanol to acetophenone in various buffer conditions.

Table 23. Oxidation of 1-phenyl ethanol in various buffer solutions.

entry	reaction temperature [°C]	reaction time [h]	(*R,S*)-1-phenylethanol concentration [mM]	Buffer	conversion [%]
1	50	26	8.2	Water	75.9
2	50	26	8.2	Tris-HCl, pH 6.0, 20 mM	73.3
3	50	26	8.2	Potassium-phosphate, pH 6.0, 20 mM	29

6.1.8. Oxidation of (*R,S*)-1-phenylalcohol to acetophenone with cell extracts of *A. vinelandii* wild-type and purified MoWSto

(*R,S*)-1-Phenylethanol (8.2 mM) was added to 20 mL of Tris-HCl buffer (pH 6.0, 20 mM) containing 3% H_2O_2, 1.9 mM $Na_2WO_4 \cdot 2H_2O$, and 2.58 mM PTC and incubated at 50 °C up to 13 days (**Scheme 18a**). After 2, 6, and 13 days, 1 mL of the reaction solutions were isolated and extracted by adding 1.5 times high volume of ethyl acetate once. The concentration of (*R,S*)-1-phenylethanol and acetophenone were quantitatively analyzed by gas chromatography. For the following research using *A. vinelandii* cell crude extract, 18 mL of cell crude extract in a Tris-HCl buffer were added into the reaction solution consisting of 8.2 mM alcohol, 3% H_2O_2 and 2.58 mM PTC (20 mL). The measured tungstate concentration of the cell crude extract was 0.14 mM. The reaction was performed for 5 days at 50 °C (**Scheme 18b**).

The same concentration of tungstate salt and tungstate ion in purified MoWSto (0.14 mM) was prepared, which was the maximum concentration we could use for one reaction. The PTC concentration was subsequently lower to 0.26 mM, while H_2O_2 concentration was kept at 3% (v/v). (*R,S*)-1-Phenylethanol (8.2 mM) was added to MOPS buffer containing 3% H_2O_2, 0.26 mM PTC, and tungstate salt or purified

MoWSto (approximately 4 mg·mL^{-1}) following incubation at 50 °C up to 5 days (total volume 2 mL) (**Scheme 19**). The 1 mM ATP and $MgCl_2$ were additionally introduced to enhance the incorporation of W to MoWSto. The conversion was analyzed by GC. The cell crude extract of *A. vinelandii* without W was added to the reaction solution separately to observe the background reaction caused by the non-specific protein. This result is shown in **Table 24**.

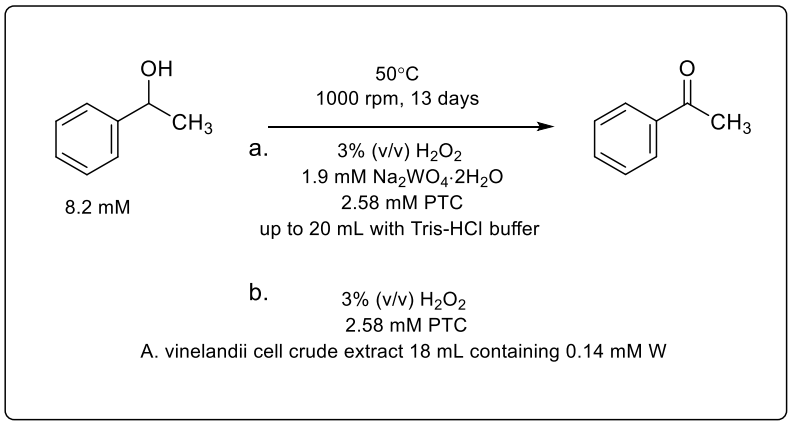

Scheme 18. Oxidation of (*R*,*S*)-1-phenylethanol to acetophenone in the presence of biocatalyst.

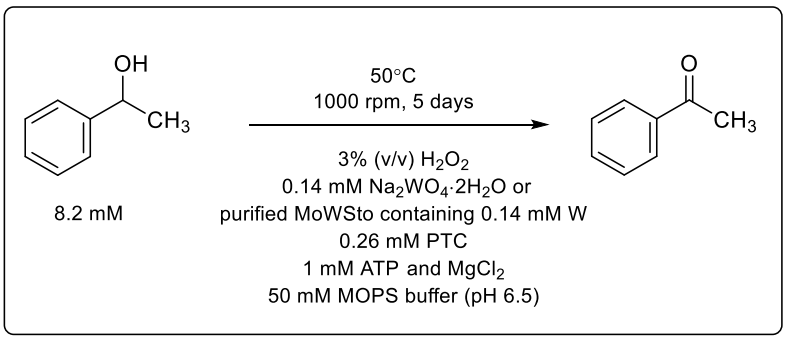

Scheme 19. Oxidation of (*R*,*S*)-1-phenylethanol to acetophenone in presence of MoWSto.

Table 24. Oxidation of phenylethanol in buffer solutions using W salt and MoWSto catalyst.

entry	reaction time[d]	buffer	Types of metal catalyst	conversion[%]
1	2	20 mM Tris-HCl, pH 6		94.5
2	6	20 mM Tris-HCl, pH 6	WO_4^{2-} salt ,1.9 mM	98.8
3	13	20 mM Tris-HCl, pH 6		96.6
4	5	50 mM MOPS, pH 6.5	WO_4^{2-} salt, 0.14 mM	7.7
5	2	20 mM Tris-HCl, pH 6	Crude extract of	4.8
6	6	20 mM Tris-HCl, pH 6	MoWSto containing W,	5.4
7	13	20 mM Tris-HCl, pH 6	0.14 mM	12.4
8	5	50 mM MOPS, pH 6.5	Purified MoWsto, 0.14 mM	2.9
9	6	50 mM MOPS, pH 6.5	Crude extract without W	n.d.

6.1.9. GC (Gas chromatography) analysis

GC analysis was performed on a Shimadzu GC 2010 plus equipped with Chiral Cyclodex B column (Agilent). GC parameters were as follows: the GC oven was kept at 100 °C for 10 min before rising to 150 °C by a linear gradient of 10 °C·min^{-1}. The temperature was kept at 200 °C for 4 min resulting in a 20 min total run time.

Retention time: (*R*,*S*)-1-phenylethanol; 15.9 and 16.2 min; acetophenone, 11.5 min

6.1.10. Analysis of protein homology

Amino acid sequences of MosA (GenBank: ACO80441.1) and MosB (GenBank: ACO80442.1) were previously reported in GeneBank. We analyzed the similarity of each sequence with previously reported protein sequences by BLAST (https://blast.ncbi.nlm.nih.gov/Blast.cgi). Sequence alignment was done by ClustalW program (http://www.ebi.ac.uk/Tools/msa/clustalw2/).

6.1.11. Determination of aspartate kinase activity

MoWSto was purified by the condition mentioned section 6.1.2.2. Kinase activity was measured by quantification of aspartate hydroxamate formed in the presence of hydroxylamine at 540 nm[64]. Five microliters of MoWSto were added to reaction solution containing a Tris-HCl buffer (pH 8.0; 200 mM), $MgSO_4 \cdot 6H_2O$ (10 mM), L-aspartate (10 mM), ATP (10 mM), and $NH_2OH \cdot HCl$ (neutralized with KOH; 160 mM). The reaction solution was incubated at 30 °C for 30 min, and the reaction was stopped by mixing with 1 mL of 5% (wt/vol) $FeCl_3$ solution. The extinction coefficient of aspartate hydroxamate was 6,000 $M^{-1} \cdot cm^{-1}$. One unit of enzyme activity is defined as the formation of 1 μmol of aspartate hydroxamate per minute under assay conditions.

6.1.12. Analysis of product from phosphorylation with MoWSto by Nuclear Magnetic Resonance (NMR)

The NMR spectra were measured by Bruker Advance 600 spectrophotometer. ^{1}H- and ^{13}C-NMR spectra of the reaction mixture after kinase activity measurement in section 6.1.11 were determined. The mixtures were added in capillaries following measurement. First, ^{1}H-NMR spectra of 10 mg of aspartate in D_2O and L-aspartate-β-hydroxamate in D_2O were analyzed. In addition, the reaction solution without hydroxylamine and enzyme was prepared and mixed with L-aspartate-β-hydroxamate for comparison. The reaction mixture after biocatalytic phosphorylation was mixed with 10% D_2O for NMR analysis, and L-aspartate-β-hydroxamate was added to this 10% D_2O-reaction mixture, following measurement

of ^{1}H-NMR. 2D ^{13}C- ^{1}H correlation spectra of the reaction mixture after biocatalytic phosphorylation containing 10% D_2O was measured. Later, L-aspartate-β-hydroxamate was added to the same reaction mixture and 2D ^{13}C- ^{1}H correlation spectra was measured. The measurements were processed with MestReNova (Mestrelab Research S.L.).

^{1}H NMR (600 MHz, D_2O, 10% D_2O in water) L-aspartate: δ [ppm]= 3.68 (dd, *J* = 7.0, 4.4 Hz, 1H), 2.64 (dd, *J* = 18.0, 4.4 Hz, 1H), 2.58 (dd, *J* = 18.0, 7.1 Hz, 1H); L-aspartate-β-hydroxamate(D_2O): 3.89 (dd, *J* = 7.7, 4.5 Hz, 1H), 2.68 (dd, *J* = 16.3, 4.5 Hz, 1H), 2.57 (dd, *J* = 16.3, 7.7 Hz, 1H); L-aspartate-β-hydroxamate (10% D_2O in reaction solution without hydroxylamine and MoWSto): δ [ppm]= 3.89 (dd, *J* = 7.9, 4.7 Hz, 1H), 2.69 (dd, *J* = 15.8, 4.6 Hz, 1H), 2.56 (dd, *J* = 15.7, 7.9 Hz, 1H); the reaction mixture containing 10% D_2O;δ [ppm]= 3.75 (t, *J* = 6.0 Hz, 1H), 2.72 – 2.65 (m, 1H), 2.61 – 2.53 (m, 1H); the reaction mixture containing L-aspartate-β-hydroxamate and 10% D_2O: δ [ppm]= 3.81 – 3.71 (m, 1H), 3.58 (s, 1H), 2.87 – 2.76 (m, 1H), 2.75 – 2.66 (m, 1H).

6.2. Process Development of a Biocatalytic Reduction of a Pitavastatin Key Intermediate

6.2.1. Materials

Nicotinamide adenine dinucleotide phosphate (NADPH) and 2,2,2-trifluoroacetophenone (TFAP) were purchased from Sigma. The carbonyl reductase OCR from *Ogataea minuta* was provided from API Corporation (Japan). OCR was cloned to customized plasmid pKV32 containing pMB1 origin, tcr promotor and kanamycin resistance gene[170].

6.2.2. General condition for analysis

6.2.2.1. General GC analysis

Quantitative gas chromatographic analysis was performed on a GC-2010 Plus (Shimadzu, Japan) equipped with a flame ionisation detector (FID). TFAP and α-(trifluoromethyl)benzyl alcohol were separated on a BGB- 174 column (BGB Analytik, Switzerland). The temperature was raised to 70 ºC with 5 mL·min^{-1} using nitrogen gas as a carrier gas from 0 to 5 min, and the temperature was held for 20 min following 20 mL·min^{-1} to 200 ºC. The retention time was 5.5 min for TFAP **20** and 24-25 min for (*R*) and (*S*)- α-(trifluoromethyl)benzyl alcohol **21**.

6.2.2.2. General HPLC analysis

Reaction solution after bioconversion was extracted by ethyl acetate, and the organic solvent was evaporated by a rotary evaporator (BUCHI, Germany). Concentrated compounds were diluted with 100%

acetonitrile or ethyl acetate to adjust concentration to 1 mg·L^{-1} and added to a clear HPLC vial for HPLC analysis. HPLC analysis was performed using CAPCELL PAK C18 MG S-3 (3 µm, 4.6x75 mm, Shiseido). The aqueous solution was prepared by mixing water: acetic acid: ammonium acetate with 650:65:5 ratio. For the preparation of mobile phase A, the aqueous solution was mixed with THF with 59:41 ratio. Mobile phase B consisted of the 10% aqueous solution and 90% THF. Mobile phase A flowed for 20 min, and after 20 min it was switched to mobile phase B for 10 min. DOLE **18**, MOLEs and DOXE **15** were analyzed for 30 min at 40 °C, 254 nm. Later, the analytical time was reduced to 15 min only with mobile phase A. The changed analytic condition did not change retention times.

Retention times: DOXE 15; 13.4 min, 5S-MOLE 16; 5 min, 3R-MOLE 17; 5.6 min, DOLE 18; 4.3-4.6 min, Lactone 19; 3.2 min.

6.2.3. Kinetics of decomposition of NADPH

To study the stability of NADPH in various conditions, we monitored the absorbance change at 340 nm using a spectrophotometer (Tecan). NADPH solutions (50 and 500 µM) were prepared in 10 mL of water and various buffer solutions. Buffer solutions were consisted of; (1) distilled water, (2) 100 mM potassium phosphate (KPi) buffer at pH 7, (3) 20% (v/v) DMSO in water, (4) 100 mM KPi buffer (pH 7) containing 20% DMSO, (5) 100 mM KPi buffer (pH 7) containing 20% DMSO and 50 mM glucose. The water and buffer solutions were pre-warmed at 25, 40, and 50 °C for 10 min in advance. NADPH was added right before the start of incubation. NADPH solution was incubated at 25, 40, and 50 °C up to 20 h, and aliquots (200 µL) were withdrawn periodically. The disappearance of NADPH was determined spectrophotometrically at 340 nm. Decrease of absorbance followed first-order kinetics (1)[97], therefore rate constant (min^{-1}; k) was obtained by calculating the slope (-*kt*/2.303).

$$\log(A_t) = \log(A_0) - kt/2.303 \quad (1)$$

A is the absorbance at 340 nm either at time zero, (A_0), or at time t, (A_t). A plot of log (A) *vs* time was linear, the slope being equal to -kt/2.303.

6.2.4. Stepwise cofactor addition in biocatalytic synthesis of α-(trifluoromethyl)benzyl alcohol

a hundred millimolar phosphate buffer (pH 7.0) containing 1 U OCR-WT (see section 6.2.3.1. for the preparation of biocatalysts), 1 U GDH2, 50 mM glucose was mixed with 100 mM TFAP stock solution in DMSO (10% (v/v)). The reaction was started by adding 0.4 mM and 0.8 mM $NADP^+$ to the reaction solution, which are corresponding to two- and four-times higher concentration of K_m value of NADPH, respectively (see section 6.2.8.3). The reaction mixture was incubated at 40 ºC in shaking incubator with 800 rpm following isolation of reaction mixture at 1 and 4 h for determination of a conversion by GC (**Scheme 20**).

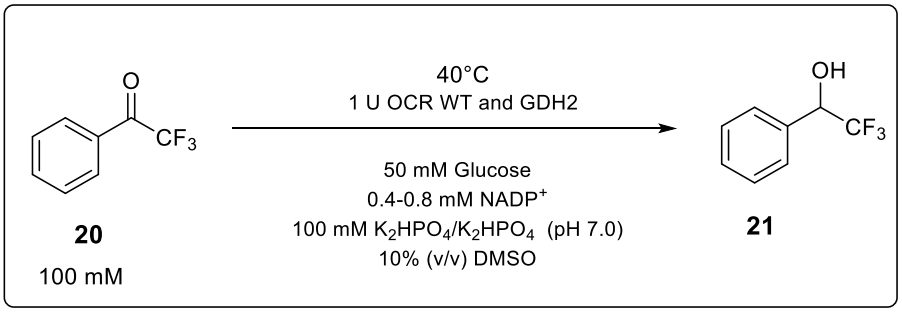

Scheme 20. Biocatalytic reduction of TFAP **20** to corresponding ethanol **21** using OCR-WT.

6.2.5. Microbial cultivation and preparation of biocatalysts

6.2.5.1. General procedures for the cultivation of microorganisms

pKV32_OCR vector was provided by API Corporation and modified for this study[77] (**Figure 73**). pKV32_OCR was transformed to *E. coli* JM109(DE3) by heat shock at 42 °C for 30 s and incubated in LB medium for 1 h at 37 °C with shaking at 150 rpm. The transformant harboring pKV32_OCR was spread on the LB-agar plate containing 50 μg·mL^{-1} kanamycin. Colonies were obtained after overnight culture in a 37 ºC incubator, following inoculation of the single colony into a round bottom tube containing 10 mL of Terrific Broth (TB) medium and 50 μg·mL^{-1} kanamycin. Fully grown cells after shaking incubation for 24 h at 37 °C with 150 rpm were inoculated again to 2 L Erlenmeyer flask containing 1 L TB medium with the antibiotic. The culture was incubated at 30 °C for 4-5 h and overexpressed by adding 0.2 mM IPTG for 20 h at 30 °C in a shaking incubator at 150 rpm. The culture was harvested by centrifugation at 5,000 rpm for 15 min (4 °C) and washed with phosphate buffer (100 mM, pH 6) once, following centrifugation at 5,000 rpm for 30 min. The cell was disrupted with ultrasonication and centrifuged at 10,000 rpm and 4 °C for 30 min. The cell crude extract was kept at -20 °C until it was used.

Cofactor regeneration was done by glucose dehydrogenase GDH mutant isolated *Bacillus subtilus* showing a good thermostability and organic solvent resistance, which was developed by Bommarius and named in this study as GDH2[101]. The GDH2 has mutated sites at E170K and Q252L (**Figure 73**, Appendix 6.4.1.5). pETDuet vector containing GDH2 was transformed into *E. coli* BL21(DE3). The transformant was cultured in LB medium containing 50 μg·mL^{-1} of ampicillin at 30 °C and 200 rpm and reinoculated to fresh LB medium to overexpress GDH2 with 1 mM IPTG at OD_{600} 0.6. The cell was harvested after 20 h and lysed by ultrasonication, and the supernatant was kept in -80 ºC until it was used.

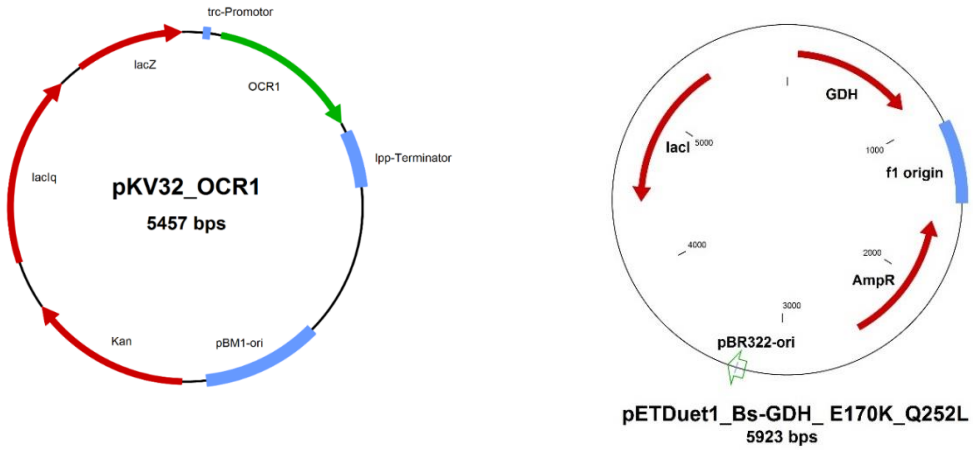

Figure 73. The vector map of pKV32_OCR harboring Trc-promoter, pBM1-ori, Kanamycin resistance gene, and OCR-WT (left). The vector map of pETDuet_GDH2 containing mutated residues (right).

6.3.5.2. Preparation of lyophilized OCR-WT cell crude extract

For the preparation of lyophilization, the cell crude extract was collected, and approximately 10-20 mL solution was added in a wide glass basin for freeze-drying over 2 days. The freeze-dried lyophilize was kept in -20°C freezer until it was used.

6.2.5.3. Construction of the error-prone PCR mutant library

Error-prone polymerase chain reaction (PCR) of OCR gene was carried out to construct a mutant library having an enhanced activity for 3R-**17** or 5S-MOLE **16**. The OCR gene was amplified using the forward primer FP-BamH1-OCR (5´-TCGGATCCACTAGTTAC-3´) and reverse primer RP-BmgBI-OCR (5´-TTCACGTCGTTGCTCAGCC-3´; the restriction sites are underlined). The PCR mixture contained pKV32_OCR as a template and 0.5 µM primers of FP-BamH1-OCR and RP-BmgBI-OCR, 0.4 mM dATP, GTP, dCTP and dTTP, and 10x PCR buffer (Thermo Fisher). Additionally, 0.25 mM $MnCl_2$ and 4.5 mM $MgCl_2$ were added to enhance mutation rates (1-5 mutations per 1,000 nucleotides). Taq polymerase (Thermo Fisher) was used at a concentration of 0.025 $U \cdot \mu L^{-1}$. The temperature program was started by incubation of the mixture for 2 min at 95 °C followed by 30 cycles of 30 s at 95 °C, 30 s at 55 °C, and 60 s at 72 °C and finished with 10 min at 72 °C. The PCR product was digested with *BamHI* and *BmgBI* (New England Biolabs Inc.) and cloned into *BamHI-BmgBI*-digested pKV32_OCR using T4 DNA ligase (Invitrogen). The ligation mixture was transformed to *E. coli* JM109(DE3)

competent cell by heat shock at 42 °C for 45 s. The transformed cells were spread on the LB-agar plate containing 50 μg·mL^{-1} kanamycin, following incubation at 37 °C for 20 h. A single clone on the agar plate was inoculated into 96 deep-well plates containing 500 μL of TB medium and 34 μg·mL^{-1} kanamycin and cultured for 24 h at a 30 °C shaking incubator with 150 rpm. Fully grown cells were inoculated to 96 deep-well plates containing 1.2 mL autoinduction medium consisted of 0.05% glucose, 0.2% lactose, and 0.5% glycerol in TB medium. Cells were incubated at 30 °C and 150 rpm for 20 h and harvested by centrifugation at 4,000 rpm for 10 min (4 °C). Fully grown cell culture was isolated, and plasmids were extracted following by manual provided by innuPREP Plasmid Mini Kit (Analytik Jena). The DNA sequences of isolated plasmid were analyzed by the cycle sequencing technology (dideoxy chain termination/cycle sequencing) using ABI 3730XL (Eurofins, Germany). Sequencing primers were designed for DNA analysis; Forward Sep Primer: 5'-CAAATATTCTGAAATGA-3'; Reverse Sep Primer: 5'-CGAAGCGAATGGCCAT-3'.

6.2.6. Colorimetric OCR mutant screening assay

Fully grown single mutant cells in 96 deep well plates were disrupted by adding 60 μL of Bugbuster protein extract reagent (Merck Millipore). The crude extract was isolated by centrifugation at 4,000 rpm over 30 min and located to 96 well plates. A colorimetric assay was started by adding an assay solution to 96 well plates. Briefly, 2.3 mM 5S-MOLE **16** was used as substrate and 0.1 mM NADPH and 20 mM glucose were added in 7.8 mM Tris-HCl buffer (pH 8.0) containing 0.01% bromothymol blue (**Table 25**). Ten microliters of the OCR mutant and GDH2 crude extract were prepared and added to 180 μL of the assay solution. After 4 and 16 h incubation at shaking incubator at room temperature, color change was monitored to collect mutants turned yellow, dramatically. The clones were named based on the vertical number and horizontal alphabet of a 96 well plate.

Selected OCR mutant clones: P2F11, P2F12, P2G6, P2G11, P3A5, P3F4, P4D2, P5B4 (P4d3 and P5B4 were excluded from further analysis).

Table 25. Composition of a colorimetric assay for screening.

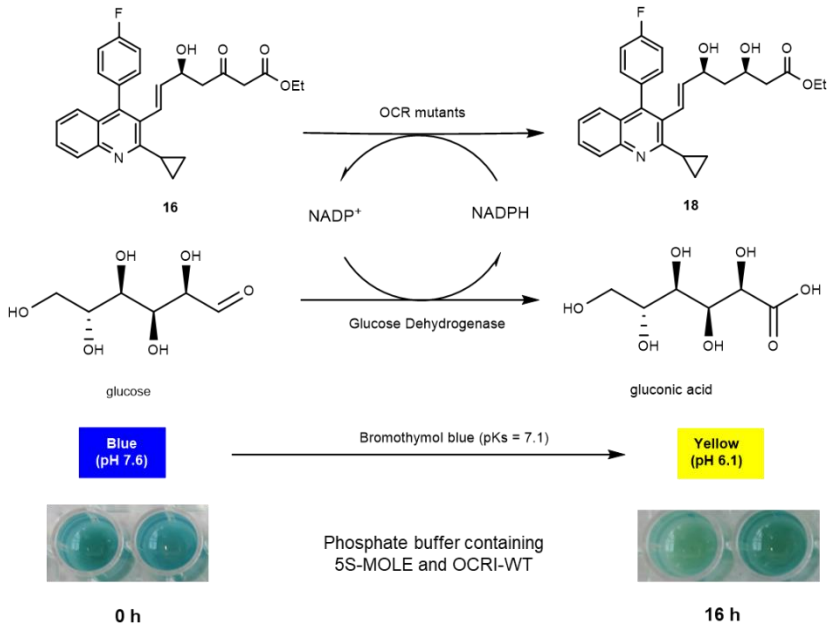

Assay composition	volume	final conc..
10 mM Tris-HCl (pH 8.0) containing 0.01% BTB	156 µL	7.8 mM
10 g/L (23 mM) of 5S-MOLE in DMSO	20 µL	2.3 mM
Glucose 2 M	2 µL	20 mM
NADPH 10 mM	2 µL	0.1 mM
GDH2	10 µL	-
OCR	10 µL	-
Total	200 µL	

6.2.7. Protein analysis and homology modelling

The deduced amino acid sequences were analysed by BLAST (https://blast.ncbi.nlm.nih.gov/Blast.cgi) to see the similarity of OCR with known enzymes. The active sites and cofactor binding sites were predicted by alignment of OCR-D54V with representative carbonyl reductase sniffer-like (SDRs) family proteins, such as neuroprotective/acting carbonyl reductase sniffer of *Drosophila melanogaster* (PDB number; 1SNY_A), putative carbonyl reductase sniffer of *Caenorhabditis Elegans* (PDB number; 1YO6_A and F), uncharacterized protein LOC415661 from *Gallus gallus* (NCBI reference number; XP_414028.1), and short-chain dehydrogenase from Coxiella burnetiid RSA 493 (GenBank accession number; AAO90484.1)[61].

6.2.8. Characterization of OCR

6.2.8.1. General condition for spectrophotometric activity measurement

Enzyme activities were determined at 25 °C by measuring the decrease in absorbance of NADPH at 340 nm using a microspectrometer (Tecan). The reaction started by adding 10 µL of cell crude extract and 10 µL NADPH (final 250 µM) to 180 µL of a reaction solution containing 100 mM potassium phosphate buffer (pH 6.0), 5 mM TFAP **20** dissolved in DMSO (final volume (v/v); 20%) in 96 well microplates (**Scheme 21**). Enzyme activity at 0 h was used as a reference activity. The millimolar extinction coefficient was 6.2 mM^{-1} cm^{-1}. One unit is the same as the concentration of reduction of TFAP (µmol) in one minute.

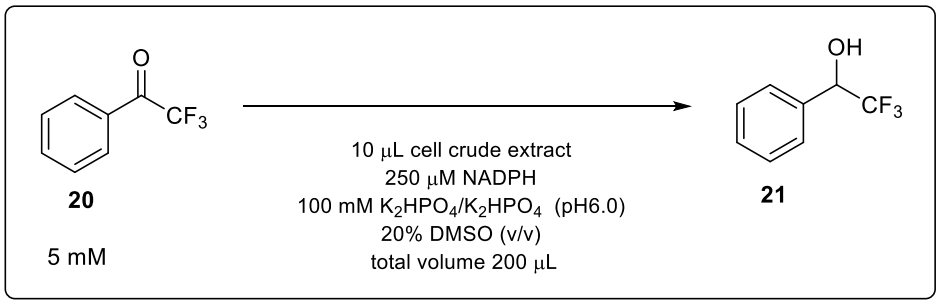

Scheme 21. Biotacatalytic reduction of TFAP **20** using OCR.

6.2.8.2. Effect of temperature and organic solvents on the catalytic activity of OCR

A hundred microliters of cell crude extracts of OCR-WT and D45V were incubated at 4 to 60 ºC for 4 h, and the cell debris was removed by centrifugation at 10,000 rpm for 10 min at 4 °C. Some of the supernatants were taken to measure residual activities by following activity measurement mentioned in section 6.2.8.1. The results are shown in **Figure 74** and **Figure 75**.

In case of stability of OCR-WT in organic solvents, five hundred microliters of cell crude extracts were incubated with organic solvents including methyl acetate, *n*-butyl acetate, methyl tetrahydrofuran (THF), and DMSO. To make 5, 25, and 50% organic solvent solutions, 50, 250, and 500 µL of each organic solvent was added into cell crude extracts, and the microtubes were filled with a potassium phosphate buffer (pH 7.0, 50 mM) up to 1,000 µL, following incubation for 4 and 16 h at 25 °C in a shaking incubator (1,000 rpm). The residual activities of incubated organic solvent-enzyme mixtures were measured using a microspectrometer. For measuring the residual activity of OCR-WT, 1.76 mM of TFAP in DMSO was added to a reaction solution consisted of 88 mM potassium phosphate and 26 mM NADPH (final volume 192.5 µL). The reaction was started by adding 50 µL of crude extract (**Scheme 22**). Optical density at 340 nm was observed for 1 min, and the activity was calculated as the

same described in section 6.2.8.1. Relative activities were calculated by dividing specific activities of OCR in organic solvents by the specific activities of OCR in a 100% buffer solution. The result is shown in **Figure 76**.

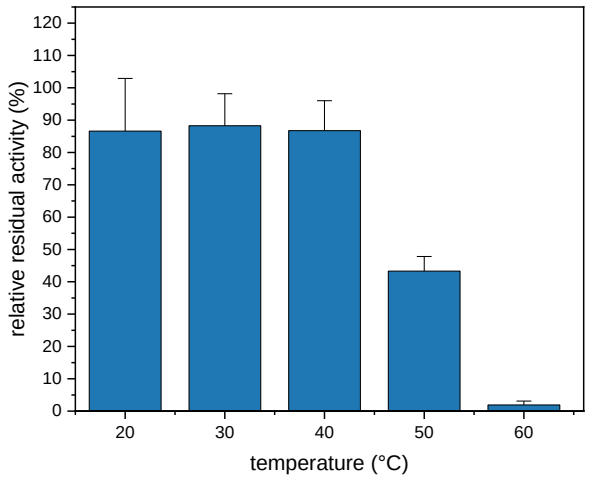

Figure 74. Residual activity of OCR at different temperatures.

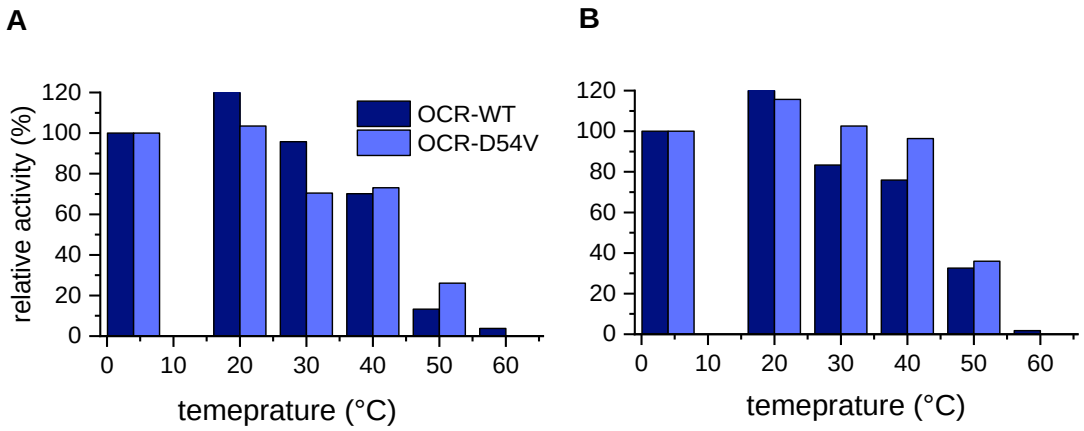

Figure 75. Relative activity of OCR-WT and D54V at various temperatures for 4 h without (A) and with 20% DMSO (B) in potassium phosphate buffer.

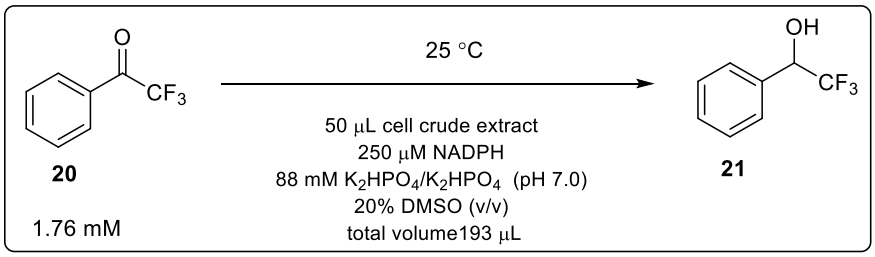

Scheme 22. Biotacatalytic reduction in various organic solvents of TFAP **20** using OCR.

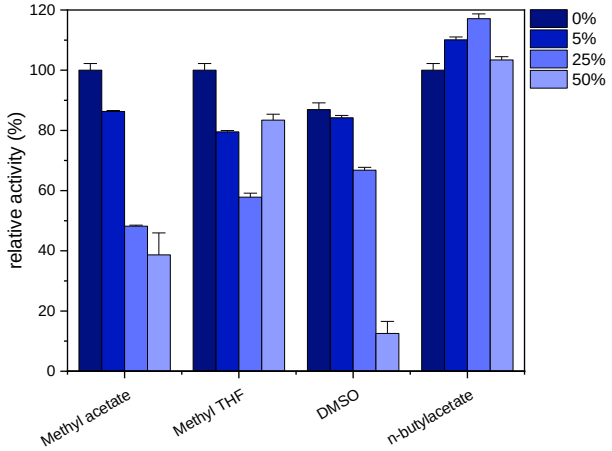

Figure 76. Enzyme stability of OCR wild-type; enzyme stability after 4 h incubation in 0-50% organic solvents.

6.2.8.3. Measurement of enzyme kinetics for NADPH

A specific activity and enzyme kinetics were analyzed by spectrophotometry following the general condition in 6.2.8.1. NADPH concentrations were changed from 0.05 to 1 mM to calculate a catalytic activity toward NADPH. The decrease in optical density at 340 nm was observed, and K_m and V_{max} values were estimated by Lineweaver-Burk equation using Origin visualizing program (**Figure 77**).
V_{max} (NADPH), 3.45 U·mL^{-1}; **K_m** (NADPH), 0.19 mM.

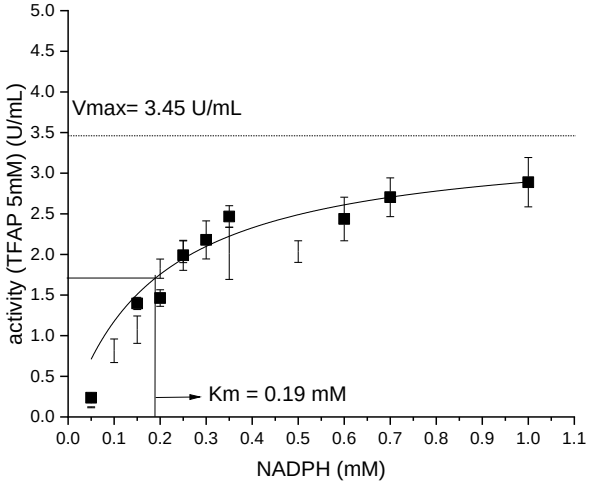

Figure 77. Calculation of V_{max} and K_m of OCR for NADPH.

6.2.9. Catalytic reduction of pitavastatin intermediate using OCR-WT and its mutants

6.2.9.1. Preparation of a reaction mixture and purification of 3R-MOLE **17** and 5S-MOLE **16** using flash chromatography

The bioconversion was done with 40 $g \cdot L^{-1}$ to synthesize 3R-, 5S-MOLE **17** and **16** using biocatalyst. The reaction solution contained 100 mM potassium buffer (pH 6.0), 120 mM glucose, 2 mol% $NADP^+$ (1.5 mM), 40% DMSO, and 10 U of OCR-WT and GDH2 (**Scheme 23**). The aqueous solution was pre-warmed in 40 mL of a glass vessel, and the reaction was started by adding 40 $g \cdot L^{-1}$ DOXE **15** in DMSO to the aqueous solution. The contents of DMSO in the whole reaction solution was 40%. The pH was adjusted to pH 6.0 by adding a 0.5 M NaOH solution using a pH titrator equipped with automatic base adding-device (TitraLab). The reaction was prolonged up to 24 h with a stepwise cofactor addition at 0, 3, 6, 24 h; then the reaction mixture was extracted with the same volume of ethyl acetate twice, following evaporating the solvent by rotary evaporator. The concentrated compounds were referred to as a reaction mixture. The reaction mixture was used as a substrate for further reaction. **Scheme 23** showed an example of the preparation of the reaction mixture. The bioconversion was repeated but for 1 h to get the reaction mixture containing DOXE **15** and MOLEs in solution, and the composition of DOXE **15** and MOLEs in the reaction mixture was different for each reaction.

After evaporating organic solvents, some concentrated compounds were loaded on SNAP® Ultra 25 g column packing with HP-Sphere™ spherical silica for purification by flash chromatography (Biotage, Sweden). Cyclohexane and ethyl acetate were used as mobile phase A and B, respectively. The initial concentration of ethyl acetate was 8%, and the concentration of ethyl acetate was gradually increased for 10 column volumes up to 66%. The concentration of ethyl acetate was kept for 2 columns. The

product was detected at UV 254 and 280 nm. MOLEs fractions were collected and evaporated using a rotary evaporator. The concentration of mixtures was determined by HPLC.

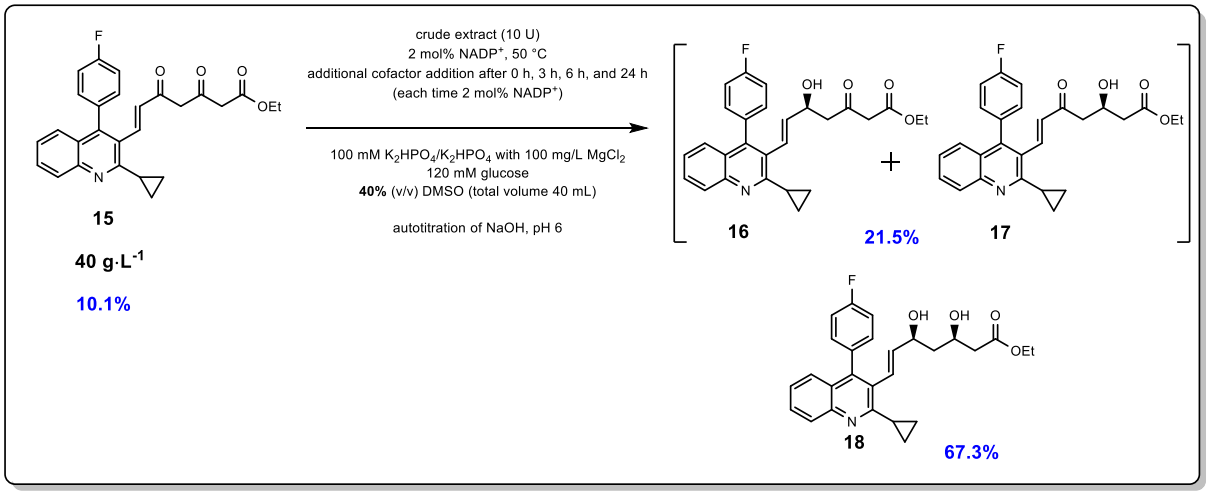

Scheme 23. Preparation of reaction mixture containing DOXE 15, MOLEs, and DOLE 18 using biocatalysts OCR-WT.

6.2.9.2. Benchmark reaction with wild-type OCR and mutants using 5S-MOLE **16**

The six selected OCR mutant clones in section 6.2.6 were subjected to benchmark reaction. The crude extract of OCR-mutants were prepared by the general procedures in section 6.2.5.1. After measuring the activity of mutant OCR, the same units of GDH2 was added in the reaction solution (0.28 U). The reaction solution contained 100 mM potassium phosphate buffer (pH 6.0), 200 mg·L^{-1} $MgCl_2$, 120 mM glucose, and 2 mol% $NADP^+$ (40 µM) (**Scheme 24**). The substrate, 1g·L^{-1} 5S-MOLE **16**, was dissolved in 2 mL DMSO and lastly added to pre-warmed 8 mL aqueous solution with stirring at 1,000 rpm using a magnetic stirring bar. The reaction was carried out at 50 °C for 20 h. A hundred microliters of the reaction mixture were isolated and extracted twice by ethyl acetate with the same volume, following HPLC analysis. The result is shown in **Table 26**.

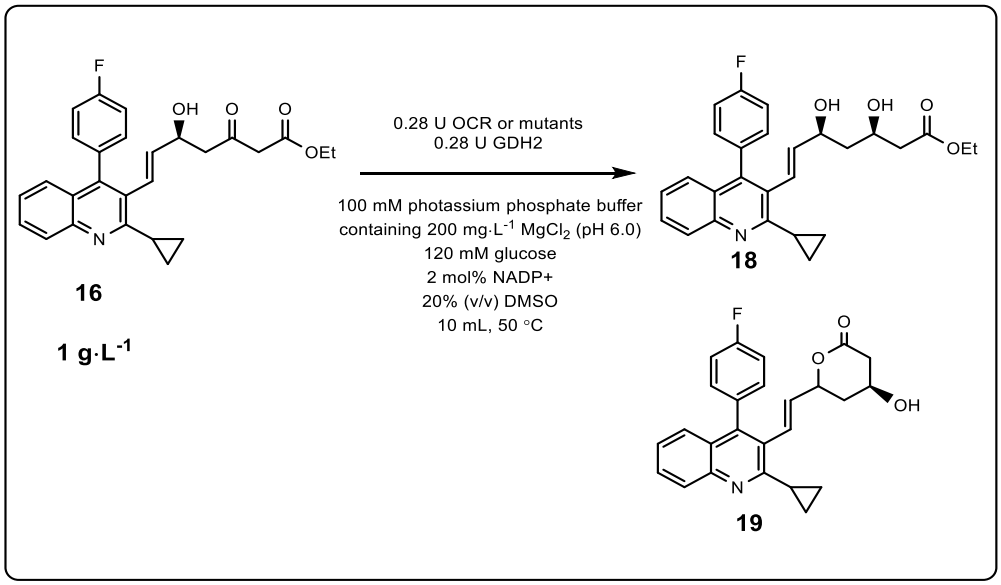

Scheme 24. Reduction of 5S-MOLE using OCR mutants.

Table 26. HPLC analysis of the biocatalytic reduction of 5S-MOLE **16** using OCR-WT and mutants.

Conversion measured by HPLC (%)			
OCR	Lactone **19**	DOLE **18**	5S-MOLE **16**
WT	3.4	96.2	0.3
P2F11	0	1	99
P2F12	4.5	92.8	2.7
P2G6	4.2	95.8	0
P2G11	2.3	97.1	0
P3A5	0	0.7	99.3
P3F4	2.3	97.4	0.3
negative control (NC)	0	0.8	99.2

6.2.9.3. Bioconversion of 3R-, 5S-MOLE mixture (**17** and **16**) using OCR-WT and D54V

A reaction solution containing 120 mM glucose and potassium phosphate buffer (pH 6, 100 mM) was prepared and prewarmed to 50 °C **(Scheme 25**). The same units of GDH2 and OCR-WT or D54V (0.6 U), and 2 mol% $NADP^+$ cofactor (100 µM) were added to the mixture followed by adding 2.6 $g \cdot L^{-1}$ MOLEs dissolved in DMSO (20% of total volume). The $NADP^+$ cofactor was added 3 times at 0, 2, 3 and 4 h to the reaction with the same concentration. The total volume of the reaction solution was 5 mL (**Scheme 26**). The reaction was done for 24 h at 50 °C. A hundred microliters of the reaction mixture were separated every 30 min up to 4 h to observe conversions. The isolated reaction solutions were extracted by the same volume of ethyl acetate for HPLC analysis. The result is shown in **Figure 78**.

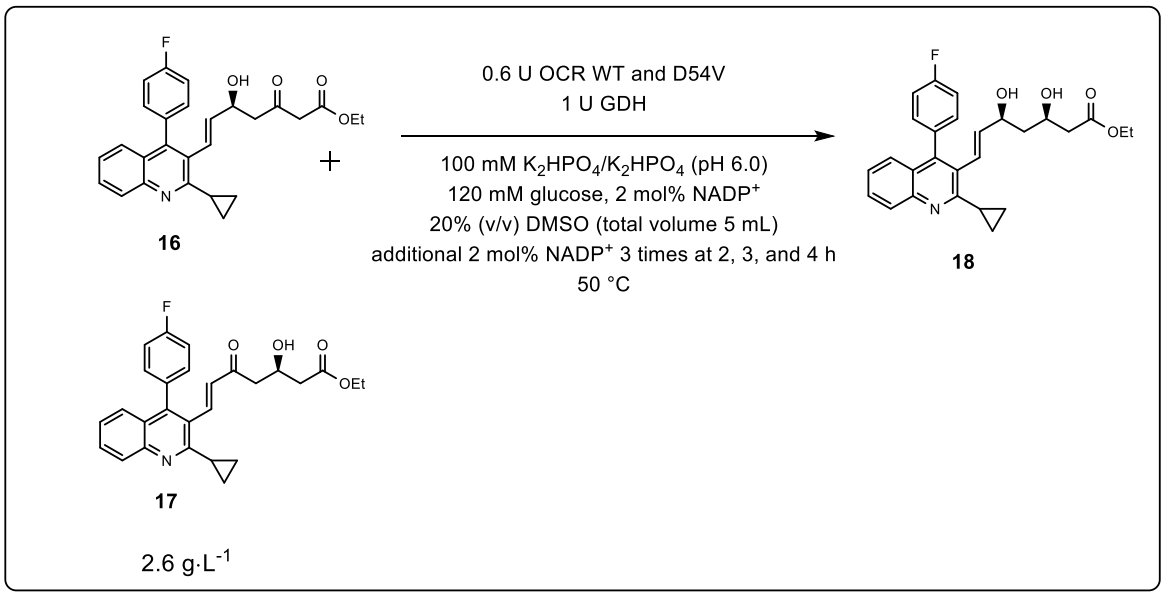

Scheme 25. The conversion of 5S-MOLE **16** and 3R-MOLE **17** to DOLE **18** using biocatalyst OCR-WT and D45V.

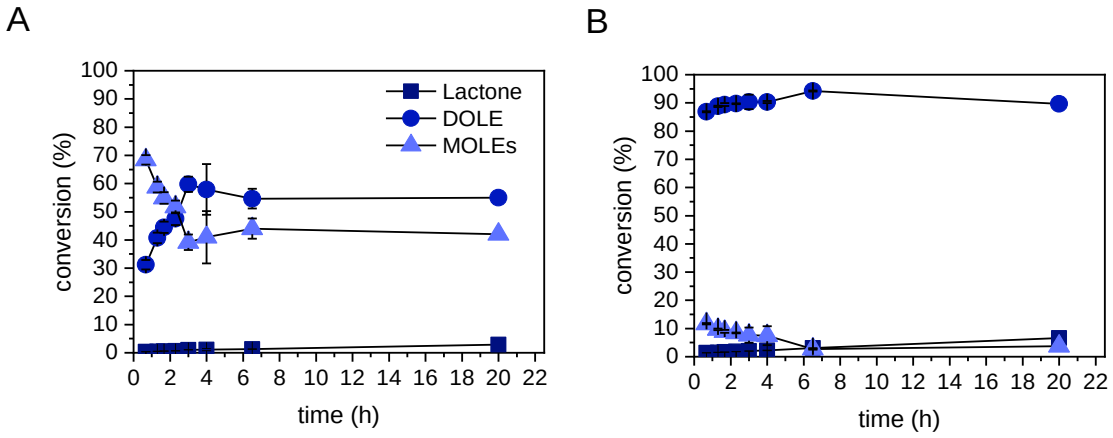

Figure 78. Reduction of MOLEs to DOLE **18** by OCR-WT (A) and D54V (B).

6.2.9.4. Bioconversion of DOXE **15** with OCR-WT and D54V

A potassium phosphate buffer (pH 6, 100 mM) containing 120 mM glucose was prepared and pre-warmed to50 °C (**Scheme 26**). Fifty microliters of GDH2, 2 mol% $NADP^+$ cofactor (400 µM), 10 U OCR WT or D54V were added to the mixture followed by adding 10 $g \cdot L^{-1}$ of DOXE **15** dissolved in DMSO (20% of total volume). The total volume of the reaction solution was 2 mL. The reaction was carried out for 24 h at 50 °C. Cofactor was repeatedly added to the reaction solution at 4 h after the reaction. A hundred microliters of the reaction mixture were isolated at 1, 2, 3, and 4 h and extracted by ethyl acetate with the same volume for 2 times. The concentrated extracted solution by a rotary evaporator was analysed by HPLC. The result is shown in **Table 27**.

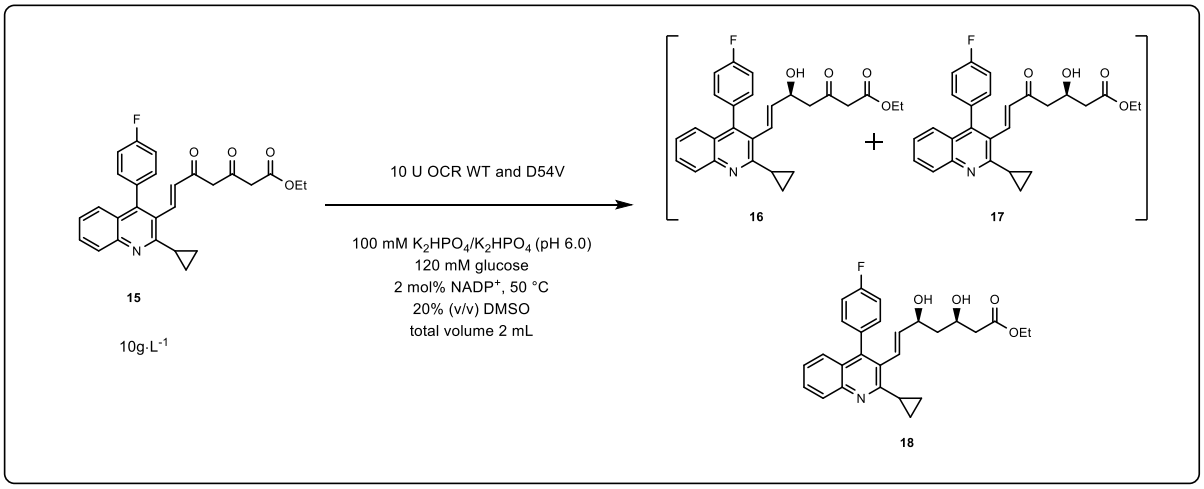

Scheme 26. Biotransformation of DOXE **15** to DOLE **18** using 10$g \cdot L^{-1}$ of the reaction mixture.

Table 27. The bioconversion of 10$g \cdot L^{-1}$ DOXE **15** to DOLE **18** by OCR-WT and D54V.

	Conversion (%)							
	1 h		2 h		3 h		4 h	
	MOLEs (**16+17**)	DOLE **18**	MOLEs (**16+17**)	DOLE **18**	MOLEs (**16+17**)	DOLE **18**	MOLEs (**16+17**)	DOLE **18**
WT	-	-	27.6	14.5	27.4	14.8	26.8	14.6
D54V	23.7	67.2	23.3	68.3	23	68.3	22.8	70.1

6.2.9.5. Bioconversion of the mixture of DOXE **15**, MOLEs and DOLE**18** by OCR-WT and D54V

An aqueous solution containing 100 mM potassium buffer (pH 6.0), 120 mM glucose, 2 mol% $NADP^+$ (80 µM), and 0.6 U GDH2, and OCR-WT or D54V was mixed thoroughly. The reaction mixture was prepared in section 6.2.9.1 was dissolved in DMSO and was added later to the pre-warmed aqueous solution to make the final concentration of 2 $g \cdot L^{-1}$ (20% of total volume). The total volume of the reaction solution was 5 mL. The cofactor was added again at 2h (**Scheme 27**). The reaction was continued up to 20 h at 50 °C. The whole reaction solution was extracted by the same volume of ethyl acetate for HPLC analysis. The result is shown in **Table 28**.

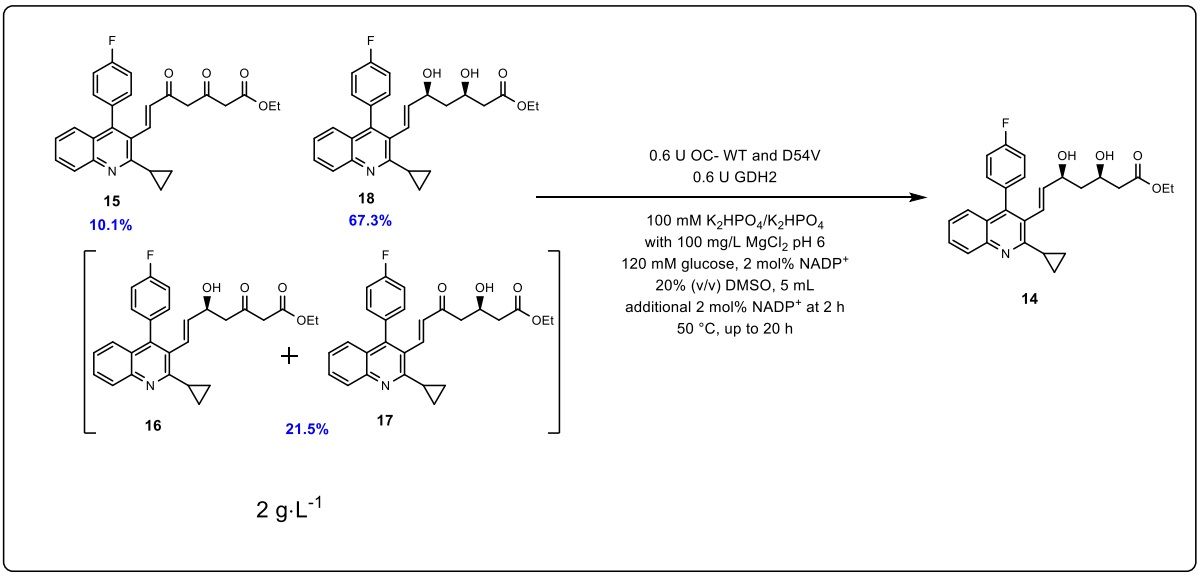

Scheme 27. Biocatalytic reduction of the reaction mixture using OCR-WT and D54V.

Table 28. Biotransformation of 2 $g \cdot L^{-1}$ reaction mixture by OCR-WT and D54V.

	HPLC analysis (%)		
	The contents of the reaction mixture	OCR-WT	OCR-D54V
lactone **19**	1.1	5.1	5.1
DOLE **18**	67.3	92.3	93.9
MOLEs	21.5	2.7	1.0
DOXE **15**	10.1	0	0

The reaction mixture was prepared following the same method in 6.2.9.1 to have DOXE **15**, MOLEs, and DOLE **18** mixture. In this time, the biocatalytic reduction was stopped at 2 h to obtain higher DOXE **15** and MOLEs ratio compared to DOLE **18** (DOXE **15** 70%, MOLEs **17.5%,** and DOLE **18** 12.3%).

The biocatalytic reduction of 10 g·L^{-1} of the above reaction mixture was carried out by OCR-D54V. The reaction condition of biocatalytic reduction with the reaction mixture was same as **Scheme 27**, however, 10 g·L^{-1} of the above reaction mixture was used for the scaled-up reaction using an autotitrator with pH adjustment at 6 (500 mM NaOH solution as a base). Five units of OCR-D54V and the same unit of GDH2 was added in the reaction mixture. $NADP^+$ was added 3 times at 2, 4, and 6 h after reaction (**Scheme 28**). The result is shown in **Figure 79**.

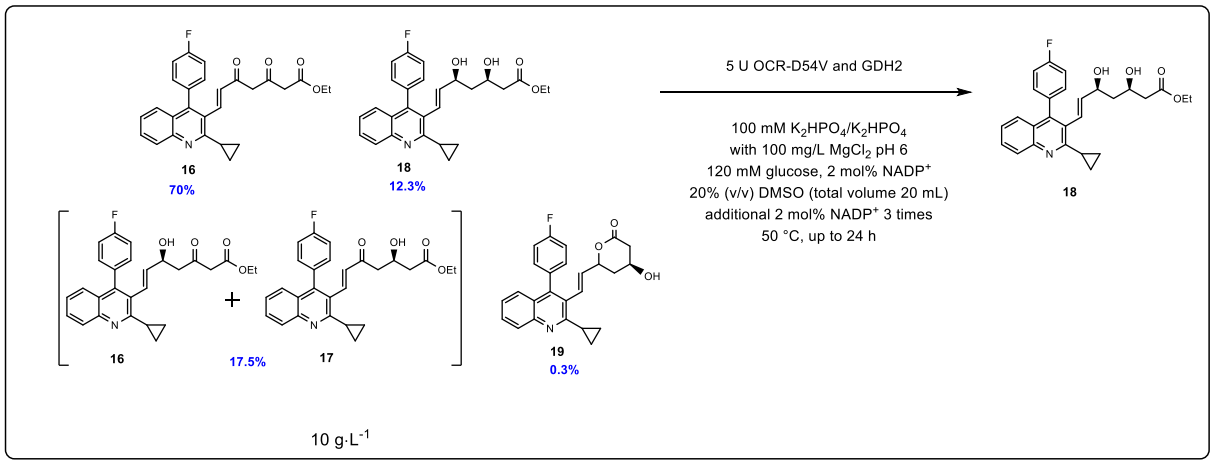

Scheme 28. Biocatalytic reduction of 10 g·L^{-1} reaction mixture using OCR-D45V.

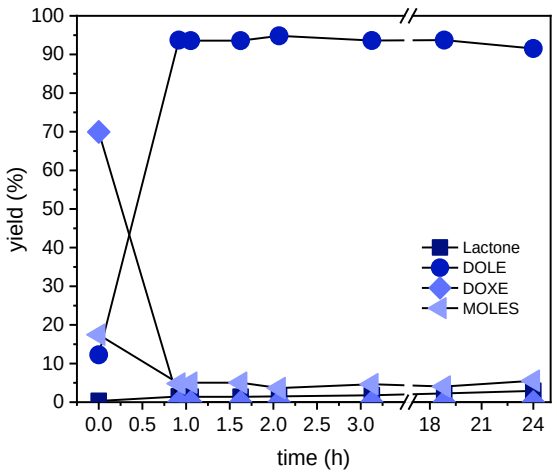

Figure 79. Scaling up of biotransformation using OCR-D54V cell crude extract containing 10 g·L^{-1} reaction mixture.

6.2.10. Synthesis of α-(trifluoromethyl)benzyl alcohol using a segmented flow reactor

OCR-WT was prepared as lyophilized powder to improve biocatalytic loading in an aqueous solution in section 6.2.5.3. The corresponding protein concentration of OCR-WT was 1.8 mg·mL^{-1}. First, the aqueous solution was prepared in a falcon tube containing 10 U·mL^{-1} OCR-WT, 20 U·mL^{-1} GDH2, 600 mM glucose, 2 mM NADP^{+}, and a 50 mM phosphate buffer (pH 7.0), and 2-3 mL of solution was transferred to a glass syringe (2.5 mL S.G.E. inner diameter;7.28 mm). The organic phase containing 200 mM TFAP **20** in MTBE was prepared in a falcon tube and transferred to another glass syringe injector (**Scheme 29**). The aqueous solution and organic solution were pumped through a Y-shape mixer to a tube reactor which has 0.8 mm inner diameter (PFE) and 0.5 mL volume. (reaction volume, 0.5 mL; pump speed, 0.5 mL·h^{-1}; residence time, 0.5 h; **Figure 80**A). The reaction condition was changed by increasing the volume of a tube reactor to 1 mL, and the pump speed kept the same (reaction volume, 1 mL; residence time, 1 h; pump speed, 0.5 mL·h^{-1}; **Figure 80**B). Apart from a volume of a tube reactor, segmented flow reaction was performed in the same condition (10 U·mL^{-1} OCR-WT, 20 U·mL^{-1} GDH2, 600 mM glucose, 2 mM NADP^{+}, 200 mM TFAP **20** in MTBE). The residence time was changed from 1 to 2 h by lowering pumping speed to 0.25 mL·h^{-1} without increment of enzyme loading (reaction volume, 1 mL; pump speed, 0.25 mL·h^{-1}, residence time 2 h; **Figure 80**C). Apart from residence time, segmented flow reaction was performed in the same condition (10 U·mL^{-1} OCR-WT, 20 U·mL^{-1} GDH2, 600 mM glucose, 2 mM NADP^{+}, 200 mM TFAP **20** in MTBE). Finally, the enzyme loading was increased (20 U·mL^{-1} OCR-WT, 20 U·mL^{-1} GDH2, 600 mM glucose, 2 mM NADP^{+}, 200 mM TFAP **20** in MTBE), and the reaction condition was kept as the last reaction (reaction volume, 1 mL; pump speed, 0.25 mL·h^{-1}, residence time 2 h , **Figure 80**D). The reaction mixture was quenched by 0.5 mL of 1 M HCl solution and followed extracting by 1 mL of ethyl acetate for GC analysis. The result was shown in **Figure 80**.

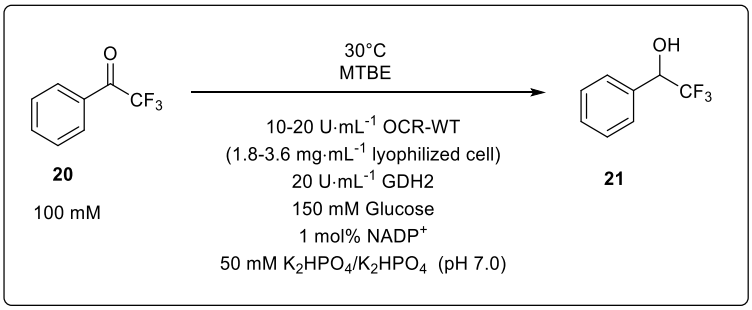

Scheme 29. Segmented flow low reaction using OCRI-WT, GDH2 and 200 mM TFAP (final concentration 100 mM).

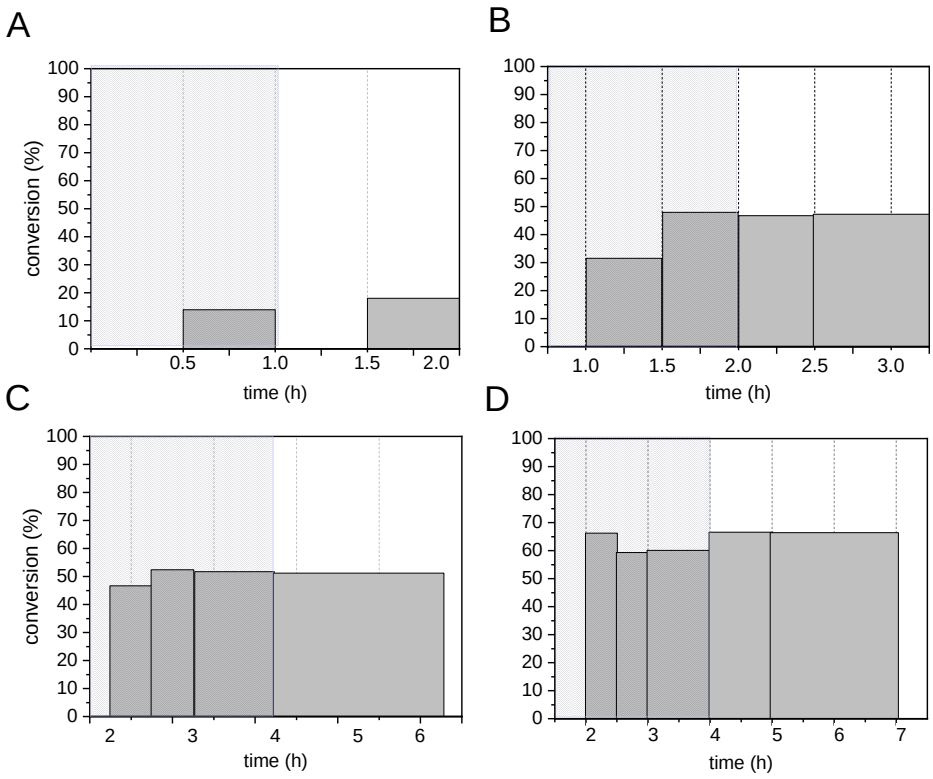

Figure 80. Conversion (%) from TFAP **20** to α-(trifluoromethyl)benzyl alcohol **21** by flow reaction using OCR-WT. The flow reactor consisted of a Y-shape mixer and a tube reactor (0.8 mm ID) having 0.5 (A) and 1 mL (B, C and D) of reaction volume. The residence time was gradually increased to 0.5 (A), 1 (B), and 2 (C and D) h, respectively. Ten units of biocatalyst were prepared in aqueous solution at 30 ºC, and organic solvent was prepared by adding 200 mM TFAP to MTBE. The conversion was determined by collecting reaction mixture at a specific time. Increased amount of OCR-WT up to 20 $U \cdot mL^{-1}$ was used (D). The blue box refers to equilibrium.

The same reaction with a tube reactor having ID 1.58 mm (reaction volume, 1 mL) was used to observe the effect of reactor size on conversion. The aqueous solution contained 600 mM glucose, 2 mM $NADP^+$, 10 $U \cdot mL^{-1}$ OCR WT, 20 $U \cdot mL^{-1}$ GDH2, and 50 mM phosphate buffer (pH 7.0). The organic solution contained 200 mM TFAP **20** in MTBE. Y shape mixer was used, and the residence time was 1 h. The same experiment with the above condition but with 0.8 mm tube reactor (reaction volume, 1 mL) and T shape mixer was done to see the effect of type of mixer on the conversion. The result was shown in **Figure 81**.

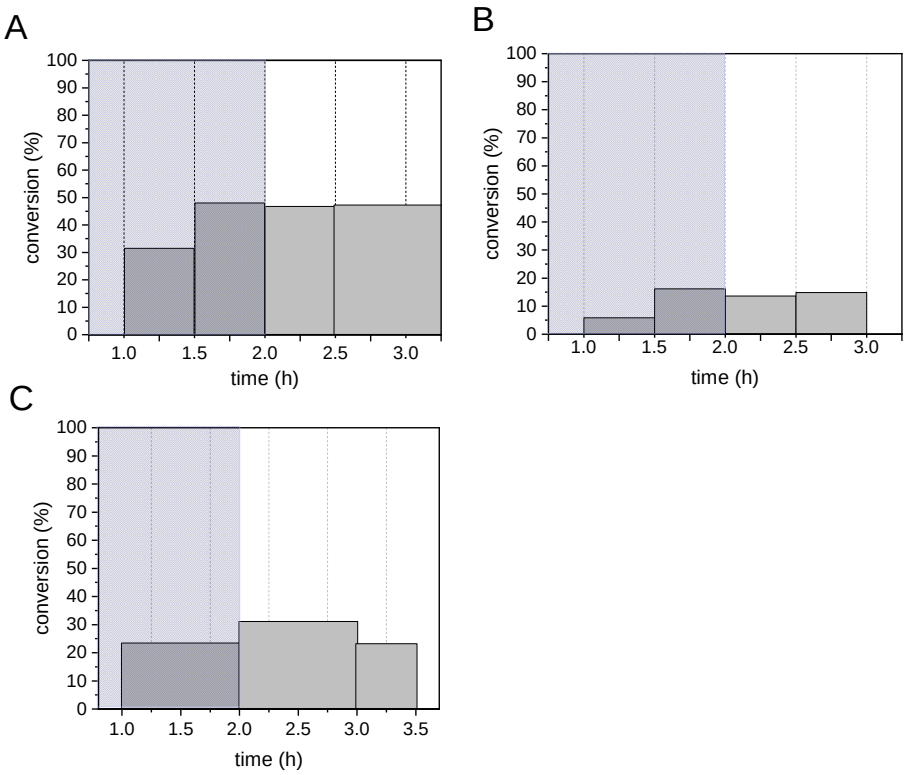

Figure 81. Conversion (%) from TFAP to α-(trifluoromethyl)benzyl alcohol by flow reaction using OCR-WT. The flow reactor consisted of a Y-shape mixer, 0.8 mm ID reaction tube with 1 mL volume (A). The residence time was 1 h. Ten units of biocatalyst was used at 30 °C, and 200 mM TFAP was dissolved in MTBE. The conversion was determined by collecting reaction mixture at a specific time. The same experiment was performed but the ID of tube reactor was changed to 1.588 mm (B). Finally, the same reaction condition as (A) but T-shape mixer was used for mixing (C).

6.2.11. Synthesis of α-(trifluoromethyl)benzyl alcohol using batch reactor for comparison of a phase separation

Benchmark reaction using a batch reactor was done in a 2 mL glass vial at 30 ºC with a magnetic bar and a stirrer. The aqueous solution contained 10 $U \cdot mL^{-1}$ OCR-WT lyophilize, 20 $U \cdot mL^{-1}$ GDH2, 1 mol% $NADP^+$, and 150 mM glucose in 50 mM phosphate buffer (pH 7.0). Five hundred microliter of aqueous and organic solution were added to a 2 mL glass vial, and the reaction mixture was mixed by stirring at 400 rpm at 30 ºC (**Scheme 30**). Two hundred millimolar TFAP **20** was prepared in 500 µL MTBE. The aqueous solution was preheated at 30 ºC, and the reaction started by adding the organic phase to the aqueous phase. The reaction was quenched by adding the same volume of 1 M HCl, and the mixture was extracted by one volume of ethyl acetate following GC analysis. The result is shown in **Figure 82**.

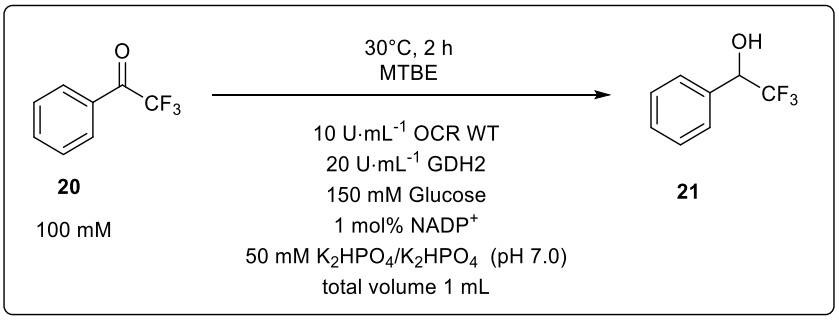

Scheme 30. Segmented flow low reaction using OCRI WT, GDH2 and 200 mM TFAP (final concentration 100 mM).

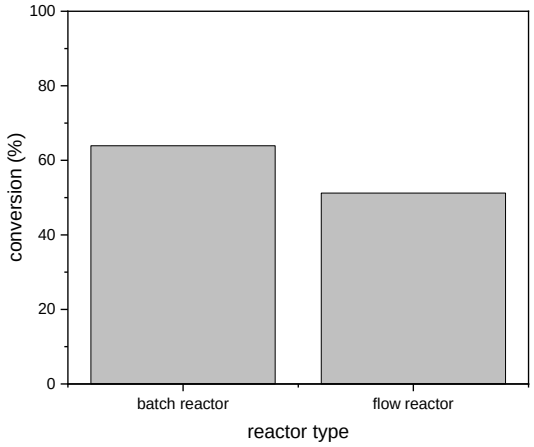

Figure 82. Comparison of conversion using a conventional batch reactor with a magnetic bar and stirrer and flow reactor. The flow reactor consisted of a Y-shape mixer, 0.8 mm ID reaction tube with 1 mL volume. The residence time was 2 h. Ten units of biocatalyst were prepared in aqueous solution at 30 ºC, and the organic solvent was prepared by adding 200 mM TFAP to MTBE. The conversion was determined by collecting reaction mixture at a specific time. The reaction was done at 30 ºC for 2 h following quenching and extraction with ethyl acetate.

6.3. Application of new type of aldoxime dehydratase isolated from *Rhodococcus* sp. YH3-3 for aldoxime synthesis and its directed evolution

6.3.1. Materials and preparation of OxdYH3-3 transformants

Chemicals including *E*-pyridine-3-aldoxime, *3*-cyanopyridine and 2-furaldehyde were purchased from Wako (Japan) and Sigma Aldrich (Germany). Furonitrile was purchased from Sigma Aldrich. OxdYH3-

3 in pETs vector was constructed by Dr Suguru Shinoda and reconstructed and provided by Inoue Lisa in Toyama Prefecture University, Japan.

6.3.2. Synthesis of 2-furfuryl aldoxime

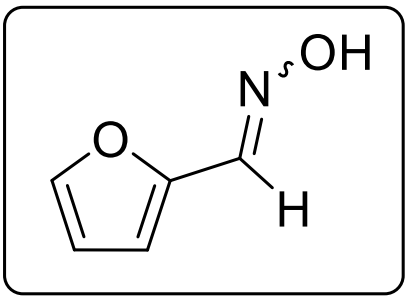

2-Furfuryl aldoxime was synthesized from 2-furaldehyde. 2-furaldehyde (120.72 mmol) was added to 20 mL water containing 144.86 mmol $NH_2OH{\cdot}HCl$. Sodium carbonate (72.43 mmol) in 30 mL water was added dropwisely to the first mixture. The reaction continued overnight and extracted three times by adding the same volume of ethyl acetate. The organic solution was washed with water once and dried by magnesium sulphate. The yellow needle-shaped powder was obtained after evaporating a solvent by a rotary evaporator. 2-Furfuryl aldoxime was dissolved in ethyl acetate, and the compounds were separated by Biotage flash chromatography (Biotage) using a silica column (SNAP Ultra 25, Biotage). Cyclohexane and ethyl acetate (1:10 v/v) were used for the elution with constant gradient for ten column volume. To synthesize 2-furonitrile, 1.48 mmol 2-furfuryl aldoxime was added to 10 mL acetonitrile containing 0.148 mmol Cu(II) acetate[163]. The reaction mixture was heated at 90 °C for 3 h. The resulting product 2-furonitrile was isolated by silica column chromatography. The formation of 2- furfuryl aldoxime and 2-furonitrile in these syntheses was confirmed by ^{1}H-NMR spectroscopic analysis. The ^{1}H-NMR spectra were measured on Bruker Avance III HD 500Mz with capillaries containing $CdCl_3$ (δ = 7.24 ppm). For the mass analysis of 2 -furfuryl aldoxime, ESI Mass spectra was recorded on a Bruker Esquire 3000 in positive and negative Ion mode.

MS (ESI): m/z = 112.0 $[M+H]^+$, 145.8 $[M+Cl]^-$.

^{1}H-NMR (500 MHz, $CDCl_3$): 2-furfuryl aldoxime: δ [ppm]= 6.54 (dd 1H), 7.26 ($CdCl_3$, 1H), 7.33 (d, 1H), 7.48 (d, 1H), 7.52 (s, 1H). 2-furonitrile: ^{1}H-NMR (400 MHz, $CDCl_3$): δ [ppm]= 6.53 (dd, 1H), 7.17 (dd, 1H), 7.47 (dt, 1H).

6.3.3. Analysis of polypeptides homology within aldoxime dehydratase enzymes (Oxd enzymes)

Constraint-based Multiple Alignment Tool from BLAST (https://blast.ncbi.nlm.nih.gov/Blast.cgi) was used for alignment and comparison of identities of Oxd enzymes.

6.3.4. Construction of recombinant OxdYH3-3 in *E. coli* host cells

The gene encoding OxdYH3-3 (GenBank accession no. WP_064442863.1, Appendix 6.4.1.3.)[158] was amplified from *Rhodococcus* sp. strain YH3-3 genomic DNA by PCR. Nde-Oxd_YH3-3-FW primer (5'-catatggaatctgcaatcggcgaacac-3') and Bam-Oxd_YH3-3-RV primer (5'-ggatcctcagtgctcgg-cggtgatcaccgcg-3') were used for PCR. The oxdYH3-3 gene was cloned into the *Nde*I and *Bam*HI site of pET28a (Novagen). pET22b-OxdYH3-3 for expression as an N-terminal his-tagged protein was similarly constructed by double digestion and ligation. The oxdYH3-3 gene prepared from OxdYH3-3-cloned plasmid by double digestion with *Xba*I and *Bam*HI and the plasmid DNA fragment prepared from pET22b vector (Novagen) using the same restriction enzymes were ligated using DNA Ligation Kit Ver.2.1 (Takara). The oxdYH3-3 gene for construction of pET28b-OxdYH3-3 was amplified from pET22b-OxdYH3-3 using primers Fw-YH3-3-Oxd (5'-aggagatataccatggaatctgcaatcggcgaacac-3') and Rv-YH3-3-Oxd (5'-gtgcggccgcaagcttgtgctcggcggtgatcac-3'). PCR parameters consisted of 30 cycles of 98 °C for 10 s, 55 °C for 5 s and 72 °C for 5 s using PrimeSTAR MAX DNA polymerase (Takara). The amplified DNA fragment was purified and cloned into *Nco*I and *Bam*HI site of pET28b vector (Novagen) using In-fusion HD Cloning Kit (Takara) to obtain pET28b-OxdYH3-3 for expression as a C-terminal His-tagged protein. For the construction of pET15b-OxdYH3-3, the oxdYH3-3 gene prepared from pET22b-OxdYH3-3 by double digestion with *Nde*I and *Bam*HI and the plasmid DNA fragment prepared from pET15b vector (Novagen) using same restriction enzymes were ligated using DNA Ligation Kit Ver.2.1 (Takara). pET15b-OxdYH3-3 *w*as used for expression as an N-terminal his-tagged protein. The DNA sequencing of the inserted gene was carried out using ABI 3500 Genetic Analyzer (Applied Biosystems). The constructed plasmids were transformed into BL21(DE3) and BL21Codonplus(DE3) *E. coli* cells, respectively.

6.3.5. Preparation of OxdYH3-3 recombinant cells and optimization of overexpression

The transformants were inoculated to LB medium containing 50 $\mu g \cdot mL^{-1}$ antibiotics (ampicillin for pET15b and pET22b; kanamycin for pET28b). After overnight cultivation at 37 °C with 150 rpm, 1% (v/v) culture was re-inoculated to LB medium for protein overexpression. IPTG (0.5 mM) was added to the culture when OD_{600} reached 0.5, and the culture was kept at 18 °C from 20 to 40 h and at 30 °C for 20 h with shaking at 150 rpm. Subsequently, for medium optimization, the transformants were inoculated to autoinduction solution containing 5 mM of 5-aminolevulinic acid and kept at 30 °C up to 18 h with shaking at 150 rpm. The autoinduction solution is composed of 6 g NaH_2PO_4, 3 g KH_2PO_4, 20 g tryptone, 5 g yeast extract, 5 g NaCl, 0.6% glycerol, 0.05% glucose, 0.2% lactose, and 1% trace elements in 1 L. Overexpressed cell was collected by centrifugation at 4,000 rpm for 30 min and washed with distilled water once. The pellet was resuspended to 5 mL of a phosphate buffer (pH 7.0, 50 mM) and stored at 4 ºC freezer until it was used in the next experiment. The cell pellet was disrupted by

ultrasonication, following centrifugation at 10,000 rpm at 4 °C to separate supernatant (soluble protein) from the insoluble pellet (insoluble protein). The supernatant was isolated, and the centrifuged pellet was washed with phosphate buffer once and resuspended in the same volume of phosphate buffer as the supernatant. Conversion from aldoxime to nitrile was measured using freshly prepared proteins following a method in section 6.3.6. The overexpression of OxdYH3-3 recombinant cells was confirmed by SDS-PAGE analysis.

6.3.6. Biotransformation of aldoximes to nitriles using whole-cells containing OxdYH3-3 WT

E. coli harbouring pET15b-, pET22b-, pET28b-OxdYH3-3 was cultivated in 5 mL of the autoinduction medium containing 50 μg·mL^{-1} antibiotics for 20 h at 30 °C with shaking at 150 rpm. After overnight cultivation, the cells were harvested by centrifugation at 4,000 rpm and 4 °C. The cell pellet was washed with 50 mM phosphate buffer (pH 7.0) and resuspended in 1 mL phosphate buffer. Twenty-five microliters of *E*-pyridine-3-aldoxime and 2-furfuryl aldoxime stock solution (200 mM in DMSO) were then added to 475 μL cell suspension (**Scheme 31**). The mixtures were incubated in a shaker with 150 rpm at 30 °C for 20 h, and the 50 μL of a reaction mixture was taken to measure HPLC. The activity of BL21(DE3)/pET28b-OxdYH3-3 toward 10 mM *E*-pyridine-3-aldoxime and 2-furfuryl aldoxime was measured as time course at 3, 4, 5, and 9 h of reaction. The results are shown in **Figure 83** and **Figure 84**.

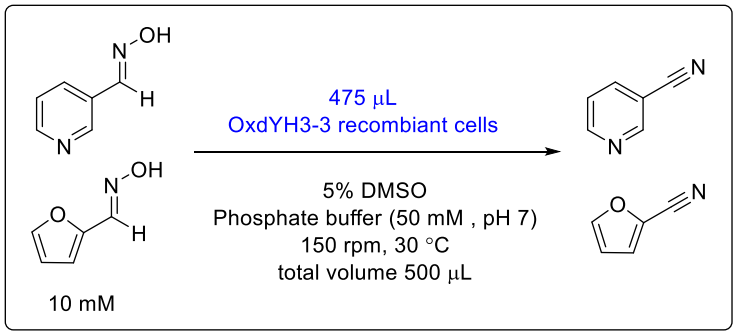

Scheme 31. The catalytic reaction of *E*-pyridine-3-aldoxime and 2-furfuryl aldoxime with OxdYH3-3 recombinant cells as a whole cell catalyst.

6.3.7. Determination of conversion by HPLC

The conversion was measured by HPLC (Shimadzu UFLC Prominence). The reaction mixture was extracted by the same volume of ethyl acetate twice, and the same volume of isopropanol was added to the extract. The mobile phase was 90% hexane and 10% isopropanol at 0 min, and the binary gradient

was applied for 10 min. The Chiralcel OD-H column (250 x 4.6 mm, Daicel, Japan) was used for analysis at 30 °C.

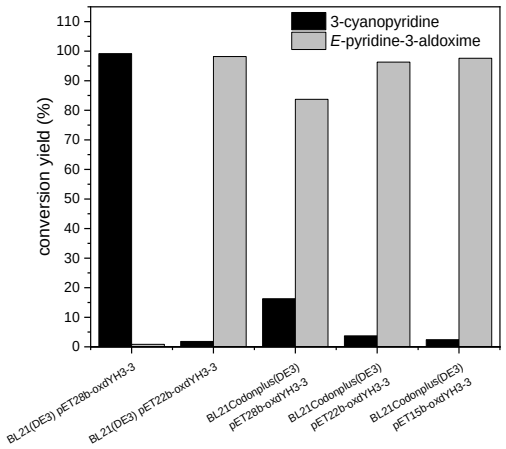

Figure 83. Conversion measured by HPLC. OxdYH3-3 was cloned to various pET plasmids and transformed to different hosts. The activity for 10 mM *E*-pyridine-3-aldoxime was measured after 20 h of reaction.

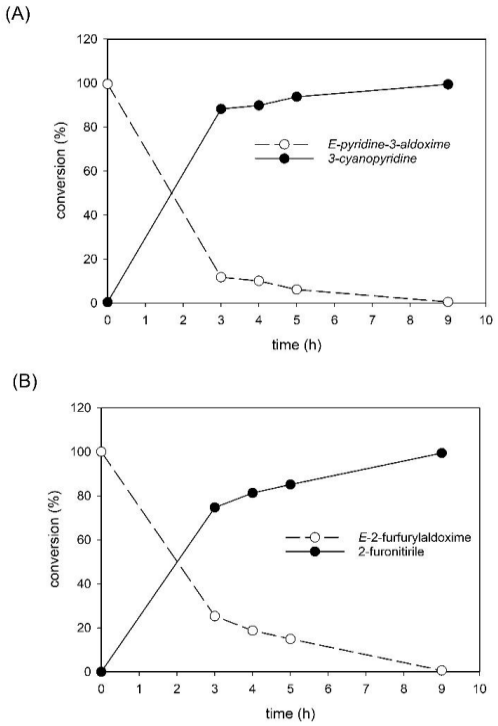

Figure 84. The conversion of *E*-pyridine-3-aldoxime and *E*-2-furfuryl aldoxime using BL21(DE3)/pET28b-*OxdYH3-3*: (A) Conversion of *E*-pyridine-3-aldoxime to 3-cyanopyridine; (B) Conversion of *E*-2-furfuryl aldoxime to 2-furonitrile.

Retention time: 2-furfuryl aldoxime, 4.08 min; 2-furonitrile, 3.16 min; *E*-pyridine-3-aldoxime, 8.15 min; 3-cyanopyridine, 5.80 min.

6.3.8. Construction of mutant library by error-prone PCR

The mutant library was constructed by using a PCR random mutagenesis kit (GeneMorph II Random Mutagenesis Kit, Agilent). Forward primer was T7 promoter primer (5'-TAATACGACTCAC-TATAGGG-3'), and the reverse primer was T7 terminator primer (5'-GCTAGTTATTGCTCAGCGG-3'). To be specific, an error-prone PCR was performed in 50 µL of a reaction solution containing 100 ng pET28b-OxdYH3-3 as a template, 1 µL of titanium Taq polymerase (Takara), 640 µM $MgSO_4$, 40 µM dGTP, 0.1 µM each of primers, 1 µL dNTP mix and 5 µL titanium PCR buffer. The PCR program consisted of 25 cycles of 94 °C for 30 s, 45 °C for 1.5 min, and 68 °C for 1 min. The amplified DNA fragments were purified and cloned into *Nco*I and *Hind*III site of pET28b vector (Novagen) using In-fusion HD Cloning Kit (Takara) (**Figure 85**). The mutated pET28b-OxdYH3-3 was transformed into *E. coli* BL21(DE3) and spread on the LB plate containing kanamycin (50 $\mu g \cdot mL^{-1}$). Colonies on the plates were inoculated to 1 mL of an autoinduction medium placed in 96 deep well plates and cultured for 18 h at 30 °C. Twenty microliters of cell suspension were transferred to 96 deep-well plates containing fresh 980 µL autoinduction medium and cultivated for 20 h at 30 °C.

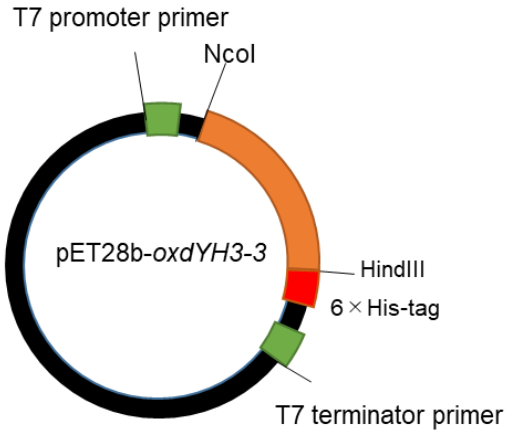

Figure 85. The plasmid map of pET28b-*OxdYH3-3* containing WT and mutant genes.

6.3.9. Measurement of the UV spectrum of aldoximes and nitriles

6.3.9.1. Screening OxdYH3-3 mutants having enhanced activity toward 2-furfuryl aldoxime by UV absorbance scan

A diluted solution of 2-furfuryl aldoxime, *E*-pyridine-3-aldoxime, 2-furonitrile, and 3-cyanopyridine were prepared by diluting 200 mM stock solution (200 mM dissolved in DMSO) with water 100 times. The diluted solutions were located to a 96 well plate, and the maximum wavelength of each aldoxime and nitrile was determined by scanning from 230 nm to 350 nm using UV microspectrometer (Biorad). To screening OxdYH3-3 mutants, fully grown OxdYH3-3 mutant clones in section 6.3.8 were harvested by centrifugation at 4 °C and 4,000 rpm for 30 min. The cell pellet was washed with 50 mM phosphate buffer (pH 7.0) and resuspended in 1mL of the phosphate buffer. 190 µL cell suspension was transferred to 96 well plates, and 10 µL of 2-furfuryl aldoxime (200 mM dissolved in DMSO) was added. After 3 and 20 h incubation at 30 °C, the reaction mixture was centrifuged at 10,000 rpm for 10 min to remove cell debris, and 5-10 µL solutions were transferred to clean 96 well plates following 10-20 time dilution with phosphate buffer to measure UV absorbance. The result is shown in **Figure 86**.

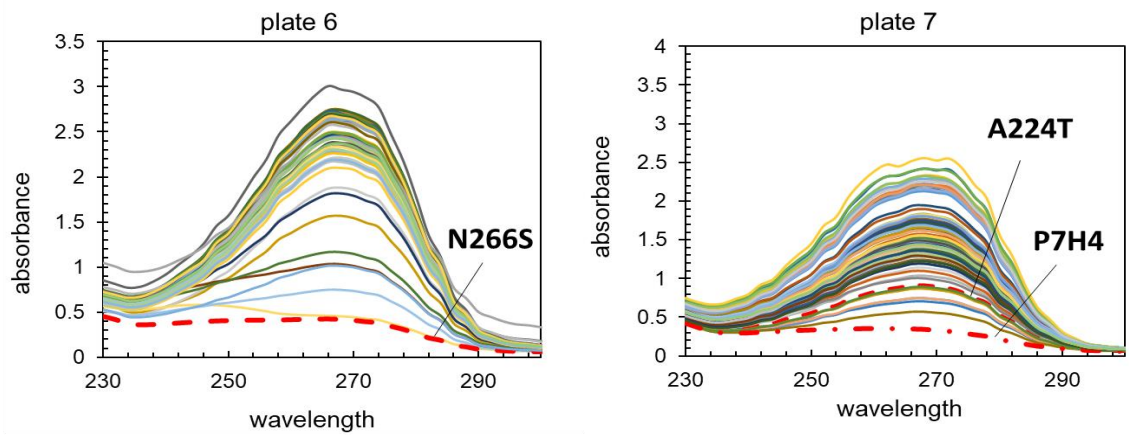

Figure 86. The UV spectrum scan of OxdYH3-3 mutants. 10 mM 2-furfuryl aldoxime was added in the plate, and after overnight, the reaction mixture was isolated and diluted. The UV absorbance between 230 and 300 nm was measured. The red dash line means the UV absorbance of selected mutants directed by arrows.

6.3.9.2. Measurement of the UV spectrum of the reaction mixtures containing OxdYH3-3 WT, N266S, A224T, and P7H4

The enhanced activity toward *E*-pyridine-3-aldoxime and 2-furfuryl aldoxime of OxdYH3-3 N266S, A224T, and P7H4 were screened by measuring UV absorbance. After biotransformation in section

6.3.10, 100 µL reaction mixture was isolated and centrifuged. The clear supernatant was diluted 20 times with phosphate buffer (pH 7.0, 50 mM) and transferred to 96 microwell plate to measure spectrophotometry. The absorbance of *E*-pyridine-3-aldoxime and 3-cyanopyridine, 2-furfuryl aldoxime and 2-furonitrile were scanned from 200 nm to 300 nm to observe the difference between aldoxime and nitrile as time course. After reaction supernatant diluted with phosphate buffer (pH 7.0, 50 mM) from 10 to 100 times, the absorbance was determined by a microplate spectrophotometer. The result is shown in **Figure 87**.

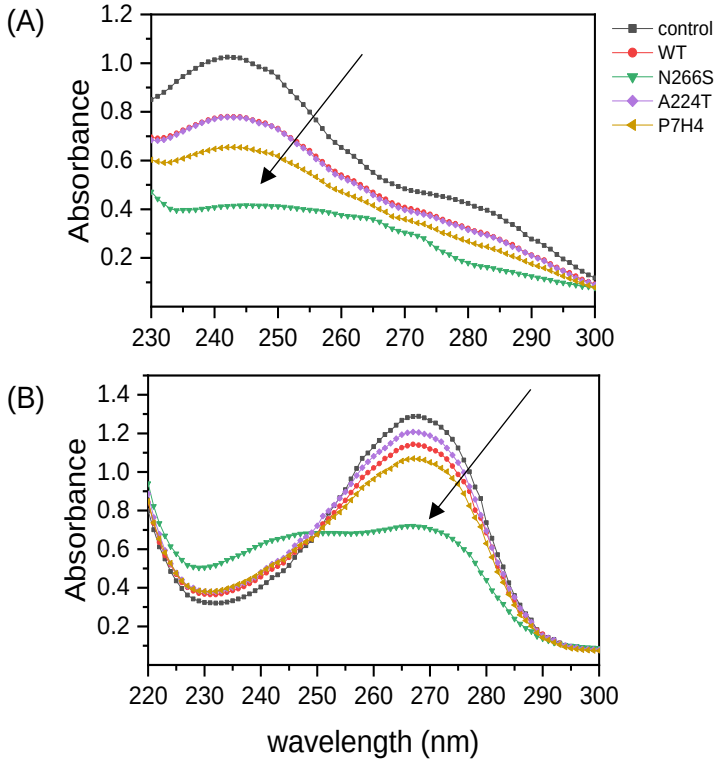

Figure 87. Absorbance scans of the reaction solution at 1 h. The reaction was done with 50 mM *E*-3-pyridine aldoxime (A) and 2-furfruyl aldoxime (B). The reaction solution was diluted with phosphate buffer up to 100 times to measure UV-scan. The arrows indicate a decrease in absorbance at 245 and 270 by OxdYH3-3 N266S, which are corresponding to decrease in *E*-pyridine-3-aldoxime and 2-furfuryl aldoxime, respectively.

6.3.10. Analysis of the DNA sequence of OxdYH3-3 mutants

Selected mutants were subjected to DNA sequence analysis. The mutant clones transformed into BL21(DE3) were spread on LB-agar plate containing 50 µg·mL^{-1} kanamycin and incubated at 37 ºC for 20 h. The single colony was inoculated in 5 mL LB broth and cultured for overnight at 37 ºC in the shaking incubator at 150 rpm. The plasmid was isolated using the plasmid isolated kit (Analytik Jena),

and nucleotide sequences were analysed by the ABI 3730XL sequencing machines using a modified Sanger method (Eurofins Genomics).

6.3.11. Determination of conversion from aldoximes to nitriles by GC

The conversion was determined by GC measurement (Shimadzu GC-2010 plus). GC conditions were optimized to efficiently separate the products from the reactants in the Phenomenex ZB-5MSi capillary column (30 m × 0.25 mm × 0.25 μm). Nitrogen was used as carrier gas at a flow rate of 2.25 $mL \cdot min^{-1}$ with an average velocity of 46.9 $cm \cdot s^{-1}$ and a pressure of 147.6 kPa. The analysis run was started with an oven temperature of 60 °C ramping to 250 °C at 15 $°C \cdot min^{-1}$.

6.3.12. Dehydration of aldoximes to nitriles using OxdYH3-3 WT and mutants

The OxdYH3-3 WT and selected mutant cells were inoculated to 5 mL of TB (terrific broth) medium containing 50 $\mu g \cdot mL^{-1}$ kanamycin. After overnight cultivation at 37 °C, the culture was re-inoculated to 50 mL of modified autoinduction medium containing 0.2% glucose, 0.5% lactose, 1.2% tryptone, 2.4% yeast extract, 0.5% glycerol, and phosphate (0.17 M KH_2PO_4 and 0.72 M K_2HPO_4) and kept at 30 °C up to 18 h with shaking. The overexpressed cell was collected by centrifugation and washed with distilled water once. The pellet was resuspended to 5 mL of phosphate buffer (pH 7.0, 50 mM) and stored at 4 ºC freezer until it is used in the next experiment (the wet cell weight; **Table 29**). The overexpression level was analyzed by SDS-PAGE of the whole cell.

Table 29. The wet weight of cells.

OxdYH3-3	wet cell weight (g)
WT	0.59
N266S	0.577
A224T	0.57
P7H4	0.595

A hundred microliters of *E*-pyridine-3-aldoxime and 2-furfuryl aldoxime stock solution (0.5 and 1 M in DMSO) were added to 900 μL the cell suspensions. The mixtures were incubated in a shaker at 30 °C with 1,000 rpm for 1 h, and the 100 μL reaction mixture was taken to measure GC (**Scheme 32**). Twenty microliters of 1 M NaOH and 180 μL ethyl acetate were added to the reaction solution to inactivate the enzyme. The reaction mixture was centrifuged to isolate the organic phase, which was subjected to GC measurement. The results are shown in **Figure 88** and **Table 30**.

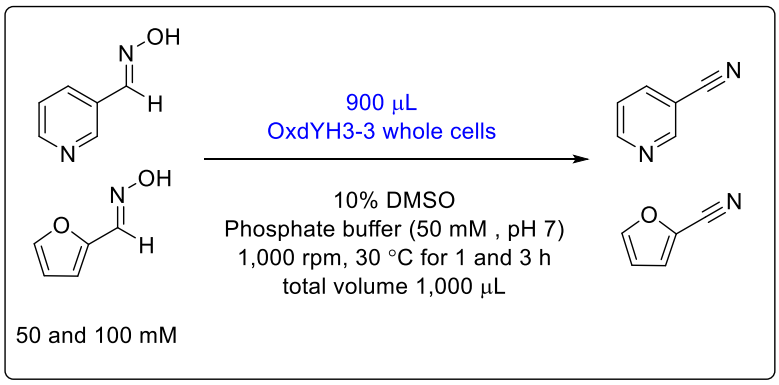

Scheme 32. The biocatalytic dehydration of 50 and 100 mM *E*-pyridine-3-aldoxime and 2-furfuryl aldoxime with OxdYH3-3 WT and mutants as a whole-cell catalyst.

Table 30. The activity of OxdYH3-3 WT and mutants. The concentration of aldoxime 50 mM (above) and the conversion was measured after 1 hand 3 h reaction at 30 °C. In the case of 100 mM aldoximes, the concentrations and activities were measured in 1h (below).

	Conversion (%)			
OxdYH3-3	*E*-pyridine-3-aldoxime		2-furfuryl aldoxime	
	1h	3h	1h	3h
WT	19.0	-	4.9	14.6
N266S	54.2	75.9	40	55
A224T	19.3	26.3	12	14.1
P7H4	25.3	40.1	16.5	21.2

	OxdYH3-3	U·g^{-1} (µmol·min^{-1}·g^{-1})	Conversion (%)
E-pyridine-3-aldoxime	WT	0.5	9.9
	N266S	1.7	31.2
	A224T	0.5	10.9
	P7H4	0.8	16.5
2-furfuryl aldoxime	WT	0.3	5.4
	N266S	1.2	20.3
	A224T	0.3	4.9
	P7H4	0.4	6.7

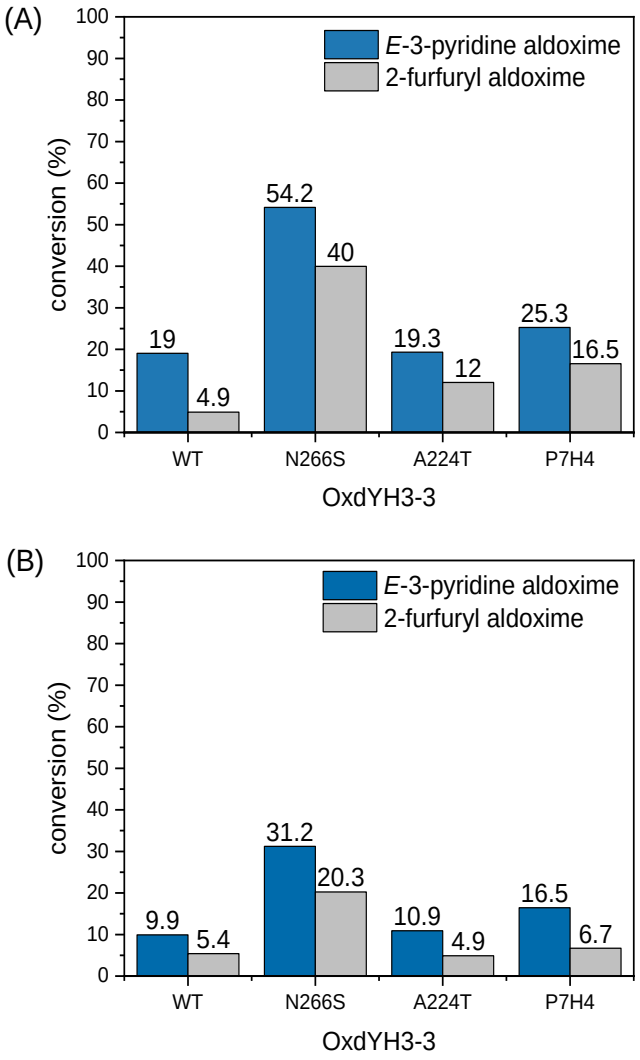

Figure 88. The conversion of OxdYH3-3 WT and mutants. The conversion in 1 h toward *E*-pyridine-3-aldoxime and 2-furfuryl aldoxime were compared. The conversion was measured for 50 mM aldoximes (A) and 100 mM aldoximes (B).

6.3.13. Homology modelling

The homology model of OxdYH3-3 wild-type and N266S were created by SWISS-MODEL (http://swissmodel.expasy.org), and Modeller using OxdRE containing heme and 1-*Z*-butanal oxime as a template and following verification by QMEAN server and ERRAT in ERRAT server[153,171]. The modelling created by SWISS-MODEL showed high scores within verification; therefore, This model used for further study. The structure optimization of 2-*E*-furfuryl aldoxime was done by Abogardro[172]. Molecular docking studies with OxdYH3-3 WT and N266S were performed by Autodock4 program[173]

and visualized by autodock tools and PyMOL (The PyMOL Molecular Graphics System, Version 1.2r3pre, Schrödinger, LLC). The hydrogen bonds between ligands adjacent residues were analyzed by LIGPLOT program[174]. Models chosen for the next step was subjected to analysis of residues network using Ring 2.0 and Cytoscape[166,167] and further analysis using UCSF Chimera program[175].

6.4. Appendix

6.4.1. Nucleotide sequences

6.4.1.1. MosA (GeneBank accession number: CP001157.1)[176]

ATGCAGCGATCACTGACCGACCCGCAGCTTCAGGCGGCAGCGGCGGCGGCGGCGGACTTCCGGATTCTGCCGGAT
GCGACGGTGATCAAGATCGGTGGACAGAGTGTCATCGATCGTGGCCGAGCGGCGGTCTATCCGCTGGTGGACGAG
ATCGTCGCCGCCCGCAAGAACCACAAGCTGCTGATCGGTACCGGTGCAGGCACCCGGGCCCGGCACCTCTACTCG
ATCGCCGCCGGGCTCGGTCTGCCGGCGGGCGTGCTCGCGCAGCTCGGCTCTTCGGTGGCCGACCAGAACGCCGCC
ATGCTGGGGCAACTCCTGGCGAAGCACGGTATCCCCGTGGTCGGCGGTGCCGGACTGTCGGCGGTGCCGCTTTCC
CTCGCCGAGGTGAACGCCGTCGTCTTCAGCGGCATGCCGCCCTACAAGTTGTGGATGCGTCCCGCTGCCGAAGGT
GTGATTCCGCCCTACCGCACCGACGCCGGCTGCTTCCTGCTGGCTGAACAGTTCGGCTGCAAGCAGATGATCTTC
GTCAAGGACGAGGACGGCCTCTACACCGCCAACCCGAAGACCTCGAAGGACGCCACCTTCATCCCGAGGATCTCG
GTCGACGAAATGAAGGCGAAGGGGCTGCACGACTCGATCCTCGAGTTCCCGGTGCTCGACCTCCTCCAGTCGGCT
CAGCATGTCCGCGAGGTGCAGGTCGTGAACGGCCTCGTCCCCGGCAACCTGACCCGCGCGCTCGCAGGCGAGCAC
GTCGGCACCATCATCACCGCGAGCTGA

6.4.1.2. MosB (GeneBank accession number: CP001157.1)[176]

ATGACCGACACTACCAACAGCATCAAGCACGTCATCTCGCCGCTCGCGCGCCAGACCCTGCAGGACCGCGATCTC
ACCCGTCCGGTCGCCGGCAAGCGCCCGATCCGCCTGCTGCCCTGGCTGCAGGTCGTCAAGATCGGTGGCCGCGTC
ATGGATCGTGGCGCCGATGCGATCCTGCCGCTCGTCGAGGAACTGCGCAAGCTGCTGCCCGAGCACCGCCTGCTG
ATCCTGACCGGTGCCGGTGTCCGTGCCCGCCACGTCTTCAGCGTCGGCCTCGACCTCGGCCTGCCGGTCGGCTCG
CTCGCCCCGCTGGCTGCCAGCGAAGCCGGGCAGAACGGCCACATCCTCGCGGCGATGCTCGCCTCCGAGGGCGTC
TCCTACGTCGAGCATCCGACCGTCGCCGACCAACTGGCGATCCACCTCTCCGCCACCCGCGCCGTGGTCGGCAGC
GCCTTCCCGCCCTACCACCACCACGAGTTCCCGGGCTCGCGCATCCCGCCGCACCGGGCCGACACCGGTGCCTTC
CTGCTCGCCGATGCATTCGGCGCGGCCGGCCTGACCATCGTCGAGAACGTGGACGGGATATACACCGCCGATCCC
AATGGCCCCGATAGGGGGCAGGCACGCTTCCTGCCGGAGACGAGCGCCACCGACCTGGCGAAGTCGGAAGGCCCA
CTGCCGGTCGACCGCGCACTCCTCGACGTCATGGCGACCGCGCGCCACATCGAGCGCGTGCAGGTGGTGAACGGA
CTCGTGCCGGGTCGACTCACCGCCGCGTTGCGCGGCGAGCACGTCGGGACGCTGATCCGTACCGGTGTGCGTCCG
GCCTGA

6.4.1.3. OCR WT[90]

ATGGCTAAAACTGTTTACTTCATCGCAGGTGCTTCCAGAGGTATCGGTCTCGAGGTTGCTTCCCAGCTGAGTGCA
AACCCAGACAATTATGTTATTGCATCCTATAGATCTGAAAAGTCTGCTTCAGGACTTTTGGAGCTGGCAAAGAAG
GATAATGTCGACACAATTGTGTTGGATATTGCAAGCCAGGAATCGATTGATGCTGTTCCAGCACAGATTTCCAAG
CTGACTGATGGAATCGATGTTGCCTTGATCAACGCTGGAATTGCCAACGCTATGTGTCCGATTCTCGAATGTTCT
AGAGAGTCCTACACTGATCACTGGACAACCAATGCCTTGGGTCCAATCATGCTCTACCAAGCTATTCATAAGTTC
ATGCTCCAGAGAGAGACCAGAAAAGTGTTCTTTACCACGAGTGCTGGTGGTTCCATTCAGGCTAAGATACCCGTG
CCTGTGAGTGGTTACGGTATGTCCAAGGCTGCGCTTAATTATGCTGTGAGAAAACTTGCTGACGAGTGCTACAAG

GACAACTTCACTATTGTGTTGCTGCATCCTGGTTTTGTTAAGACGGACATGGGTCAAAGCGCCATTCAGAAGATG
TCAAATGGAAATGCTGAGCTTCTTGCTTACATTGACTCAATGACTATTGATGTTCCTACCAGTGCTGGCCAAATC
GTCGGTGCCATTATGACCTTGGACAAGCAGAGCAGCGGTAGATTTATCAACGCTGCTGACCAGTTTGACATGCCA
TTTTAGTAA

6.4.1.4. OCR-P2G6 (in this study)

ATGGCTAAAACTGTTTACTTCATCGCAGGTGCTTCCAGAGGTATCGGTCTCGAGGTTGCTTCCCAGCTGAGTGCA
AACCCAGACAATTATGTTATTGCATCCTATAGATCTGAAAAGTCTGCTTCAGGACTTTTGGAGCTGGCAAAGAAG
GATAATGTCGTCACAATTGTGTTGGATATTGCAAGCCAGGAATCGATTGATGCTGTTCCAGCACAGATTTCCAAG
CTGACTGATGGAATCGATGTTGCCTTGATCAACGCTGGAATTGCCAACGCTATGTGTCCGATTCTCGAATGTTCT
AGAGAGTCCTACACTGATCACTGGACAACCAATGCCTTGGGTCCAATCATGCTCTACCAAGCTATTCATAAGTTC
ATGCTCCAGAGAGAGACCAGAAAAGTGTTCTTTACCACGAGTGCTGGTGGTTCCATTCAGGCTAAGATACCCGTG
CCTGTGAGTGGTTACGGTATGTCCAAGGCTGCGCTTAATTATGCTGTGAGAAAACTTGCTGACGAGTGCTACAAG
GACAACTTCACTATTGTGTTGCTGCATCCTGGTTTTGTTAAGACGGACATGGGTCAAAGCGCCATTCAGAAGATG
TCAAATGGAAATGCTGAGCTTCTTGCTTACATTGACTCAATGACTATTGATGTTCCTACCAGTGCTGGCCAAATC
GTCGGTGCCATTATGACCTTGGACAAGCAGAGCAGCGGTAGATTTATCAACGCTGCTGACCAGTTTGACATGCCA
TTTTAG

6.4.1.5. GDH2[101]

ATGTATCCGGATTTAAAAGGAAAAGTCGTCGCTATTACAGGAGCTGCTTCAGGGCTCGGAAAGGCGAT
GGCCATTCGCTTCGGCAAGGAGCAGGCAAAAGTGGTTATCAACTATTATAGTAATAAACAAGATCCGA
ACGAGGTAAAAGAAGAGGTCATCAAGGCGGGCGGTGAAGCTGTTGTCGTCCAAGGAGATGTCACGAAA
GAGGAAGATGTAAAAAATATCGTGCAAACGGCAATTAAGGAGTTCGGCACACTCGATATTATGATTAA
TAATGCCGGTCTTGAAAATCCTGTGCCATCTCACGAAATGCCGCTCAAGGATTGGGATAAAGTCATCG
GCACGAACTTAACGGGTGCCTTTTTAGGAAGCCGTGAAGCGATTAAATATTTCGTAGAAAACGATATC
AAGGGAAATGTCATTAACATGTCCAGTGTGCACGAAGTGATTCCTTGGCCGTTATTTGTCCACTATGC
GGCAAGTAAAGGCGGGATAAAGCTGATGACAAAGACATTAGCGTTGGAATACGCGCCGAAGGGCATTC
GCGTCAATAATATTGGGCCAGGTGCGATCAACACGCCAATCAATGCTGAAAAATTCGCTGACCCTAAA
CAGAAAGCTGATGTAGAAAGCATGATTCCAATGGGATATATCGGCGAACCGGAGGAGATCGCCGCAGT
AGCAGCCTGGCTTGCTTCGAAGGAAGCCAGCTACGTCACAGGCATCACGTTATTCGCGGACGGCGGTA
TGACACTCTATCCTTCATTCCAGGCAGGCCGCGGTTAA

6.4.1.6. OxdYH3-3 WT[162]

ATGGAATCTGCAATCGGCGAACACCTTCAATGCCCGCGCACTCTGACCAGGCGGGTCCCGGATACCTATTCGCCA
CCGTTTCCCATGTGGGTCGGGCGCGCAGACGACACATTGCACCAGGTCGTGATGGGCTATCTCGGCGTGCAGTTC
CGCGGCGAGGATCAGCGCCCGGCAGCACTGCGGGCGATGCGGGATATCGTCGCCGGCTTCGACTTGCCGGACGGA
CCGGCACACCACGATCTCACCCATCACATCGACAACCAGGGCTACGAGAACCTGATCGTGGTCGGTTACTGGAAA
GATGTTTCTTCCCAACATCGTTGGAGCACATCACCTCCAGTGTCCTCCTGGTGGGAGTCCGAAGACCGCCTGTCG

GACGGATTGGGGTTCTTCCGCGAGATCGTGGCACCGAGAGCCGAACAATTCGAAACGCTCTACGCGTTCCAAGAC
GACCTCCCCGGGGTGGGAGCCGTCATGGACGGTGTCAGCGGCGAAATCAACGAGCACGGCTACTGGGGTTCGATG
CGCGAGCGGTTTCCGATCTCCCAAACCGACTGGATGCAGGCCTCGGGCGAACTGCGGGTCGTCGCCGGTGACCCC
GCCGTAGGTGGACGCGTAGTAGTGCGGGGACACGACAACATCGCACTGATCAGGTCCGGGCAGGACTGGGCCGAC
GCGGAAGCAGACGAACGCAGCCTCTACCTGGACGAAATCCTGCCCACTCTTCAATCGGGCATGGACTTCCTCCGC
GACAACGGCCCGGCCGTCGGGTGCTACAGCAACCGATTCGTACGCAATATCGACATCGACGGAAACTTCCTCGAC
CTGAGCTACAACATCGGCCACTGGGCCTCCCTCGACCAACTCGAACGGTGGTCGGAATCCCACCCGACCCATCTA
CGGATCTTCACGACGTTCTTCCGGGTGGCCGAGGGCCTGTCGAAATTGCGTCTCTACCATGAGGTCTCGGTATTC
GATGCCGCCGATCAGCTCTACGAGTACATCAATTGCCATCCCGGGACCGGAATGCTGCGCGACGCGGTGATCACC
GCCGAGCACTGA

6.4.1.7. OxdYH3-3 N266S (in this study)

ATGGAATCTGCAATCGGCGAACACCTTCAATGCCCGCGCACTCTGACCAGGCGGGTCCCGATACCTATTCGCCAC
CGTTTCCCATGTGGGTCGGGCGCGCAGACGACACATTGCACCAGGTCGTGATGGGCTATCTCGGCGTGCAGTTCC
GCGGCGAGGATCAGCGCCCGGCAGCGCTGCGGGCGATGCGGGATATCGTCGCCGGCTTCGACTTGCCGGACGGAC
CGGCACACCACGATCTCACCATCACATCGACAACCAGGGCTACGAGAACCTGATCGTGGTCGGTTACTGGAAAGA
TGTTTCTTCCCAACATCGTTGGAGCACATCACCTCCAGTGTCCTCCTGGTGGGAGTCCGAAGACCGCCTGTCGGA
CGGATTGGGGTTCTTCCGCGAGATCGTGGCACCGAGAGCCGAACAATTCGAAACGCTCTACGCGTTCCAAGACGA
CCTCCCCGGGGTGGGAGCCGTCATGGACGGTGTCAGCGGCGAAATCAACGAGCACGGCTACTGGGGTTCGATGCG
CGAGCGGTTTCCGATCTCCCAAACCGACTGGATGCAGGCCTCGGGCGAACTGCGGGTCGTCGCCGGTGACCCCGC
CGTAGGTGGACGCGTAGTAGTGCGGGGACACGACAACATCGCACTGATCAGGTCCGGGCAGGACTGGGCCGACGC
GGAAGCAGACGAACGCAGCCTCTACCTGGACGAAATCCTGCCCACTCTTCAATCGGGCATGGACTTCCTCCGCGA
CAACGGCCCGGCCGTCGGGTGCTACAGCAACCGATTCGTACGCAGTATCGACATCGACGGAAACTTCCTCGACCT
GAGCTACAACATCGGCCACTGGGCCTCCCTCGACCAACTCGAACGGTGGTCGGAATCCCACCCGACCCATCTACG
GATCTTCACGACGTTCTTCCGGGTGGCCGAGGGCCTGTCGAAATTGCGTCTCTACCATGAGGTCTCGGTATTCGA
TGCCGCCGATCAGCTCTACGAGTACATCAATTGCCATCCCGGGACCGGAATGCTGCGCGACGCGGTGATCACCGC
CGAGCACAAGCTTGCGGCCGCACTCGAGCACCACCACCACCACCACTGA

6.4.1.8. OxdYH3-3 A224T (in this study)

ATGGAATCTGCAATCGGCGAACACCTTCAATGCCCGCGCACTCTGACCAGGCGGGTCCCGGATACCTATTCGCCA
CCGTTTCCCATGTGGGTCGGGCGCGCAGACGACACATTGCACCAGGTCGTGATGGGCTATCTCGGCGTGCAGTTC
CGCGGCGAGGATCAGCGCCCGGCAGCACTGCGGGCGATGCGGGATATCGTCGCCGGCTTCGACTTGCCGGACGGA
CCGGCACACCACGATCTCACCCATCACATCGACAACCAGGGCTACGAGAACCTGATCGTGGTCGGTTACTGGAAA
GATGTTTCTTCCCAACATCGTTGGAGCACATCACCTCCAGTGTCCTCCTGGTGGGAGTCCGAAGACCGCCTGTCG
GACGGATTGGGGTTCTTCCGCGAGATCGTGGCACCGAGAGCCGAACAATTCGAAACGCTCTACGCGTTCCAAGAC
GACCTCCCCGGGGTGGGAGCCGTCATGGACGGTGTCAGCGGCGAAATCAACGAGCACGGCTACTGGGGTTCGATG
CGCGAGCGGTTTCCGATCTCCCAAACCGACTGGATGCAGGCCTCGGGCGAACTGCGGGTCGTCGCCGGTGACCCC
GCCGTAGGTGGACGCGTAGTAGTGCGGGGACACGACAACATCGCACTGATCAGGTCCGGGCAGGACTGGACCGAC
GCGGAAGCAGACGAACGCAGCCTCTACCTGGACGAAATCCTGCCCACTCTTCAATCGGGCATGGACTTCCTCCGC
GACAACGGCCCGGCCGTCGGGTGCTACAGCAACCGATTCGTACGCAATATCGACATCGACGGAAACTTCCTCGAC

CTGAGCTACAACATCGGCCACTGGGCCTCCCTCGACCAACTCGAACGGTGGTCGGAATCCCACCCGACCCATCTA
CGGATCTTCACGACGTTCTTCCGGGTGGCCGAGGGCCTGTCGAAATTGCGTCTCTACCATGAGGTCTCGGTATTC
GATGCCGCCGATCAGCTCTACGAGTACATCAATTGCCATCCCGGGACCGGAATGCTGCGCGACGCGGTGATCACC
GCCGAGCACAAGCTTGCGGCCGCACTCGAGCACCACCACCACCACCACTGA

6.4.1.9. OxdYH3-3 P7-H4 (in this study)

ATGGAATCTGCAATCGGCGAACACCTTCAATGCCCGCGCACTCTGACCAGGCGGGTCCCGGATACCTATTCGCCA
CCGTTTCCCATGTGGGTCGGGCGCGCAGACGACACATTGCACCAGGTCGTGATGGGCTATCTCGGCGTGCAGTTC
CGCGGCGAGGATCAGCGCCCGGCAGCACTGCGGGCGATGCGGGATATCGTCGCCGGCTTCGACTTGCCGGACGGA
CCGGCACACCACGATCTCACCCATCACATCGACAACCAGGGCTACGAGAACCTGATCGTGGTCGGTTACTGGAAA
GATGTTTCTTCCCAACATCGTTGGAGCACATCACCTCCAGTGTCCTCCTGGTGGGAGTCCGAAGACCGCCTGTCG
GACGGATTGGGGTTCTTCCGCGAGATCGTGGCACCGAGAGCCGAACAATTCGAAACGCTCTACGCGTTCCAAGAC
GACCTCCCCGGGGTGGGAGCCGTCATGGACGGTGTCAGCGGCGAAATCAACGAGCACGGCTACTGGGGTTCGATG
CGCGAGCGGTTTCCGATCTCCCAAACCGACTGGATGCAGGCCTCGGGCGAACTGCGGGTCGTCGCCGGTGACCCC
GCCGTAGGTGGACGCGTAGTAGTGCGGGGACACGACAACATCGCACTGATCAGGTCCGGGCAGGACTGGGCCGAC
GCGGAAGCAGACGAACGCAGCCTCTACCTGGACGAAATCCTGCCCACTCTTCAATCGGGCATGGACTTCCTCCGC
GACAACGGCCCGGCCGTCGGGTGCTACAGCAACCGATTCGCACGCAATATCGACATCGACGGGAACTTCCTCGAC
CTGAGCTACAACATCGGCCACTGGGCCTCCCTCGACCAACTCGAACGGTGGTCGGAATCCCACCCGACCCATCTA
CGGAGCTTCACGACGTTCTTCCGGGTGGCCGAGGGCCTGTCGAAATTGCGTCTCTACCATGAGGTCTCGGTATTC
GATGCCGCCGATCTGCTCTACGAGTACATCAATTGCCATCCCGGGACCGGAATGCTGCGCGACGCGGTGATCACC
GCCGAGCACAAGCTTGCGGCCGCACTCGAGCACCACCACCACCACCACTGA

7. References

[1] R. A. Sheldon, J. M. Woodley, *Chem. Rev.* **2018**, *118*, 801–838.

[2] U. Yoko, S. Kazuhiko, *Green Chem.* **2003**, *5*, 373–375.

[3] K. Sato, M. Hyodo, M. Aoki, X.-Q. Zheng, R. Noyori, *Tetrahedron* **2001**, *57*, 2469–2476.

[4] K. Sato, M. Hyodo, J. Takagi, M. Aoki, R. Noyori, *Tetrahedron Lett.* **2000**, *41*, 1439–1442.

[5] K. Sato, J. Takagi, M. Aoki, R. Noyori, *Tetrahedron Lett.* **1998**, *39*, 7549–7552.

[6] U. Markel, D. F. Sauer, J. Schiffels, J. Okuda, U. Schwaneberg, *Angew. Chemie Int. Ed.* **2019**, *58*, 4454–4464.

[7] J. T. Lecomte, D. A. Vuletich, A. M. Lesk, *Curr. Opin. Struct. Biol.* **2005**, *15*, 290–301.

[8] E. T. Kaiser, D. S. Lawrence, *Science* **1984**, *226*, 505–11.

[9] M. T. Reetz, *Acc. Chem. Res.* **2019**, *52*, 336–344.

[10] M. T. Reetz, J. J. P. Peyralans, A. Maichele, Y. Fu, M. Maywald, *Chem. Commun.* **2006**, 4318–4320.

[11] M. T. Reetz, *Top. Organomet. Chem.* **2009**, *25*, 63–92.

[12] D. Fenske, M. Gnida, K. Schneider, W. Meyer-Klaucke, J. Schemberg, V. Henschel, A.-K. K. Meyer, A. Knöchel, A. Müller, *ChemBioChem* **2005**, *6*, 405–413.

[13] A. Zaks, A. M. Klibanov, *Science* **1984**, *224*, 1249–1251.

[14] C. C. C. R. de Carvalho, *Microb. Biotechnol.* **2017**, *10*, 250–263.

[15] M. Breuer, K. Ditrich, T. Habicher, B. Hauer, M. Keßeler, R. Stürmer, T. Zelinski, *Angew. Chemie Int. Ed.* **2004**, *43*, 788–824.

[16] M. Brovetto, D. Gamenara, P. Saenz Méndez, G. A. Seoane, *Chem. Rev.* **2011**, *111*, 4346–4403.

[17] B. M. Nestl, S. C. Hammer, B. A. Nebel, B. Hauer, *Angew. Chemie Int. Ed.* **2014**, *53*, 3070–3095.

[18] G. Grogan, *Annu. Rep. Prog. Chem., Sect. B* **2009**, *105*, 206–231.

[19] L. A. Hulshof, J. H. Roskam, *Enzymic Resolution of Racemic Phenylglycidic Acid Esters in the Manufacture of Diltiazem*, **1989**, EP343714 A1 19891129.

[20] R. A. Sheldon, P. C. Pereira, *Chem. Soc. Rev.* **2017**, *46*, 2678–2691.

[21] C. K. Savile, J. M. Janey, E. C. Mundorff, J. C. Moore, S. Tam, W. R. Jarvis, J. C. Colbeck, A. Krebber, F. J. Fleitz, J. Brands, et al., *Science* **2010**, *329*, 305–309.

[22] J. Liang, J. Lalonde, B. Borup, V. Mitchell, E. Mundorff, N. Trinh, D. A. Kochrekar, R. Nair Cherat, G. G. Pai, *Org. Process Res. Dev.* **2010**, *14*, 193–198.

[23] R. N. Patel, *Biomolecules* **2013**, *3*, 741–777.

[24] M. Hara, Y. Takuma, M. Katsurada, A. Hosokawa, Y. Matsumoto, Y. Kasuga, N. Watanabe, *Process for Producing (3R,5S)-(E)-7-[2-Cyclopropyl-4-(4-Fluorophenyl)-Quinolin- 3-Yl]-3, 5-Dihydroxyhept-6-Enic Acid Esters*, **2003**, US20040030139A1.

[25] W. R. Streit, R. A. Schmitz, *Curr. Opin. Microbiol.* **2004**, *7*, 492–498.

[26] F. G. Healy, R. M. Ray, H. C. Aldrich, A. C. Wilkie, L. O. Ingram, K. T. Shanmugam, *Appl. Microbiol. Biotechnol.* **1995**, *43*, 667–674.

[27] S. Voget, C. Leggewie, A. Uesbeck, C. Raasch, K.-E. Jaeger, W. R. Streit, *Appl. Environ. Microbiol.* **2003**, *69*, 6235–6242.

[28] W. H. Eschenfeldt, L. Stols, H. Rosenbaum, Z. S. Khambatta, E. Quaite-Randall, S. Wu, D. C. Kilgore, J. D. Trent, M. I. Donnelly, *Appl. Environ. Microbiol.* **2001**, *67*, 4206–4214.

[29] G. DeSantis, Z. Zhu, W. A. Greenberg, K. Wong, J. Chaplin, S. R. Hanson, B. Farwell, L. W. Nicholson, C. L. Rand, D. P. Weiner, et al., **2002**, *124*, 9024–9025.

[30] K. Hult, P. Berglund, *Trends Biotechnol.* **2007**, *25*, 231–238.

[31] H. Renata, Z. J. Wang, F. H. Arnold, *Angew. Chemie Int. Ed.* **2015**, *54*, 3351–3367.

[32] M. T. Reetz, R. Mondie`re, J. D. Carballeira, *Tetrahedron Lett.* **2007**, *48*, 1679–1681.

[33] Z. Sun, Y. Wikmark, J.-E. Bäckvall, M. T. Reetz, *Chem. A Eur. J.* **2016**, *22*, 5046–5054.

[34] R. Singh, M. Bordeaux, R. Fasan, *ACS Catal.* **2014**, *4*, 546–552.

[35] D. Röthlisberger, O. Khersonsky, A. M. Wollacott, L. Jiang, J. DeChancie, J. Betker, J. L. Gallaher, E. A. Althoff, A. Zanghellini, O. Dym, et al., *Nature* **2008**, *453*, 190–195.

[36] F. Rosati, G. Roelfes, *ChemCatChem* **2010**, *2*, 916–927.

[37] C. M. Thomas, T. R. Ward, *Chem. Soc. Rev.* **2005**, *34*, 337.

[38] M. E. Wilson, G. M. Whitesides, *J. Am. Chem. Soc.* **1978**, *100*, 306–307.

[39] C.-C. Lin, C.-W. Lin, A. S. C. Chan, *Tetrahedron: Asymmetry* **1999**, *10*, 1887–1893.

[40] M. Ohashi, T. Koshiyama, T. Ueno, M. Yanase, H. Fujii, Y. Watanabe, *Angew. Chemie Int. Ed.* **2003**, *42*, 1005–1008.

[41] T. Ueno, M. Suzuki, T. Goto, T. Matsumoto, K. Nagayama, Y. Watanabe, *Angew. Chemie Int. Ed.* **2004**, *43*, 2527–2530.

[42] S. Nimri, E. Keinan, *J. Am. Chem. Soc.* **1999**, *121*, 8978–8982.

[43] T. Heinisch, T. R. Ward, *Am. Chem. Soc.* **2016**, *49*, 1711–1721.

[44] J. Steinreiber, T. R. Ward, *Coord. Chem. Rev.* **2008**, *252*, 751–766.

[45] T. M. Rana, C. F. Meares, *J. Am. Chem. Soc.* **1991**, *113*, 1859–1861.

[46] R. R. Davies, M. D. Distefano, *J. Am. Chem. Soc.* **1997**, *119*, 11643–11652.

[47] B. Kowalewski, J. Poppe, U. Demmer, E. Warkentin, T. Dierks, U. Ermler, K. Schneider, *J. Am. Chem. Soc.* **2012**, *134*, 9768–9774.

[48] J. Schemberg, K. Schneider, U. Demmer, E. Warkentin, A. Müller, U. Ermler, *Angew. Chemie Int. Ed.* **2007**, *46*, 2408–2413.

[49] J. Poppe, E. Warkentin, U. Demmer, B. Kowalewski, T. Dierks, K. Schneider, U. Ermler, *J. Inorg. Biochem.* **2014**, *138*, 122–128.

[50] J. Poppe, S. Brünle, R. Hail, K. Wiesemann, K. Schneider, U. Ermler, *FEBS J.* **2018**, *285*, 4602–4616.

[51] S. Brünle, J. Poppe, R. Hail, U. Demmer, U. Ermler, *J. Inorg. Biochem.* **2018**, *189*, 172–179.

[52] J. Schemberg, K. Schneider, D. Fenske, A. Müller, *ChemBioChem* **2008**, *9*, 595–602.

[53] D. Sippel, J. Schlesier, M. Rohde, C. Trncik, L. Decamps, I. Djurdjevic, T. Spatzal, S. L. A. Andrade, O. Einsle, *J. Biol. Inorg. Chem.* **2017**, *22*, 161–168.

[54] F. Sainsbury, P. V Jutras, J. Vorster, M.-C. Goulet, D. Michaud, *Front. Plant Sci.* **2016**, *7*, DOI 10.3389/fpls.2016.00141.

[55] S. Boivin, S. Kozak, R. Meijers, *Protein Expr. Purif.* **2013**, *91*, 192–206.

[56] D. Kishore, S. Kundu, A. M. Kayastha, *PLoS One* **2012**, *7*, DOI 10.1371/journal.pone.0050380.

[57] K. Sato, M. Aoki, R. Noyori, *Science* **1998**, *281*, 1646–1647.

[58] R. Noyori, M. Aoki, K. Sato, *Chem. Commun.* **2003**, *16*, 1977–1986.

[59] H. Bisswanger, *Perspect. Sci.* **2014**, *1*, 41–55.

[60] P. V Attwood, P. G. Besant, M. J. Piggott, *Amino Acids* **2011**, *40*, 1035–1051.

[61] A. Marchler-Bauer, Y. Bo, L. Han, J. He, C. J. Lanczycki, S. Lu, F. Chitsaz, M. K. Derbyshire, R. C. Geer, N. R. Gonzales, et al., *Nucleic Acids Res.* **2017**, *45*, D200–D203.

[62] S. Ramón-Maiques, A. Marina, F. Gil-Ortiz, I. Fita, V. Rubio, *Structure* **2002**, *10*, 329–342.

[63] S. Ramón-Maiques, A. Marina, M. Uriarte, I. Fita, V. Rubio, *J. Mol. Biol.* **2000**, *299*, 463–476.

[64] Z. Chen, W. Meyer, S. Rappert, J. Sun, A.-P. Zeng, *Appl. Environ. Microbiol.* **2011**, *77*, 4352–60.

[65] M. N. Cahyanto, H. Kawasaki, M. Nagashio, K. Fujiyama, T. Seki, *Microbiology* **2006**, *152*, 105–112.

[66] M. S. M. Jetten, M. T. Follettie, A. J. Sinskey, *Appl. Microbiol. Biotechnol.* **1995**, *43*, 76–82.

[67] I. Shiio, R. Miyajima, *J. Biochem.* **1969**, *65*, 849–859.

[68] S. Black, N. G. Wright, *J. Biol. Chem.* **1955**, *213*, 27–38.

[69] G. Sun, R. J. A. Budde, *Biochemistry* **1997**, *36*, 2139–2146.

[70] J. P. Walsh, R. M. Bell, in *Methods Enzymol.*, Elsevier B.V, **1992**, pp. 153–162.

[71] S. Cheek, H. Zhang, N. V Grishin, *J. Mol. Biol.* **2002**, *320*, 855–881.

[72] J. Cremer, L. Eggeling, H. Sahm, *Appl. Environ. Microbiol.* **1991**, *57*, 1746–1752.

[73] M. Boros, J. Kökösi, J. Vámos, I. Kövesdi, B. Noszál, *Amino Acids* **2007**, *33*, 709–717.

[74] K. Drauz, H. Gröger, O. May, *Enzyme Catalysis in Organic Synthesis*, WiVCH, **2012**.

[75] K. Sato, M. Aoki, J. Takagi, R. Noyori, *J. Am. Chem. Soc.* **1997**, *119*, 12386–12387.

[76] N. Adebar, J. E. Choi, L. Schober, R. Miyake, T. Iura, H. Kawabata, H. Gröger, *ChemCatChem* **2019**, *11*, 5788–5793.

[77] T. Iura, Y. Dekishima, T. Sakamoto, M. Hara, H. Hiraoka, H. Gröger, J. E. Choi, *Carbonyl Reductase, Gene Encoding It and Process for Producing Optically Active Compounds Using the Same*, **2019**, JP2019-211797.

[78] P. Alagona, *Core Evid.* **2010**, *5*, 91–105.

[79] S. D. Dwivedi, D. J. Patel, A. P. Shah, B. Khera, *Pitavastatin Calcium and Process for Its*

Preparation, **2011**, WO2012025939A1.

[80] M. Suzuki, Y. Yanagawa, H. Iwasaki, H. Kanda, K. Yanagihara, H. Matsumoto, Y. Ohara, Y. Yazaki, R. Sakoda, *Bioorg. Med. Chem. Lett.* **1999**, *9*, 2977–2982.

[81] K. Kajinami, N. Takekoshi, Y. Saito, *Cardiovasc. Drug Rev.* **2006**, *21*, 199–215.

[82] Y. Ohara, M. Suzuki, Y. Yanagawa, Y. Takada, *Process for the Preparation of Quinoline Derivative and Intermediate Therefor*, **1999**, EP1099694B1.

[83] G.-P. Chen, P. K. Kapa, E. M. Loeser, U. Beutler, W. Zaugg, M. J. Girgis, *Process for the Manufacture of Organic Compounds*, **2003**, WO2003064382A2.

[84] A. Shafiee, H. Motamedi, A. King, *Appl. Microbiol. Biotechnol.* **1998**, *49*, 709–717.

[85] B. Das, P. Madhusudhan, A. Kashinatham, *Bioorg. Med. Chem. Lett.* **1998**, *8*, 1403–1406.

[86] R. N. Patel, A. Banerjee, L. Chu, D. Brozozowski, V. Nanduri, L. J. Szarka, *J. Am. Oil Chem. Soc.* **1998**, *75*, 1473–1482.

[87] R. N. Patel, *Curr. Opin. Biotechnol.* **2001**, *12*, 587–604.

[88] R. N. Patel, A. Banerjee, C. G. McNamee, D. Brzozowski, R. L. Hanson, L. J. Szarka, *Enzyme Microb. Technol.* **1993**, *15*, 1014–1021.

[89] H. Hiraoka, M. Ueda, M. Hara, *Carbonyl Reductase, Gene Encoding the Same, and Process for Producing Optically Active Alcohols Using the Same*, **2008**, US 7335757B2.

[90] H. Hiraoka, M. Ueda, M. Hara, *Novel Carbonyl Reductase, Gene Encoding It and Process for Producing Optically Active Alcohols Using the Same*, **2003**, EP1491633B1.

[91] N. Kizaki, M. Yano, M. Funaki, T. Takesue, S. Yasohara, Yoshihiko Morikawa, T. Nakai, S. Kataoka, Michihiko Shimizu, *Carbonyl Reductase, Gene Thereof and Method of Using the Same*, **2005**, US7794993B2.

[92] H. K. Chenault, E. S. Simon, G. M. Whitesides, *Biotechnol. Genet. Eng. Rev.* **1988**, *6*, 221–270.

[93] C.-H. Wong, G. M. Whitesides, *J. Am. Chem. Soc* **1981**, *243*, 4890–4899.

[94] K. Honda, N. Hara, M. Cheng, A. Nakamura, K. Mandai, K. Okano, H. Ohtake, *Metab. Eng.* **2016**, *35*, 114–120.

[95] S. Hachisuka, T. Sato, H. Atomi, *J. Bacteriol.* **2017**, *199*, e00162-17.

[96] H. Taniguchi, S. Sungwallek, P. Chotchuang, K. Okano, K. Honda, *J. Bacteriol.* **2017**, *199*, e00359-17.

[97] J. T. Wu, L. H. Wu, J. A. Knight, *Clin. Chem.* **1986**, *32*, 314–319.

[98] P. E. Smith, J. J. Tanner, *J. Mol. Recognit.* **2000**, *13*, 27–34.

[99] K. Honda, M. Inoue, T. Ono, K. Okano, Y. Dekishima, H. Kawabata, *J. Biosci. Bioeng.* **2017**, *123*, 673–678.

[100] K. Honda, T. Ono, K. Okano, R. Miyake, Y. Dekishima, H. Kawabata, *J. Biosci. Bioeng.* **2019**, *127*, 145–149.

[101] E. Vázquez-Figueroa, J. Chaparro-Riggers, A. S. Bommarius, *ChemBioChem* **2007**, *8*, 2295–2301.

[102] A. Hibino, H. Ohtake, *Process Biochem.* **2013**, *48*, 838–843.

[103] E. Keinan, E. K. Hafeli, K. K. Seth, R. Lamed, *J. Am. Chem. Soc.* **1986**, *108*, 162–169.

[104] A. L. Serdakowski, J. S. Dordick, *Trends Biotechnol.* **2008**, *26*, 48–54.

[105] A. Kumar, K. Dhar, S. S. Kanwar, P. K. Arora, *Biol. Proced. Online* **2016**, *18*, DOI 10.1186/S12575-016-0033-2.

[106] T. D. Hurley, W. F. Bosron, J. A. Hamilton, L. M. Amzel, *Proc. Natl. Acad. Sci. U. S. A.* **1991**, *88*, 8149–53.

[107] A. M. Klibanov, *Trends Biotechnol.* **1997**, *15*, 97–101.

[108] V. Stepankova, S. Bidmanova, T. Koudelakova, Z. Prokop, R. Chaloupkova, J. Damborsky, *ACS Catal.* **2013**, *3*, 2823–2836.

[109] E. Riesel, E. Katciialyki, *J. Biol. Chem.* **1964**, *239*, 1521–1524.

[110] G. Johansson, L. Ögren, B. Olsson, *Anal. Chim. Acta* **1983**, *145*, 79–85.

[111] B. Orsat, B. Wirz, S. Bischof, *Chimia (Aarau).* **1999**, *53*, 579–584.

[112] C. Wiles, P. Watts, *Green Chem.* **2012**, *14*, 38–54.

[113] P. He, G. Greenway, S. J. Haswell, *Process Biochem.* **2010**, *45*, 593–597.

[114] F. Costantini, E. M. Benetti, D. N. Reinhoudt, J. Huskens, G. J. Vancso, W. Verboom, *Lab Chip* **2010**, *10*, 3407.

[115] K. Koch, R. J. F. van den Berg, P. J. Nieuwland, R. Wijtmans, H. E. Schoemaker, J. C. M. van Hest, F. P. J. T. Rutjes, *Biotechnol. Bioeng.* **2008**, *99*, 1028–1033.

[116] R. Karande, A. Schmid, K. Buehler, *Adv. Synth. Catal.* **2011**, *353*, 2511–2521.

[117] P. Domínguez de María, *Industrial Biorenewables – a Practical Approach*, Wiley-Blackwell, **2016**.

[118] K. Weissermel, H.-J. Arpe, *Industrial Organic Chemistry*, VCH, **1997**.

[119] T. Betke, J. Higuchi, P. Rommelmann, K. Oike, T. Nomura, Y. Kato, Y. Asano, H. Gröger, *ChemBioChem* **2018**, *19*, 768–779.

[120] F. F. Fleming, L. Yao, P. C. Ravikumar, L. Funk, B. C. Shook, *J. Med. Chem.* **2010**, *53*, 7902–7917.

[121] S. T. Murphy, H. L. Case, E. Ellsworth, S. Hagen, M. Huband, T. Joannides, C. Limberakis, K. R. Marotti, A. M. Ottolini, M. Rauckhorst, et al., *Bioorg. Med. Chem. Lett.* **2007**, *17*, 2150–2155.

[122] R. M. Oballa, J.-F. Truchon, C. I. Bayly, N. Chauret, S. Day, S. Crane, C. Berthelette, *Bioorg. Med. Chem. Lett.* **2007**, *17*, 998–1002.

[123] J. A. Ziemniak, R. J. Wynn, J. V. Aranda, B. J. Zarowitz, J. J. Schentag, *Dev. Pharmacol. Ther.* **1984**, *7*, 30–38.

[124] H. A. Strong, M. Spino, *J. Chromatogr. B Biomed. Sci. Appl.* **1987**, *422*, 301–308.

[125] A. W. Patterson, W. J. L. Wood, M. Hornsby, S. Lesley, G. Spraggon, Jonathan A. Ellman, *J. Med. Chem.* **2006**, *49*, 6298–6307.

[126] K. V. Raghavan, B. M. Reddy, *Industrial Catalysis and Separations: Innovations for Process*

Intensification, Apple Academic Press In, **2014**.

[127] J. Dowling, G. Yao, H. Chang, H. Peng, J. Vessels, R. C. Petter, G. Kumaravel, *Triazolopyrazines and Methods of Making and Using the Same*, **2004**, WO2004092177A1.

[128] Takashi Sato, Hiroaki Yuasa, Shinya Nakashima, Takashi Sato, Hiroaki Yuasa, Shinya Nakashima, *Additive for Imparting Low Heat Build-up to Rubber Component*, **2016**, US20180273723A1.

[129] P. M. Pitis, R. E. Boyd, T. A. M. Daubert, M. J. Hawkins, G. Liu, A. C. Speerschneider, *Compounds for Modulating S1P1 Activity and Methods of Using the Same*, **2018**, WO2018231745.

[130] C. Zhu, C. Sun, Y. Wei, *Synthesis (Stuttg).* **2010**, *2010*, 4235–4241.

[131] I. Dutta, S. Yadav, A. Sarbajna, S. De, M. Hölscher, W. Leitner, J. K. Bera, *J. Am. Chem. Soc.* **2018**, *140*, 8662–8666.

[132] P. Capdevielle, A. Lavigne, M. Maumy, *Synthesis (Stuttg).* **1989**, *1989*, 451–452.

[133] B. P. Bandgar, S. S. Makone, *Synth. Commun.* **2006**, *36*, 1347–1352.

[134] Y. M. Hijji, R. Rajan, H. Darwish Tabba, A. Abu-Yousef, H. Ben Yahia, *Eur. J. Chem.* **2018**, *9*, 269–274.

[135] X.-Y. Ma, Y. He, T.-T. Lu, M. Lu, *Tetrahedron* **2013**, *69*, 2560–2564.

[136] M. Sridhar, M. K. K. Reddy, V. V. Sairam, J. Raveendra, K. R. Godala, C. Narsaiah, B. C. Ramanaiah, C. S. Reddy, *Tetrahedron Lett.* **2012**, *53*, 3421–3424.

[137] K. Yamaguchi, H. Fujiwara, Y. Ogasawara, M. Kotani, N. Mizuno, *Angew. Chemie Int. Ed.* **2007**, *46*, 3922–3925.

[138] R. Mariscal, P. Maireles-Torres, M. Ojeda, I. Sádaba, M. López Granados, *Energy Environ. Sci.* **2016**, *9*, 1144–1189.

[139] Y. Kato, R. Ooi, Y. Asano, *Arch. Microbiol.* **1998**, *170*, 85–90.

[140] Y. Asano, Y. Kato, *FEMS Microbiol. Lett.* **1998**, *158*, 185–190.

[141] Y. Kato, R. Ooi, Y. Asano, *Appl. Environ. Microbiol.* **2000**, *66*, 2290–2296.

[142] Y. Kato, S. Yoshida, S.-X. Xie, Y. Asano, *J. Biosci. Bioeng.* **2004**, *97*, 250–259.

[143] K.-I. Oinuma, Y. Hashimoto, K. Konishi, M. Goda, T. Noguchi, H. Higashibata, M. Kobayashi, *J. Biol. Chem.* **2003**, *278*, 29600–29608.

[144] Y. Kato, Y. Asano, *Biosci. Biotechnol. Biochem.* **2005**, *69*, 2254–2257.

[145] K. Kobayashi, S. Yoshioka, Y. Kato, Y. Asano, S. Aono, *J. Biol. Chem.* **2005**, *280*, 5486–90.

[146] Y. Kato, Y. Asano, *Appl. Microbiol. Biotechnol.* **2006**, *70*, 92–101.

[147] K. Kobayashi, B. Pal, S. Yoshioka, Y. Kato, Y. Asano, T. Kitagawa, S. Aono, *J. Inorg. Biochem.* **2006**, *100*, 1069–1074.

[148] K. Konishi, K. Ishida, K.-I. Oinuma, T. Ohta, Y. Hashimoto, H. Higashibata, T. Kitagawa, M. Kobayashi, *J. Biol. Chem.* **2004**, *279*, 47619–47625.

[149] K. Konishi, T. Ohta, K.-I. Oinuma, Y. Hashimoto, T. Kitagawa, M. Kobayashi, *Proc. Natl. Acad.*

Sci. **2006**, *103*, 564–568.

[150] R.-Z. Liao, W. Thiel, *J. Phys. Chem. B* **2012**, *116*, 9396–9408.

[151] X.-L. Pan, F.-C. Cui, W. Liu, J.-Y. Liu, *J. Phys. Chem. B* **2012**, *116*, 5689–5693.

[152] J. Nomura, H. Hashimoto, T. Ohta, Y. Hashimoto, K. Wada, Y. Naruta, K.-I. Oinuma, M. Kobayashi, *Proc. Natl. Acad. Sci.* **2013**, *110*, 2810–2815.

[153] H. Sawai, H. Sugimoto, Y. Kato, Y. Asano, Y. Shiro, S. Aono, *J. Biol. Chem.* **2009**, *284*, 32089–32096.

[154] Y. Kato, R. Ooi, Y. Asano, *J. Mol. Catal. - B Enzym.* **1999**, *6*, 249–256.

[155] S.-X. Xie, Y. Kato, H. Komeda, S. Yoshida, A. Yasuhisa, *Biochemistry* **2003**, *42*, 12056–12066.

[156] A. Bohre, S. Dutta, B. Saha, M. M. Abu-Omar, *ACS Sustain. Chem. Eng.* **2015**, *3*, 1263–1277.

[157] T. Eicher, S. Hauptmann, A. Speicher, *The Chemistry of Heterocycles : Structure, Reactions, Syntheses, and Applications*, Wiley-VCH, **2003**.

[158] T. Yamaguchi, Y. Asano, *Genome Announc.* **2016**, *4*, e00406-16.

[159] N. Jain, A. Kumar, S. M. S. Chauhan, *Tetrahedron Lett.* **2005**, *46*, 2599–2602.

[160] Y. Kato, K. Nakamura, H. Sakiyama, S. G. Mayhew, Y. Asano, *Biochemistry* **2000**, *39*, 800–809.

[161] R. Rädisch, M. Chmátal, L. Rucká, P. Novotný, L. Petrásková, P. Halada, M. Kotik, M. Pátek, L. Martínková, *Int. J. Biol. Macromol.* **2018**, *115*, 746–753.

[162] J. E. Choi, S. Shinoda, R. Inoue, D. Zheng, H. Gröger, Y. Asano, *Biocatal. Biotransformation* **2019**, *37*, 414–420.

[163] T. Betke, P. Rommelmann, K. Oike, Y. Asano, H. Gröger, *Angew. Chemie Int. Ed.* **2017**, *56*, 12361–12366.

[164] Y. Asano, A. Nakazawa, K. Endo, *J. Biol. Chem.* **1987**, *262*, 10346–10354.

[165] Y. Asano, *J. Biotechnol.* **2002**, *94*, 65–72.

[166] D. Piovesan, G. Minervini, S. C. E. Tosatto, *Nucleic Acids Res.* **2016**, *44*, W367–W374.

[167] P. Shannon, A. Markiel, O. Ozier, N. S. Baliga, J. T. Wang, D. Ramage, N. Amin, B. Schwikowski, T. Ideker, *Genome Res.* **2003**, *13*, 2498–504.

[168] S. Kumar, C. S. Chen, D. J. Waxman, J. R. Halpert, *J. Biol. Chem.* **2005**, *280*, 19569–19575.

[169] P. R. Wilderman, S. C. Gay, H.-H. Jang, Q. Zhang, C. D. Stout, J. R. Halpert, *FEBS J.* **2012**, *279*, 1607–1620.

[170] K. Yamada, *Plasmid Vector for Promoting Expression of Foreign Gene in Escherichia Coli, Recombinant Escherichia Coli, Method for Producing Chemical Substance with Recombinant Escherichia Coli, and Method for Producing Recombinant Protein*, **2003**, JP2003199014A.

[171] C. Colovos, T. O. Yeates, *Protein Sci.* **1993**, *2*, 1511–1519.

[172] M. D. Hanwell, D. E. Curtis, D. C. Lonie, T. Vandermeersch, E. Zurek, G. R. Hutchison, *J. Cheminform.* **2012**, *4*, 17.

[173] G. M. Morris, R. Huey, W. Lindstrom, M. F. Sanner, R. K. Belew, D. S. Goodsell, A. J. Olson,

J. Comput. Chem. **2009**, *30*, 2785–2791.

[174] A. C. Wallace, R. A. Laskowski, J. M. Thornton, *Protein Eng. Des. Sel.* **1995**, *8*, 127–134.

[175] E. F. Pettersen, T. D. Goddard, C. C. Huang, G. S. Couch, D. M. Greenblatt, E. C. Meng, T. E. Ferrin, *J. Comput. Chem.* **2004**, *25*, 1605–1612.

[176] J. C. Setubal, P. Dos Santos, B. S. Goldman, H. Ertesvåg, G. Espin, L. M. Rubio, S. Valla, N. F. Almeida, D. Balasubramanian, L. Cromes, et al., *J. Bacteriol.* **2009**, *191*, 4534–4545.